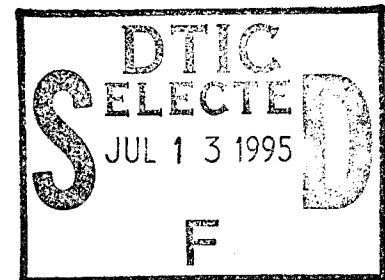RL-TR-95-67, Vol I (of two)
Final Technical Report
April 1995

ULTRA WIDE BAND (UWB) RADAR DETECTION ANALYSIS AND DEMONSTRATION PROGRAM, PHASES I AND II

Syracuse University

APPROVED FOR PUBLIC RELEASE; DISTRIBUTION UNLIMITED.
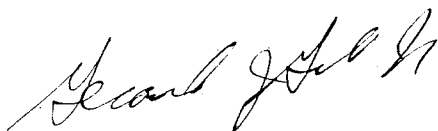
19950707 042

DTI‍ QUALITY INSPECTED 5

Rome Laboratory
Air Force Materiel Command
Griffiss Air Force Base, New York

This report has been reviewed by the Rome Laboratory Public Affairs Office (PA) and is releasable to the National Technical Information Service (NTIS). At NTIS it will be releasable to the general public, including foreign nations.

RL-TR-95-67, Vol I (of two) has been reviewed and is approved for publication.

APPROVED:

GERARD J. GENELLO
Project Engineer

FOR THE COMMANDER:

DONALD W. HANSON
Director of Surveillance & Photonics

ULTRA WIDE BAND (UWB) RADAR DETECTION ANALYSIS AND DEMONSTRATION PROGRAM, PHASES I AND II

Dr. Donald D. Weiner
Dr. Tapan K. Sarkar
Dr. Hong Wang

Approved for public release; distribution unlimited.

REPORT DOCUMENTATION PAGE

Form Approved
OMB No. 0704-0188

1. AGENCY USE ONLY (Leave Blank)	2. REPORT DATE	3. REPORT TYPE AND DATES COVERED
	April 1995	Final Feb 91 – Dec 94

4. TITLE AND SUBTITLE
ULTRA WIDE BAND (UWB) RADAR DETECTION ANALYSIS AND DEMONSTRATION PROGRAM, PHASES I AND II

5. FUNDING NUMBERS
C - F30602-91-C-0035
PE - 63737D
PR - 1706
TA - 06
WU - 02

6. AUTHOR(S)
Dr. Donald D. Weiner, Dr. Tapan K. Sarkar, and Dr. Hong Wang

7. PERFORMING ORGANIZATION NAME(S) AND ADDRESS(ES)
Syracuse University
Electrical & Computer Engineering Department
121 Link Hall
Syracuse NY 13244

8. PERFORMING ORGANIZATION REPORT NUMBER
N/A

9. SPONSORING/MONITORING AGENCY NAME(S) AND ADDRESS(ES)
Advanced Research Projects Agency
3701 N. Fairfax Dr.
Arlington VA 22203-1714
Phillips Lab/WSH
3550 Aberdeen Ave SE, Kirtland NM 87117-5776

Rome Laboratory (OCTS)
26 Electronic Pky
Griffiss AFB NY 13441-4514

10. SPONSORING/MONITORING AGENCY REPORT NUMBER
RL-TR-95-67, Vol I (of two)

11. SUPPLEMENTARY NOTES
Rome Laboratory Project Engineer: Clifford Tsao/OCTS/(315) 330-3576
Subcontractor: Technology Service Corporation

12a. DISTRIBUTION/AVAILABILITY STATEMENT
Approved for public release; distribution unlimited.

12b. DISTRIBUTION CODE

13. ABSTRACT (Maximum 200 words)
This report presents the T-pulse concept. The first part presents the T-pulse as a flexible tool for the analysis of waveforms exhibiting time-frequency localization. This is useful when T-pulse processing is performed on receive. It is shown how the T-pulse generalizes the Fourier, Gabor and Wavelet transforms. The analysis includes both the continuous and the discrete cases. The second part of this report presents the T-pulse as a waveshaping technique for target identification through parameter estimation. In this case one desires to transmit a T-pulse. An example is presented to illustrate how the T-pulse technique can be used to examine the fine structure of the electromagnetic response of a target. Since the T-pulse may be very narrow band, conventional equipment may be used on transmit and receive. Finally, a user oriented computer program is presented to illustrate how a T-pulse can be generated.

14. SUBJECT TERMS T-pulse technique, waveforms, time-frequency localization, parameter estimation, electromagnetic

15. NUMBER OF PAGES
268

16. PRICE CODE

17. SECURITY CLASSIFICATION OF REPORT	18. SECURITY CLASSIFICATION OF THIS PAGE	19. SECURITY CLASSIFICATION OF ABSTRACT	20. LIMITATION OF ABSTRACT
UNCLASSIFIED	UNCLASSIFIED	UNCLASSIFIED	UL

NSN 7540-01-280-5500

Standard Form 298 (Rev. 2-89)
Prescribed by ANSI Std. Z39-18
298-102

Contract No. F30602-91-C-0035

ULTRA WIDE BAND (UWB) RADAR DETECTION ANALYSIS AND DEMONSTRATION PROGRAM

Phase I: 15 Feb 91 - 15 June 92

Final Technical Report

Vol. I

Submitted by

D. D. Weiner
Principal Investigator
Syracuse University
Electrical & Computer Engineering Department
121 Link Hall
Syracuse, NY 13244
Tel/Fax: (315) 443-4428

PREFACE

This two volume report presents results from the first phase of the Ultra-Wide Band (UWB) Radar Detection Algorithm Analysis and Demonstration Program, conducted for the Air Force Rome Laboratory (AFRL) and the Defense Advanced Research Projects Agency (DARPA) by Syracuse University (Volume I) and Technology Service Corporation (Volume II).

Unlike many other UWB programs conducted out in recent years, this research and development effort emphasizes surveillance applications utilizing UWB radar technology, designed for reliable real-time detection of airborne low-observables. Therefore, much of the work in this report (especially in Volume I) focuses on signal processing issues impacting the subclutter visibility of UWB radar systems. It's well known that both the time domain resolution (i.e., the range cell size) and the capability of the system to discriminate the target and clutter are crucial to the system's subclutter visibility. Although the clutter power reduction gain of wideband/UWB systems has been well understood since 1950, there have been no documented studies of the discrimination capability provided by UWB radar systems, and its associated subclutter visibility performance gain. The main objective of this research is to document the improved discrimination capability of UWB radar systems in both the velocity and polarization domains. As shown in Volume I of this report, UWB technology can offer a subclutter visibility performance gain of 20 to 30 dB, over narrow band technology, **in addition to** its well known clutter power reduction gain. This report illustrates the performance potential of UWB wide area surveillance systems, which is severely underestimated by the radar community. This conclusion applies to UWB systems using either short pulse or spread spectrum technology with large or small relative bandwidth. Intuitively speaking, the additional performance gain in the velocity (range rate) domain is derived from the fact that the fine range resolution provided by a UWB system amplifies the effective velocity difference between the target and clutter, resulting in a much more effective discriminant against clutter. Moreover, processing in the polarization domain with the use of UWB radar waveforms to resolve the target into multiple dominant scatterers eliminates the so-called "signal cancellation" problem associated with any narrow band clutter polarization canceler, thus producing a much more reliable polarization discriminant which is needed to exploit the additional performance gain.

Another main objective of this effort is to develop the signal processing algorithms in both the velocity and polarization domains that approach the performance potential of a UWB

surveillance system. In Phase I, our efforts for achieving this objective are limited to a preliminary development in the velocity domain, while a major effort is planned for Phase II.

In Part I of Volume I of this report, two Moving Target Detection (MTD) algorithms are developed for UWB surveillance applications. The first one is a simple, nonadaptive algorithm designed for ground-based radar applications, where the clutter spectrum is usually quite simple. The second algorithm is a more sophisticated adaptive MTD algorithm, designed for the airborne UWB surveillance radar applications, where the clutter is severely nonhomogeneous with a very complicated angle-"doppler" spectrum. It should be noted that these UWB MTD algorithms for weak signal detection are developed not based upon a trivial extension of the narrow band radar signal processing algorithms. Although the clutter suppression filter portion of the UWB MTD can remain essentially unchanged from that designed for the application to the narrow band radar system, the multiple-pulse integration portion, designed for maximally enhancing the target return over the multiple-pulse processing interval in the presence of still relatively strong clutter suppression residue, demands careful thoughts. This is due to the fact that the target components at the output of the clutter suppression filter are significantly distorted from pulse to pulse by the clutter suppression filter, especially when the range-walk rate of the target is less than one range cell per Pulse Repetition Interval (PRI). If one can assume that the target components at the output of the clutter suppression filter are already sufficiently stronger than the clutter suppression residue (i.e, with a SCR above 6 dB) and do not have significant distortion, then a "line-up" operation can be performed on the already strong target components before the multipulse integration if the integration is still necessary. The above special case is investigated by TSC and reported in Volume II of this report. The two UWB MTD algorithms developed in Part I of Volume I are designed for near optimal **weak**-target detection, since their multipulse integration functions well even if clutter suppression residue is still much stronger than the target components at the output of the clutter suppression filter. Hardware implementation of these two algorithms, especially of the nonadaptive UWB MTD, is well within the state of the art of processor technology.

In addition to the system performance evaluation and algorithm development, this effort also contains laboratory experimentation and demonstration. The objective is to demonstrate the performance potential of a UWB surveillance system with selected signal processing algorithms, using the existing radar facilities at the AFRL. Due to limited funding, only the demonstration

of a UWB system employing an adaptive polarization canceler is planned. Since experimental results documenting UWB target polarization characteristics are essentially nonexistent, the demonstration has been pursued with much caution. In Phase I a preliminary demonstration of the adaptive multiband (i.e, multiple narrow band) polarization canceler developed in Volume I Part II of this report is conducted. The purpose of starting with a multiband demonstration is not just to gain laboratory experience required for performing the UWB polarization processing demonstration. As mentioned earlier, the elimination of the signal cancellation problem associated with narrow band polarization processing is the main reason for employing a UWB system to obtain the additional significant performance gain in the polarization domain. With respect to the elimination of the signal cancellation problem, however, multiple dominant target scatterers obtained by using a UWB waveform basically serve the same role as a single-dominant scatterer measured using a multiband system. At the same time, the distributed-clutter components of concern obtained by these two different systems statistically differ only in their power. Therefore, performing a relatively simple, low cost multiband demonstration can equivalently illustrate the most critical factors required to eliminate the signal cancellation problem. Of course, multiband systems can't emulate UWB systems with respect to range resolution, clutter power, etc., and a demonstration of a UWB system with polarization processing is still necessary. The results of the successful multiband demonstration are included in Volume I Part II of this report, together with the development of the multiband polarization canceler algorithm and the evaluation of the performance potential of the UWB system employing polarization processing.

Volume II of this report contains the results of the work performed by Messrs. Allan Corbeil and Lee Moyer of TSC under a subcontract from Syracuse University. All three parts of this report are basically self-contained with overlap and cross reference minimized. The work in Volume I Part I is carried out by Dr. Lujing Cai and Prof. Hong Wang, and in Volume I Part II by Mr. C.J. Lee and Prof. Hong Wang, all with Syracuse University.

Messrs. R. Brown, G. Genello, D. Mokry, C. Tsao (Project Engineer), M. Wicks of AFRL and Dr. D. Giglio of DARPA have provided many helpful suggestions during the performance of the contract work. Their help is greatly appreciated.

CONTENTS OF VOLUME I

Part II Adaptive Multiband and Optimum Ultra-Wideband Polarization Cancelers 75

Multiple Pulse Processing for Over-Resolved Moving Target Detection

LIST OF FIGURES

LIST OF PRINCIPAL SYMBOLS

$s_r(t)$		transmitted waveform
$x_r(t)$		received data waveform
$\mathbf{x}_r(t)$		received data waveform vector
$\tilde{\mathbf{x}}(t)$		complex representation of received waveform
$s_r(t),$	$\mathbf{s}_r(t)$	target signal return
$n_c(t),$	$\mathbf{n}_c(t)$	interference/clutter return
$n_n(t),$	$\mathbf{n}_n(t)$	receiver noise
T		total observation time
T_p		pulse repetition interval of transmitted waveform
T'_p		data segmentation interval
$\Delta\tau$		pulse width
M		number of pulses
J		number of scatterers
c		wave propagation velocity
v_s		target velocity
v_c		interference/clutter velocity
α_s		time scale of a moving target
α_c		time scale of interference/clutter
f_s		normalized Doppler frequency shift of target
f_c		normalized Doppler frequency shift of interference
Δf		Doppler frequency difference of target and interference
ρ		range walk rate
$g(t)$		transmitted single pulse waveform
$G(f)$		Fourier transform of $g(t)$
$\mathbf{g}(t)$		received signal waveform vector
$\mathbf{G}(t)$		scatterer waveform matrix
τ_j		arrival time of jth scatterer
j		amplitude of jth scatterer
$K_c(t,\tau)$		covariance function of interference
$\mathbf{K}_c(t,\tau)$		waveform covariance matrix of interference/clutter
$\mathbf{K}(t,\tau)$		total waveform covariance matrix of interference and noise
$K_{dr}(\tau,\lambda)$		interference scattering function in time and range
$K_d(\tau)$		interference scattering function in time
$\kappa(t,\tau)$		covariance kernel
$\kappa^{-1}(t,\tau)$		inverse covariance kernel
$\phi(t)$		eigen function of $\kappa(t,\tau)$

B	signal bandwidth
RBW	relative bandwidth
β	bandwidth ratio
N_0	power spectrum level of receiver noise
σ_s^2	signal variance
σ_c^2	interference power
$\mathbf{R}_c$	inter-pulse covariance matrix of interference/clutter
$\mathbf{R}$	inter-pulse covariance matrix of interference and noise
$h(\tau)$	single pulse correlation function
L_c	interference/clutter range extent
$f(\cdot)$	probability density function
$\mathrm{I}_J(\cdot)$	Jth order modified Bessel function of first kind
η	test statistic
η_0	decision threshold
P_f	probability of false alarm
P_d	probability of detection
$\mathbf{s}$	signal vector
$\mathbf{w}$	weight vector
γ_c	pulse compression ratio
Δd	range cell separation
N	number of range cells under test
ν	normalized range cell spacing
σ_f	interfere/clutter spread of Gaussian-shaped spectrmun
$\mathbf{T}$	operation matrix of canceler
$\mathrm{Cov}(\cdot)$	covariance matrix of
$\mathrm{E}(\cdot)$	mean of
$(\cdot)^*$	complex conjugate
$(\cdot)^H$	conjugate transpose
$\mathrm{tr}(\cdot)$	trace of a square matrix

I.1   INTRODUCTION

It is well known that ultra-wideband (UWB) radar systems have much improved range resolution, which has been widely used in radar imaging and remote sensing for target signature analysis and identification/classification[1,2]. During the past decades, great research efforts have been focused on these topics and many encouraging results have been achieved. In contrast, how the UWB technology can benefit traditional radar tasks such as target detection and tracking remains largely untouched without a systematic investigation.

From the viewpoint of information theory, one should expect to receive more information about the presence, location, and identity of the targets under observation, since the large signal bandwidth can provide a wider viewing aspect in the frequency domain. Of course, such an advantage should also be important for weak target detection in an increasingly hostile surveillance environment. The additional information provided by UWB waveforms will improve the quality of the hypothesis test to determine the presence or absence of targets.

In fact, it is already known that high resolution can largely reduce the clutter power contained in a single range cell, leading to a significant performance improvement in the presence of strong distributed clutter. Also, due to the reduction of the range cell size, the familiar point-target modeling is no longer adequate to describe the received target return from the transmitted UWB waveform. The individual parts of a target can be well resolved so that the multiple dominant scattering (MDS) centers of the target may appear in a number of well-separated range cells [3]. The effects of the clutter reduction and MDS target model on the system detection performance have been studied in [4,5], where the detectability of the range-extended targets as a function of signal bandwidth has been considered based on *single pulse processing*. It has been shown that the performance improvement reaches maximum when the system utilizes the so-called critical bandwidth which just resolves the individual scatterers. The major reason for the improvement is that the resolved scatterers introduce much less fluctuation than the point target formed by summing the scatterers. Further increasing the signal bandwidth beyond the critical bandwidth will offer no significant improvement of the detection performance for single pulse processing, as the *total* clutter power involved in the processing will not be further reduced.

When *coherent multiple pulse processing* [1] is applied to the target detection for interference rejection, however, it is unknown whether one should use a bandwidth much greater than the critical bandwidth, as the so-called range migration may occur for fast moving targets. The return from the individual scatterers will "walk" from one range cell to another among the pulses during the coherent processing interval (CPI). The range walk has little effects on single pulse processing as we can always track the target echo for compensation if the interference is sufficiently small[1]. The track-based compensation is not suitable to multiple pulse processing as the interference correlation among the pulses would be severely destroyed, resulting in very poor interference rejection performance. Furthermore, the useful information associated with the range walk data would be neglected. As we will show in Part I of this report, proper use of the information can lead to further performance improvement in severe interference environment, since the range walk can provide another discrimination means for interference suppression in addition to the Doppler frequency shift of frequency/phase modulated systems with small relative bandwidth.

The above promising features associated with the UWB waveforms doesn't necessarily mean we are benefiting from the high resolution all the time. One should note that the global false alarm rate will rise as the increase of the range resolution, since the number of the test cells increases dramatically. To maintain the global false alarm at a desired level, the false alarm at each test cell must be chosen lower than normal, which will certainly degrade the system detection performance. Meanwhile, the scatterer distribution across range is usually unknown to the system, thus the so-called collapsing loss is inevitable. Clearly, the clutter and fluctuation reduction, together with the false alarm adjustment and collapsing loss, reflect opposite effects on the system detection performance. In the other words, we are playing trade-off on those factors when raising the system bandwidth.

The modeling and processing complexity also poses a issue for the UWB technology. Even if the UWB system uses F/PM waveforms, the relative bandwidth, defined as the ratio of the signal bandwidth over its central frequency, can easily goes beyond the small relative bandwidth assumption for the UWB waveforms. Thus the conventional process-

---

[1] "coherent processing" in this report has a more general meaning than the tradition definition associated with the use of phase information. It is loosely defined as processing methods which have pre-thresholding integration of the desired signal components over multiple returns. In contrast, noncoherent processing means any post-thresholding integration.

ing and analysis tools good for the narrowband waveform, such as the orthognal receiver structure and complex data representation, are no longer adequate for the UWB waveforms, necessitating more sophisticated waveform-based modeling and processing. Although one can maintain the small relative bandwidth assumption by using a very high frequency band, the propagation attenuation at such a high frequency is usually too severe to be tolerable in practice.

Part I of this report is organized as follows. The data model directly based on the received waveform is set up in Section I.2. Section I.3 derives the waveform-based optimal UWB processor, together with its detection performance. The suboptimal UWB processor using *ad hoc* scatterer integration schemes for unknown scatterer separation is also investigated in Section I.3. Section I.4 conducts the performance comparison of the UWB and narrowband systems, where the trade-offs of the clutter reduction versus false alarm adjustment, as well as the fluctuation reduction versus collapsing loss, are systematically investigated. We presents the conventional canceler-based UWB processor in Section I.5, followed by Section I.6 which introduces the adaptive implementation of the optimal UWB processor.

I.2 DATA MODELING

Due to the fact that the data model for the UWB waveforms with large relative bandwidth (RBW) could be totally different from those under the conventional narrowband assumptions, we begin with continuous waveforms of a more general form. The data modeling with either UWB waveforms for small relative bandwidth, or the narrowband waveforms, will be considered as special cases.

2.1 Waveform-based Data Modeling of Moving Targets

Let $x_r(t)$ be the waveform received by a radar system at the front end of its receiver. It consists of the returns from the target and interference/clutter, as well as the internal receiver noise

$$x_r(t) = s_r(t) + n_c(t) + n_n(t) \qquad 0 < t < T \qquad (2\text{—}1)$$

where T is the total observation time. For coherent multiple pulse processing, the target signal $s_r(t)$ usually consists of a train of M narrow pulses. For convenience of analysis, we introduce the vector representation

$$\mathbf{x}_r(t) = \begin{bmatrix} x_{r1}(t) \\ x_{r2}(t) \\ \vdots \\ x_{rM}(t) \end{bmatrix} \qquad 0 < t < T'_p \qquad (2-2)$$

where $x_{rm}(t), m = 1, 2, ..., M$ are segmented pieces from $x_r(t)$

$$x_{rm}(t) = x_r(t + (m-1)T'_p) \qquad 0 < t < T'_p \qquad (2-3)$$

with T'_p being the segmentation interval close to the pulse repetition interval (PRI) of the pulse train. Thus the received signal is represented in a vector form

$$\mathbf{x}_r(t) = \mathbf{s}_s(t) + \mathbf{n}_c(t) + \mathbf{n}_n(t) \qquad 0 < t < T'_p. \qquad (2-4)$$

The target and interference components contained in the received data will be modeled as follows.

11

Target Modeling

Let $s_t(t)$ be the transmitted waveform. Since the signal transmitted at the moment t' will be received at moment t, the relation between $s_t(t)$ and $s_r(t)$ is given by

$$s_r(t) = as_t(t'), \qquad (2-5)$$

where

$$t = t' + 2t_1 \qquad (2-6)$$

with t_1 being the single-trip delay time. The attenuation factor a includes the effects of the antenna gain, the two-way path loss, and the radar cross section of the target. Consider a target with constant radial velocity v_s whose range is specified by the equation

$$R(t') = R_0 + v_s t'. \qquad (2-7)$$

Thus the single-trip delay satisfies

$$R(t' + t_1)/c = t_1, \qquad (2-8)$$

which leads to

$$t_1 = \frac{R_0/c + v_s t'/c}{1 - v_s/c}, \qquad (2-9)$$

where c is the wave propagation velocity. Substituting it in Eq.(2-6) yields

$$t' = \frac{t - \frac{2R_0}{c}/(1 - \frac{v_s}{c})}{1 + \frac{2v_s}{c}/(1 - \frac{v_s}{c})} = \frac{t - \tau_0}{\alpha} \qquad (2-10)$$

where

$$\alpha = 1 + \frac{2v_s}{c}/(1 - \frac{v_s}{c}) \qquad (2-11)$$

and

$$\tau_0 = \frac{2R_0}{c}/(1 - \frac{v_s}{c}). \qquad (2-12)$$

Since

$$v_s \ll c, \qquad (2-13)$$

Eq.(2-11) and Eq.(2-12) can be approximated by

$$\alpha_s = 1 + \frac{2v_s}{c} \qquad (2-14)$$

12

and

$$\tau_0 = \frac{2R_0}{c}. \qquad (2-15)$$

Finally, substituting Eq.(2-14) and Eq.(2-15) into Eq.(2-5), we obtain

$$s_r(t) = a s_t((t - \tau_0)/\alpha). \qquad (2-16)$$

We see that the received signal return is the time-scaled, delayed, and attenuated version of the transmitted waveform. Now we assume the transmitted waveform is a train of M pulses with pulse repetition interval T_p

$$s_t(t) = \sum_{m=1}^{M} g(t - (m-1)T_p), \qquad (2-17)$$

where $g(t)$ is a single pulse waveform of unit energy

$$g(t) = \begin{cases} g(t) & 0 < t < \Delta\tau \qquad \Delta\tau \ll T_p \\ 0 & \text{elsewhere} \end{cases} . \qquad (2-18)$$

Then the target return will be

$$s_r(t) = \sum_{m=1}^{M} g\left(\frac{t - \tau_0}{\alpha_s} - (m-1)T_p\right) \qquad (2-19)$$

For vector representation, we segment $s_r(t)$ into M pieces each of which has duration of $T_p' = \alpha T_p$. Note that the segmentation interval used for vectorizing $s_r(t)$ is usually not equal to T_p for the reason of interference suppression. If α is chosen to be very close to 1, i.e., the difference $T_p - T_p'$ is much smaller than T_p itself, the mth piece will have the form of

$$s_{rm}(t) = s_r(t + (m-1)T_p') = ag\left(\frac{t - \Delta\alpha(m-1)T_p - \tau_0}{\alpha_s}\right)$$

$$\simeq ag(t - \Delta\alpha(m-1)T_p - \tau_0) \qquad 0 < t < T_p' \qquad (2-20)$$

where $\Delta\alpha = \alpha_s - \alpha$ and the approximation is made based on the fact $v_s \ll c$ and thus $\alpha_s \approx 1$. One can see that the effect of the time scaling on the waveform itself is less important than the inter-pulse shift caused by $\Delta\alpha$. Now the signal waveform has a vector form as follows

$$\mathbf{s}_r(t) = \begin{bmatrix} s_{r1}(t) \\ s_{r2}(t) \\ \vdots \\ s_{rM}(t) \end{bmatrix}$$

13

$$= a\mathbf{g}(t - \tau_0) \qquad\qquad (2-21)$$

with $\mathbf{g}(t)$ being defined as

$$\mathbf{g}(t) = \begin{bmatrix} g(t) \\ g(t - \Delta\alpha T_p) \\ \vdots \\ g(t - \Delta\alpha(M-1)T_p) \end{bmatrix}. \qquad\qquad (2-22)$$

With sufficiently large signal bandwidth, a target usually exhibits itself as multiple dominant scatterers (MDS) distributed across certain range extent. If we assume the returns of the scatterers have the similar features of a point target as described above, the received waveform will be

$$\mathbf{s}_r(t) = \sum_{j=1}^{J} a_j \mathbf{g}(t - \tau_j) = \mathbf{G}(t)\mathbf{a} \qquad\qquad (2-23)$$

where J is the number of the scatterers, a_j and τ_j are the amplitude and arrival time of the jth scatterer, respectively. The matrix $\mathbf{G}(t), M \times J$, and $\mathbf{a}, J \times 1$ are defined by

$$\mathbf{G}(t) = [\mathbf{g}(t - \tau_1) \quad \mathbf{g}(t - \tau_2) \quad \cdots \quad \mathbf{g}(t - \tau_J)], \qquad\qquad (2-24)$$

and

$$\mathbf{a} = \begin{bmatrix} a_1 \\ a_2 \\ \vdots \\ a_J \end{bmatrix}. \qquad\qquad (2-25)$$

An example of the MDS waveform is shown in Fig. 1.

Interference and Receiver Noise Modeling

Under the assumption that the interference is rough compared to the carrier wavelength, the covariance function of the interference/clutter component $n_c(t)$ in Eq.(2-1) is found to be [6]

$$K_c(t,\tau) = \int s(\frac{t-\lambda}{\alpha_c})K_{dr}(t-\tau,\lambda)s^*(\frac{\tau-\lambda}{\alpha_c})d\lambda \qquad\qquad (2-26)$$

where $K_{dr}(t,\tau)$ is the interference scattering function and α_c the time scaling factor due to the interference motion

$$\alpha_c = 1 + \frac{2v_c}{c}, \qquad\qquad (2-27)$$

14
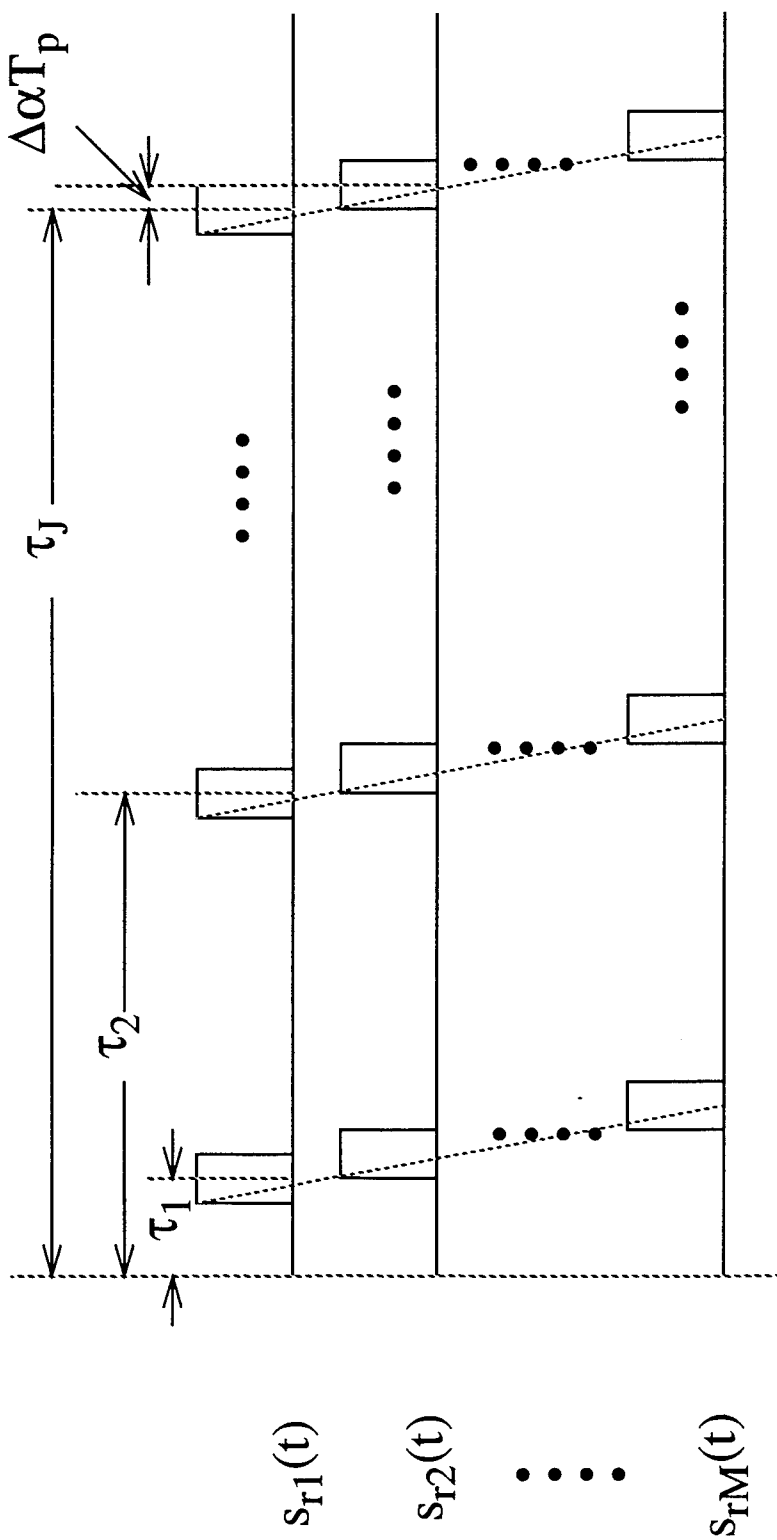
Fig. 1. An example of the MDS data of a moving target.

with v_c being the interference velocity. Note that we have omitted the integration interval for simplicity, which actually goes from minus infinity to plus infinity. We assume the interference/clutter is uniformly distributed in the range extent $[0, \quad L_c]$, i.e.,

$$K_{dr}(t - \tau, \lambda) = \begin{cases} K_d(t - \tau) & 0 < \lambda < L_c \\ 0 & \text{elsewhere} \end{cases}. \qquad (2-28)$$

Then

$$K_c(t, \tau) = K_d(t - \tau) \int_0^{L_c} s(\frac{t - \lambda}{\alpha_c}) s^*(\frac{\tau - \lambda}{\alpha_c}) d\lambda \qquad (2-29)$$

Substituting the multiple pulse waveform $s(t) = \sum_{m=1}^{M} g(t - (m-1)T_p)$ into the above gives

$$K_c(t, \tau) = K_d(t - \tau) \sum_{m=1}^{M} \sum_{n=1}^{M} \int_0^{L_c} g(\frac{t - \lambda}{\alpha_c} - (m-1)T_p) g^*(\frac{\tau - \lambda}{\alpha_c} - (n-1)T_p) d\lambda. \qquad (2-30)$$

Assume that L_c is much larger than the pulse width $\Delta\tau$ of $g(t)$, the integration interval $[0, \quad L_c]$ can be extended to $[-\infty, \quad , \infty]$ without changing the result of the integral. Define the correlation function for the pulse waveform $g(t)$,

$$h(\tau) = \int g(t) g^*(t - \tau) dt. \qquad (2-31)$$

The correlation function of $n_c(t)$ becomes

$$K_c(t, \tau) = \alpha_c K_d(t - \tau) \sum_{m=1}^{M} \sum_{n=1}^{M} h(\frac{t - \tau}{\alpha_c} - (m-n)T_p). \qquad (2-32)$$

Now we segment $n_c(t)$ the same way as we did to the target return $s_r(t)$:

$$\mathbf{N}_c(t) = \{ n_c(t + (m-1)T_p') \} \qquad 0 < t < T_p'. \qquad (2-33)$$

The mnth element of its waveform covariance matrix $\mathbf{K}_c(t, \tau)$ is

$$r_{cmn}(t, \tau) = \mathrm{E}\{ n_c(t + (m-1)T_p') n_c^*(\tau + (n-1)T_p') \}$$

$$= K_c(t + (m-1)T_p', \tau + (n-1)T_p')$$

$$= \alpha_c K_d(t - \tau + (m-n)T_p') \sum_{m'=1}^{M} \sum_{n'=1}^{M} h(\frac{t - \tau + (m-n)T_p'}{\alpha_c} - (m' - n')T_p).$$

$$= \alpha_c K_d(t - \tau + (m-n)T_p') h(\frac{t - \tau + (m-n)T_p'}{\alpha_c} - (m-n)T_p). \qquad (2-34)$$

16

Taking $T_p' = \alpha_c T_p$, we have

$$r_{cmn}(t, \tau) = \alpha_c K_d(t - \tau + (m - n)T_p')h(\frac{t - \tau}{\alpha_c})$$

$$\approx K_d((m - n)T_p)h(t - \tau) \qquad (2 - 35)$$

where we have used the facts that $K_d(\tau)$ changes very slow within the pulse duration $\Delta \tau$ and $\alpha_c \approx 1$ for the approximation above. Thus

$$\mathbf{K}_c(t, \tau) = \mathbf{R}_c h(t - \tau) \qquad (2 - 36)$$

where $\mathbf{R}_c$ is the interference inter-pulse covariance matrix defined by

$$\mathbf{R}_c = \{K_d((m - n)T_p)\}. \qquad (2 - 37)$$

With very large bandwidth, $h(\tau)$ is very narrow so it can be approximated by

$$h(\tau) \approx \int |h(t)|dt\delta(\tau)$$

$$= |G(f_0)|^2\delta(\tau), \qquad (2 - 38)$$

where $G(f)$ is the Fourier transform of $g(t)$ and f_0 its carrier frequency. Consider the definition of the equivalent rectangular bandwidth [7]

$$B = \frac{\int |g(t)|^2 dt}{2|G(f_0)|^2}$$

$$= \frac{1}{2|G(f_0)|^2}, \qquad (2 - 39)$$

we get

$$\mathbf{K}_c(t, \tau) = \frac{1}{2B}\mathbf{R}_c\delta(t - \tau). \qquad (2 - 40)$$

Clearly, a large bandwidth shows a advantage against the interference/clutter.

Assume that the receiver noise $n_n(t)$ is a white process, i.e., its covariance function is specified by

$$K_n(t, \tau) = \mathrm{E}\{n_n(t)n_n^*(\tau)\} = \frac{N_0}{2}\delta(t - \tau) \qquad (2 - 41)$$

where N_0 is the noise power spectral density level. For its vector representation $\mathbf{N}_n(t) = \{n_n(t + (m - 1)\alpha_c T_p)\}$, $\quad 0 < t < \alpha_c T_p$, the waveform covariance matrix is thereby

$$\mathbf{K}_n(t, \tau) = \mathrm{E}\{\mathbf{N}_n(t)\mathbf{N}_n^H(\tau)\} = \frac{N_0}{2}\mathbf{I}\delta(t - \tau) \qquad (2 - 42)$$

17

where $\mathbf{I}$ is an $M \times M$ identity matrix.

Therefore, the total waveform covariance matrix of the interference and receiver noise is given by

$$\mathbf{K}(t,\tau) = \mathrm{E}\{(\mathbf{N}_c(t) + \mathbf{N}_n(t))(\mathbf{N}_c(\tau) + \mathbf{N}_n(\tau))^H\} = (\frac{1}{2B}\mathbf{R}_c + \frac{N_0}{2}\mathbf{I})\delta(t - \tau) = \mathbf{R}\delta(t - \tau).$$

$$(2 - 43)$$

2.2   Some Special Cases

The data model given in the previous subsection is more general in the sense that it is suitable for all types of waveforms. In this subsection we will consider two special cases: (1) the waveform that has very large bandwidth, but its relative bandwidth is less than 10%; (2) the narrowband waveform.

UWB waveform with small relative bandwidth

We assume that the single pulse waveform has the following form

$$g(t) = A(t)\cos(2\pi f_0 t + \theta(t)) \qquad (2 - 44)$$

where $A(t)$ and $\theta(t)$ are the amplitude and phase modulation of the waveform, and the carrier frequency f_0 is very high compared to the bandwidth B of $A(t)$ and $\theta(t)$. As the relative bandwidth $RBW = B/f_0$ is less than 10%, the conventional orthogonal receiver using in-phase and quadrature channels can be applied to reduce the effect of phase fluctuation. Thus the complex representation means for the target return is valid here

$$g(t) = A(t)e^{i2\pi f_0 t + i\theta(t)} \qquad (2 - 45)$$

Substituting it into Eq.(2-22) gives

$$\mathbf{g}(t) = \begin{bmatrix} A(t)e^{i2\pi f_0 t + i\theta(t)} \\ A(t - \Delta\alpha T_p)e^{i2\pi f_0(t - \Delta\alpha T_p) + i\theta(t - \Delta\alpha T_p)} \\ \dots \\ A(t - (M-1)\Delta\alpha T_p)e^{i2\pi f_0(t - (M-1)\Delta\alpha T_p) + i\theta(t - (M-1)\Delta\alpha T_p)} \end{bmatrix}$$

$$= e^{i2\pi f_0 t} \begin{bmatrix} \tilde{A}(t) \\ \tilde{A}(t - \Delta\alpha T_p)e^{-i2\pi f_0 \Delta\alpha T_p} \\ \dots \\ \tilde{A}(t - (M-1)\Delta\alpha T_p)e^{-i2\pi(M-1)f_0 \Delta\alpha T_p} \end{bmatrix} \qquad (2 - 46)$$

18

where $\tilde{A}(t) = A(t)e^{i\theta(t)}$. Obviously, the high frequency term before the vector can be removed by passband-to-baseband conversion. Thus after the passband-to-baseband and orthogonal preprocessing, the signal envelop vector becomes

$$\tilde{g}(t) = \begin{bmatrix} \tilde{A}(t) \\ \tilde{A}(t - \Delta\alpha T_p)e^{-i2\pi f_0 \Delta\alpha T_p} \\ \ldots \\ \tilde{A}(t - (M-1)\Delta\alpha T_p)e^{-i2\pi(M-1)f_0\Delta\alpha T_p} \end{bmatrix}$$

$$= \begin{bmatrix} \tilde{A}(t) \\ \tilde{A}(t - \Delta\alpha T_p)e^{-i2\pi\Delta f} \\ \ldots \\ \tilde{A}(t - (M-1)\Delta\alpha T_p)e^{-i2\pi(M-1)\Delta f} \end{bmatrix} \qquad (2-47)$$

where

$$= f_s - f_0(1-\alpha)T_p. \qquad (2-48)$$

with $f_s = 2f_0 v_s T_p/c$. Apparently, f_s is the conventional normalized Doppler frequency shift for moving targets. It is seen from the above that the target movement not only cause Doppler shift on the phase of the sinusoid-based signal, but also results in the inter-pulse shift on its amplitude, which is often referred to as "range walk". We define the range walk rate

$$\rho = BT_p 2v/c,$$

which reflects the number of the resolution cells the target travels between the two adjacent pulses.

Narrowband Waveform

The form of the narrowband waveform is the same as Eq.(2-44), but $A(t)$ and $\theta(t)$ now have a very narrow bandwidth. With $T'_p = T_p$, Eq.(2-22) becomes

$$\tilde{g}(t) = \begin{bmatrix} \tilde{A}(t) \\ \tilde{A}(t - \alpha_s T_p)e^{-i2\pi f_s} \\ \ldots \\ \tilde{A}(t - (M-1)\alpha_s T_p)e^{-i2\pi(M-1)f_s} \end{bmatrix}.$$

$$\approx \tilde{A}(t) \begin{bmatrix} 1 \\ e^{-i2\pi f_s} \\ \ldots \\ e^{-i2\pi(M-1)f_s} \end{bmatrix}. \qquad (2-49)$$

The last expression is obtained by using the fact $\tilde{A}(t - (m-1)\Delta\alpha T_p) \approx \tilde{A}(t), m = 1, 2, ..., M$, since the narrowband envelop $\tilde{A}(t)$ changes too slow to make difference. Define the signal vector

$$\mathbf{s} = \begin{bmatrix} 1 \\ e^{-i2\pi f_s} \\ \cdots \\ e^{-i2\pi(M-1)f_s} \end{bmatrix}. \tag{2-50}$$

Eq.(2-49) becomes

$$\tilde{\mathbf{g}}(t) = \tilde{A}(t)\mathbf{s}. \tag{2-51}$$

As shown by Eq.(2-23), the target returns are actually composed of many scattering centers. So the total received target waveform for the narrowband case is

$$\tilde{\mathbf{s}}_r(t) = \sum_j \tilde{a}_j \mathbf{g}(t - \tau_j) = \sum_j \tilde{a}_j \tilde{A}(t - \tau_j)\mathbf{s} \approx \tilde{a}_0 \tilde{A}(t - \tau_0)\mathbf{s}, \tag{2-52}$$

where $\tilde{a}_0 = \sum_j \tilde{a}_j$ and $\tau_0 = \sum_j \tau_j / J$. Here again, we have used the fact that $\tilde{A}(t)$ is narrowband to make the approximation. We note that $\tilde{a}_0$ will fluctuate since it is the sum of many complex variables of random phases, even though each individual scattering center may have little fluctuation. We will model $\tilde{a}_0$ as a Gaussian random variable with zero mean and variance σ_s^2, which represents the total received energy of the point target.

For interference part, if we take $T_p' = T_p$, Eq.(2-34) becomes

$$r_{cmn}(t, \tau) = \alpha_c K_d((m-n)T_p) h \left(\frac{t - \tau + (m-n)T_p}{\alpha_c} - (m-n)T_p \right)$$

$$\approx K_d((m-n)T_p) h(t - \tau - (m-n)T_p \frac{2v_c}{c}). \tag{2-53}$$

With the narrowband waveform given by Eq.(2-45), it is easy to show that

$$h(\tau + \Delta) \approx e^{i2\pi f_0 \Delta} h(\tau), \tag{2-54}$$

for a small increment Δ. Then we have

$$r_{cmn}(t, \tau) \approx K_d((m-n)T_p) e^{-i2\pi(m-n)f_c} h(t - \tau) \tag{2-55}$$

where f_c is the normalized Doppler frequency of the interference. So the waveform covariance matrix of $\mathbf{N}_c(t)$ can still be expressed as

$$\mathbf{K}_c(t, \tau) = \tilde{\mathbf{R}}_c h(t - \tau). \tag{2-56}$$

20

But $\tilde{\mathbf{R}}_c$ is now given by

$$\tilde{\mathbf{R}}_c = \{K_d((m-n)T_p)e^{-i2\pi(m-n)f_c}\} \qquad (2-57)$$

which involves with the interference Doppler shift.

I.3 Optimum Detection of Over-resolved Moving Targets

3.1 Waveform-based Optimum UWB processing

With the general data model presented in Section I.2, this section will derive the optimum processor directly based on the received waveform. The interference statistics and target characteristics are all assumed to be known to the system. Therefore the optimum processor such derived explores the performance potential achievable by a UWB system.

3.1.1 Waveform-based Optimum Processor and Its Detection Performance

Based on the received UWB waveform $\mathbf{x}(t)$, the waveform-based optimum processor forms its decision rule for over-resolved target detection in the following way:

$$\eta = \mathbf{x}^H \mathbf{C}^{-1} \mathbf{x} \underset{H_0}{\overset{H_1}{\underset{<}{\gtrless}}} \eta_0, \qquad (3-1)$$

where

$$\mathbf{x} = \int \mathbf{G}(t)^H \mathbf{R}^{-1} \mathbf{x}(t) dt \quad J \times 1 \qquad (3-2)$$

and

$$\mathbf{C} = \int \mathbf{G}(t)^H \mathbf{R}^{-1} \mathbf{G}(t) dt \quad J \times J. \qquad (3-3)$$

The derivation is given in Section I.3.1.3 as a appendix.

It is seen that the above optimum UWB processor requires the exact knowledge of the interference statistics $\mathbf{R}$ and the target waveform $\mathbf{G}(t)$, which is controlled by the pulse shift rate difference $\Delta\alpha = \alpha_s - \alpha_c$ and the scatterer arrival time τ_k.

Fig. 2-3 illustrates the waveform-based optimum UWB processor, from which we see that it breaks into several major parts:

- optimum interference canceler
- multiple pulse correlator
- incoherent inter-scatterer integrator.

The detection performance of the UWB processor is shown in Section I.3.1.3 as follows:

$$P_f = \int_{\eta_0}^{\infty} \frac{\eta^{J/2-1}}{\Gamma(J/2)} e^{-\eta} dt \qquad (3-4)$$

22
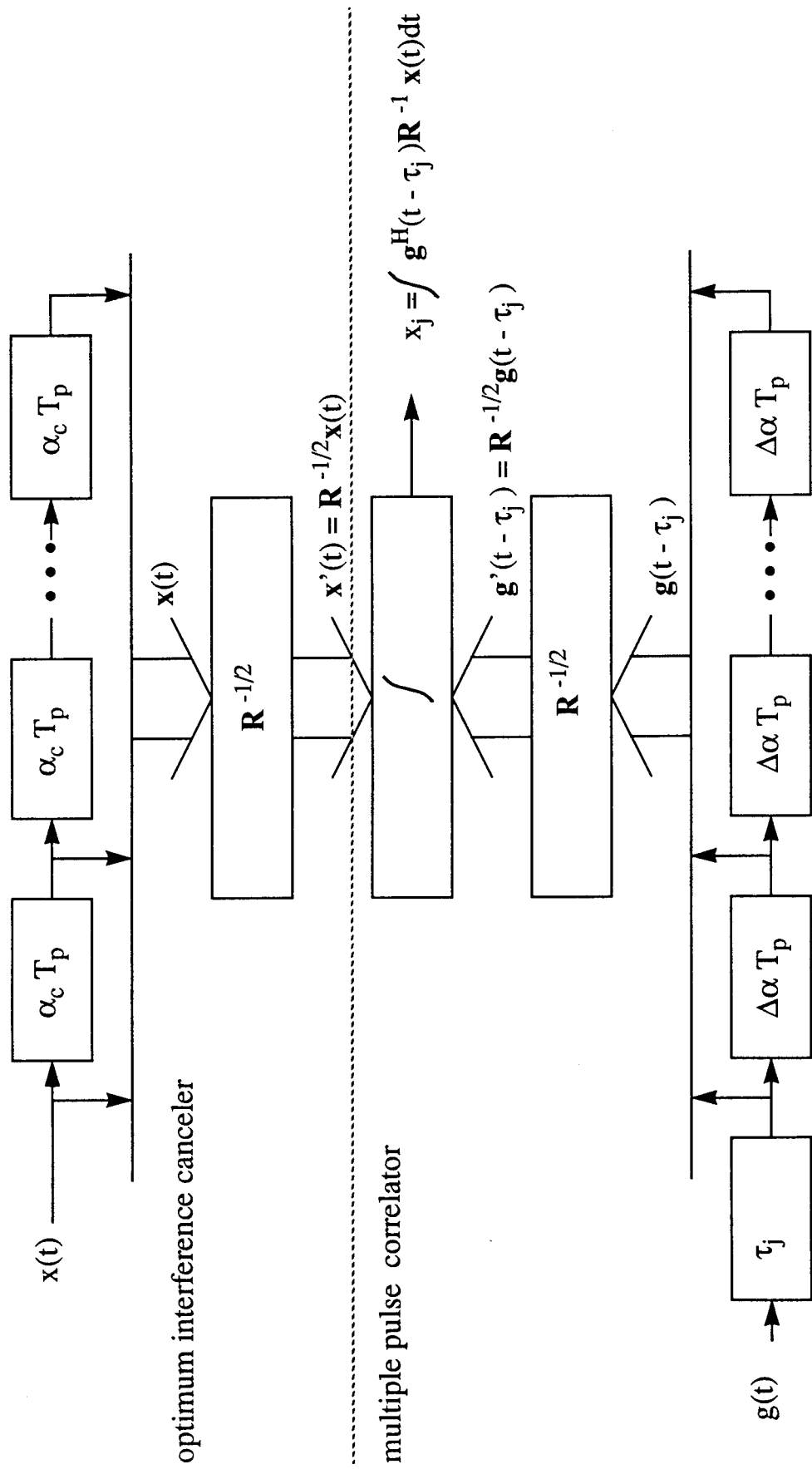
Fig. 2. Structure of the waveform-based optimal UWB processor: optimum interference canceler and multiple pulse correlator.

23
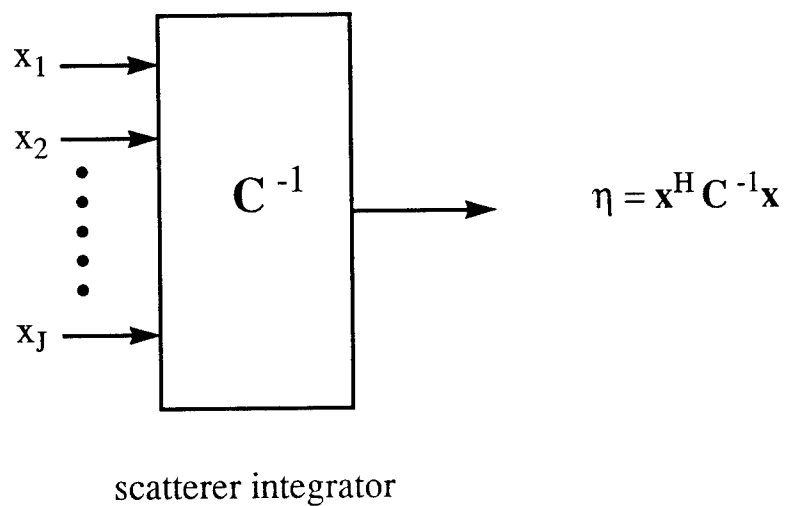
Fig. 3. Structure of the waveform-based optimal UWB processor: Inter-scatterer integrator.

and

$$P_d = \int_{\eta_0}^{\infty} e^{-(\gamma+t)} \left[\frac{t}{\gamma}\right]^{\frac{J/2-1}{2}} I_{J/2-1}(2\sqrt{\gamma t}) \qquad (3-5)$$

where

$$\gamma = \mathbf{a}^H \mathbf{C} \mathbf{a}/2, \qquad (3-6)$$

and $I_{J/2-1}(\cdot)$ is the $(J/2-1)$th order modified Bessel function of the first kind.

3.1.2 Optimum Processing with Some Particular Waveforms

The optimum processing provided in the previous section is directly based on the received waveform without any preprocessing. Even though it is necessary for the signal waveform having a very larger relative bandwidth, the implementation complexity would be greatly increased as we have to process the data at very high frequency. For the waveforms with small relative bandwidth (either narrowband or ultra-wideband), however, we will see below that the complexity problem can be largely avoided.

Optimum processing with UWB waveforms of small relative bandwidth

As discussed in Section I.2, the orthogonal receiver structure and passband-to-baseband conversion are applicable to the UWB waveform with small relative bandwidth. Let $\tilde{x}(t)$ be the waveform after the preprocessing. It consists of

$$\tilde{x}(t) = \tilde{s}_r(t) + \tilde{n}_c(t) + \tilde{n}_n(t) \qquad (3-7)$$

where $\tilde{n}_c(t)$ and $\tilde{n}_n(t)$ are complex random vectors representing the interference and noise, respectively, and

$$\tilde{s}_r(t) = \sum_{j=1}^{J} \tilde{a}_j \tilde{g}(t - \tau_j) = \tilde{G}(t)\tilde{a} \qquad (3-8)$$

with $\tilde{g}(t)$ being specified by Eq.(2-51) and $\tilde{a}_j$ the complex amplitude of jth scatterer. We note that $\tilde{x}(t)$ is within baseband and its carrier component is removed.

Applying the optimum processing given by the previous subsection to the complex waveform, we have the test rule

$$\eta = \tilde{x}^H \tilde{C}^{-1} \tilde{x} \underset{\substack{< \\ H_0}}{\overset{\substack{H_1 \\ >}}{}} \eta_0 \qquad (3-9)$$

25

where $\tilde{\mathbf{x}}$ and $\tilde{\mathbf{C}}$ denote

$$\tilde{\mathbf{x}} = \int \tilde{\mathbf{G}}(t)^H \mathbf{R}^{-1} \tilde{\mathbf{x}}(t) dt \qquad J \times 1 \qquad (3-10)$$

and

$$\tilde{\mathbf{C}} = \int \tilde{\mathbf{G}}(t)^H \mathbf{R}^{-1} \tilde{\mathbf{G}}(t) dt \qquad J \times J. \qquad (3-11)$$

We note that $\tilde{\mathbf{n}}_c(t)$ and $\tilde{\mathbf{n}}_n(t)$ become the complex Gaussian processes if $\mathbf{n}_c(t)$ and $\mathbf{n}_n(t)$ are real Gaussian. So in a similar way to Section I.3.1, the detection performance is found to be

$$P_f = \exp(-\eta_0) \sum_{j=1}^{J} \frac{\eta_0^{J-j}}{(J-j)!} \qquad (3-12)$$

and

$$P_d = \int_{\eta_0}^{\infty} e^{-(\gamma+t)} \left[\frac{t}{\gamma} \right]^{\frac{J-1}{2}} I_{J-1}(2\sqrt{\gamma t}) dt \qquad (3-13)$$

where

$$\gamma = \tilde{\mathbf{a}}^H \tilde{\mathbf{C}} \tilde{\mathbf{a}}. \qquad (3-14)$$

We note that it differs from Eq.(3-4)-Eq.(3-6) of the real case.

Optimum processing with narrowband waveform

From Eq.(2-52)

$$\tilde{\mathbf{s}}_r(t) = \tilde{a}_0 \tilde{A}(t - \tau_0) \mathbf{s}. \qquad (3-15)$$

Substituting it into Eq.(3-10) and Eq.(3-11) yields

$$\tilde{\mathbf{C}} = \int \tilde{A}^*(t - \tau_0) \mathbf{s}^H \mathbf{R}^{-1} \mathbf{s} \tilde{A}(t - \tau_0) dt = \mathbf{s}^H \mathbf{R}^{-1} \mathbf{s}, \qquad (3-16)$$

and

$$\tilde{\mathbf{x}} = \int \tilde{A}^*(t - \tau_0) \mathbf{s}^H \mathbf{R}^{-1} \tilde{\mathbf{x}}(t) dt = \mathbf{s}^H \mathbf{R}^{-1} \mathbf{y}, \qquad (3-17)$$

where we have assumed that $\tilde{A}(t)$ has unit energy and $\mathbf{y}$ is obtained by the matched filtering

$$\int \tilde{A}^*(t - \tau_0) \tilde{\mathbf{x}}(t) dt. \qquad (3-18)$$

Note that $\mathbf{R}$ now is defined by $\tilde{\mathbf{R}}_c / 2B + N_0 \mathbf{I}/2$, which involves the Doppler frequency shift of the interference.

The test statistic now becomes

$$\eta = \frac{s^H R^{-1} y y^H R^{-1} s}{s^H R^{-1} s} = |w^H y|^2, \tag{3-19}$$

with the weight vector being defined

$$w = \frac{R^{-1} s}{[s^H R^{-1} s](1/2)}. \tag{3-20}$$

We see that it turns into the familiar optimum processor of the conventional form.

As we have discussed in Section I.2, the deterministic assumption no longer holds for the signal amplitude $\tilde{a}_0$. We model it as a complex Gaussian variable with zero mean and variance σ_s^2. Thus the mean of y is both zero under the hypotheses H_0 and H_1, and its covariance matrix is found to be

$$\text{Cov}(x) = \begin{cases} E(x x^H) = R & \text{under } H_0 \\ E(x x^H) = R + \sigma_s^H s s^H & \text{under } H_1 \end{cases}. \tag{3-21}$$

Then η has a χ^2 distribution under both H_0 and H_1

$$p(\eta | H_0) = \exp(-\eta) \tag{3-22}$$

and

$$p(\eta | H_1) = \exp(-\eta/(1 + \gamma)) \tag{3-23}$$

with γ being defined as

$$\gamma = \sigma_s^H s^H R^{-1} s. \tag{3-24}$$

Therefore the probabilities of false alarm and detection are found to be

$$P_f = \exp(-\eta_0) \tag{3-25}$$

and

$$P_d = \exp(-\eta_0/(1 + \gamma)). \tag{3-26}$$

3.1.3 Appendix: Derivation of The Optimum UWB Processor

For convenience of derivation, we first introduce the vector likelihood function.

Assume the received data $x(t)$, $M \times 1$, has a waveform covariance matrix given as follows

$$K(t, \tau) = R\kappa(t, \tau). \tag{3-27}$$

27

Denote $\phi_k(t), k = 1, 2, ...$, as the eigen functions of the covariance kernel $\kappa(t, \tau)$. The received signal vector $\mathbf{x}(t)$ can be expanded by the Karhunen-Loeve expansion:

$$\mathbf{x}(t) = \sum_{k=1}^{\infty} \mathbf{x}_k \phi_k(t) \qquad (3-28)$$

where

$$\mathbf{x}_k = \int \mathbf{x}(t) \phi_k^*(t) dt, \qquad M \times 1. \qquad (3-29)$$

Under H_0, i.e., no-signal-presence hypothesis

$$\mathrm{E}(\mathbf{x}_k) = \mathbf{0} \qquad k = 1, 2, ... \qquad (3-30)$$

and their covariance matrices are found to be

$$\mathrm{Cov}(\mathbf{x}_k, \mathbf{x}_l) = \mathrm{E}(\mathbf{x}_k \mathbf{x}_l^H) = \mathbf{R} \lambda_k \delta_{k-l}, \qquad (3-31)$$

where λ_k is the eigenvalue of $\kappa(t, \tau)$ corresponding to the eigenfunction $\phi_k(t)$, and δ_{k-l} has a non-zero value equal to 1 only if $k = l$.

Under the assumption that $\mathbf{x}(t)$ is a multivariate Gaussian process, $\mathbf{x}_k, k = 1, 2, ...$ are also multivariate Gaussian vectors independent each other based on Eq.(3-31). Thus the joint distribution of the first K vectors is given by

$$f(\mathbf{x}_k, k = 1, 2, ..., K | H_0) = c_0 \exp -\frac{1}{2} \sum_{k=1}^{K} \frac{\mathbf{x}_k^H \mathbf{R}^{-1} \mathbf{x}_k}{\lambda_k} \qquad (3-32)$$

where c_0 is a constant independent of $\mathbf{x}_k$. Replacing $\mathbf{x}_k$ in the above by Eq.(3-29) gives

$$p(\mathbf{x}_k, k = 1, 2, ..., K | H_0) = c_0 \exp -\frac{1}{2} \int \int \mathbf{x}(t)^H \mathbf{R}^{-1} \kappa_K^{-1}(t, \tau) \mathbf{x}(\tau) dt d\tau \qquad (3-33)$$

where

$$\kappa_K^{-1}(t, \tau) = \sum_{k=1}^{K} \frac{\phi_k(t) \phi_k^*(\tau)}{\lambda_k}. \qquad (3-34)$$

Let K approach to infinity, we have

$$\kappa^{-1}(t, \tau) = \sum_{k=1}^{\infty} \frac{\phi_k(t) \phi_k^*(\tau)}{\lambda_k} \qquad (3-35)$$

which is referred to as the inverse kernel of $\kappa(t, \tau)$. It is known that $\kappa(t, \tau)$ and $\kappa^{-1}(t, \tau)$ has the following relation

$$\int \kappa(t, u) \kappa^{-1}(u, \tau) du = \delta(t - \tau). \qquad (3-36)$$

The likelihood function with K approaching to infinity now becomes

$$f(\mathbf{x}(t)|H_0) = c_0 \exp -\frac{1}{2} \int \int \mathbf{x}(t)^H \mathbf{R}^{-1} \kappa^{-1}(t,\tau) \mathbf{x}(\tau) dt d\tau. \qquad (3-37)$$

In particular, if $\kappa(t,\tau) = \delta(t-\tau)$ as given in Eq.(2-43), we have

$$f(\mathbf{x}(t)|H_0) = c_0 \exp -\frac{1}{2} \int \int \mathbf{x}(t)^H \mathbf{R}^{-1} \mathbf{x}(t) dt. \qquad (3-38)$$

Similarly, the likelihood function under H_1 is given by

$$p(\mathbf{x}(t)|H_1) = c_0 \exp -\frac{1}{2} \int \int (\mathbf{x}(t) - \mathbf{s}(t))^H \mathbf{R}^{-1} (\mathbf{x}(t) - \mathbf{s}(t)) dt. \qquad (3-39)$$

Under the multiple dominant scatterer (MDS) data model, the signal component $\mathbf{s}_r(t)$ consists of the returns from all the scattering centers

$$\mathbf{s}_r(t) = \sum_{j=1}^{J} a_j \mathbf{g}(t - \tau_j) = \mathbf{G}(t)\mathbf{a} \qquad (3-40)$$

where τ_j is arrival time of the jth scatterer, and $\mathbf{G}(t)$ and $\mathbf{a}$ are specified by Eq.(2-22) and Eq.(2-25). Substitute Eq.(3-40) into Eq.(3-39), and expand the exponential part, we have

$$\int (\mathbf{x}(t) - \mathbf{G}(t)\mathbf{a})^H \mathbf{R}^{-1} (\mathbf{x}(t) - \mathbf{G}(t)\mathbf{a}) dt$$

$$= \int \mathbf{x}(t)^H \mathbf{R}^{-1} \mathbf{x}(t) dt - \mathbf{a}^H \mathbf{x} - \mathbf{x}^H \mathbf{a} + \mathbf{a}^H \mathbf{C}\mathbf{a}$$

$$= \int \mathbf{x}(t)^H \mathbf{R}^{-1} \mathbf{x}(t) dt + [\mathbf{a} - \mathbf{C}^{-1}\mathbf{x}]^H \mathbf{C}[\mathbf{a} - \mathbf{C}^{-1}\mathbf{x}] - \mathbf{x}^H \mathbf{C}^{-1}\mathbf{x} \qquad (3-41)$$

where $\mathbf{x}$ and $\mathbf{C}$ denote

$$\mathbf{x} = \int \mathbf{G}(t)^H \mathbf{R}^{-1} \mathbf{x}(t) dt \qquad J \times 1 \qquad (3-42)$$

and

$$\mathbf{C} = \int \mathbf{G}(t)^H \mathbf{R}^{-1} \mathbf{G}(t) dt \qquad J \times J. \qquad (3-43)$$

As we are assuming the amplitudes of the scatterers are unknown, the likelihood ratio test is performed in the following way

$$\lambda = \max_{\mathbf{a}} f(\mathbf{x}(t)|H_1)/f(\mathbf{x}(t)|H_0) \overset{H_1}{\underset{H_0}{\gtrless}} \lambda_0. \qquad (3-44)$$

By Eq.(3-41), the maximum of $f(\mathbf{x}(t)|H_1)$ is achieved at $\mathbf{a} = \mathbf{C}^{-1}\mathbf{x}$ and is given by

$$= c_0 \exp(-\frac{1}{2} \int \mathbf{x}(t)^H \mathbf{R}^{-1} \mathbf{x}(t) dt + \mathbf{x}^H \mathbf{C}^{-1}\mathbf{x}) \qquad (3-45)$$

The test rule then follows

$$\exp(\mathbf{x}^H \mathbf{C}^{-1}\mathbf{x}/2) \mathop{\gtrless}\limits_{H_0}^{H_1} \lambda_0. \tag{3-46}$$

Obviously, it is equivalent to

$$\eta = \mathbf{x}^H \mathbf{C}^{-1}\mathbf{x} \mathop{\gtrless}\limits_{H_0}^{H_1} \eta_0, \tag{3-47}$$

since $\exp(x)$ is a monotonically increasing function of x.

To derive the detection performance of the above UWB processor, we notice that the $J \times 1$ vector $\mathbf{x}$ is also Gaussian distributed with covariance

$$\mathrm{Cov}(\mathbf{x}) = \mathbf{C}, \tag{3-48}$$

and its mean differs under different hypotheses

$$E(\mathbf{x}) = \begin{cases} \mathbf{0} & \text{under} \quad H_0 \\ \mathbf{Ca} & \text{under} \quad H_1 \end{cases}. \tag{3-49}$$

Thus η will have χ^2 distribution under H_0 and noncentral χ^2 distribution under H_1, i.e., its probability density function is given by

$$f_\eta(\eta|H_0) = \frac{\eta^{J/2-1}}{\Gamma(J/2)} e^{-\eta} \tag{3-50}$$

or

$$f_\eta(\eta|H_1) = e^{-(\gamma+t)} \left[\frac{t}{\gamma}\right]^{\frac{J/2-1}{2}} I_{J/2-1}(2\sqrt{\gamma t}) \tag{3-51}$$

where γ is the noncentralilty

$$\gamma = \mathbf{a}^H \mathbf{Ca}/2. \tag{3-52}$$

and $I_{J/2-1}(\cdot)$ is the $(J/2 - 1)$th order modified Bessel function of the first kind.

Then the probabilities of false alarm and detection can be obtained by integration:

$$P_f = \int_{\eta_0}^{\infty} \frac{\eta^{J/2-1}}{\Gamma(J/2)} e^{-\eta} dt \tag{3-53}$$

and

$$P_d = \int_{\eta_0}^{\infty} e^{-(\gamma+t)} \left[\frac{t}{\gamma}\right]^{\frac{J/2-1}{2}} I_{J/2-1}(2\sqrt{\gamma t}) \tag{3-54}$$

30

3.2 Suboptimal UWB Processor–Unkown Scatterer Separation

The application of the optimum processor described in Section I.3.1 requires *a priori* information about the range distribution of the scatterers, which is not usually available to the processor in practice. Obviously, processing without knowing the exact target geometry will lead to some performance degradation. In this section, we will study the suboptimum processor which utilizes some *ad hoc* inter-scatterer integration schemes while still assumes the known interference covariance.

3.2.1 *Ad Hoc* Inter-Scatterer Integration Schemes

As the arrival time of the scatterers is unknown, the time interval of interest is divided evenly into N range cells. The centers of the range cell, denoted by $\tau_l, l = 1, 2, ..., N$, are assumed to be the arrival time of the scatterers. Thus we can obtain the test data for each range cells

$$\mathbf{x} = \int \mathbf{G}(t)^H \mathbf{R}^{-1} \mathbf{x}(t) dt \qquad J \times 1, \qquad (3-55)$$

where the matrix $\mathbf{G}(t), M \times N$, consists of the signal vectors for all the range cells

$$\mathbf{G}(t) = [\mathbf{g}(t - \tau_1) \quad \mathbf{g}(t - \tau_2) \quad \cdots \quad \mathbf{g}(t - \tau_N)]. \qquad (3-56)$$

The separation between the adjacent range cells, denoted by Δd, is chosen small so that the time interval of interest can be densely covered. Thus the total number of the range cells N is usually much greater than the actual number of the scatterers J. This in turn will introduce some performance loss since the interference and noise components in those non-scatterer-existing range cells are unnecessarily included. The performance loss should differ with the ways how the data from the range cells enter into the hypothesis test. Given below are some possible choices of *ad hoc* scatterer integration schemes.

(a). *integration-of-all*. All the data from the range cells are simply used to perform the hypothesis test, i.e., the test statistic is formed by

$$\eta = \mathbf{x}^H \mathbf{C}^{-1} \mathbf{x} \mathop{\gtrless}_{H_0}^{H_1} \eta_0 \qquad (3-57)$$

where $\mathbf{C}$ is decoupling matrix for all the range cells

$$\mathbf{C} = \int \mathbf{G}(t)^H \mathbf{R}^{-1} \mathbf{G}(t) dt \qquad N \times N. \qquad (3-58)$$

31

The detection performance is still governed by Eq.(3-52)-Eq.(3-54), but with large portion of the elements of **a** being zero.

(b). *integration-of-m.* The m largest elements of the data vector **x** are integrated to form the test statistic, i.e., the hypothesis test is performed by

$$\eta = \mathbf{x}'^H \mathbf{C}'^{-1} \mathbf{x}' \underset{H_0}{\overset{H_1}{\gtrless}} \eta_0 \qquad (3-59)$$

where $\mathbf{x}'$ consists of the m largest elements of **x**, and $\mathbf{C}'$ is calculated in terms of Eq.(3-58) with $\mathbf{G}(t)$ being formed by those arrival time indexes corresponding to the m largest range cells. We note that the term of $\mathbf{C}'^{-1}$ is still included to perform the inter-scatterer decoupling, which is shown necessary by computer simulation.

(c). *m-out-of-N.* All the data from the range cells are compared with a chosen threshold η_0. If at least m of them surpass the threshold, target presence is claimed. Otherwise, reject the hypothesis H_1.

(d). *maximum-of.* The largest element of **x** is simply taken out to perform the hypothesis testing.

It is easy to see that the integration scheme (a) and (d) are actually the extreme cases of (b) if we set $m = N$ and $m = 1$, respectively.

3.2.2   Performance Evaluation by Computer Simulation

Because of the statistical dependence among the elements of **x**, it is difficult to perform analytical performance analysis for the *ad hoc* scatterer integration schemes except the integration-of-all. Therefore the performance evaluation of the integration schemes performed in this subsection will be largely based on computer simulation.

Under the assumption that the received waveform $\mathbf{x}(t)$ is a Gaussian process, it is not necessary to start the computer simulation from the uneasy job of generating the continuous waveform, since the data vector **x** is found to be a Gaussian distributed random vector with its covariance matrix specified by **C** and mean vector given by

$$E\{\mathbf{x}\} = \mathbf{Ca} \qquad (3-60)$$

where $\mathbf{C}, N \times N$, depends on the single pulse waveform and the range cell separation Δd.

We choose the rectangular linear FM waveform in the performance evaluation, i.e.,

$$g(t) = \frac{1}{\sqrt{\Delta\tau}} \text{rect}(\frac{t}{\Delta\tau}) \cos(2\pi(Bt^2/\Delta\tau + f_0 t)) \qquad (3-61)$$

where f_0 is the carrier frequency and

$$\text{rect}(t) = \begin{cases} 1 & -1/2 < t < 1/2 \\ 0 & \text{elsewhere} \end{cases}. \qquad (3-62)$$

Its correlation function is found to be [8]

$$h(\tau) = \frac{\sin 2\pi B\tau(1 - |B\tau|/\gamma_c)}{2\pi B\tau} \cos(2\pi f_0 \tau) = \frac{\sin 2\pi B\tau(1 - |B\tau|/\gamma_c)}{2\pi B\tau} \cos(2\pi B\tau/RBW) \qquad (3-63)$$

where $\gamma_c = \Delta\tau B$ is the pulse compression ratio and RBW the relative bandwidth. In practice, γ_c is chosen very large so that

$$h(\tau) \approx \frac{\sin 2\pi B\tau}{2\pi B\tau} \cos(2\pi B\tau/RBW). \qquad (3-64)$$

This type of waveform is quite commonly used in radar pulse compression for improving range resolution. The amplitude spectrum of the waveform with $\gamma_c = 100$ and $RWB = 0.5$ is shown in Fig. 4.

To calculate $\mathbf{C}$, we note that the klth element of $\mathbf{C}$ is

$$c_{lk} = \int \mathbf{g}^H(t - (l-1)\Delta d)\mathbf{R}^{-1}\mathbf{g}(t - (k-1)\Delta d)dt = \sum_{m=1}^{M} \sum_{n=1}^{M} r^{mn} g_{lkmn} \qquad (3-65)$$

where r^{mn} is the mnth element of $\mathbf{R}^{-1}$ and

$$g_{lkmn} = \int g^*(t - (l-1)\Delta d - (m-1)\Delta\alpha T_p)g(t - (k-1)\Delta d - (n-1)\Delta\alpha T_p)dt$$

$$= \int g(t)g^*(t - (l-k)\Delta d - (m-n)\Delta\alpha T_p)dt$$

$$= h((l-k)\Delta d + (m-n)\Delta\alpha T_p). \qquad (3-66)$$

Denote

$$\rho = B\Delta\alpha T_p \qquad (3-67)$$

and

$$\nu = B\Delta d. \qquad (3-68)$$

33
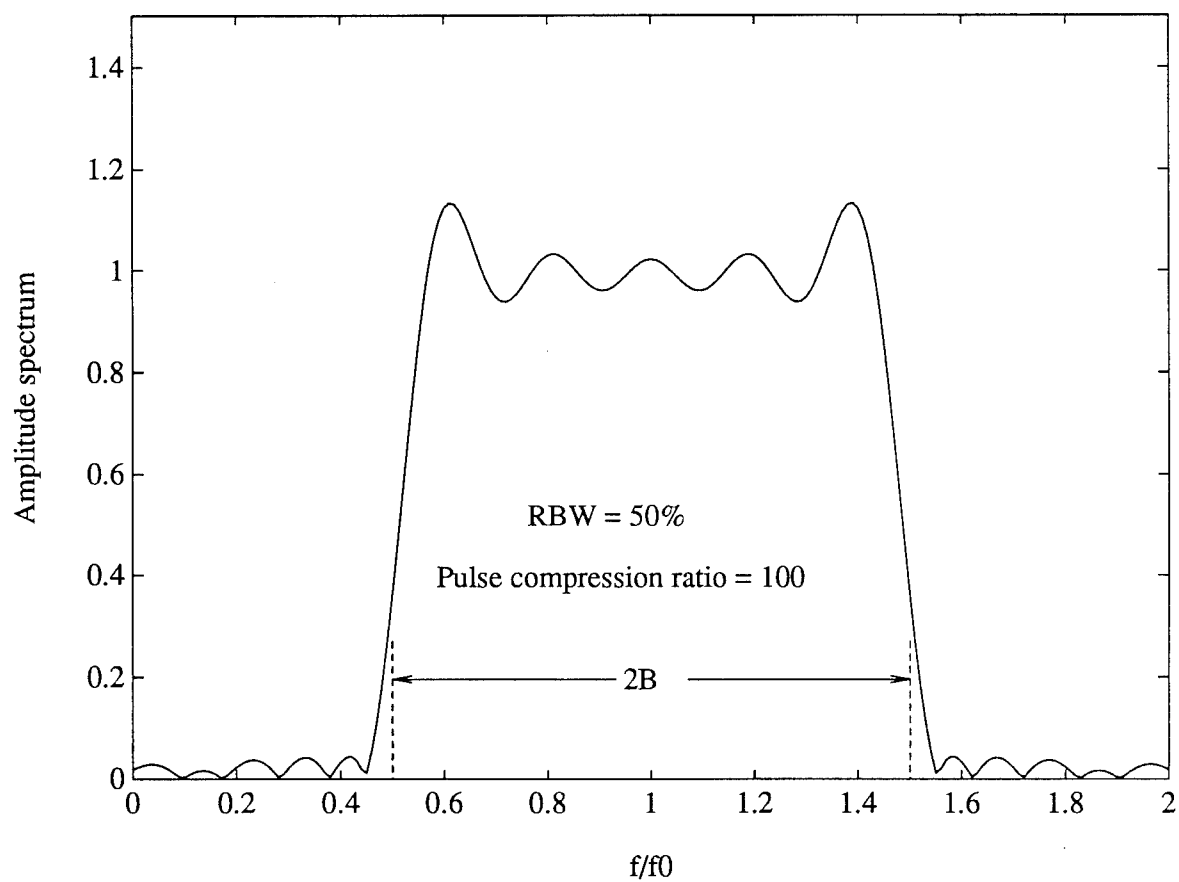
Fig. 4. Amplitude spectrum of the rectangular FM waveform

Obviously, Eq.(3-67) defines the difference of the range walk rate of the target and interference, and Eq.(3-68) is the normalized range cell separation with respect to the system range resolution. Then we have

$$g_{lkmn} = \frac{\sin 2\pi((l-k)\nu + (m-n)\rho)(1 - |(l-k)\nu + (m-n)\rho|/\gamma_c)}{2\pi((l-k)\nu + (m-n)\rho)}$$

$$\times \cos(2\pi((l-k)\nu + (m-n)\rho)/RBW). \qquad (3-69)$$

For the inter-pulse covariance matrix $\mathbf{R}$, we assume

$$\mathbf{R} = \sigma_c^2 \mathbf{R}_{c0} + \frac{N_0}{2}\mathbf{I} \qquad (3-70)$$

where σ_c^2 is the clutter power and

$$\mathbf{R}_{c0} = \{\exp -2(\pi\sigma_f(m-n))^2\}, \qquad (3-71)$$

with σ_f being the parameter controlling the interference spectrum spread. We note that the interference covariance setting given in Eq.(3-71) corresponds to a Gaussian shaped spectrum.

As we mentioned before, large portion of $\mathbf{a}$ will be zero as there are only few scatterers distributed in the range extent of interest. We are interested in the general behaviors of the processors with respect to the scatterer range distribution. Thus, given the number of the scatterers, we assume each scatterer is randomly scattered in the N range cells with equal probabilities and energy. Since the waveform is real under the large relative bandwidth assumption, the phases of the scatterers is represented only by the sign of the scatterer amplitudes, which is assumed to change between plus and minus with equal probability.

The computer simulation results are given in Fig. 5–Fig. 7. Due to computer resource limit, the probability of false alarm is set to $P_f = 10^{-3}$, although a practical value should be smaller. The total number of the range cells under test is chosen to be $N = 20$ with the normalized range cell separation $\nu = 1$. With $\rho = 0.8$, INR$= 2\sigma_c^2/N_0 = 50dB$, the closeness of the detection performance to the optimum is examined for the four scatterer integration schemes. Fig. 5 compares the detection performance of the int-of-m and m-out-of-N schemes. The actual number of the scatterers in the figure varies from 1 to 9, giving a sparse scatterer range distribution. The additional SNR, defined as the extra signal-to-receiver-noise ratio

required to catch up the detection performance of the optimum, is drawn as a function of the number of scatterers. Different m settings are set for both integration schemes: fixed case (m=5) and matched case ($m = J$) in order to see how sensitive the detection performance is to the selection of m. Fig. 6 gives the comparison of the int-of-all, int-of-m, and max-of schemes with the same parameter settings, followed by Fig. 7 as an example of the detection performance when $J = 5$.

Based on Fig. 5–Fig. 7, we have the following conclusions

(1) m-out-of-N performs worse than the int-of-m almost all the time. Its performance degradation becomes more severe when m is over-estimated as compared to the actual number of the scatterers. In contrast, the int-of-m shows much less sensitivity to the selection of the value of m.

(2) If $J = 1$, max-of has a better performance than the others. When J increases, however, the int-of-all and int-of-m pick up rapidly. In fact, at $J = 3$, the two already outperforms the max-of.

(3) If J is less than a quarter of N, the int-of-m delivers a best performance if m matches the number of the scatterers.

(4) When J is greater than a quarter of N, there is not much difference between the matched int-of-m and int-of-all. In this sense, exactly knowing J is not important since int-of-all already achieves the desired performance for a quite wide range of J.

(5) When $J > N/2$, both int-of-m and int-of-all show a very small performance degradation (< 1dB).

Based upon the above facts, int-of-m and int-of-all are recommended depending on the number of the scatterers. We are in favor of the latter one as it shows a good detection performance over a wide range of J, and doesn't require the knowledge of J.
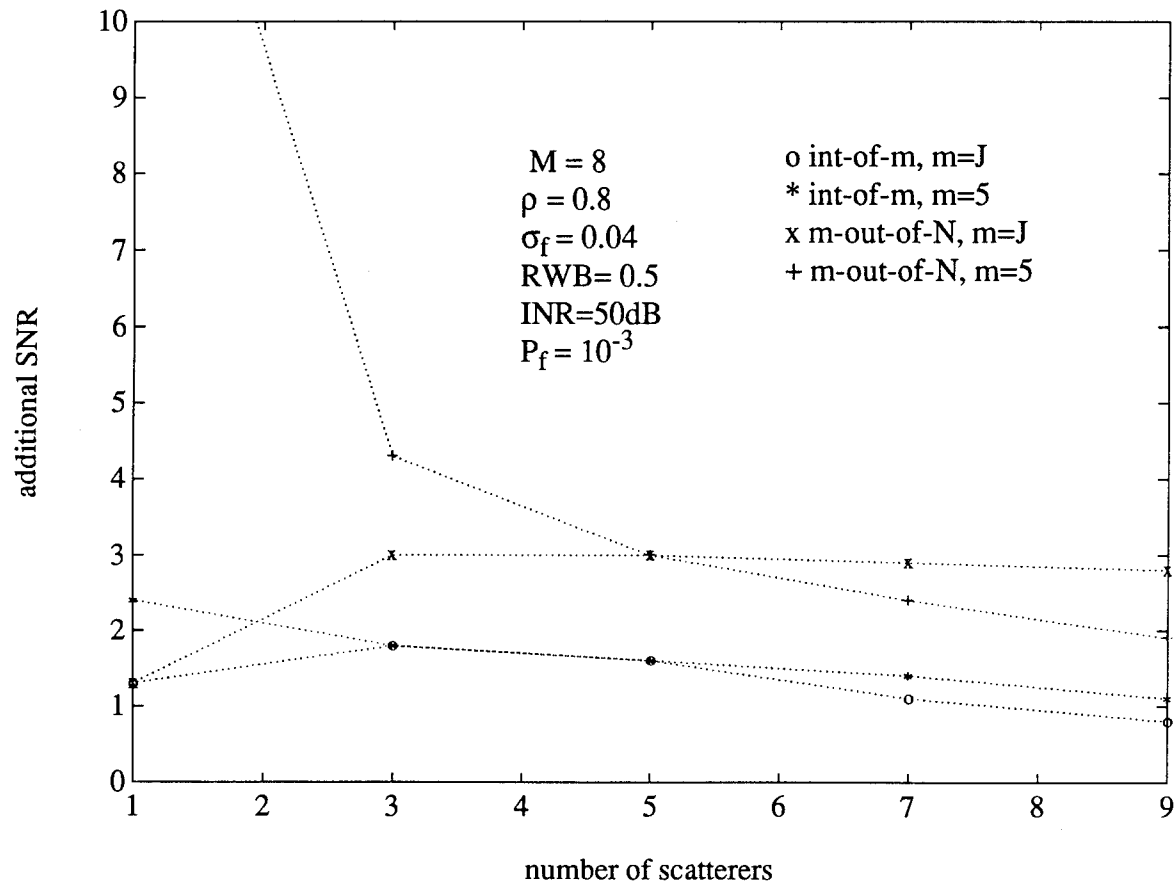
Fig. 5. Performance comparison of the integration-of-m and m-out-of-N inter-scatterer integration schemes.
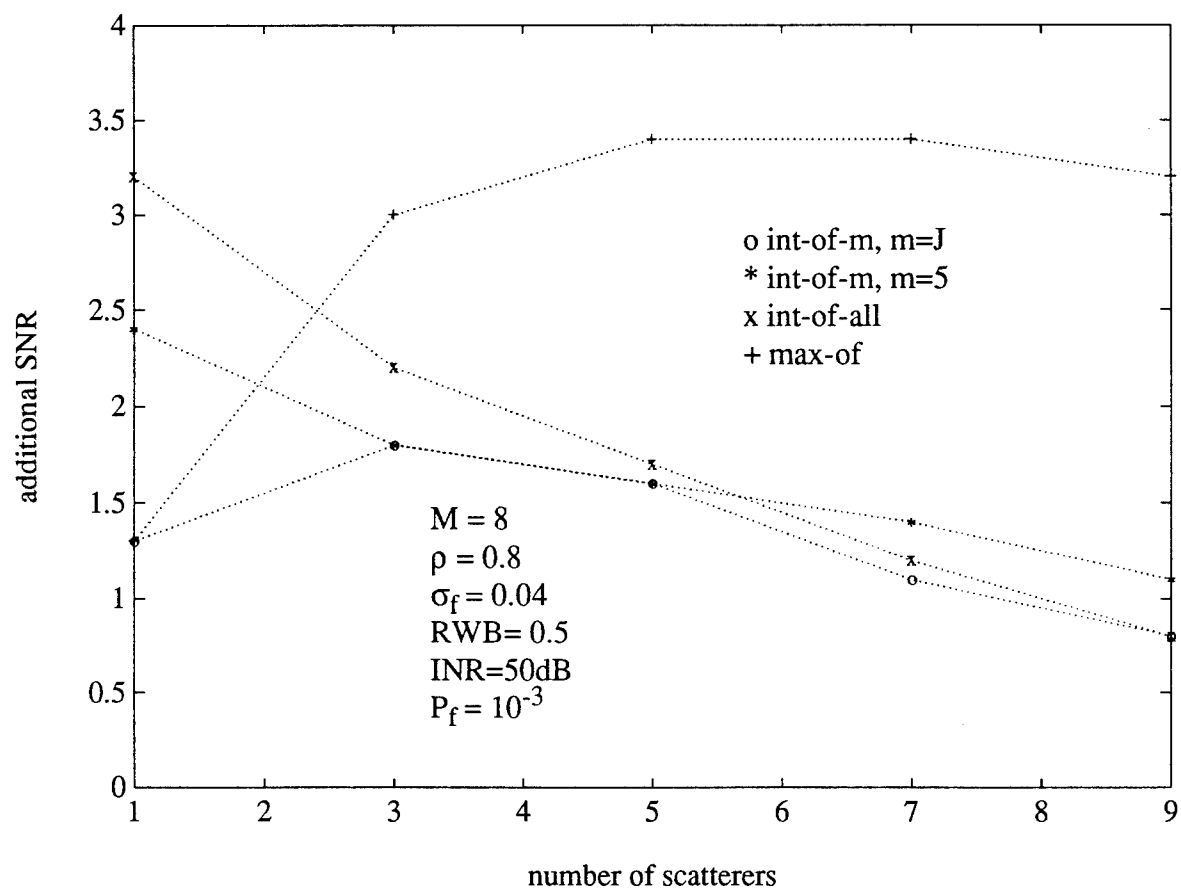
Fig. 6. Performance comparison of the integration-of-all, integration-of-m, and max-of inter-scatterer integration schemes.
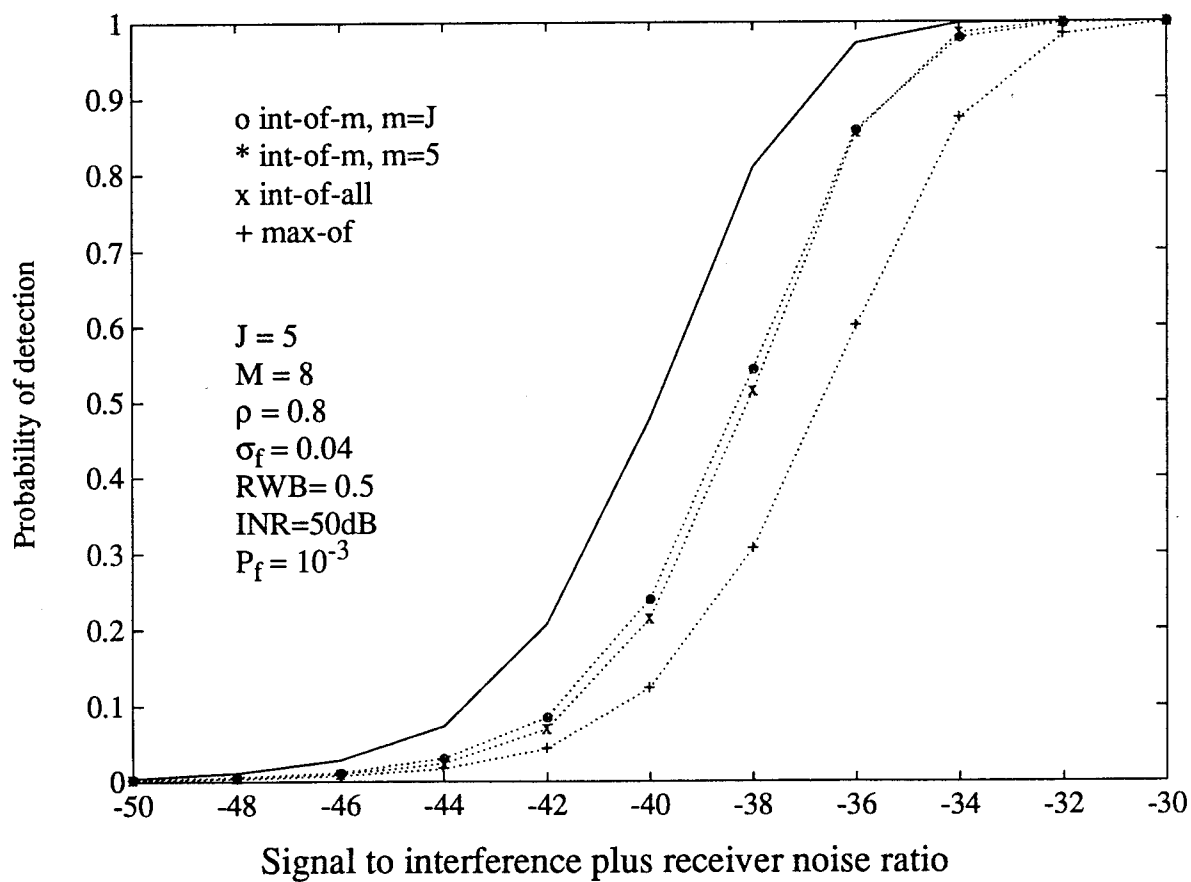
Fig. 7. Detection Performance of the integration-of-all, integration-of-m, and max-of inter-scatterer integration schemes.

I.4 Performance Comparison of Narrowband and UWB Systems

In this section, we will compare the detection performance potential achievable by the narrowband (NB) and UWB systems. The optimum processors under comparison are the waveform-based optimum UWB processor given in Section I.3.1.1, and the conventional optimum narrowband processor specified by Eq.(3-19)-Eq.(3-20) of Section I.3.1.2.

As the NB and UWB systems differ significantly in their range resolution, target modeling, and level of interference, it is not easy to make a fair comparison in a straightforward way. It would be beneficial for us to carry out the investigation by steps so that the problems can be isolated for easy understanding. In general, the UWB gains include the clutter reduction gain, the fluctuation reduction gain, and the discrimination gain, each of which shows up under different bandwidth. In order to individually identify the gains, we classify the following four typical cases in terms of the signal bandwidth:

Case 1. The bandwidth of the system, denoted by B_1, is narrow, so that the signal return can be considered as point target, which corresponds to the data modeling discussed in Section I.2.2. Obviously this is the conventional narrow band system.

Case 2. The bandwidth B_2 of the system is greatly increased, but not to a level at which the multiple dominant scattering centers of the target can be resolved, so that the point target assumption still holds. For comparison, we will set B_2 equal to the so-called critical bandwidth, which is just about to resolve the individual scatterers. For this case the target is comparable in size to the range resolution.

Case 3. The system bandwidth is well beyond the critical bandwidth, so that the signal returns consist of the well-resolved scatterers as modeled in Section I.2.1. For moving targets, the pulse shift due to the scatterer movement will result in sufficient Doppler shift, but the corresponding range walk is essentially small.

Case 4. The system bandwidth is further increased. The range resolution is so fine that the return from the individual scatterers will "walk" form one resolution cell to another among the pulses during the coherent processing interval (CPI), which is usually referred to as range walk or range migration.

Obviously, the bandwidth of the above four cases follows the order of $B_1 \ll B_2 \ll$

$B_3 \ll B_4$. For convenience of discussion, parameters associated with difference cases will be distinguished by an additional subscript corresponding to the case number whenever necessary. Performance evaluation will be carried out in the following on a basis of case-to-case comparison. We will see how the bandwidth will dominantly affect the system detection performance.

4.1   Comparison of Cases 1 and 2: Clutter Reduction Versus False Alarm Adjustment

The performance comparison is conducted for Case 1 and Case 2 in this subsection.

Basically, there is not much fundamental difference between the two as the point target modeling is suitable for both cases. Since the range-cell size resolved by the bandwidth B_2 becomes much smaller than that of B_1, however, the associated interference power contained in each range cell will be greatly reduced. Of course, less clutter power implies better target detectability. The clutter reduction effect is clearly indicated in Eq.(2-40) of Section I.2.1, where the effective interference power is inversely proportional to the bandwidth. Define the average interference power for both cases

$$\sigma_{c1}^2 = \frac{1}{2B_1} \text{tr}(\tilde{\mathbf{R}}_c)/M \qquad (4-1)$$

and

$$\sigma_{c2}^2 = \frac{1}{2B_2} \text{tr}(\tilde{\mathbf{R}}_c)/M. \qquad (4-2)$$

Then we have the interference power constraint for the comparison

$$\sigma_{c2}^2 = \beta_1 \sigma_{c2}^2, \qquad (4-3)$$

where β_1 stands for the bandwidth ratio $\beta_1 = B_2/B_1$ for the two cases.

In the mean time, also due to the smaller rang-cell size, the system with B_2 will have to process more range cells for a given spatial volume, which in turn would introduce more global false alarm. Maintaining the same level of global false alarm in the given volume requires lower false alarm rate in a single range cell and thus will degrade the detection performance. Under the assumption that the decision are independently made in each range cells, it is easy to find the probability of false alarm in each range cell for the two systems,

41

denoted by P_{f1} and P_{f2}, satisfies

$$P_{f2} = 1 - (1 - P_{f1})^{1/\beta_1} \qquad (4-4)$$

to maintain the same level of global false alarm rate.

It is clear that the constraints imposed by Eq.(4-3) and Eq.(4-4) have opposite effects on the system detection performance. In other words, when the bandwidth increases, we are playing trade-off between the interference power and probability of false alarm.

Before we proceed further, some other conditions are specified below for convenience of conducting comparison:

(1) the noise spectrum level N_0 and signal variance σ_s^2 of the two systems are set to equal.

(2) the interference covariance matrix $\tilde{\mathbf{R}}_c$ is defined by

$$\tilde{\mathbf{R}}_c = \sigma_c^2 \{ e^{-2(\pi \sigma_f(m-n))^2 + i2\pi(m-n)f_c} \} \qquad (4-5)$$

where σ_f is the parameter controlling the interference spectrum spread, σ_c the interference power, and f_c the normalized Doppler frequency of the interference. Recall the difference between f_c and f_s is denoted by $\Delta f = f_s - f_c$.

(3) for both cases, we use the same optimum processor as given in Eq.(3-19)-Eq.(3-20) Section I.3.1.2. Thus the analytical detection performance the of optimum processor is found in Eq.(3-24)-Eq.(3-26).

In Fig. 8, the detection performance curves as a function of signal-to-receiver-noise ratio (SNR) are plotted for investigating the performance loss due to the false alarm constraint governed by Eq.(4-4). In order to single out the effects of the P_f constraint, the interference power constraint in Eq.(4-3) is omitted. Instead, we purposely set the interference power equal, not changing with the bandwidth. It is seen that even for a very large bandwidth ratio, the detect performance loss is negligibly small ($< 2\text{dB}$). In fact, the performance loss factor, defined as the ratio of SNR's requires by the two systems to achieve the same probability of detection, is found to be

$$\text{SNR}_1/\text{SNR}_2 \approx \frac{\ln(P_{f1})}{\ln(P_{f2})} \approx \frac{\ln(P_{f1})}{\ln(P_{f1}/\beta_1)}. \qquad (4-6)$$

We note that the performance loss factor is independent of the signal and interference characteristics, and is related to the logarithm of the probability of false alarm only, which indicates a slight change even if P_{f1} varies several orders of magnitude.

Fig. 9 illustrates the effects of the interference power constraint with the probability of false alarm unchanged. For INR_1=60dB, $\sigma_f = 0.06$, and $\Delta f = 0.2$, the performance improvement is apparent. It is easy to see that the performance gain, measure by the amount of SNR adjustment to maintain the same P_d, depends on the severity of the interference environment. It approaches its maximum $(10 \log(\beta_1)\text{dB})$ for tough interference conditions such as high INR, small Δf, and large σ_f.

The joint effects of the two constraints are shown in Fig. 10. The bandwidth ratio is set to $\beta_1 = 10$. The dotted line in this figure is drawn to illustrate a intermediate result, which imposes the interference power constraint only. Obviously, the gain due to the reduction of the interference power is much larger than the loss caused by the false alarm constraint. In other words, the trade-off between the two constraints can lead to significant detection performance improvement, exhibiting the advantages of increasing signal bandwidth.

4.2 Comparison of Cases 2 and 3: Fluctuation Reduction Versus Collapsing Loss

The goal of this subsection is to investigate the effects of the multiple dominant (MDS) target model on the system detection performance as compared to the point target model. The major difference between the two models is that the MDS target model can largely reduce target fluctuation and the resolved scatterers are distributed in a number well-separated range cells.

Although the interference power in a single range cell will continually drop as we further raise the signal bandwidth to the level in Case 3, the total amount of the interference power contained in those range cells that join the hypothesis testing would remain approximately the same as in Case 2. Moreover, the false alarm rate will not change too much since the test is now performed over the range cells with a total dimension comparable to target. For these reasons, the trade-off between the interference power and false alarm will no longer play a dominant role in the performance comparison in this subsection.

The waveform-based UWB optimal processor is applied to Case 3 for target detection and the related detection performance can be obtained by numerically evaluating Eq.(3-52)-Eq.(3-54). The rectangular FM waveform given in Section I.3.2 is also used here for comparison.
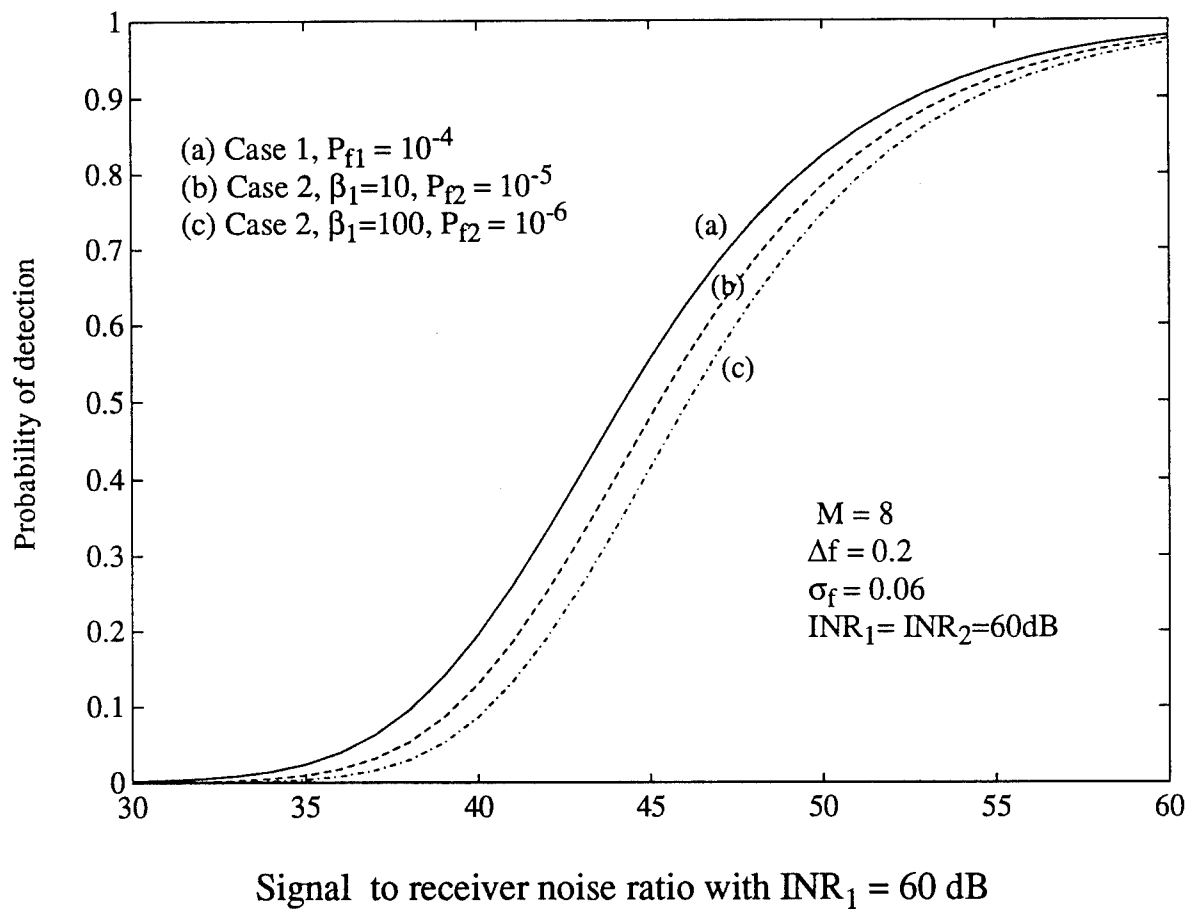
Fig. 8. Performance comparison of Case 1 and Case 2:
effect of false alarm constraint.
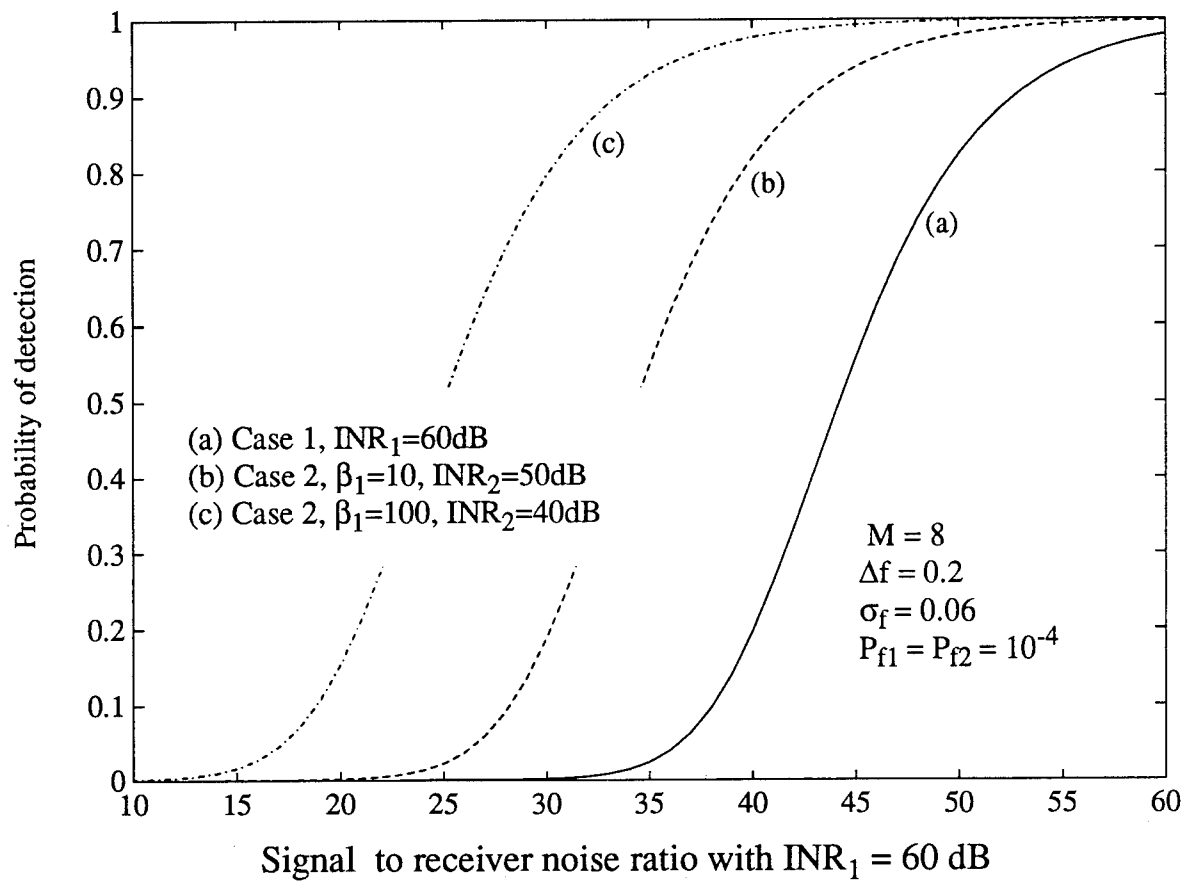
Fig. 9. Performance comparison of Case 1 and Case 2:
effect of interference power constraint.
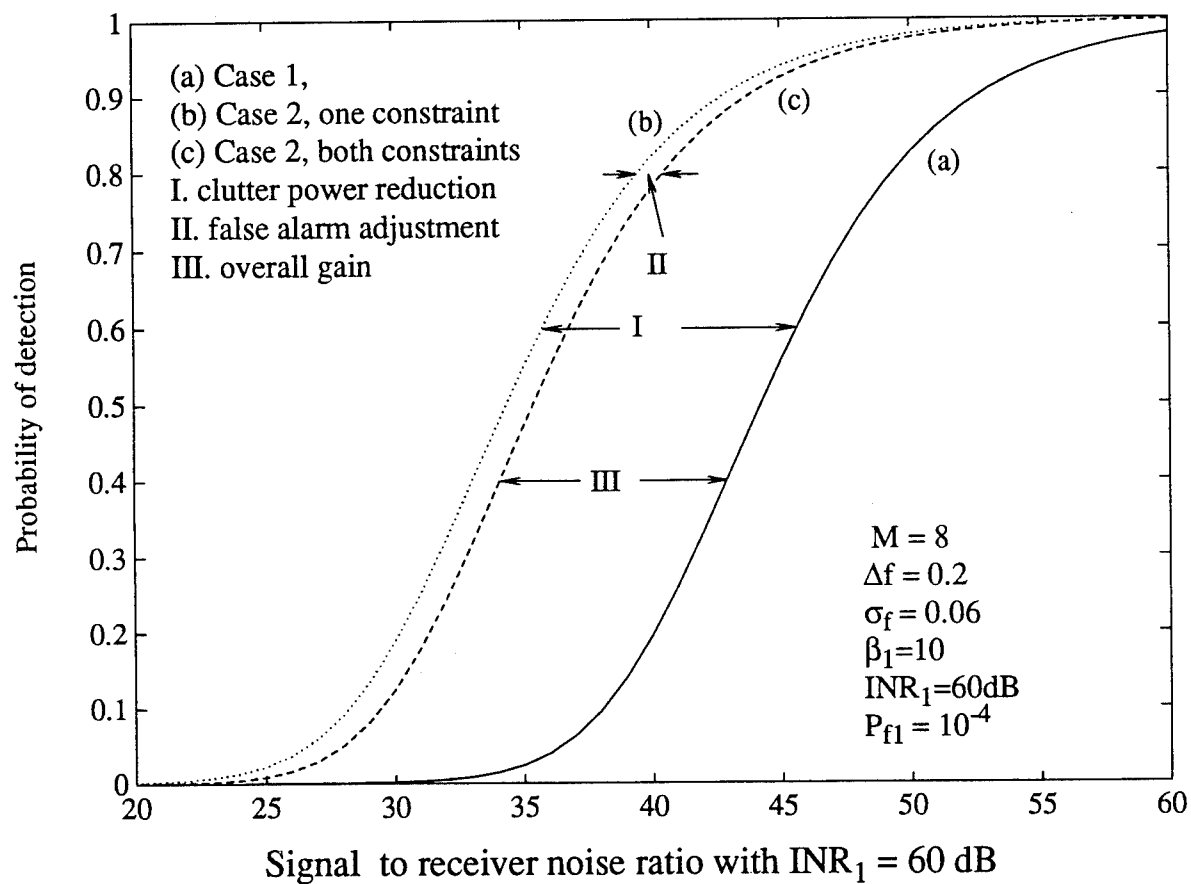
Fig. 10. Performance comparison of Case 1 and Case 2:
interference reduction versus false alarm adjustment.

In case of unknown scatterer separation, the integration-of-all scheme recommended by Section I.3.2 is used for inter-scatterer integration in the suboptimum processing. The performance difference from the optimum due to the unknown scatterer separation is conventionally termed "collapsing loss" [9]. Obviously, the fluctuation reduction gain and the collapsing loss, both of which are the consequence of raising system bandwidth, plays a trade-off role in controlling the detection performance.

For the MDS target model, the amplitudes of the scatterers, $a_j, j = 1, 2, ..., J$, are modeled as unknown deterministic constants, since little fluctuation associated with them is observed [3] in practice. For comparison, the total signal energy of the scatterers, denoted by $\sigma_{s3}^2 = \sum_{j=1}^{J} |a_j|^2$, is set equal to σ_{s2}^2 of Case 2. The interference power follows the relation $\sigma_{c3}^2 = \sigma_{c2}^2/\beta_2$. The probability of false alarm is fixed at $P_{f2} = P_{f3} = 10^{-6}$ for both cases.

Fig. 11 shows an example of the comparison of the detection performance of the MDS and point target models using the corresponding optimum processors. The number of scatterers J equals to 5 in the figure. With $\beta_2 = B_3/B_2 = 10$, Fig. 11 plots the detection performance of Case 2, together with that of Case 3 with both known and unknown scatterer separation. We can see that the probability of detection for the MDS model climbs up much faster than that of the point target model. To achieve a reasonably good detection performance (such as $P_d = 0.8$) the MDS UWB processor requires much lower SNR (around 10dB), leading to a significant improvement.

Fig. 11 also illustrates the fact that the collapsing loss is much smaller than the fluctuation reduction gain, since the difference between the performance of the UWB processors with known and unknown separation is much less significant ($< 2dB$), which was already shown in Section I.3.2.

4.3 Comparison of Cases 3 and 4: Extra Discrimination Gain

In this subsection, we are mainly concerned about the effects of the range walk on the system detection performance.

The carrier frequencies is set equal for both cases under the comparison. Thus for the same target and interference environment, both systems will have the same Doppler shift Δf. However, the range walk rate $\Delta \rho$ will differ greatly for the two systems. It can be shown that the ratio of the range walk rates for the two systems will also be $\Delta \rho_3/\Delta \rho_4 = \beta_3$.
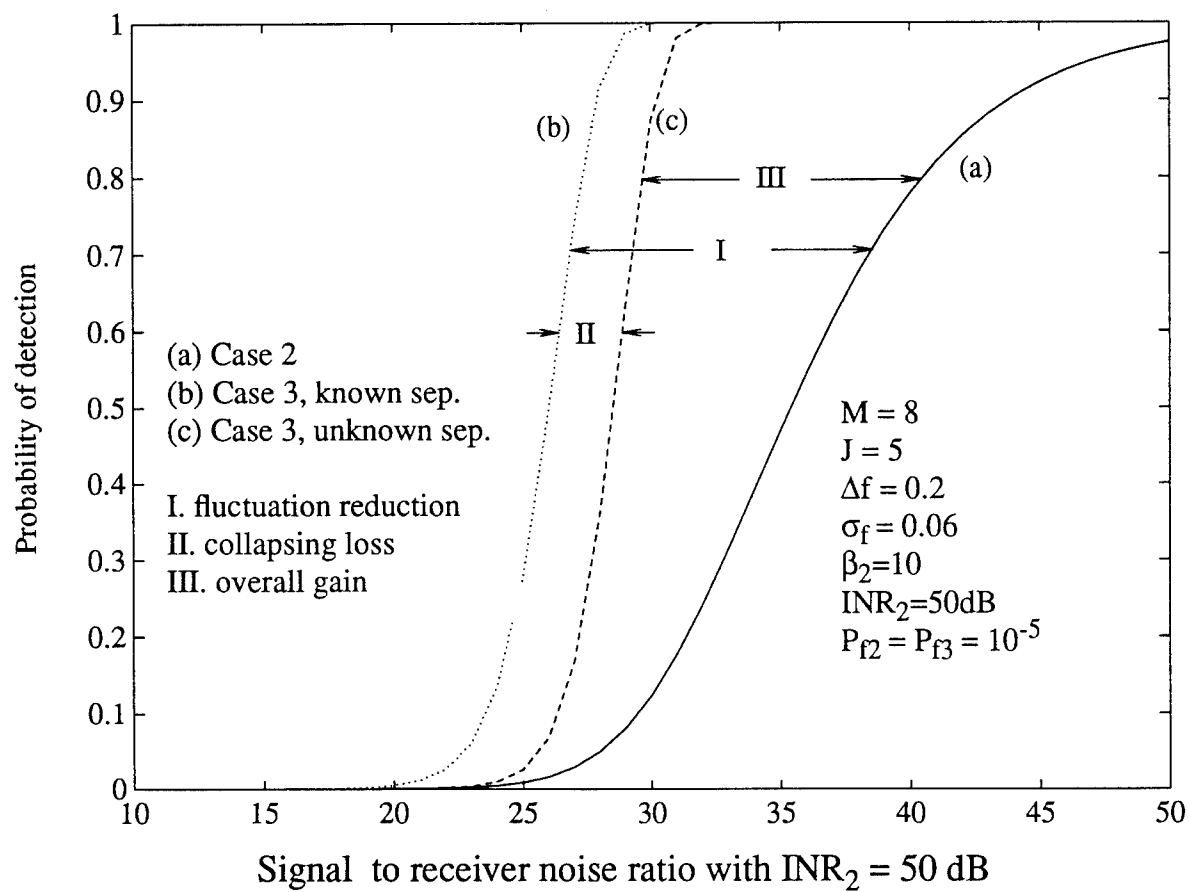
Fig. 11. Performance comparison of Case 2 and Case 3:
fluctuation reduction versus collapsing loss.

For convenience of comparison, we assume that the scatterers are well separated and their separation is known. In order to single out the effect of the range walk on the system detection performance, we purposely chose the same interference power for both systems, (i.e., $\sigma_3^2 = \sigma_4^2$), although in fact it largely depends on the system bandwidth.

Fig. 12 plots the probability of detection as a function of the signal-to-receiver-noise ratio. Target velocity and thus its Doppler frequency are fixed for both cases, so that the variation of $\Delta\rho$ is simply due to different system bandwidth. The interference conditions are considered severe as we have high interference-to-recever-noise ratio (INR), large interference spread σ_f, and small target-interference Doppler separation Δf as shown in the figure. For the system with bandwidth B_4, the relative bandwidth is set to RBW=0.5, which leads to $\Delta\rho = 0.1$ if $\Delta f = 0.2$. The bandwidth ratio of the two systems is chosen $\beta_3 = 10$, hence the range walk rate of the smaller bandwidth is almost equal to zero ($\Delta\rho = 0.01 \approx 0$). It is seen from the figure that the detection performance with larger $\Delta\rho$ outperforms that with smaller $\Delta\rho$ under server interference conditions. Clearly, the range walk discrimination now comes into play when the Doppler shift discrimination alone is not sufficient.

When the interference conditions become mild as given in Fig. 13, however, larger $\Delta\rho$ does not necessarily mean better performance. This is because the total noise power included by the system with bandwidth B_4 is larger than that of B_3, which will dominate the detection performance when the clutter can be well suppressed by Doppler processing already.

For coherent multiple pulse Doppler processing, the problem of multiple blind speeds is well recognized, especially for UWB systems operating with a very high carrier frequency that would lead to a fairly large Doppler shift. Fig. 14 shows that the Doppler ambiguity problem can be largely solved if the range walk discrimination is used. The normalized Doppler shift Δf, which is conventionally confined within [-1/2, 1/2] to avoid Doppler ambiguity, is now extended to 3. For the system with larger range walk rate contributed by B_4, Fig. 14 shows that a fairly flat performance can be achieved over those previous blind Doppler frequencies. In fact, when $\Delta f > 1$, the detection performance can be maintained nearly as a constant, insensitive to the change of the Doppler frequency shift. We note that Fig. 14 only shows the results for incoming targets. For negative Doppler frequency the conclusion should be similar.
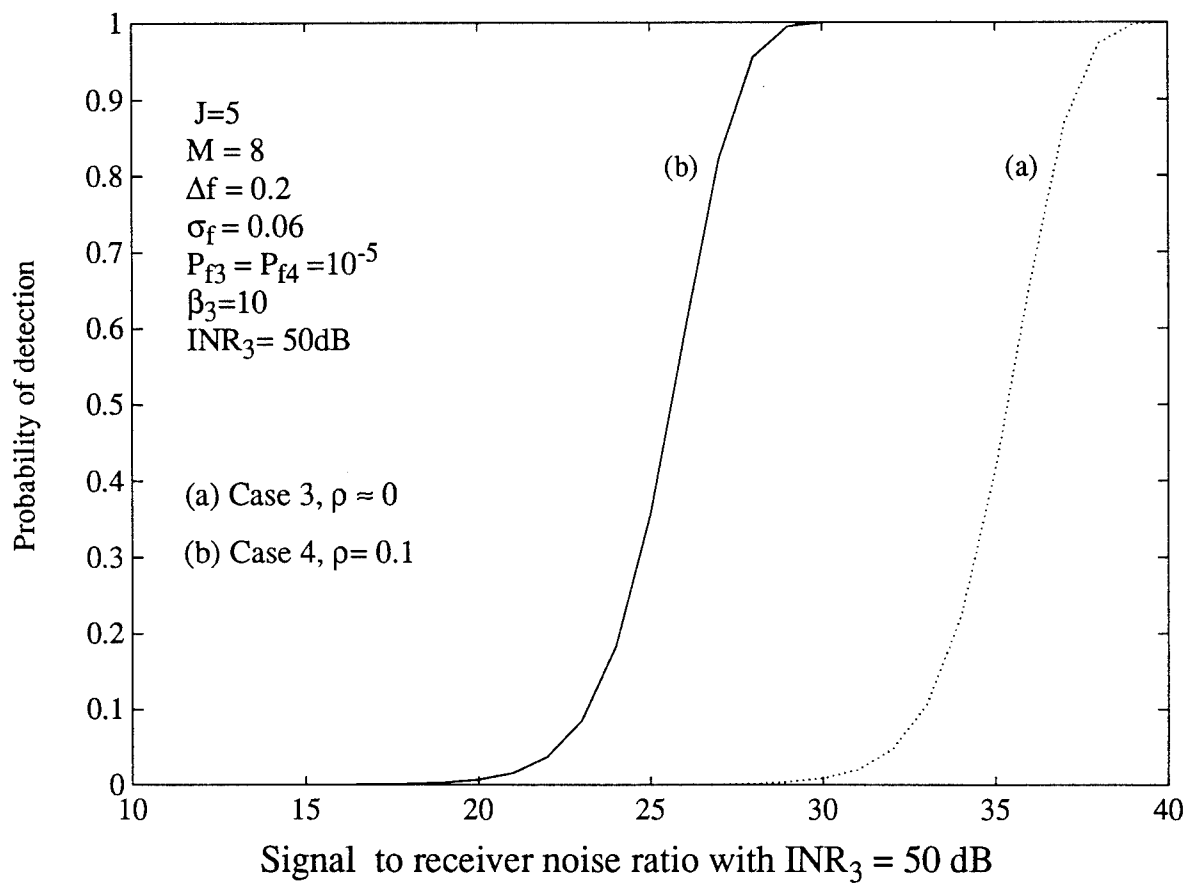
Figure 12. Performance comparison of Case 3 and Case 4:
severe interference conditions.
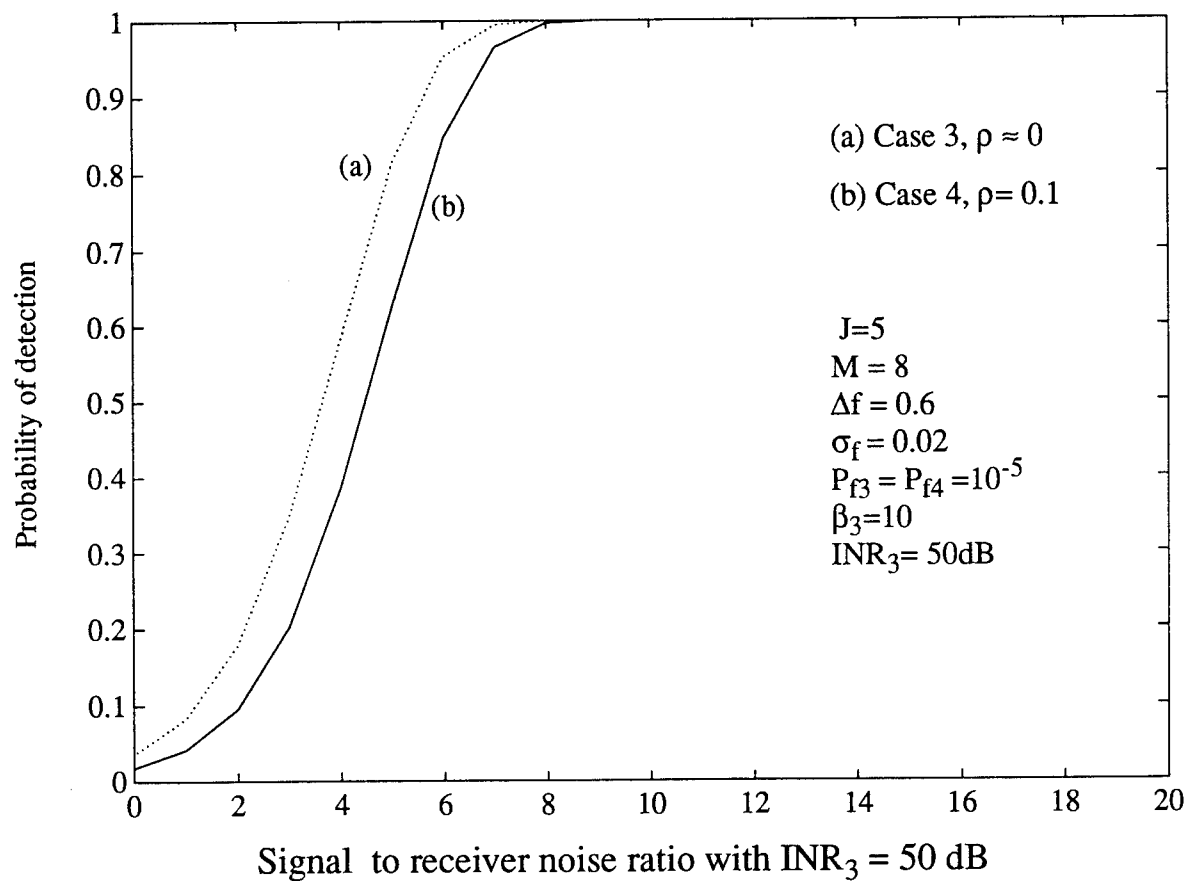
Figure 13. Performance comparison of Case 3 and Case 4:
mild interference conditions.

4.4 Overall Comparison: NB versus UWB

So far, we have separately investigated the performance gain due to different factors that come into play when we raise the system bandwidth by steps. Three essential aspects were considered:

1. clutter reduction versus false alarm adjustment
2. fluctuation reduction versus collapsing loss
3. extra discrimination gain due to range walk.

Comparisons were made between the four typical cases, each of which represents different bandwidth range.

To see the joint effects of the UWB technology, the detection performance curves for all the cases are plotted together in Fig. 15. The following conditions and parameter specifications for signal, interference, and false alarm are set for the four cases:

$$\sigma_{c4}^2 = \frac{\sigma_{c3}^2}{\beta_1} = \frac{\sigma_{c2}^2}{\beta_1 \beta_2} = \frac{\sigma_{c1}^2}{\beta_1 \beta_2 \beta_3}, \qquad (4-7)$$

$$\sigma_{s1}^2 = \sigma_{s2}^2 = \sigma_{s3}^2 = \sigma_{s4}^2, \qquad (4-8)$$

and

$$P_{f4} = P_{f3} = P_{f2} = 1 - (1 - P_{f1})^{1/\beta_1}, \qquad (4-9)$$

where $\beta_1 = B_2/B_1$, $\beta_2 = B_3/B_2$, and $\beta_3 = B_4/B_3$. The contributions due to each individual factor are clearly shown in the figure and the overall performance gain is seen by the performance difference between Case 1 and Case 4, which is obviously an significant improvement for the server interference conditions as given in the figure.
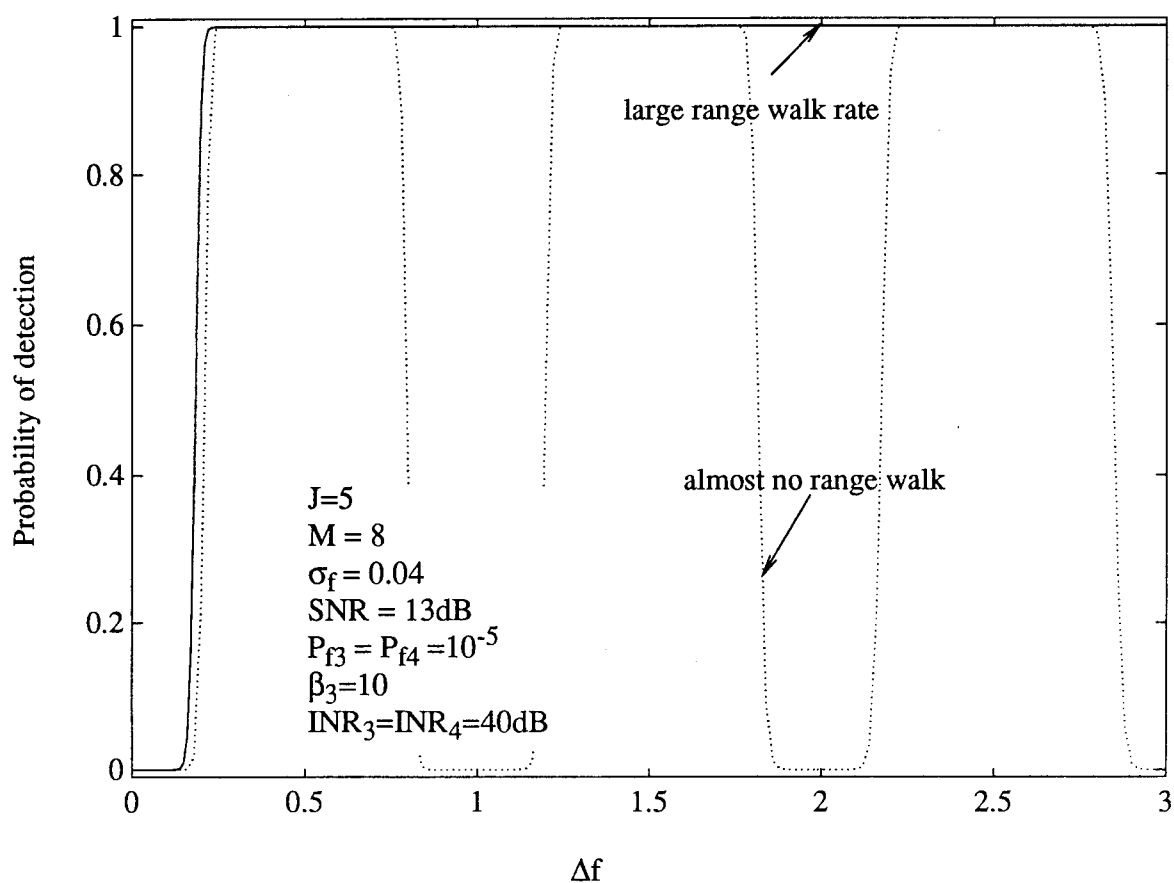
Figure 14. Performance comparison of Case 3 and Case 4: detection performance vs. Doppler shift difference of target and interference.
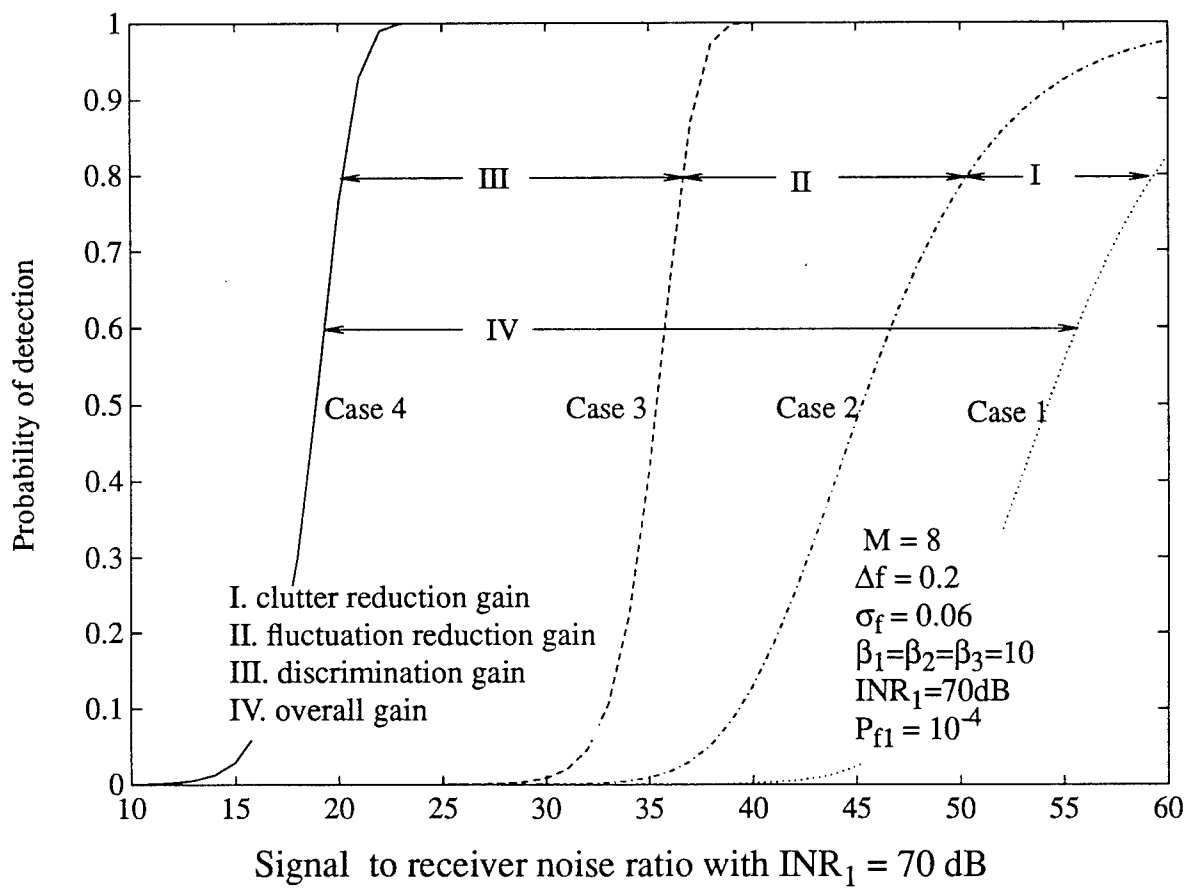
Fig. 15. Performance comparison of UWB and NB systems:
overall UWB gain.

I.5 Conventional Canceler-Based UWB Processing

5.1 Conventional Canceler-based UWB Processor

This section will present the conventional pulse-canceler-based UWB processor. It is realizable in the sense that it doesn't requir *a priori* knowledge about the interference covariance and the scatterer separation, which is usually not available in practice.

Let $\mathbf{T}$ be an $M' \times M$ transform matrix representing the operation of a conventional pulse canceler, where M' is the dimension of the data after the cancellation. An example is given below for a three pulse canceler

$$\mathbf{T} = \begin{bmatrix} 1 & -2 & 1 & 0 & \cdots & \cdots & \cdots & 0 \\ 0 & 1 & -2 & 1 & \ddots & & & \vdots \\ \vdots & \ddots & \ddots & & \ddots & \ddots & & \vdots \\ \vdots & & \ddots & \ddots & & \ddots & \ddots & \vdots \\ \vdots & & & \ddots & \ddots & & \ddots & 0 \\ 0 & \cdots & \cdots & \cdots & 0 & 1 & -2 & 1 \end{bmatrix}. \tag{5-1}$$

As the interference covariance is assumed unknown, we replace the optimum clutter canceler part of the optimal processor by the conventional pulse canceler, i.e., $\mathbf{R}^{-1}$ in Eq.(3-42)-Eq.(3-43) is replaced by a constant matrix $\mathbf{P}$

$$\mathbf{P} = \mathbf{T}^H \mathbf{T}. \tag{5-2}$$

Thus the test statistic of the processor becomes

$$\eta = \mathbf{x}^H \mathbf{C}^{-1} \mathbf{x} \mathop{\gtrless}_{H_0}^{H_1} \eta_0 \tag{5-3}$$

where

$$\mathbf{x} = \int \mathbf{G}'^H(t) \mathbf{x}'(t) dt \qquad J \times 1 \tag{5-4}$$

and

$$\mathbf{C} = \int \mathbf{G}'^H(t) \mathbf{G}'(t) dt \qquad J \times 1 \tag{5-5}$$

with $\mathbf{x}'(t)$ and $\mathbf{G}'(t)$ being defined by

$$\mathbf{x}'(t) = \mathbf{T}\mathbf{x}(t) \tag{5-6}$$

$$\mathbf{G}'(t) = \mathbf{T}\mathbf{G}(t). \qquad (5-7)$$

We should note that it works well only under the assumption that the interference has zero-velocity.

The block diagram of the processor is illustrated in Fig. 16 and 17. Similar to the optimum UWB processor, the conventional processor can be devided into three major parts: the conventional interference canceler, the velocity-based multiple pulse correlator, and the inter-scatterer integrator. The interference canceler supresses clutter by the convertional MTI pulse cancellation principle. The effects of Doppler shift and range walk, both of which are due to the inter-pulse shift, are jointly compensated in the velocity-based correlator in order to obtain coherent integration gain. Clearly, the velocity-based correlator is the unique part of the UWB processing with large relative bandwidth, as it attempts to make the best use of the velocity-associated discrimination against clutter. For the scatterer integration part, any of schemes discussed in Section I.3.2 can be applied to the processor. We will select the integration-of-all scheme for the reasons given in Section I.3.2.

The application of the above proposed conventional UWB processor requires *a priori* knowledge of the target velocity. In the case of unknown target velocity, a bank of the velocity-based correlators can be placed to cover the velocity range of interest. Fig. 18 shows such a configuration, where the time scaling factor α_s in the taped delay line of each correlator is tuned at the corresponding velocity.

If we use a UWB waveform with small relative bandwidth, the processor still has the above form. The only difference is that all the data waveforms are now replaced by its complex representation without the carrier frequency component.

With the similar way used in Section I.3.1, it is found that the above processor degenerates to the conventional MTI processor if no range walk is observed for slowly moving targets. Then the test rule is given by

$$\eta = |\mathbf{w}^H \mathbf{T} \mathbf{y}|^2 \underset{H_0}{\overset{H_1}{\gtrless}} \eta_0 \qquad (5-8)$$

where

$$\mathbf{y} = \int \tilde{A}^*(t - \tau_0) \tilde{\mathbf{x}}(t) dt, \qquad (5-9)$$

and

$$\mathbf{w} = \mathbf{T}\mathbf{s}. \qquad (5-10)$$

56
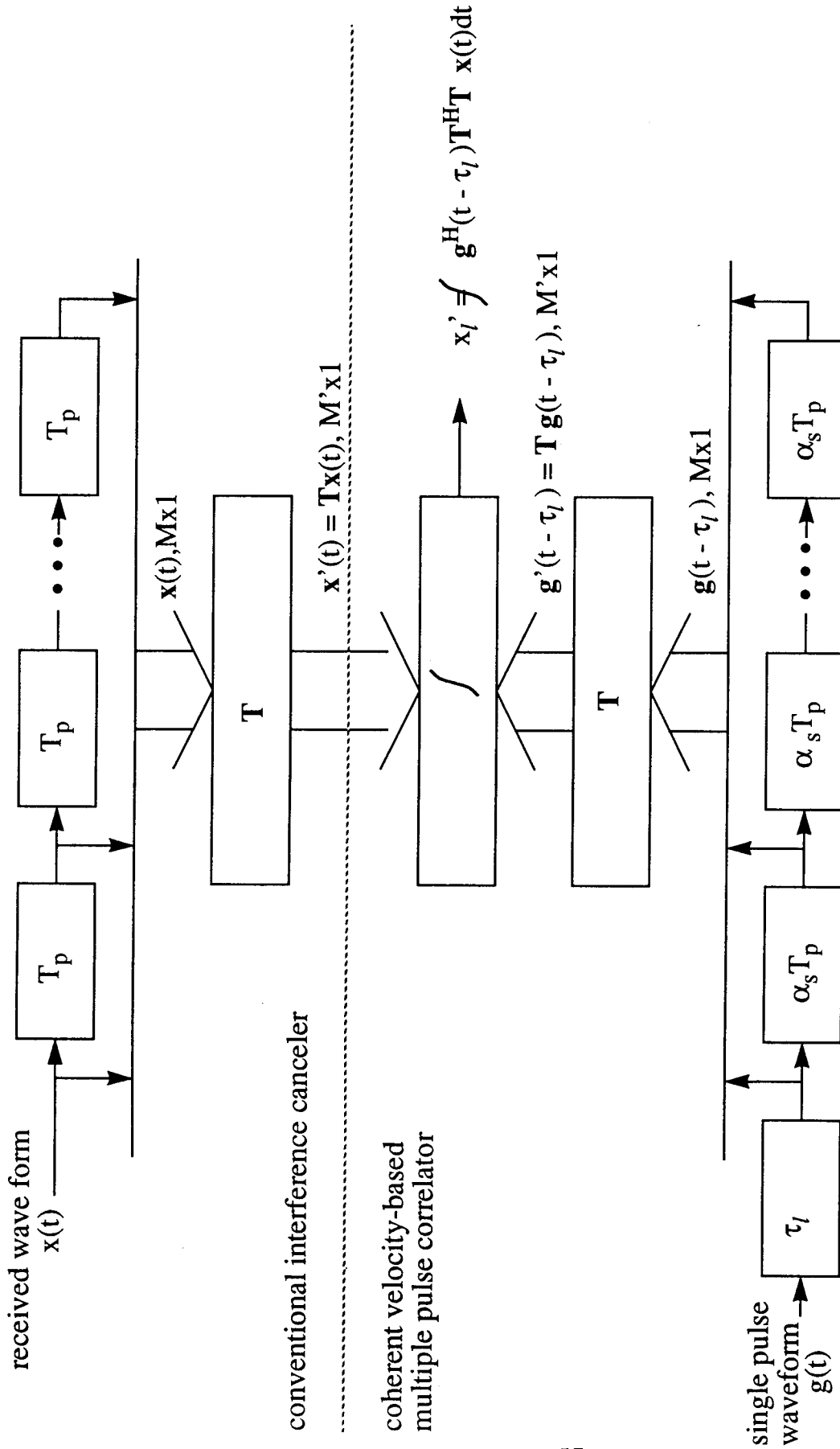
Fig. 16. Structure of the conventional UWB processor: interference canceler and multiple pulse correlator.
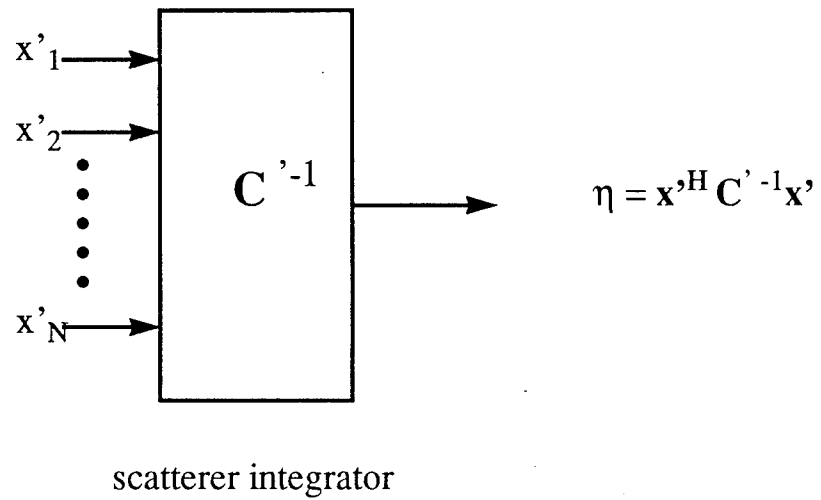
Fig. 17. Structure of the conventional UWB processor:

inter-scatterer integrator.
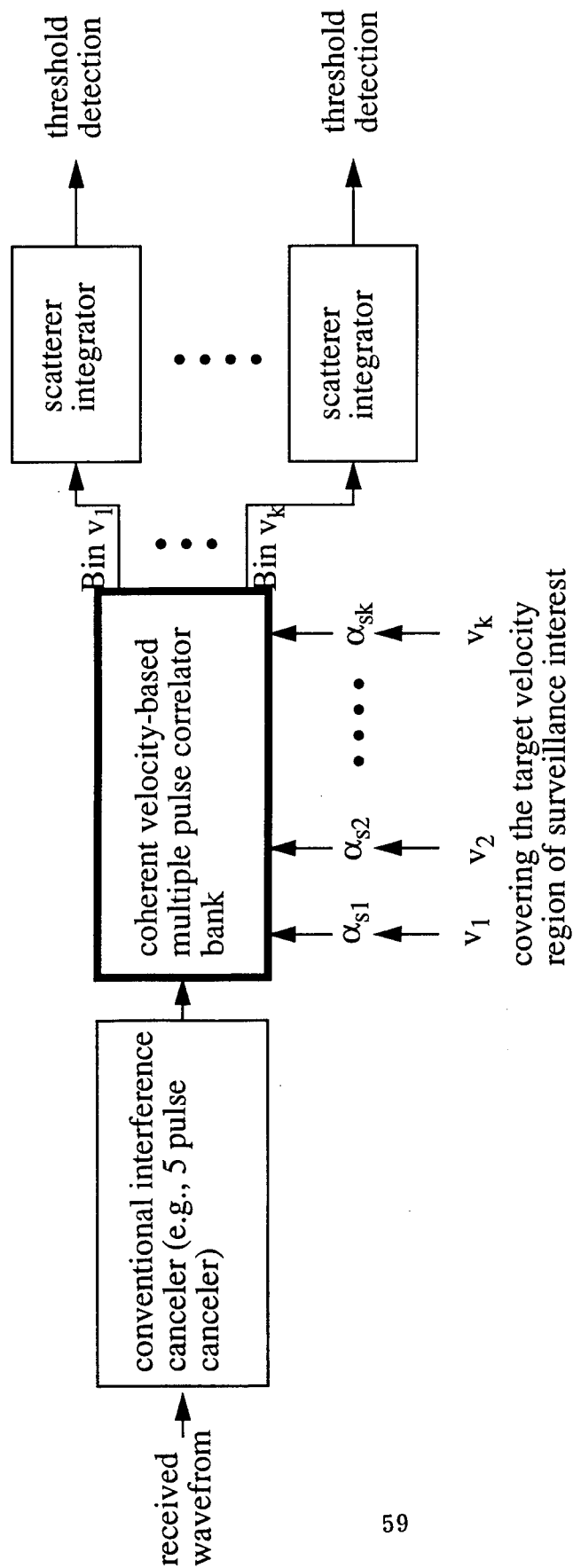
Fig. 18. The conventional UWB processor for detection of targets with unknown velocity.

It is easy to see that the above processor shows a structure of a convention MTI pulse canceler followed by an FIR filter.

Under the assumption that $\tilde{a}_0$ is modeled by a Gaussian variable with zero mean and covariance σ_s^2, the detection performance with small relative bandwidth is found to be

$$P_f = \exp(-\eta_0') \qquad (5-11)$$

and

$$P_d = \exp(-\eta_0'/(1+\gamma)). \qquad (5-12)$$

where γ is given by

$$\gamma = \sigma_s^H \frac{|\mathbf{w}^H \mathbf{T} \mathbf{s}|^2}{\mathbf{w}^H \mathbf{T}^H \mathbf{R} \mathbf{T} \mathbf{w}} \qquad (5-13)$$

and η_0' is related the actual threshold by

$$\eta_0' = \frac{\eta_0}{\mathbf{w}^H \mathbf{T}^H \mathbf{R} \mathbf{T} \mathbf{w}}. \qquad (5-14)$$

5.2   Performance Evaluation

This subsection evaluates the detection performance of the canceler-based UWB processor. We will compare the processor with the UWB optimum to see how it performs with unknown interference and target characteristics.

Even though we can find a close-form expression for the detection performance of the canceler-based UWB processor, the result is tedious and inconvenient to perform numerical evaluation. Instead, we will conduct the performance evaluation based on computer simulation.

Fig. 19 plots the detection performance curves as a function of signal-to-receiver-noise ratio (SNR) for the conventional and optimum UWB processors, where the UWB waveform and the interference covariance are the same as those in Section I.3.2. Due to computer resource limit, the false alarm rate is set to 10^{-3}. M, the total number of pulses in the coherent processing, is chosen large (M=28) in order to gain sufficient coherent integration gain. A five pulse canceler with binomial coefficients is used for the interference canceler. The performance of the suboptimum processor with integration-of-all scatterer integration scheme is also included for reference. The performance difference between the optimum and suboptimum processors is considered as the performance loss due to unknown number

60

and separation of the scatterers, while that between the suboptimum and the conventional indicates the loss caused by unknown interference covariance. It is seen from Fig. 19, with a interference-to-recever-noise ratio INR=50dB, the conventional UWB processor delivers a reasonably good performance close to the optimum.

In order to show the effectiveness of the velocity-based correlator, a UWB processor without the correlator, formed by setting $M = N_p$ and directly applying the scatterer integrator at the output of the pulse canceler, is compared with the previous one with the correlator. An equal total signal energy constraint is imposed over the received pulse train for fair comparison. Fig. 20 shows the comparison results, where the detection performance is depicted as a function of residual signal-to-interference-pluse-noise ratio at the output of the canceler.The performance difference between the two processor is clearly seen in Fig. 20, which reflects the coherent integration gain obtained by the velocity-based multiple pulse correlator.

The interference-to-receiver-noise ratio is increased to INR=70dB in Fig. 21. It is seen that the canceler-based processor will experience more performance degradation under more severer interference conditions.
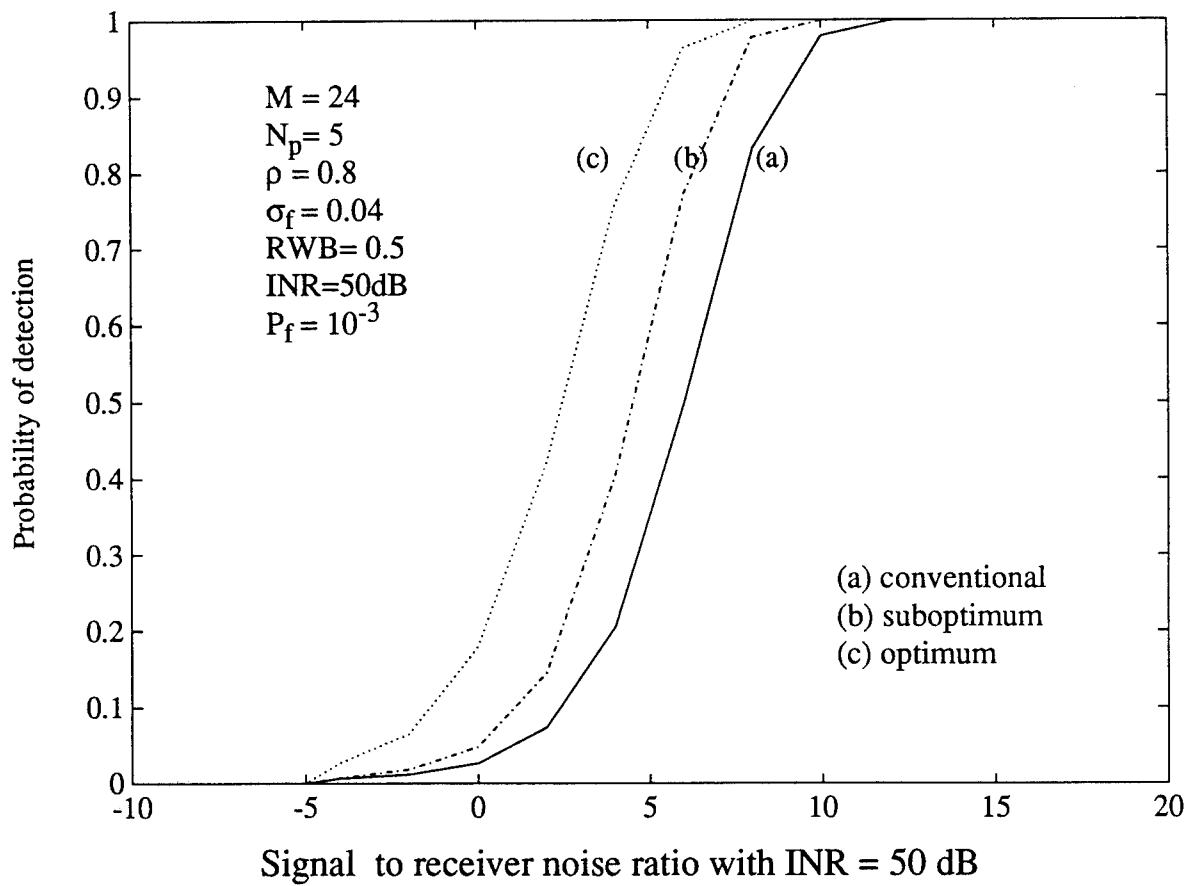
Fig. 19. Detection performance of the conventional UWB processor: mild interference.
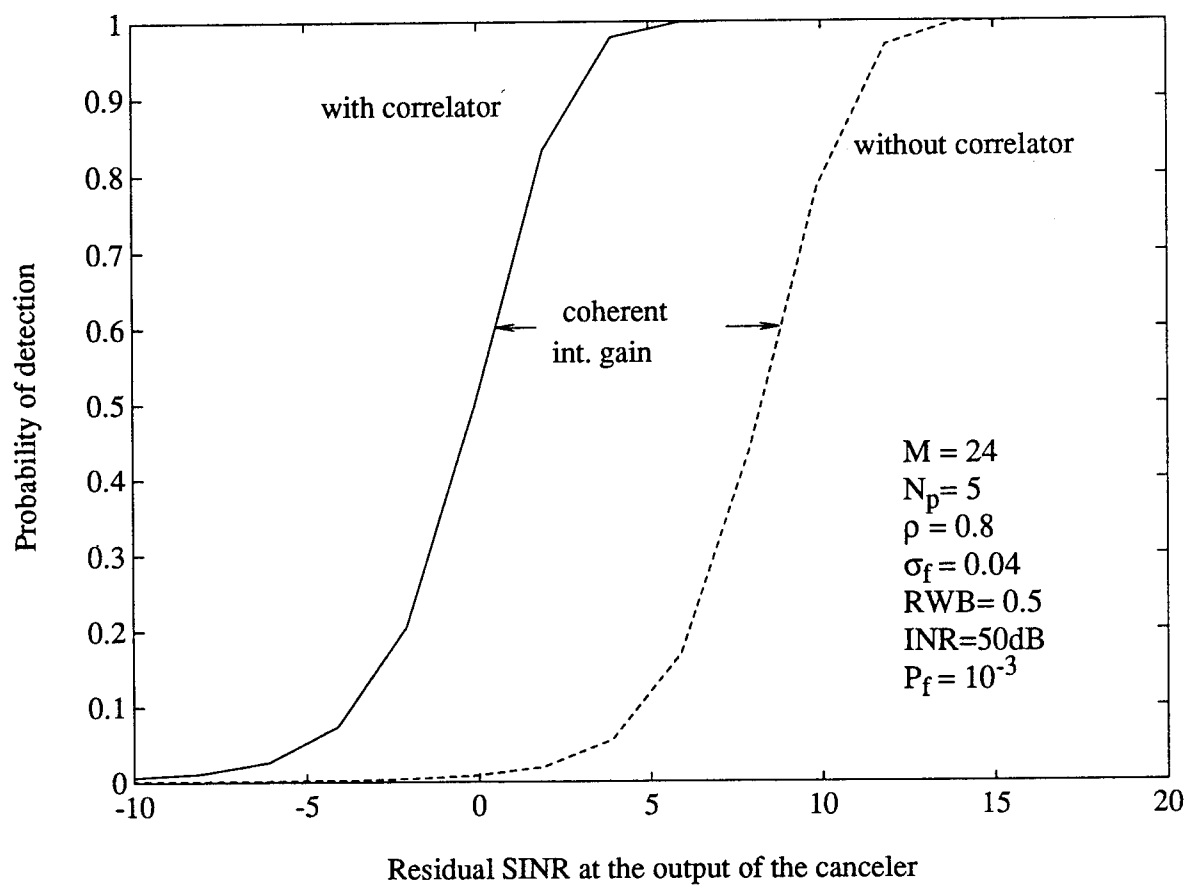
Fig. 20. Effectiveness of the velocity-based multiple pulse correlator.
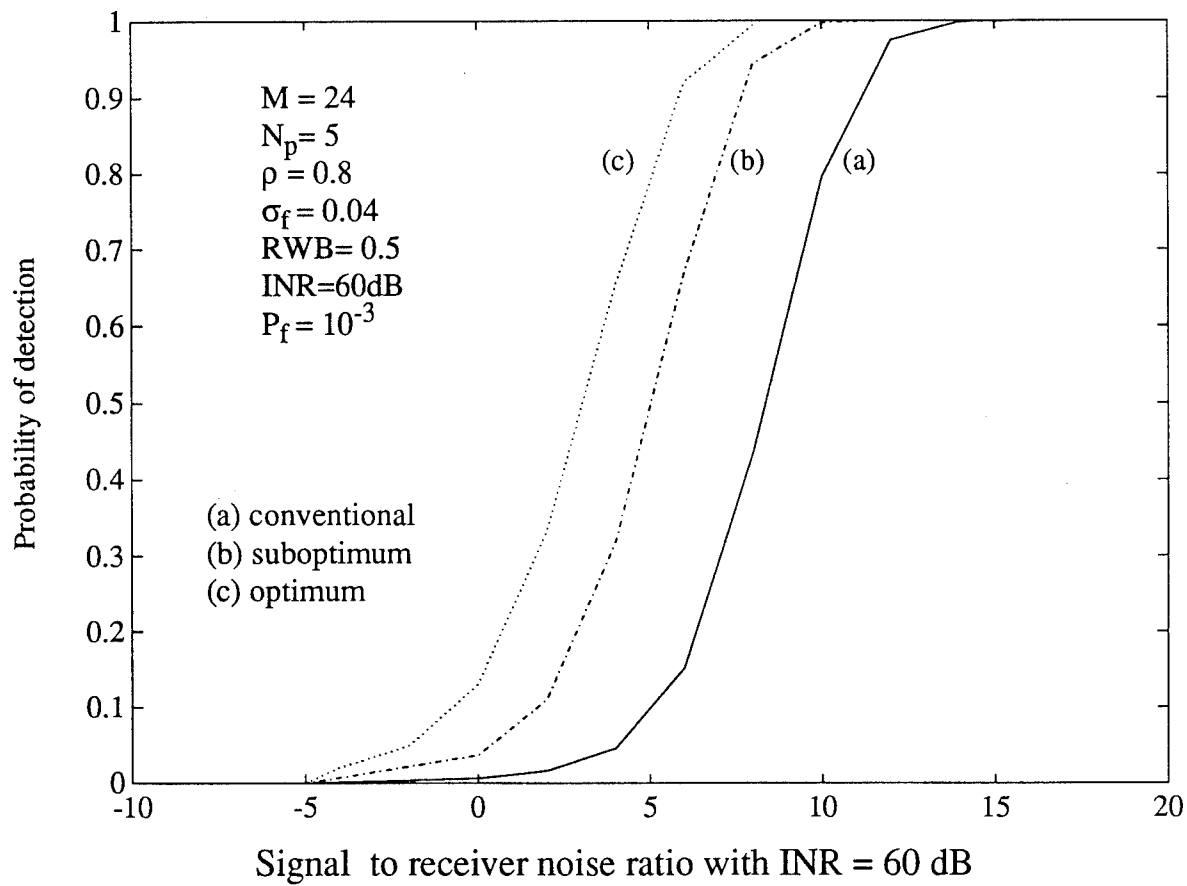
Fig. 21. Detection Performance of the conventional UWB processor: strong interference.

I.6 ADAPTIVE PROCESSING WITH UWB WAVEFORMS

6.1 Generalized-Likelihood-Ratio UWB Processor with Large Relative Bandwidth

This section will consider adaptive implementation of the optimum UWB processor when the interference statistics is unknown to the system. The data from those adjacent target-free range cells, named as secondary data, are used by the processor to learn the interference background for a better detection performance. In comparison, the data form the range cells under test are called primary data.

As the scatterer arrival time and separations are also unknown, similar to the treatment used in Section I.3.2, the test interval is partitioned into N test range cells, each of which is labeled by the time index τ_l. The primary data are then formed in the following way:

$$\mathbf{X}_l = \int \mathbf{x}(t)\mathbf{g}^H(t - \tau_l)dt, \qquad M \times M. \qquad (6-1)$$

It is not difficult to verify that the waveform-based optimum UWB processor presented in the previous sections is basically constructed by the data set given above. For convenience of representation, we use the notation $\text{Vec}(\mathbf{X}_l)$ to denote an $M^2 \times 1$ column vector formed by the columns of $\mathbf{X}_l$ stacked together. We assume that the scatterers are well separated, i.e., no scatterer crossover occurs due to the range walk, the mean of $\text{Vec}(\mathbf{X}_l)$ is given by

$$\text{E}(\text{Vec}(\mathbf{X}_l)) = \begin{cases} a_l\text{Vec}(\mathbf{G}) & \text{under } H_1 \\ 0 & \text{under } H_0 \end{cases}, \qquad l = 1, 2, ..., N \qquad (6-2)$$

with

$$\mathbf{G} = \int \mathbf{g}(t)\mathbf{g}^H(t)dt. \qquad (6-3)$$

With some simple linear algebra manipulation, the covariance matrix of $\text{Vec}(\mathbf{X}_l)$ is found to be

$$\text{Cov}(\text{Vec}(\mathbf{X}_l)) = \mathbf{G}^* \otimes \mathbf{R} = \mathbf{R}_{MM}, \qquad (6-4)$$

where $\otimes$ stands for Kronecker product.

The secondary data set is taken from the range interval where no target is present and the interference bears the same statistics as that of the interval under test. Let $\tau_k, k = 1, 2, ..., K$

be the time indices for the range cells covering the secondary range interval. The secondary data set is constructed by

$$\mathbf{Y}_k = \int \mathbf{x}(t)\mathbf{g}^H(t - \tau_k)dt, \qquad M \times M, \qquad k = 1, 2, ..., K. \qquad (6-5)$$

Their covariance is assumed to be equal to that of the primary data

$$\text{Cov}(\text{Vec}(\mathbf{Y}_k)) = \text{Cov}(\text{Vec}(\mathbf{X}_l)) = \mathbf{R}_{MM}. \qquad (6-6)$$

The range cells, both for primary and secondary data, are chosen to be well separated so that the primary and secondary vectors, $\text{Vec}(\mathbf{X}_l)$ and $\text{Vec}(\mathbf{Y}_k)$, are independent each other across both l and k.

Applying the generalized likelihood ratio test principle to the above data model, with $\mathbf{R}_{MM}$ and $a_l, l = 1, 2, ..., N$ being the unknown parameters over which the likelihood is maximized, the resulting test rule is

$$\eta = \frac{\text{Vec}^H(\mathbf{G})\hat{\mathbf{R}}_{MM}^{-1}\mathbf{X}[\mathbf{I} + \mathbf{X}^H\hat{\mathbf{R}}_{MM}^{-1}\mathbf{X}]^{-1}\mathbf{X}^H\hat{\mathbf{R}}_{MM}^{-1}\text{Vec}(\mathbf{G})}{\text{Vec}^H(\mathbf{G})\hat{\mathbf{R}}_{MM}^{-1}\text{Vec}(\mathbf{G})}, \qquad (6-7)$$

where $\mathbf{X}$ and $\mathbf{Y}$ are composed of the primary and secondary data sets, respectively

$$\mathbf{X} = [\text{Vec}(\mathbf{X}_1) \quad \text{Vec}(\mathbf{X}_2) \quad \cdots; \quad \text{Vec}(\mathbf{X}_N)], \qquad (6-8)$$

$$\mathbf{Y} = [\text{Vec}(\mathbf{Y}_1) \quad \text{Vec}(\mathbf{Y}_2) \quad \cdots; \quad \text{Vec}(\mathbf{Y}_K)], \qquad (6-9)$$

and $\hat{\mathbf{R}}_{MM}$ is the maximum likelihood estimate of $K\mathbf{R}_{MM}$:

$$\hat{\mathbf{R}}_{MM} = \mathbf{Y}\mathbf{Y}^H = \sum_{k=1}^{K} \text{Vec}(\mathbf{Y}_k)\text{Vec}^H(\mathbf{Y}_k). \qquad (6-10)$$

The derivation follows the similar procedures given in [9]. We note that the above detector is similar to the Multiband Generalize Likelihood Ratio test (MB-GLR) algorithm in [9], which has some practically important features such as integrated Constant False Alarm Rate (CFAR) and robustness to non-Gassian interference. Of course, the desirable features should remain valid here.

One of the essential problems associated with the above adaptive UWB processor is its high dimension, since the order of the unknown covariance matrix $\mathbf{R}_{MM}$ is $M \times M$, and the number of primary data vectors joining the test, N, could be very large. The

computation difficulty is clear as the algorithm requires two matrix inversion operations of very high dimension. Furthermore, it is known that the number of secondary data vectors, K, is required to exceed the order of $\mathbf{R}_{MM}$ at least by a factor of two in order to deliver an acceptable detection performance. Although the high resolution could provide a better approach to increase the size of the secondary data set, such a requirement is not easy to meet when the interference background is highly nonhomogeneous and nonstationary.

The reason of the above problem is due to ignoring the fact that the unknown covariance matrix $\mathbf{R}_{MM}$ is a highly structured matrix as seen in Eq.(6-4). In fact, $\mathbf{R}$, $M \times M$, is the only unknown part of the matrix, since $\mathbf{G}$ purely depends on the waveform. The ideal solution to the problem is to apply the GLR principle directly over the unknown parameters in $\mathbf{R}$ by taking into account the structure of $\mathbf{R}_{MM}$. Due to mathematical difficulty, however, the closed-form solution is not available yet and the numerical way to complete the maximum searching in the GLR procedure needs too much computation to be acceptable in practice.

One alternative solution is to replace $\hat{\mathbf{R}}_{MM}$ in Eq.(6-7) by

$$\hat{\mathbf{R}}_{MM} = \mathbf{G}^* \otimes \hat{\mathbf{R}}, \qquad (6-11)$$

where

$$\hat{\mathbf{R}} = \sum_{k=1}^{K} \mathbf{Y}_k \mathbf{G}^{-1} \mathbf{Y}_k^H. \qquad (6-12)$$

Thus we actually use $M \times K$ secondary data vectors to estimate an $M \times M$ covariance matrix, which will lead to a better detection performance even though K is small as limited by the environment. The computation load can be partially released by the above approach since the inverse of $\hat{\mathbf{R}}_{MM}$ now becomes

$$\hat{\mathbf{R}}_{MM}^{-1} = \mathbf{G}^{*-1} \otimes \hat{\mathbf{R}}^{-1}. \qquad (6-13)$$

Note that the "modified GLR" algorithm described above will not have the high quality integrated CFAR feature possessed by the original GLR given in Eq.(6-7), as its false alarm could change with the interference covariance. However, it should be pointed out that the false alarm rate of the algorithm is invariant to the interference level change, which in turn indicates a "weak form" of CFAR. Furthermore, if $M \times K$ is very large, the $\mathbf{R}_{MM}$ estimation performed by Eq.(6-12) will tend to be constant. As a result, the false alarm is expected not to change too much as the covariance matrix of interference varies.

67

The closed-form detection performance of the modified GLR algorithm is not easy to find. The performance evaluation of the algorithm, together with its robustness investigation to non-Gaussian interference, should be performed based on extensive computer simulation.

Another major problem with the adaptive UWB processor is that it require exact knowledge of the interference velocity when forming the data vector $\mathbf{x}(t)$ by segmentation of the pulse train waveform $x(t)$. If the waveform is not properly segmented according to the interference velocity, the structure of $\mathbf{R}_{MM}$ as given in Eq.(6-4) will be completely destroyed, making it difficult to apply the modified GLR algorithm. Furthermore, even though the original high order GLR processor can be applied by assuming large number of secondary data vectors available, the detection performance will not be good since the interference components are not able to be effectively canceled due to poor pulse-to-pulse alignment for the interference. Therefore, how to accurately estimate the interference velocity is an important part of the adaptive processing with the UWB waveforms, and is a research topic requiring further investigation.

6.2 Generalized-Likelihood-Ratio UWB processor with Small Relative Bandwidth

Under the assumption that the system relative bandwidth is small, i.e., the carrier frequency is sufficiently high so that the ratio of the bandwidth over the carrier frequency is less than 10%, as given in Eq.(2-47) in Section I.2.2.2, we may use the complex representation for the single scatterer waveform vector:

$$\tilde{\mathbf{g}}(t) = \begin{bmatrix} \tilde{A}(t) \\ \tilde{A}(t - \alpha_s T_p)e^{-i2\pi f_s} \\ \cdots \\ \tilde{A}(t - (M-1)\alpha_s T_p)e^{-i2\pi(M-1)f_s} \end{bmatrix} \qquad (6-14)$$

where we have taken $T_p = T_p'$ so that $\Delta\alpha = \alpha_s$ and $f_0 \Delta\alpha T_p = f_s$. For slowly moving target, the effect of the of the inter-pulse shift in the amplitude $A(t)$, namely the range walk, is negligible. Then we have the approximation:

$$\tilde{\mathbf{g}}(t) \approx \tilde{A}(t)\mathbf{s}. \qquad (6-15)$$

68

where

$$\mathbf{s} = \begin{bmatrix} 1 \\ e^{-i2\pi f_s} \\ \dots \\ e^{-i2\pi(M-1)f_s} \end{bmatrix}. \qquad (6-16)$$

The bandwidth of the waveform is assumed to be larger than the critical bandwidth so that the individual scattering centers can still be resolved by the system. Therefore the received target return can be expressed by the MDS model

$$\tilde{\mathbf{s}}_r(t) = \sum_j \tilde{a}_j \tilde{A}(t - \tau_j)\mathbf{s} \qquad (6-17)$$

where τ_j is the delay time for jth scatterer.

Now we construct our primary data set:

$$\mathbf{x}_l = \int \mathbf{x}(t)\tilde{A}(t - \tau_l)dt, \qquad M \times 1, \qquad l = 1, 2, ..., N, \qquad (6-18)$$

where τ_l is the time index corresponding to the lth of test cells covering the whole test interval. With the signal complex envelop $\tilde{A}(t)$ being normalized to have unit energy, it is not difficult to show that the covariance matrix of $\mathbf{x}_l$ is given by:

$$\mathbf{R} = \mathrm{E}(\mathbf{x}_l\mathbf{x}_l^H|H_0) = \tilde{\mathbf{R}}_c/2B + \frac{N_0}{2}\mathbf{I}, \qquad (6-19)$$

where $\tilde{\mathbf{R}}_c$ is given in Eq.(2-57).

For the secondary data set, the same operation is performed on those adjacent range cell without target returns:

$$\mathbf{y}_l = \int \mathbf{x}(t)\tilde{A}(t - \tau_k)dt, \qquad M \times 1, \qquad k = 1, 2, ..., K. \qquad (6-20)$$

which should have the same covariance matrix as $\mathbf{x}_l$.

The above data model is similar to that in [9], where a multiband GLR (MB-GLR) algorithm is presented for target detection. Applying the same algorithm to our multiple dominant scatterer (MDS) data, we have the MDS-GLR algorithm given below:

$$\eta = \frac{\mathbf{s}^H\hat{\mathbf{R}}^{-1}\mathbf{X}[\mathbf{I} + \mathbf{X}^H\hat{\mathbf{R}}^{-1}\mathbf{X}]^{-1}\mathbf{X}^H\hat{\mathbf{R}}^{-1}\mathbf{s}}{\mathbf{s}^H\hat{\mathbf{R}}^{-1}\mathbf{s}}, \qquad (6-21)$$

where

$$\mathbf{X} = [\mathbf{x}_1 \quad \mathbf{x}_2 \quad \cdots; \quad \mathbf{x}_N], \qquad (6-22)$$

$$\mathbf{Y} = [\mathbf{y}_1 \quad \mathbf{y}_2 \quad \cdots \quad \mathbf{y}_K], \tag{6-23}$$

and

$$\hat{\mathbf{R}} = \mathbf{Y}\mathbf{Y}^H, \qquad M \times M. \tag{6-24}$$

Obviously, the high dimension problem associated with the high order GLR given in Section I.6.1 is avoided here since the order of the estimated covariance matrix $\hat{\mathbf{R}}$ is only M.

Under the assumption that both the primary and secondary data vectors are complex Gaussian distributed, the probability of false alarm of the MDS-GLR processor is found to be

$$P_f = \frac{(1 - \eta_0)^{K-M+1}}{(K - M)!} \sum_{j=1}^{N} \frac{[K + N - M - j]!}{(N - j)!} \eta_0^{N-j}. \tag{6-25}$$

The above expression indicates the fact that the algorithm has the integrated CFAR feature, as the false alarm is independent of the covariance matrix interference $\tilde{\mathbf{R}}_c$.

Assuming the complex scatterer amplitudes $\tilde{a}_j$ are all unknown constants due to much reduced target fluctuation, the probability of detection is shown to be:

$$P_d = \int_0^1 P_{d|\nu} f_\nu(\nu) d\nu \tag{6-26}$$

where

$$f_\nu(\nu) = \frac{[K + N - 1]!}{(M - 2)![K + N - M]!}(1 - \nu)^{M-2}\nu^{K+N-M}, \tag{6-27}$$

and

$$P_{d|\nu} = 1 - \eta_0^{N-1}(1 - \eta_0)^{K-M+1} \sum_{k=1}^{K-M+1} \binom{K + N - M}{k + N - 1}$$

$$\times \left(\frac{\eta_0}{1 - \eta_0}\right)^k e^{-\nu\beta(1-\eta_0)} \sum_{m=0}^{k-1} \frac{[\nu\beta(1 - \eta_0)]^m}{m!}, \tag{6-28}$$

with

$$\beta = \sum_{j=1}^{J} |\tilde{a}_j|^2 \mathbf{s}^H \mathbf{R}^{-1} \mathbf{s}. \tag{6-29}$$

The derivation procedures follow those given in [9].

The detection performance of the MDS-GLR is evaluated in Fig. 22 with a Gaussian shaped interference spectrum. The number of the secondary data vectors is chosen large ($K = 60$) since the high range resolution can provide more independent and identically distributed data for given size of homogeneous range. The optimum performance, where

we assume known interference covariance and scatterer separation, is included for reference. We note that among the N range cells under test, only a small portion contains the target scatterer returns. Thus the collapsing loss will result if the MDS-GLR processes all the test cells without knowing the range distribution of target scatterers. To single out collapsing loss, we also include the suboptimum performance using the integration-of-all inter-scatterer integration scheme. It is clear that the gap between the optimum and suboptimum indicates the collapsing loss and the gap between the suboptimum and the MDS-GLR stands for the estimation loss due to unknown interference covariance. With $J = 5$ scatterers out of $N = 20$ test range cells, one can see from Fig. 22 both collapsing and estimation losses are less than 3dB.

M = 8
K = 60
N = 20
J = 5
$\Delta f = 0.3$
$\sigma_f = 0.04$
INR=40dB
$P_f = 10^{-6}$

(a) MDS GLR
(b) MDS suboptimum
(c) MDS optimum
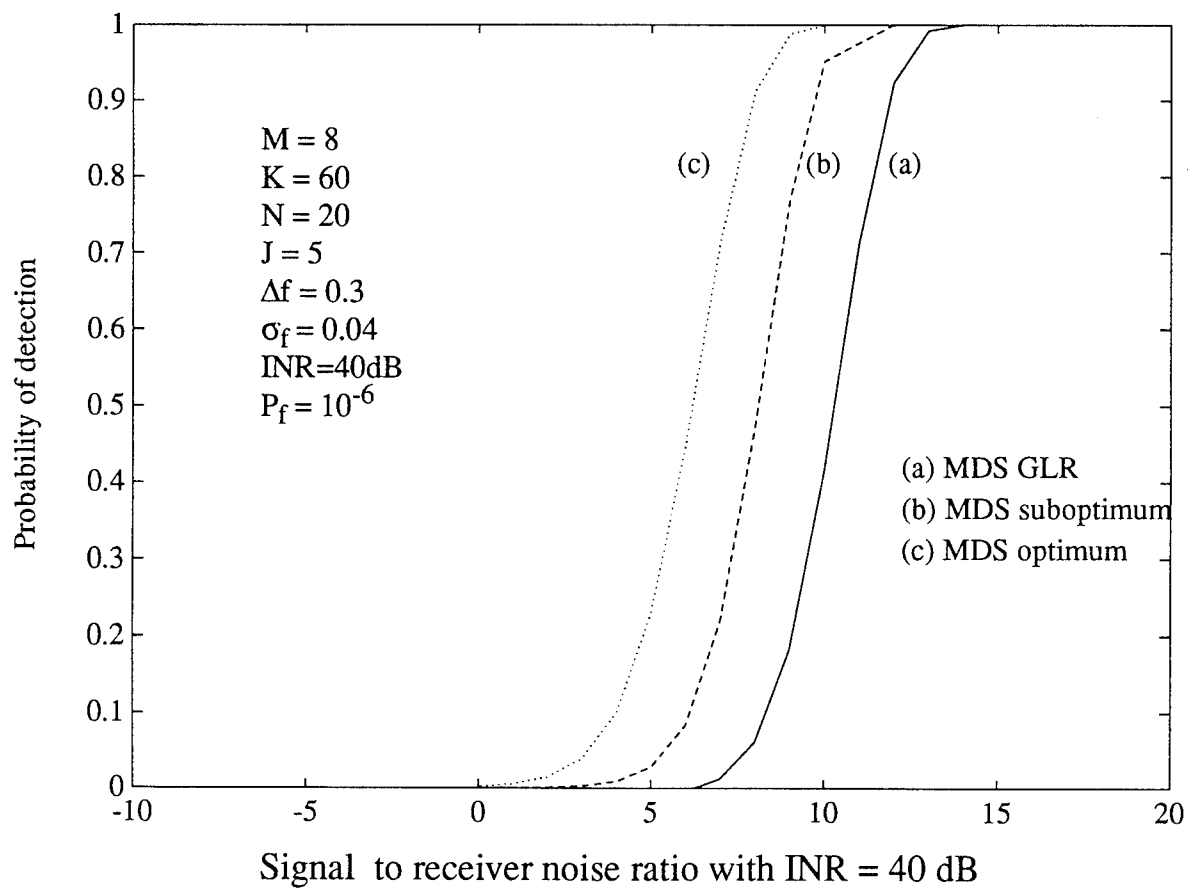
Fig. 22. Detection performance of the MDS-GLR processor.

I.7 Conclusions and Discussions of Part I

UWB systems, using either an impulse or frequency/phase modulated waveform with large or small relative bandwidth, potentially have a significant moving target detection (MTD) performance gain over the conventional narrowband/low-range-resolution systems, **in addition to** the well known gain due to the clutter power reduction in the range cell. This additional gain, in the range of 15~20dB, indicates that the subclutter visibility performance potential of UWB surveillance systems is severely underestimated previously. This conclusion is obtained via careful comparisons of optimum UWB and narrowband/low-range-resolution systems.

To approach the performance potential for reliable detection of weak moving targets in strong clutter, the UWB system's MTD processor should maximally exploit the velocity based discrimination against the clutter, which also demands careful thoughts in the development of its multipulse target component integration part, especially when the clutter suppression residue is still much larger than the target component.

The simple nonadaptive UWB MTD processing algorithm developed in Section I.5 is capable to approach the optimum performance even at very low SINR. This algorithm can be used for ground-based systems whose clutter spectrum is usually quite simple. Whether the UWB waveform is impulse or frequency/phase modulated, its implementation is well within the reach of currently available processor hardware.

For the airborne UWB surveillance application where the clutter is severely nonhomogeneous/nonstationary with very complicated spectrum, the GLR-based adaptive MTD processing algorithm of Section I.6 becomes necessary. As planned for Phase I, only a simplified GLR for over-resolved moving target detection is derived and studied, under the assumption that the UWB system has a small relative bandwidth and that the target velocity only produces a doppler frequency shift. This GLR-based UWB MTD, still sufficiently simple to implement, offers near optimum performance with fast convergence and an embedded robust CFAR. A more complete GLR-based UWB MTD without the restrictive assumptions above will be part of Phase II work.

References of Part I

[1] D. R. Wehner, *High Resolution Radar*, MA: Artech House, 1987

[2] A. W. Rihaczek, *Principles of High-resolution Radar*, New York: McGraw-Hill, 1969.

[3] C. G. Backman, "Some recent developments in RCS measurement techniques," *Proc. IEEE,* vol. 53, pp. 962-972, Aug. 1965.

[4] R. Nitzberg, "Effect of a few dominant specular reflectors target model upon target detection," *IEEE Trans. Aerosp. Electron. Syst.,* vol. AES-14, No. 4, pp. 670-673, July 1978.

[5] P. Swerling, "Detection analysis for range-extended targets," TSC Course Notes, April 1977.

[6] H. L. Van Trees, *Detection Estimation and Modulation Theory, Part III*, New York: Wiley, p. 448, 1971.

[7] S. Haykin, *Communication Systems*, New York: Wiley, p. 102, 1983.

[8] N. S. Tzannes, "Communication and Radar Systems", Englewood Cliffs, NJ: Prentice-Hall, p. 174, 1985.

[9] H. Wang and L. Cai, "On adaptive multiband signal detection with the GLR algorithm," *IEEE Trans. Aerosp. and Electron. Syst.* , vol. AES-27, no. 2, pp. 225-233, March 1991. P. K. Hughes, "A high-resolution radar detection strategy", *IEEE Trans. Aerosp. Electron. Syst.,* vol. AES-19, No. 5, pp. 663-667, Sept. 1983.

Part II of Volume I

Phase I Report

F30602-91-C-0035

Adaptive Multiband and Optimum Ultra-Wideband Polarization Cancelers

LIST OF FIGURES

76

LIST OF TABLES

LIST OF PRINCIPAL SYMBOLS

$\mathbf{x}_j$	primary data vector for j^{th} subband
$\mathbf{x}_{jk}$	secondary data vector for j^{th} subband
$\mathbf{x}_s$	target vector
α	target amplitude
$\mathbf{x}_w$	internal receiver noise
$\mathbf{x}_c$	clutter data vector
$\mathbf{x}_{cp}$	completely polarized portion of clutter data vector
$\mathbf{x}_{up}$	unpolarized portion of clutter data vector
$\mathbf{x}_n$	unpolarized portion of clutter plus white noise data vector
z_j	output of polarization canceler for j^{th} subband
$\mathbf{R}$	covariance matrix of clutter plus noise
σ_c^2	input variance of clutter
σ_n^2	input variance of noise
σ_s^2	input variance of signal amplitude
σ_w^2	input variance of white receiver noise
K	number of secondary vectors
J	number of subbands in a multiband system
SCNR	input signal-to-clutter-plus-noise ratio
SNR	input signal-to-noise ratio
CNR_i	input clutter-to-noise ratio
P_{fa}	probability of false alarm
P_d	probability of detection
η	test statistic in MB system
η_o	threshold in MB system
η_o'	threshold in UWB system
$\mathbf{p}$	optimum weight vector (receiver polarization state vector)
$\hat{\mathbf{p}}$	estimated weight vector
$\mathbf{f}(\mathbf{p}_r)$	optimum receiver *Stokes* polarization vector
$f_v(t)$	transmit UWB signal normalized to unit energy
$\mathbf{r}(t)$	UWB wave return vector
$\mathbf{r}_c(t)$	clutter portion of UWB wave return vector
$\mathbf{r}_w(t)$	receiver noise portion of UWB wave return vector

II.1 Introduction of Part II

1.1 Review of Previous Work and Problem Statement

Maximizing the target signal-to-clutter ratio for optimum detectability in a radar system can be achieved through processing of polarization dependent scatterer. The main objective of this research is to identify optimal/adaptive polarimetric techniques for processing Multiband (MB) and Ultra-Wideband (UWB) returns, develop these techniques into algorithms,and quantify their detection performance.

The theoretical framework for optimum dual-polarization target detection is presented by Guili [10]. Polarization diversity techniques may require polarization adaptation on transmission and/or reception. On reception, this can be, under the Gaussian assumption, accomplished using a coherent linear combination of the signals received from the two orthogonally polarized channels. This linear receiver is utilized in processing measured data to evaluate detection performance even though the interference may not follow the Gaussian assumption. On transmission, a virtual polarization adaptation method can be applied [11,12]. This requires consecutive return echoes received from the target with orthogonal polarizations on successive transmissions, be coherently and linearly combined on reception. The virtual polarization adaptation method is well described in [13], and the reception only polarization adaptation method in [14]. A simple and effective way to implement polarization processing is through a canceler based approach on reception only. This is similar to the basic approach for adaptive sidelobe cancellation of jamming signals received through two (main and auxiliary) antennas [3]. For implementing a polarization processor, the polarization canceler based technique is widely prefered because receive-only polarization diversity can provide a considerable amount of performance improvement [10], and will not require multiple pulse processing [3], [11].

In addition to the polarization diversity on reception, frequency variational signaling is applied in the Adaptive Polarization Canceler (APC) based detector to improve detection performances for slowly or tangentially moving weak targets, which typically go undetected when only doppler processing is used. Previous work in this area has largely focused on optimum Single Band (SB) polarimetric radar processing, with performance improvements presented as a processing gain. In this report, we investigate both the optimum and adaptive

performance of frequency variational polarimetric radar processing.

Two frequency variational signaling schemes are presented, Multiband (MB) and Ultra-Wideband (UWB). System requirements, and signaling methods for obtaining the MB and UWB polarimetric data are discussed. Implementation considerations and performance analysis of these technique are presented. The detection performance improvement due to frequency variational signaling is obtained from a closed-form expression for detection probability (P_d). The polarization canceler based detector with SB signaling exhibits problems [15], such as target signal cancellation along with the clutter, and clutter power cancellation limitations due to the low degree of polarizaiton problem determined by the ratio of completely polarized portion of clutter power to the total clutter power. These two problems severely degrade detection performance, and limit applications of this polarization canceler in practice. To solve these problems, the MB signaling scheme is applied in conjunction with a polarization canceler based detector. Motivating this work is the variability of clutter polarization, relative to the target, as a function of radar frequency. Since the target polarization varies with the carrier frequency, independent of the clutter's, a frequency diversity (i.e., multiband) system should have the potential to solve the signal cancellation problem. Also, the degree of polarization varies with carrier frequency, a frequency diversity system may have the potential to obtain a high degree of polarization at least from one of subband channels. Based on these ideas, the first part of this report introduces the Adaptive Multiband Polarization Canceler (AMBPC) based system, and it is to establish its performance gain over the corresponding SB system. The detection performance improvement due to MB signaling has been quantified with respect to the signal cancellation and degree-of-polarization problems, and is compared with the SB signaling scheme on the basis of equal system constraints, (without giving any favor to MB system). Furthermore, the AMBPC based detector performance evaluation spans from analytic development to the experimental performance demonstration using measured data to verify the feasibility of this technique. The use of MB waveforms applied in various radar systems to improve target detectability is well-established [17,18,19]. Alternatively, the use of UWB thchnology in polarimetric radar detection remains essentially unknown, and is *not* well-established. The performance improvement obtained using frequency diverse adaptive polarization processing provides sufficient justification to investigate Ultra-Wideband (UWB) polarization processing capabilities.

If the clutter statistics were known *a priori*, the covariance matrix could be formulated, and the optimal solution for the canceler weights obtained. In practice the clutter statistics are not known *a priori*, and furthermore, the interference environment frequently changes due to the presence of moving near-field scatterers, antenna motion, interference, and jamming. Consequently the adaptive processor must continually update the weight vector to meet the new requirements posed by varying conditions. The need to update the weight vector in the absence of detailed *a priori* information leads to the expedient of obtaining estimates of the clutter covariance matrix from a finite range observation interval, and employing these estimates to obtain the desired weight vector. This method of implementing the adaptive processor, referred as the Sample Matrix Inversion (SMI) technique, is considered here as a candidate adaptive algorithm. Theoretically, it would be possible to improve performance by increasing the observation interval (more range cell data for instance), but as a practical matter, the observation interval is severely limited due to the nonhomogeneous nature of the enviornment. MB signaling improves performance by increasing the quantity of independent and identically distributed (*i.i.d.*) date vectors available for clutter estimation, whereas UWB signaling improves performance by increasing the information available for clutter characterization. In the UWB radar polarization processor, due to the reduced size of the resolution cell, down-range images of target and clutter returns are provided . In this case, each resolution cell contains a reduced number of closely-spaced scatterers. Therefore, polarization becomes a less ambiguous descriptor of the target and clutter returns. Frequency variational signaling will enhance the performance of the adaptive system by providing additional information for formulating estimates of the covariance matrix.

The second part of report developes UWB signaling in a polarization processor to examime the state-of-the-art, potential performance benefits, and limitation of UWB technology, with particular emphasis on radar detection application. Under the toughest system constraint, the detection performance of the optimum UWB polarization processor will be compared with optimum Narrow Band (NB), as well as the MB system. The overall gain achievable by UWB signaling over the NB signaling is divided into separate gains, which will enable the readers to understand the reason for UWB signaling.

The radar system considered in Part II of this report transmits a single polarized (vertically) pulse, and receives target and clutter backscatter with dual-polarized (horizontally

and vertically) receivers. (see Fig. 1)
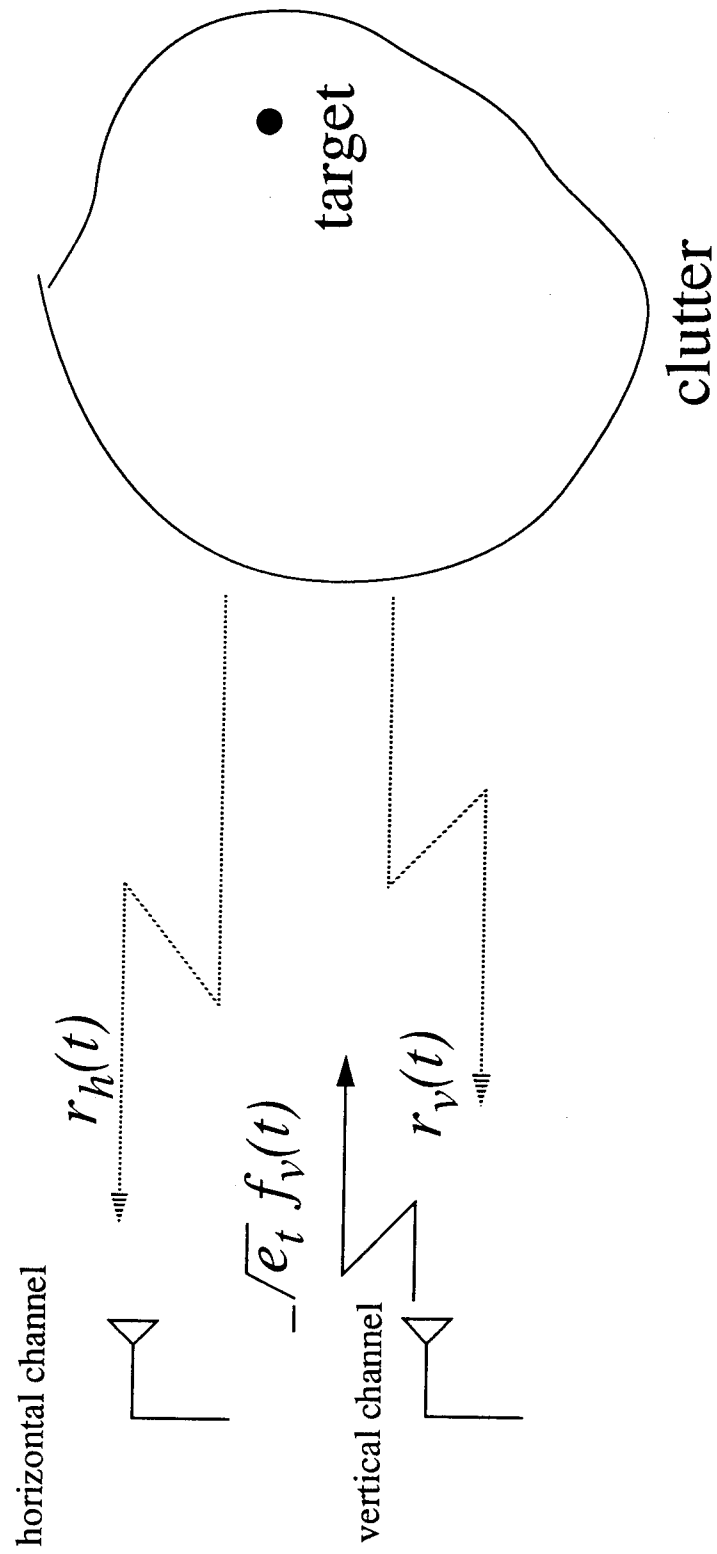
Figure 1: Vertically polarized transmit waveform and dual-polarized returns.

1.2 Organization of Part II

Part II of this report consists of two main parts : The optimum/adaptive MB polarization canceler based detector, and the optimum UWB polarization processor. Analytic and experimental performance analysis of the AMBPC based detector are presented. The second half of this Part II report presents the optimum UWB polarization processor, and its performance analysis is presented, and compared to the optimum NB and MB polarization processor.

In Chapter 2, the problems associated with SB signaling in a polarization canceler based detector are discussed. Two canceler based detectors are presented : The Optimum MB Polarimetric Detector (OMBPD) and the optimum/adaptive MB Polarization Canceler (optimum/adaptive MBPC) based detector. The OMBPD is mainly studied here so as specifically to highlight the problems with SB signaling, and to clearly show the improvement associated with MB signaling. The detection probability of the OMBPD is expressed in terms of signal cancellation and degree-of-polarization parameters. The performance of the AMBPC based detector is obtained from the detection probability, and compared to its optimum, which provides a reference for comparison. Also, its performance evaluation includes an experimental performance demonstration using measured data, to verify the feasibility of this technique.

Chapter 3 introduces UWB signaling in a polarization processor to examine the state-of-the-art, the potential performance benefits and limitations of UWB polarimetric technology, with particular emphasis on radar detection application. The mathematical representation of waveform-based UWB data returns are developed, and is extended to the cases of small relative bandwidths of UWB and NB systems. Log-likelihood ratio tests are formulated, and their performance analysis are followed accordingly.

In Chapter 4, The optimum UWB and NB polarization processors are compared under the most severe system constraints. The purpose of this chapter is to quantified the UWB signaling gain over NB and MB signaling in the polarimetric radar system.

In Chapter 5, contribution and discussion are included.

II.2 Adaptive Multiband Polarization Canceler Based Detector

The non-coherent Adaptive Polarization Canceler (APC) receiver provides a simple an efficient implementation of an optimum polarization processor, for a partially polarized clutter environment. Based on this receiver, the detection performance improvement obtained through frequency diversity will be evaluated by deriving a closed-form expression for probability detection (P_d). Furthermore, this Adaptive Multiband Polarization Canceler (AMBPC) based detector performance evaluation spans from analytic development to experimental performance demonstration using measured data.

2.1 Detection Performance Evaluation

Analytic evaluation of the AMBPC based detector is obtained by deriving the detection probability, and compared with its optimum realization which will provide a reference against AMBPC based detector. Besides the optimum/adaptive MBPC based detector, an Optimum MB Polarimetric Detector (OMBPD) is presented specifically to evaluate problems associated with SB signalling in a polarization canceler based detector, and to clearly show the improvement obtained through MB signalling. This section consists of an introduction to the SBPC based detector problems, the MB data model, the OMBPD, the AMBPC based detector, and a derivation of detection and false alarm probabilities. Performance comparison and conclusion are presented.

2.1.1 Introduction

The fundamental phenomenon of polarization can be explained by conceiving of an electromagnetic wave as a transverse-wave motion. The polarization state is the orientation of the electric field vector at a given point in space during one period of oscillation, and, in general case, the terminus of this vector describes an ellipse such that, looking along the direction of propagation; the direction of rotation is either right handed or left handed. The polarization state (generally ellipse) is completely determined by the geometrical parameters; an elliptically polarized state with ellipticity axial ratio (r) and orientation angle (ε) can be uniquely represented by a point having parameters θ_a and θ_e as asumuth and elevation,

respectively, on a sphere - this sphere is called the Poincare sphere (see Fig.2 of [10]). Also, θ_a and θ_e can be expressed in terms of r and ε, i.e., $\theta_a=2\varepsilon$, and $\theta_e = \pm 2 \cdot tan^{-1}(|r|)$.

The polarization of the received wave can vary. This is mainly connected with the nonstationary behavior of interaction with both the propagation medium and the target. The received polarization state may result in being time-varying elliptically polarized, even though the orignal trasmitted wave was the time invariant linearly polarized. In this case, the received wave can generally still be expressed by θ_a and θ_e with $\theta_a = \theta_a(t)$ and $\theta_e = \theta_e(t)$. During the observation time, this time variation of the received wave can be attributed to the random phenomena. Under this condition, the received wave is said to be *partially polarized*. A partially polarized wave can generally be decomposed into two components: one is completely polarized (its polarization state does not change with time) and the other is unpolarized (its polarization state changes randomly).

Signal Cancellation and Sensitivity Problems in SBPC Based Detector:

Our basic assumption is that the complex received clutter backscatter echo is *partially polarized* [10,11] so that it can be decomposed into the *completely polarized* component and *unpolarized* component. Furthermore, we assume that the unpolarized component is white noise process which can be incorporated into the receiver noise model. In fact, the power ratio of the completely polarized portion to the total clutter, called the *degree-of-polarization*, and is an important factor in evaluating detection performance of the Polarization Canceler (PC), because the level of cancellation which may ultimately be achieved is limited by the unpolarized component of the clutter backscatter. The detection performance degradation is expected with backscatter having low degree of polarization, here we named that as *sensitivity* problem.

If no desired target is present, PC will do the job of eliminating a completely polarized component, and possibly some of unpolarized component of the clutter. In the presence of the desired target (target polarization vector unknown), it is expected that PC will cancel the desired signal, (called the *signal cancellation problem*), when the polarization vectors (states) of target and completely polarized portion of clutter are not orthogonal each other. In fact, this polarization vector difference (can be expressed as the azimuth and elevation angles), between target and the completely polarized portion of clutter, is a random quantity.

Consequently, it yields detection loss. This signal cancellation problem in SBPC based detector has, also, been reported in [12].

The two polarization states are said to be orthogonal each other characterized by having identical $|r|$ and $|\varepsilon|$, and 90° difference in θ_a. Once the magnitudes of geometrical parameters of target and clutter polarization are set to equal, the target portion of PC output response can be expressed in terms of the angle of ξ which is interpreted as polarization angle difference away from the maximum response [16], i.e., $\xi=90^o - \Delta\theta_a$, $-90^o < \xi < 90^o$. The maximum response is obtained when target and completely polarized portion of clutter vector are orthogonal (ξ=0, or $\Delta\theta_a = 90^o$). Fig. 2 presents the normalized target amplitude response with respect to $\Delta\theta_a$: When the target polarization state is linear ($\theta_e = 0^o$) and the clutter polarization state is (a) linear ($\theta_e = 0^o$), (b) and (c) elliptical ($\theta_e = 30^o, 60^o$), and (d) circular ($\theta_e = 90^o$). It indicates that the target of polarization canceler output is completely canceled when both polarization states are linear and zero angle difference, and 3 dB. target power cancellation is expected when $\Delta\theta_e = 90^o$ for all $\Delta\theta_a$. The Eq.(3) in [10] is utilized to make this plot. The curves in Fig.2 are the slices of response once the target and clutter polarization states are determined. Fig.3 is included to present the all the elliptical cases. As such the signal cancellation problem in PC is apparent and inevitable.

A Multiband Polarization Canceler (MBPC) is developed to combat the signal cancellation problem. The MBPC based detector can be implemented by establishing a bank of polarization cancelers across frequency. (see Fig. 4) In this way, the target return can be preserved in at least some of the diversity channels with a high probability, since measurements with the different frequencies yield the different polarization states for the same clutter. It is expected that for some diversity frequencies, the receiver polarization state used to null the clutter will allow passage of the target signal. This condition is not assured by a single frequency polarization canceler based detector. Based on this proposed MBPC based system of Fig. 4, the first part of dissertation is to establish its performance gain over the corresponding SB system. The MB detection performance evaluation and comparison will be carried out, using a closed-form expression of the detection probability. The MB data model is presented in the next section.

87
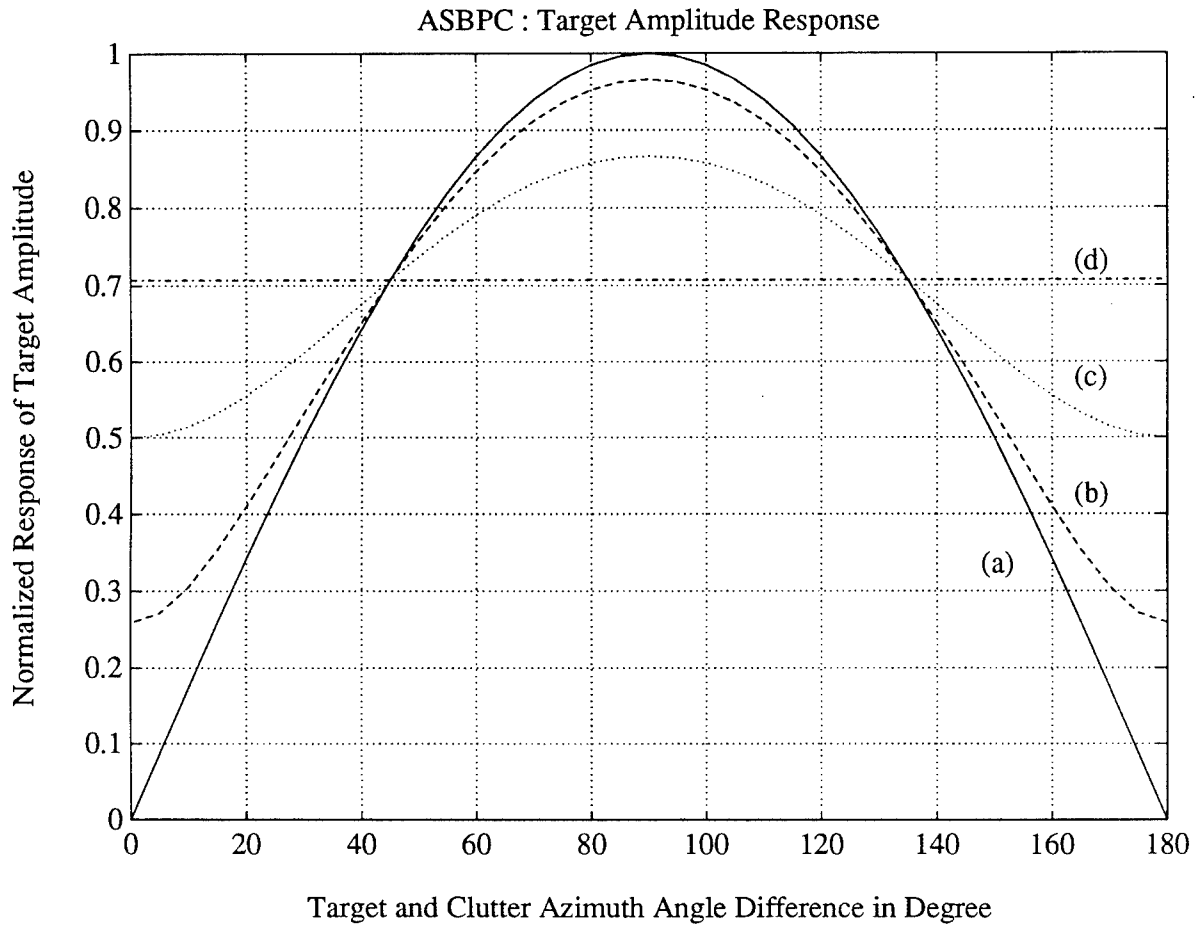
Figure 2: Target Amplitude Response of Polarization Canceler Output with respect to target and clutter polarization angle difference in degree : when the target polarization state is linear, the clutter polarization state is (a) linear, (b) and (c) elliptical, and (d) circular.
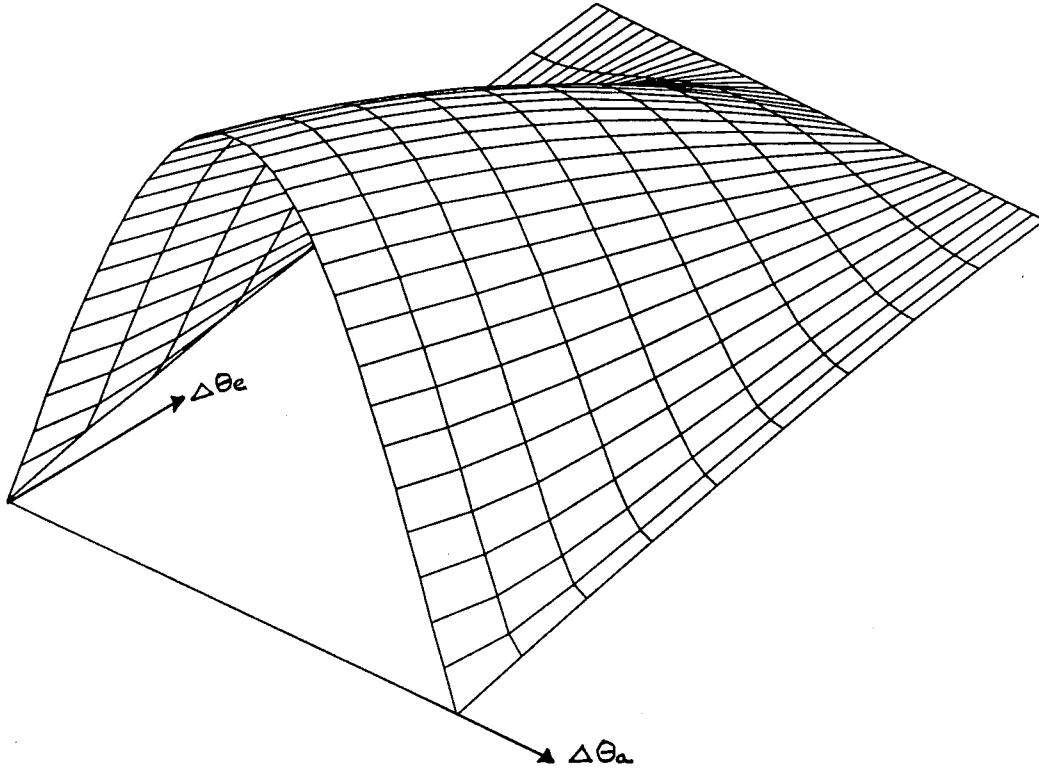
Figure 3: Target Amplitude Response of Polarization Canceler Output with respect to target and clutter polarization difference in angles
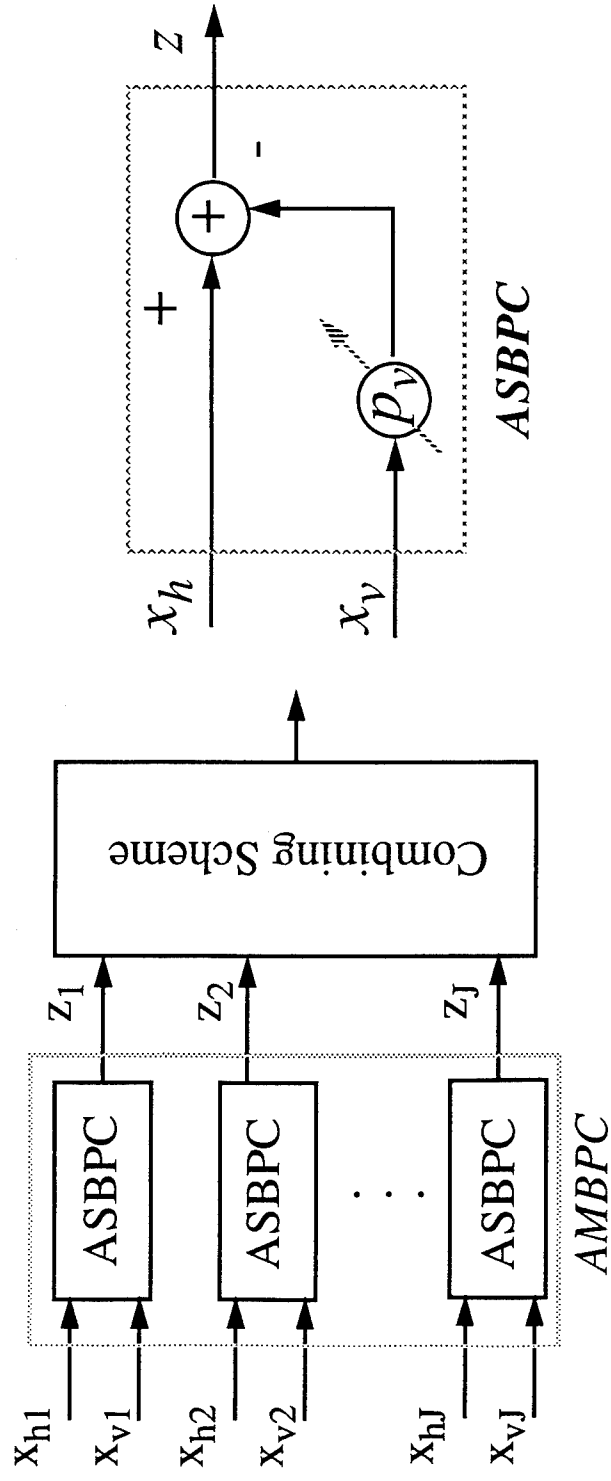
Figure 4: A Multiband Polairzation Canceler Based Detector Implementation

2.1.2 Multiband Data Model

Consider a polarization receiver with a single polarization transmitter employing an intra-pulse frequency diverse waveform as illustrated in Fig. 11, where each subpulse of width $\tau'=\tau/J$ has a different carrier frequency with an arbitrary narrow band modulation of its own. An example of the spectrum of such a simple frequency diversity signalling is given in Fig. 12, where $\tau=8$ *usec.* and $f_{j+1}-f_j=\delta f=2$ MHz., $j=1,2,3$ with no additional subpulse modulation. Without the loss of generality, we assume that the single transmit polarization is vertical.

The following received multiband data model for signal detection has arrived after proper preprocessing (via J subbands for both v and h channels), such as amplification, filtering, passband to baseband conversion, analog to digital (A/D) conversion and time domain matched filtering (matched to each subpulse). For each of J subbands the receiver output will be expressed by a set of 2×1 complex vectors whose first element is set for the h channel output.

The dual-channel polarization receiver from a single polarization transmitter and frequency diverse measurement can be expressed in matrix form as :

$$\mathbf{X} = \left[\begin{array}{cccccc} x_{vh1} & x_{vh2} & \cdots & x_{vhj} & \cdots & x_{vhJ} \\ x_{vv1} & x_{vv2} & \cdots & x_{vvj} & \cdots & x_{vvJ} \end{array} \right] , \qquad (2-1)$$

where the first two subscripts refer to the transmit and receive polarization, respectively, and $j = 1, ..., J$ is the diversity frequency index.

The whole data set is divided into two sets which will be called the primary data set and secondary data set, respectively, with the former denoting the data of a currently chosen test range cell and the latter of the surrounding cells.

The primary data set consists of J complex vectors, $\mathbf{x}_j$, 2×1, $j = 1, 2, ...J$. Under H_o, i.e., the clutter-and-noise-alone hypothesis, we have

$$\begin{aligned} \mathbf{x}_j &= \mathbf{x}_{cj} + \mathbf{x}_{wj} \\ &= \mathbf{x}_{cpj} + \mathbf{x}_{nj} \end{aligned} \qquad (2\text{-}2)$$

where $\mathbf{x}_{cj}$, and $\mathbf{x}_{wj}$ represent the clutter and receiver noise components and are assumed to be independent, also, $\mathbf{x}_j$, $j = 1, 2, ..., J$ are assumed to be independent and have identical

complex-Gaussian distributions with zero mean and covariance matrix $\mathbf{R}_j$, (size 2×2), and $\mathbf{x}_{cj}$ is the *partially polarized* clutter so that it can be decomposed into completely polarized portion, $\mathbf{x}_{cpj}$, and unpolarized portion, $\mathbf{x}_{upj}$, which is incorporated into the receiver noise, ended up being $\mathbf{x}_{nj}$.

Under H_1, the signal-plus-clutter-and noise hypothesis, we have

$$\mathbf{x}_j = \mathbf{x}_{sj} + \mathbf{x}_{cpj} + \mathbf{x}_{nj} \qquad (2-3)$$

where $\mathbf{x}_{sj}$ is the target part of the received data and it can be represented by the completely polarized state, $\mathbf{p}_{sj}$, and complex amplitude α_j, i.e., $\mathbf{x}_{sj} = \alpha_j\mathbf{p}_{sj}$. In this analysis, α_j is modeled by a complex Gaussian random variable with zero mean and variance σ_{sj}^2. $\mathbf{p}_{sj}$ is an unit normalized vector, and is unknown to the processor in practice. We also assume that the target vector $\mathbf{x}_{sj}$ is independent of $\mathbf{x}_{cpj}$ and $\mathbf{x}_{nj}$.

Under both H_0 and H_1, the secondary data $\mathbf{x}_{jk}, 2 \times 1, j = 1, 2, \cdots, J$ and $k = 1, 2, \cdots, K$, are assumed to be *i.i.d.* complex-Gaussian vectors with zero mean and a covariance matrix $\mathbf{R}$. The range index K refers to sample periods, as from the output of an analog to digital converter. Often range samples are extracted from a range window whereby the index span $1, \cdots, K$ translates to an actual range[1] interval of (r_1, r_2). It is assumed that the secondary data set is independent of the primary data set.

Based on JK number of the secondary data, the clutter and receiver noise covariance matrix $\mathbf{R}$ can be estimated by

$$\hat{\mathbf{R}} = \frac{1}{JK}\sum_{j=1}^{J}\sum_{k=1}^{K}\mathbf{x}_{jk}\mathbf{x}_{jk}^{H} = \left[\begin{array}{cc} \hat{\sigma}_h^2 & \hat{\sigma}_{hv} \\ \hat{\sigma}_{vh} & \hat{\sigma}_v^2 \end{array}\right] \qquad (2-4)$$

where "H" denotes the complex conjugate and transpose. The quantity given by Eq.(2-4) can usefully be employed for the selective cancellation of clutter in the central radar resolution cell contained in the set window, to enhence the signal-to-clutter power ratio under the following assumptions :

(1). The observed clutter has stationary polarization behaviour within the set window.

(2). The signal samples are mainly contributed by the clutter to be cancelled. (supper-clutter visibility condition)

---

[1]In practice, the range extent, K, over which the *i.i.d.* assumpton applies is severely limited. It is precisely this case for which frequency diversity is expected to improve the performance of adaptive processing, as found by Wang and Cai [13].

(3). The observed clutter presents a sufficiently high degree-of-polarization when measured within the set window.

The true clutter plus receive noise covariance matrix $\mathbf{R}$ will be obtained by taking the expectations of Eq.(2-4). The polarimetric model parameters are as follows:

$$
\begin{aligned}
\mathbf{R} &= \mathbf{R}_c + \mathbf{R}_n \\
&= \sigma_c^2 \cdot \begin{bmatrix} \varepsilon & \varrho\sqrt{\varepsilon} \\ \varrho^*\sqrt{\varepsilon} & 1 \end{bmatrix} + \begin{bmatrix} \sigma_n^2 & 0 \\ 0 & \sigma_n^2 \end{bmatrix}
\end{aligned}
\tag{2-5}
$$

where $\mathbf{R}_c$, and $\mathbf{R}_n$ are the completely polarized portion of clutter covariance, and unpolarized plus receive noise covariance matrix, respectively. This is similar to the single transmit and dual receiver version of a meadow clutter example given in [22]. The power ratio between co-polarized and cross-polarized channels is specified by ε, with $0 \leq \varepsilon \leq$. The complex correlation coefficient ϱ between the voltages x_h and x_v is defined as

$$
\varrho = \frac{E(x_h x_v^*)}{[E(x_h x_h^*) \cdot E(x_v x_v^*)]^{1/2}}
\tag{2-6}
$$

with $0 \leq |\varrho| \leq 1$. Together with degree of polarization parameter, it provides a useful description of the time-varying polarized waves. The matrix $\mathbf{R}$ is a Hermitian matrix ($\mathbf{R}^H = \mathbf{R}$); hence, it can be represented by the Stokes parameters [7], g_0, g_1, g_2 and g_3, which are four real numbers defined as follows,

$$
\mathbf{g} = \begin{bmatrix} g_0 \\ g_1 \\ g_2 \\ g_3 \end{bmatrix} = \begin{bmatrix} \sigma_h^2 + \sigma_v^2 \\ 2Im[\sigma_{hv}] \\ \sigma_h^2 - \sigma_v^2 \\ 2Re[\sigma_{hv}] \end{bmatrix} = \begin{bmatrix} \sigma_c^2(1+\varepsilon) \\ 2Im[\varrho\sqrt{\varepsilon}\sigma_c^2] \\ \sigma_c^2(\varepsilon-1) \\ 2Re[\varrho\sqrt{\varepsilon}\sigma_c^2] \end{bmatrix}
\tag{2-7}
$$

and the total average power, given by g_0, meets the following condition:

$$
g_0^2 \geq g_1^2 + g_2^2 + g_3^2.
\tag{2-8}
$$

In Eq.(2-8), the equality holds when the wave is completely polarized, while $g_1 = g_2 = g_3 = 0$ when the wave is completely unpolarized. In terms of the Stokes vector, a partially polarized wave can be uniquely decomposed as

$$
\mathbf{g} = \begin{bmatrix} g_{cp} \\ g_1 \\ g_2 \\ g_3 \end{bmatrix} + \begin{bmatrix} g_0 - g_{cp} \\ 0 \\ 0 \\ 0 \end{bmatrix}
\tag{2-9}
$$

where $g_{cp} = (g_1^2 + g_1^2 + g_1^2)^{1/2}$ and $(g_0 - g_{cp})$ are the powers contained in the completely polarized and unpolarized wave ocmponents, respectively. Then the degree of polarization of the wave corresponding to the second-order statistic model of Eq.(2-5) is obtained as

$$
\begin{aligned}
\gamma &= \frac{g_{cp}}{g_0} \\
&= \frac{(g_1^2 + g_1^2 + g_1^2)^{1/2}}{g_0} \\
&= \frac{\{(\sigma_h^2 + \sigma_v^2)^2 + [2Re(\sigma_{hv})]^2 + [2Im(\sigma_{hv})]^2\}^{1/2}}{\sigma_h^2 + \sigma_v^2} \\
&= \frac{\{[\sigma_c^2(\varepsilon - 1)]^2 + (2\sigma_c^2)^2 \cdot [(Re(\varrho))^2 + (Im(\varrho))^2]\}^{1/2}}{\sigma_c^2(\varepsilon + 1) + 2 \cdot \sigma_n^2} \\
&= \frac{\{[\sigma_c^2(\varepsilon - 1)]^2 + (2\sigma_c^2)^2 \cdot |\varrho|^2\}^{1/2}}{\sigma_c^2(\varepsilon + 1) + 2 \cdot \sigma_n^2}
\end{aligned}
\tag{2-10}
$$

In particular, when $\varepsilon=1$, i.e., $|x_h| = |x_v|$, the following relationship of degree of polarization and the complex correlation coefficient can be obtained from the above equation

$$
\gamma = |\varrho| \cdot \left(\frac{\sigma_c^2}{\sigma_c^2 + \sigma_n^2}\right) \tag{2-11}
$$

It shows that the magnitude of correlation coefficient is always less than and equal to the degree of polarization, $|\varrho| \leq \gamma$, and is always true for every value of ε. Note that an anticipation of detection performance in a polarimetric processor is relied on knowing the degree of polarization parameter value, but it is almost unpractical to find, while the estimation of complex correlation coefficient is possible with reasonable accuracy, and it will serve as the lower bound for a deree of polarization parameter value.

Based on the MB data model described in this section, two canceler-based detectors will be presented in the next consecutive sections.

94

2.1.3 Optimum Multiband Polarimetric Detector

In OMPD, $\mathbf{R}_j$ and γ_j are assumed to be known as well as σ_{hj}^2, σ_{vj}^2, and σ_{hvj}. Where σ_{hj}^2, and σ_{vj}^2 are the input clutter-plus-noise powers of h and v channels, and σ_{hvj} is the cross-covariance between the channels, respectively, under H_o hypothesis. The power for completely polarized portion of the clutter can be calculated from the known quantities, i.e., $\sigma_{cpj}^2 = \gamma_j \cdot (\sigma_{hj}^2 + \sigma_{vj}^2)$

The following proposed OMBPC based detector is studied, specifically in order to identify the problems with SB signaling in the polarization canceler based detector, and to clearly show the improvement of MB signaling. A detailed explanation of SB version for this algorithm is in [10,13].

1. Compute the receiving optimum normalized *Stokes* polarization vector $\mathbf{f}(\mathbf{p}_{rj})$ (which minimizes the canceler output power) :

$$
\mathbf{f}(\mathbf{p}_{rj}) = \begin{bmatrix} f_0 \\ f_1 \\ f_2 \\ f_3 \end{bmatrix} = \begin{bmatrix} 1 \\ -2\,Im(\sigma_{hvj})/\sigma_{cpj}^2 \\ -(\sigma_{hj}^2 - \sigma_{vj}^2)/\sigma_{cpj}^2 \\ -2\,Re(\sigma_{hvj})/\sigma_{cpj}^2 \end{bmatrix} \tag{2-12}
$$

2. Calculate the optimum receiver polarization weight vector $\mathbf{p}_{rj} = [p_{rhj}, p_{rvj}]^T$:

$$
\mathbf{p}_{rj} = \begin{bmatrix} \sqrt{(1/2)(f_0 + f_2)} \\ \sqrt{(1/2)(f_0 - f_2)} \end{bmatrix} \cdot \exp[i \cdot tan^{-1}(f_1/f_3)] \ ; j = 1, 2, ..., J \tag{2-13}
$$

3. Construct the test statistic

$$
\eta = \sum_{j=1}^{J} |\,z_j\,|^2 \underset{H_0}{\overset{H_1}{\underset{<}{>}}} \eta_o \tag{2-14}
$$

where

$$
z_j = \mathbf{x}_j^H \mathbf{p}_{rj} \ ; \ \ j = 1, 2, ..., J, \tag{2-15}
$$

where "H" denotes the complex conjugate and transpose operator, and z_j is the residual output signal after polarization cancellation of the disturbance. H_1 is accepted if η is larger than a chosen threshold η_o.

2.1.4 Adaptive Multiband Polarization Canceler Based Detector

The Sample Matrix Inversion (SMI) class of adaptive algorithm for weight vector computation has been studied. We start by investigating the polarization canceler with an adjustable gain on the main channel (horizontal, cross-polarized channel). The adaptive weight vector in this canceler will be the solution to

$$\hat{\mathbf{p}}_r = \mu \hat{\mathbf{R}}^{-1} \mathbf{u}, \tag{2-16}$$

where $\hat{\mathbf{p}}_r$, 2×1, is the estimate of the weight vector (receiver polarization state), μ is a gain constant, $\mathbf{u}$ is the desired signal vector, and

$$\hat{\mathbf{R}} = \frac{1}{JK} \sum_{j=1}^{J} \sum_{k=1}^{K} \mathbf{x}_{jk} \mathbf{x}_{jk}^H = \begin{bmatrix} \hat{\sigma}_h^2 & \hat{\sigma}_{hv} \\ \hat{\sigma}_{vh} & \hat{\sigma}_v^2 \end{bmatrix}, \tag{2-17}$$

is the estimate of MB covariance matrix based on JK number of the secondary data. Because the cross-polarized channel (horizontal) employees higher gain (desired signal present) than the copolarized channel (vertical), a target return in the horizontal channel produces larger output signals than an equivalent input to the vertical channel. Hence, for this desired signal vector $\mathbf{u}$ we have approximately

$$\mathbf{u} = \begin{bmatrix} 1 \\ 0 \end{bmatrix}. \tag{2-18}$$

Then Eq.(2-16) may be rewritten as

$$\begin{bmatrix} \hat{\sigma}_h^2 & \hat{\sigma}_{hv} \\ \hat{\sigma}_{vh} & \hat{\sigma}_v^2 \end{bmatrix} \begin{bmatrix} \hat{p}_{rh} \\ \hat{p}_{rv} \end{bmatrix} = \begin{bmatrix} \mu \\ 0 \end{bmatrix} \tag{2-19}$$

This equation is equivalent to two scalar equations

$$\hat{\sigma}_h^2 \hat{p}_{rh} + \hat{\sigma}_{hv} \hat{p}_{rv} = \mu, \tag{2-20}$$

and

$$\hat{\sigma}_v^2 \hat{p}_{rv} = -\hat{p}_{rh} \hat{\sigma}_{vh}. \tag{2-21}$$

We choose a value of μ in Eq.(2-20) that results in $\hat{p}_{rh}$ being unity. Then Eq.(2-21) reduced to

$$\hat{p}_{rv} = -\frac{\hat{\sigma}_{hv}}{\hat{\sigma}_v^2}. \tag{2-22}$$

The output of the canceler obtained using Eq.(2-15) is

$$z_j = x_{hj} + \hat{p}_{rv} x_{vj}^*, \quad j = 1, 2, \cdots, J, \qquad (2-23)$$

where "*" denotes the complex conjugate. Eq.(2-22) is a well known form of the APC weight, and its output is given by Eq.(2-23).

The final test statistic is the sum of magnitude squared for all J subband outputs

$$\eta = \sum_{j=1}^{J} \mid z_j \mid^2 \underset{H_0}{\overset{H_1}{\gtrless}} \eta_o \qquad (2-24)$$

This adaptive processor will be compared with its optimum processor of known clutter statistic case, i.e., $\hat{\mathbf{R}} = \mathbf{R}$.

2.1.5 Derivation of Detection and False Alarm Probabilities

To simplify the derivation of the detector performance, without loss of generality, assume that the separations among the subbands are sufficiently large so that the returns of the J subpulses are statistically independent [2]. The assumption on the relative bandwidth of the system leads to

$$\sigma_{s1}^2 = \sigma_{s2}^2 = \cdots = \sigma_{sJ}^2 \qquad (2-25)$$

For the same purpose we also assume that the target polarization vectors do not change over the J subbands, i.e.,

$$\mathbf{p}_{s1}^2 = \mathbf{p}_{s2}^2 = \cdots = \mathbf{p}_{sJ}^2 \qquad (2-26)$$

We thus drop the subscript j on both Eq.(2-25) and Eq.(2-26), i.e., using σ_s^2 and $\mathbf{p}_s$, respectively. With a careful selection of the subband frequency separation, these two assumptions can be approximately valid [19]. However, it should be note that the operation of the AMBPC based system does not rely on these two assumption.

The subband Signal-to-Clutter-plus-Noise-Ratio $(SCNR_j)$ is defined as

$$SCNR_j = SNR_j/(1 + CNR_j). \qquad (2-27)$$

where SNR_j and CNR_j refer to the subband Signal-to-Noise Ratio and Clutter-to-Noise Ratio, respectively.

Derivations of P_d and P_{fa} for OMBPD

The output power, for each subband, under H_0 and H_1, respectively, can be found [13] in terms of the degree-of-polarization γ, input total power under H_0 $\sigma_{x|H_0}^2$, the input target power σ_s^2, and the angle deviation (degree away) from the maximum response ξ,

$$\sigma_{z|H_0}^2 = \frac{\sigma_{x|H_0}^2}{2} \cdot (1 - \gamma), \qquad (2-28)$$

and

$$\sigma_{z|H_1}^2 = \sigma_s^2 \cdot cos^2(\xi) + \sigma_{z|H_0}^2. \qquad (2-29)$$

---

[2] Experiments observing small targets with ground clutter at RL, 1989, indicate that 1 MHz. frequency steps are sufficient to meet these requirement with a maximum of twelve diversity frequencies.

Here, the degree of polarization (γ) is defined under H_0 hypothesis, i.e., $\gamma = \sigma_{cp}^2/\sigma_{x|H_0}^2$. We assumed that the target and the clutter polarization states are both linear, so $\cos^2(\xi)$ term explicitly shown in Eq.(2-29), which correponds the response curve (a) in Fig. 2.

The subband signal-to-noise ratio SNR_j and subband clutter-to-noise ratio CNR_j are defined, respectively, as

$$SNR_j = \frac{\sigma_s^2}{\sigma_w^2} \ , \tag{2-30}$$

and

$$CNR_j = \frac{\sigma_c^2}{\sigma_w^2} \ . \tag{2-31}$$

The output of the linear polarization filter, z_j, will have a complex Gaussian probability density if the dual channel inputs, $\mathbf{x}_{hj}$ and $\mathbf{x}_{vj}$ are complex Gaussians. Under the condition, the statistically optimum method for combining the outputs of a multiple channel frequency diverse waveform is the Square-Law Detector. When the Square-Law Detector is applied to Gaussian measurement data, the output will follow the *Chi-square* distribution with $2J$ degrees of freedom [1]. Thus, the detection probability, $P_d = P(\eta \geq \eta_o \mid H_1)$, and the false alarm probability, $P_{fa} = P(\eta \geq \eta_o \mid H_0)$ can be written as [1].

$$P_d = exp(-m_d) \cdot \sum_{j=1}^{J} (m_d)^{J-j}/(J-j)! \ , \tag{2-32}$$

and

$$P_{fa} = exp(-m_{fa}) \cdot \sum_{j=1}^{J} (m_{fa})^{J-j}/(J-j)! \ . \tag{2-33}$$

where $m_{fa} = \eta_o/\sigma_{z|H_0}^2$ which can be found using Neyman-Pearson criterion with a predetermined P_{fa}, and $m_d = \eta_o/\sigma_{z|H_1}^2$ can be factored out from Eq.(2-29), as a function of m_{fa}, i.e.,

$$m_d = \frac{m_{fa}}{[1 + (2 \cdot cos^2(\xi) \cdot SCNR_j)/(1-\gamma)]} \ . \tag{2-34}$$

Eq .(2-32), (2-33), and (2-34) complete the derivations of detection and false alarm probabilities for the OMBPD.

This optimum processor is specifically presented to clearly show the performance improvement obtained using MB signalling, in terms of detection probability expressed by the parameters of degree of polarization (γ) and degree away from the maximum response (ξ).

99

DERIVATIONS OF P_d AND P_{fa} FOR AMBPC BASED DETECTOR

The averaged output power for each subband channel under H_1, and H_o hypothesis, respectively, are

$$
\begin{aligned}
\hat{\sigma}^2_{z|H_1} &= E[z_j z_j^*] \quad , j = 1, 2, \cdots, J \\
&= \hat{\mathbf{p}}_r^H [\sigma_s^2 \mathbf{p}_s \mathbf{p}_s^H + \mathbf{R}] \, \hat{\mathbf{p}}_r
\end{aligned}
\tag{2-35}
$$

and

$$
\hat{\sigma}^2_{z|H_0} = \hat{\mathbf{p}}_r^H \mathbf{R} \hat{\mathbf{p}}_r \ .
\tag{2-36}
$$

As the test statistic η is the sum of $|z_j|^2$, $j = 1, 2, ...J$, its probability density functions are

$$
f_\eta(\eta \mid H_1, \hat{\mathbf{p}}_r) = \frac{1}{\hat{\sigma}^{2J}_{z|H_1} (J-1)!} \cdot \eta^{J-1} \cdot exp(-\eta / \hat{\sigma}^2_{z|H_1})
\tag{2-37}
$$

and

$$
f_\eta(\eta \mid H_0, \hat{\mathbf{p}}_r) = \frac{1}{\hat{\sigma}^{2J}_{z|H_0} (J-1)!} \cdot \eta^{J-1} \cdot exp(-\eta / \hat{\sigma}^2_{z|H_0}) \ .
\tag{2-38}
$$

The conditional probabilities of detection and false alarm are thus found by integrating Eq.(2-37) and Eq.(2-38), respectively, above the threshold η_o,

$$
\begin{aligned}
P_{d|\hat{\mathbf{p}}_r} &= P(\eta \geq \eta_o \mid H_1, \hat{\mathbf{p}}_r) \\
&= \int_{\eta_o}^{\infty} f_\eta(\eta \mid H_1, \hat{\mathbf{p}}_r) d\eta \\
&= exp(-\hat{m}_d) \cdot \sum_{j=1}^{J} (\hat{m}_d)^{J-j} / (J-j)! \ ,
\end{aligned}
\tag{2-39}
$$

and

$$
\begin{aligned}
P_{fa|\hat{\mathbf{p}}_r} &= P(\eta \geq \eta_o \mid H_0, \hat{\mathbf{p}}_r) \\
&= \int_{\eta_o}^{\infty} f_\eta(\eta \mid H_0, \hat{\mathbf{p}}_r) d\eta \\
&= exp(-\hat{m}_{fa}) \cdot \sum_{j=1}^{J} (\hat{m}_{fa})^{J-j} / (J-j)! \ ,
\end{aligned}
\tag{2-40}
$$

where $\hat{m}_d = \eta_o / \hat{\sigma}^2_{z|H_1}$ and $\hat{m}_{fa} = \eta_o / \hat{\sigma}^2_{z|H_0}$.

Eq.(2-16) can be written as

$$
\hat{\mathbf{p}}_r = \frac{\hat{\mathbf{R}}^{-1} \mathbf{u}}{(\mathbf{u}^H \hat{\mathbf{R}}^{-1} \mathbf{p}_s)},
\tag{2-41}
$$

with $\mu = 1/(\mathbf{u}^H \hat{\mathbf{R}}^{-1} \mathbf{p}_s)$.

Substituting it into Eq.(2-35) yields

$$
\begin{aligned}
\hat{\sigma}^2_{z|H_1} &= [\mathbf{u}^H \hat{\mathbf{R}}^{-1}(\mathbf{R} + \sigma_s^2 \mathbf{p}_s \mathbf{p}_s^H)\hat{\mathbf{R}}^{-1} \mathbf{u}]/(\mathbf{u}^H \hat{\mathbf{R}}^{-1} \mathbf{p}_s)^2 \\
&= \frac{\mathbf{u}^H \hat{\mathbf{R}}^{-1} \mathbf{R} \hat{\mathbf{R}}^{-1} \mathbf{u}\mathbf{u}^H \mathbf{R}^{-1} \mathbf{p}_s}{(\mathbf{u}^H \hat{\mathbf{R}}^{-1} \mathbf{p}_s)^2} \cdot \frac{1}{\mathbf{u}^H \mathbf{R}^{-1} \mathbf{p}_s} + \sigma_s^2
\end{aligned}
\tag{2-42}
$$

Define

$$
\rho = \frac{(\mathbf{u}^H \hat{\mathbf{R}}^{-1} \mathbf{p}_s)^2}{\mathbf{u}^H \hat{\mathbf{R}}^{-1} \mathbf{R} \hat{\mathbf{R}}^{-1} \mathbf{u}\mathbf{u}^H \mathbf{R}^{-1} \mathbf{p}_s}
\tag{2-43}
$$

and

$$
\beta = \mathbf{u}^H \mathbf{R}^{-1} \mathbf{p}_s
\tag{2-44}
$$

Eq.(2-42), then, becomes

$$
\hat{\sigma}^2_{z|H_1} = \frac{1}{\rho\beta} + \sigma_s^2.
\tag{2-45}
$$

Under the target absent hypothese H_0, Eq. (2-45) truns out

$$
\hat{\sigma}^2_{z|H_0} = \frac{1}{\rho\beta}.
\tag{2-46}
$$

Note that ρ of Eq.(2-43) is similar to the "normalized signal-to-noise ratio" in [20], which has a *Beta* distribution for dual-channel data, i.e., $M = 2$

$$
f_\rho(\rho) = KJ\,\rho^{(KJ-1)}, \quad 0 \le \rho \le 1.
\tag{2-47}
$$

The detection and false alarm probabilities for adaptive processor can be obtained by averaging above conditional probabilities over the random variable ρ, respectively,

$$
\hat{P}_d = \int_0^1 exp(-\hat{m}_d) \cdot \sum_{j=1}^{J} (\hat{m}_d)^{J-j}/(J-j)! \cdot f_\rho(\rho)\ d\rho,
\tag{2-48}
$$

and

$$
\hat{P}_{fa} = \int_0^1 exp(-\hat{m}_{fa}) \cdot \sum_{j=1}^{J} (\hat{m}_{fa})^{J-j}/(J-j)! \cdot f_\rho(\rho)\ d\rho,
\tag{2-49}
$$

where

$$
\hat{m}_d = \hat{m}_{fa}/(1 + \rho\beta\sigma_s^2),
\tag{2-50}
$$

and

$$
\hat{m}_{fa} = \rho\eta_o\beta.
\tag{2-51}
$$

Performance evaluation follows from the above expressions by using Eq.(2-49) to determine $\hat{m}_{fa}$ to meet a specified false alarm probability given J and K. $K=2$ is the minimum number of auxiliary range indices necessary for single band clutter estimation. The number of frequency diversity channels, J, will be a variable parameter. For a specified clutter covariance and target signal, detection probability is calculated from Eq.(2-47) and (2-48). The optimum MBPC based detector as an upper bound to adaptive MBPC based detector is defined for $\hat{\mathbf{R}} = \mathbf{R}$, when the clutter statistic is known a priori. Note that although the MBPD and MBPCBD are developed for the MB system, they are also applicable for the SB system and all of them become their corresponding SB algorithm just by letting $J=1$.

2.1.6 Performance Comparison and Conclusion

The above theoretical expressions provide a means for evaluating the false alarm and detection performance in specific cases. The performance comparison will be conducted in the following two parts. One is made by varying the signal cancellation and degree-of-polarization parameters in order to examine whether the MB system ($J¿1$) can outperform the SM ($J=1$). This performance comparison has done with the OMBPD, whose detection probability is expressed in term of these two prameters, which are troublesome for SB system. The other one is to compare not only MB vs. SB, but also optimum vs. adaptive system with the MBPC based detector.

The system constraint used here for comparison of SB and MB is that the two to be compared have the same $SCNR$. Under this constraint, therefore, a system with the larger J has the lower $SCNR_j$. This chosen constraint says to be the least favorable to MB system [19] [23]. The SB input $SCNR$ is, thus, defined by

$$SCNR_{SB} = J \cdot SCNR_j \qquad (2-52)$$

The first part of comparison presents the MB signaling as the cure for the problems occurred by SB signaling. The OMBPD will be the basis for this performance evaluation.

The signal cancellation problem in OSBPD is illustrated in Fig. 5, which is a plot of detection probability vs. input $SCNR$ with different ξ values. It can be seen that there is 15 dB. loss, for 90 % desired detection probability, when the angle away from the maximum response (ξ) is 80 degree.

In addition to the *signal cancellation problem*, there is another problem with SBPC based detector. That is the severe degradation of performance due to low *degree of polarization*, called the *sensitivity problem*. Fig. 6 shows the probability of detection vs input $SCNR$ for OSBPD based detector with different *degree of polarizations*, i.e., $\gamma = .1, .3, .5$ and .95. It indicates that the degree of polarization is the important factor in SB based detector. It shows that the level of cancellation which may be achieved by the polarization canceler is limited by the unpolarized component of the clutter backscatter.

The MB signaling, again, takes care of this *sensitivity problem*, since the degree of polarization induced in each channel is depended on frequency, and the largest degree of polarization among channels is going to primarily affect detection performance.

Fig . 7 and Fig . 8 represent the performance comparisons of MB ($J = 4$) and SB polarimetric detector under equal system constraint with the signal cancellation, and the sensitivity problem, respectively. Reasonable hypothetical parameters are used for the comparisons : For Fig.7, $\gamma = .9$, for MB : $\xi_1 = 85$, $\xi_2 = 80$, $\xi_3 = 70$ and $\xi_4 = 5$ vs. for SB : $\xi = 80$, and ; for Fig.8, $\xi = 0$, for MB : $\gamma_1 = .01$, $\gamma_2 = .1$, $\gamma_3 = .15$ and $\gamma_4 = .95$, vs. for SB : $\gamma = .2$. These two particular examples show that MB system yields considerable amount of gains (7 and 4 dB., respectively) against the SB system.

The optimum performance analysis developed in this first part of computer simulation not only reveals that MB signaling for polarization canceler based detection significantly outperforms the conventional SB signaling under the toughest system constraint characterized in Eq. (2-52), but also serves as the performance bounds for the SB and MB polarization canceler based detectors when a radar system transmits a single polarized waveform and receives the dual-polarized return.
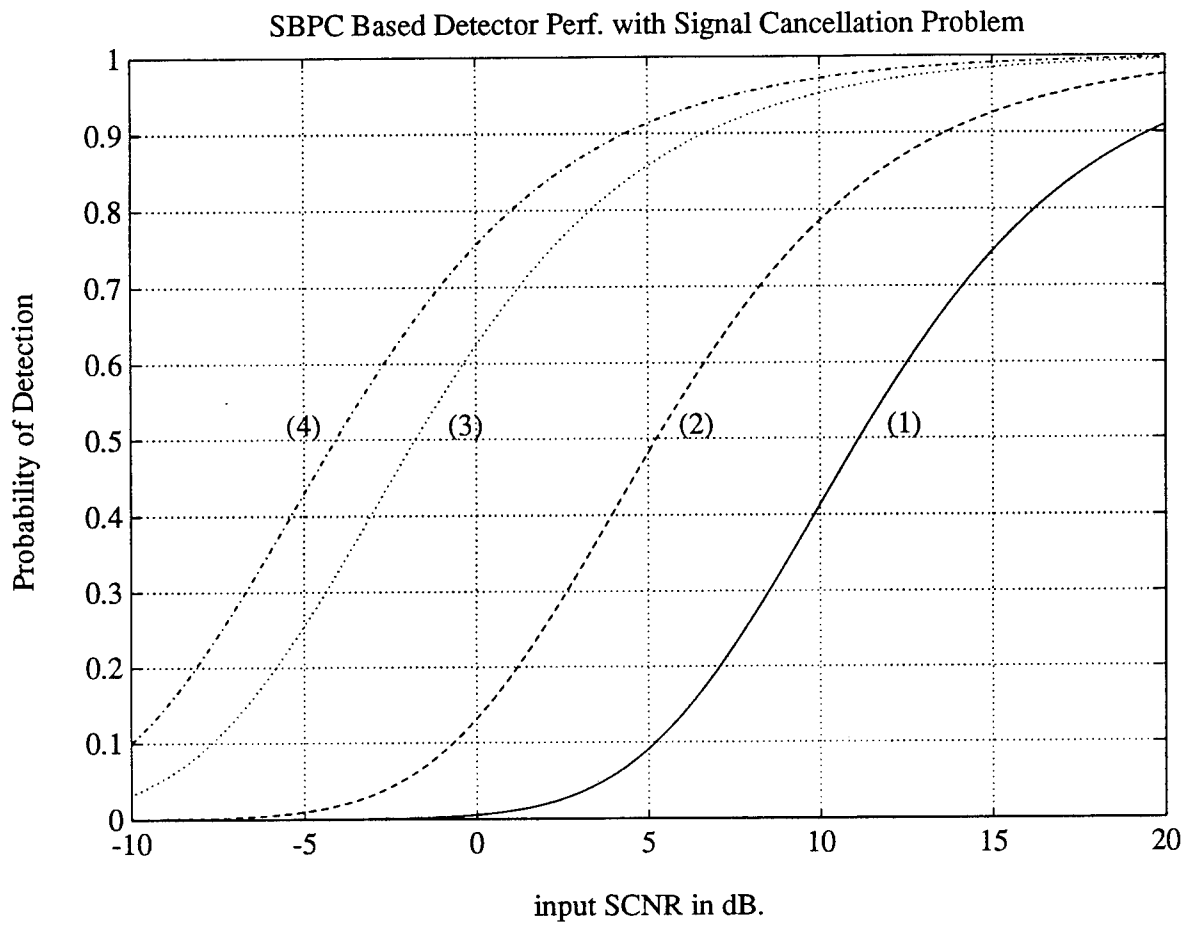
Figure 5: OSBPD Performance with *Signal Cancellation Problem* when $\gamma = .95$: (1) $\xi = 80$, (2) $\xi = 70$, (3) $\xi = 40$, and (4) $\xi = 0$ degree.
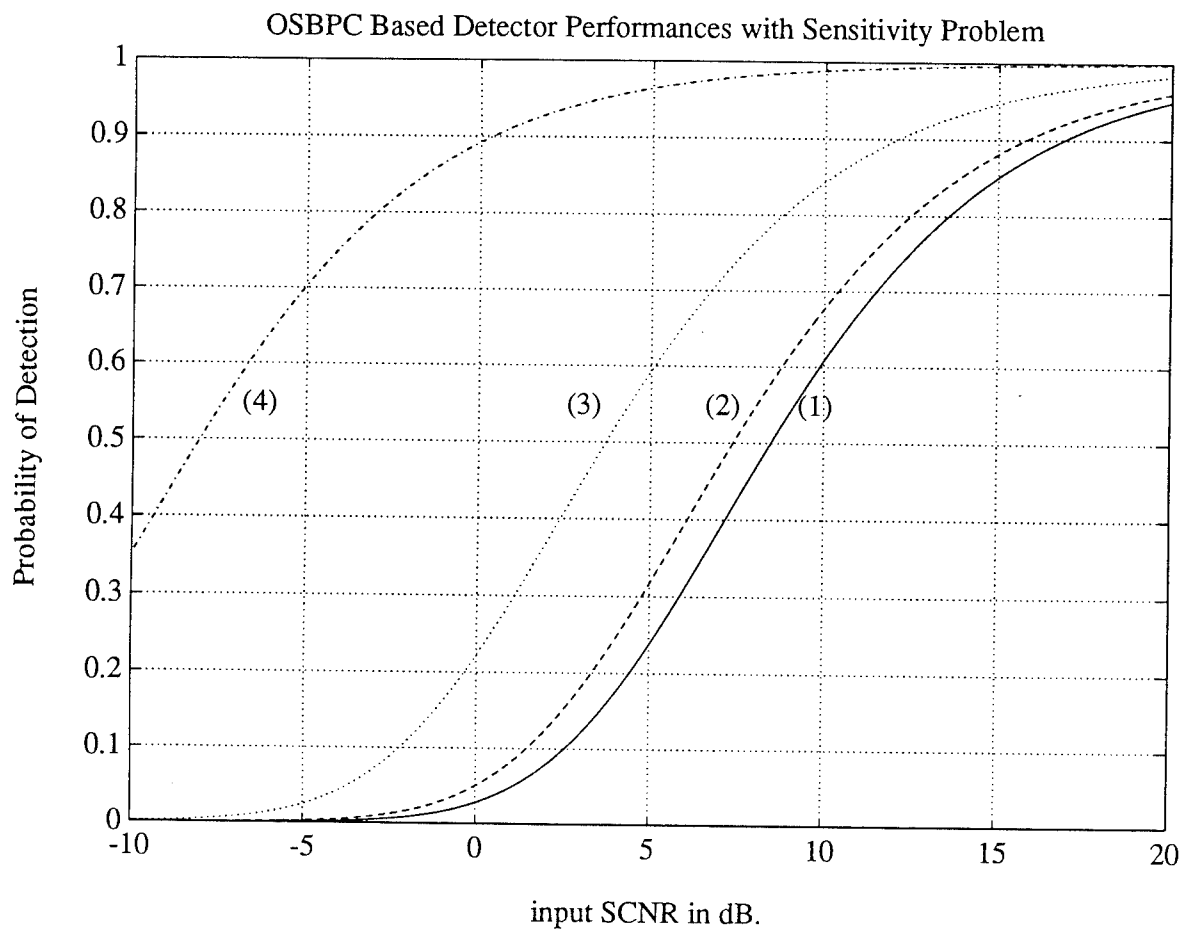
Figure 6: OSBPD Performance with *Sensitivity Problem* when $\xi = 0$ degree : (1) $\gamma = .1$, (2) $\gamma = .3$, (3) $\gamma = .7$, and (4) $\gamma = .95$.

MB vs. SB with Signal Cancellation Problem
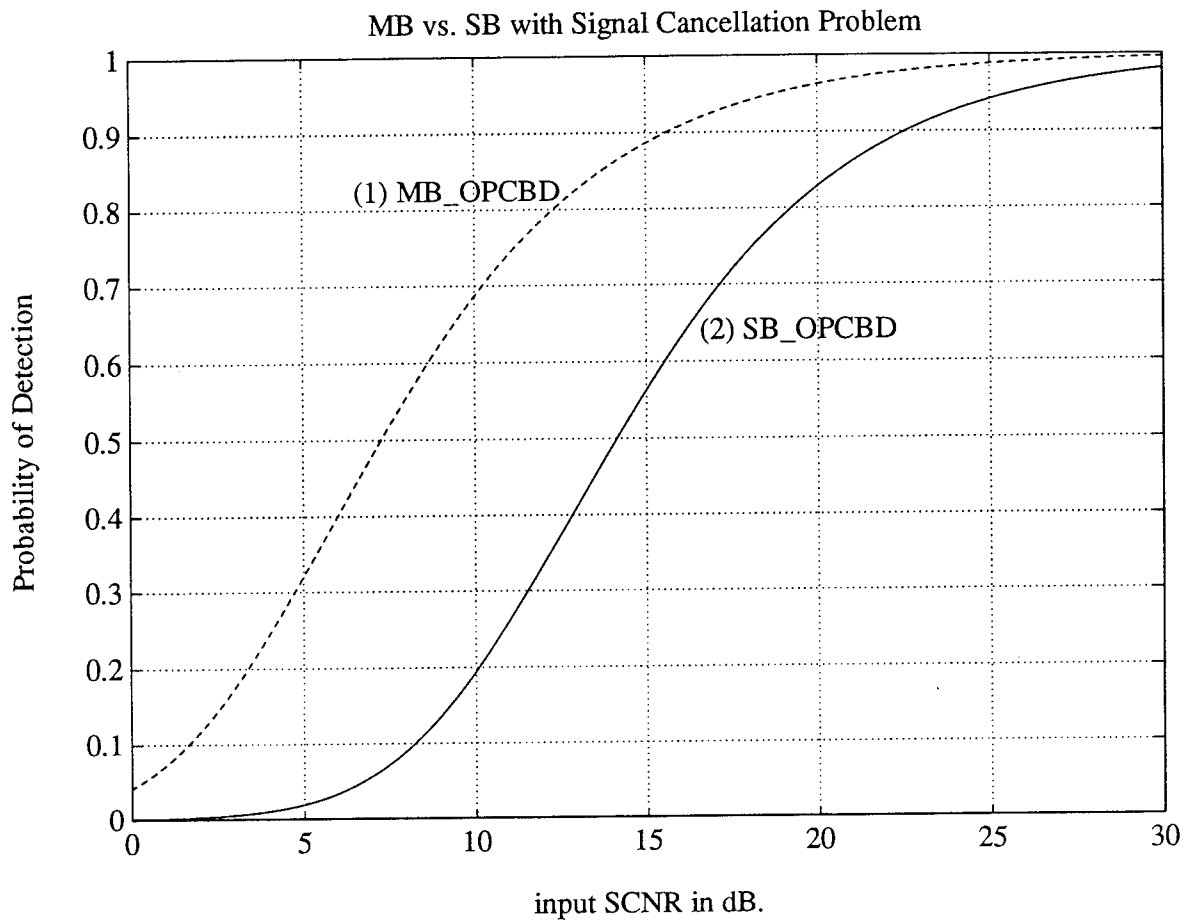
Figure 7: OMBPD vs. OSBPD with *Signal Cancellation Problem* under the Equal-$SCNR$ System Constraint when $\gamma = .9$: (1) for MB $\xi_1 = 85$, $\xi_2 = 80$, $\xi_3 = 70$ and $\xi_4 = 5$ degree, and (2) for SB $\xi = 80$ degree.
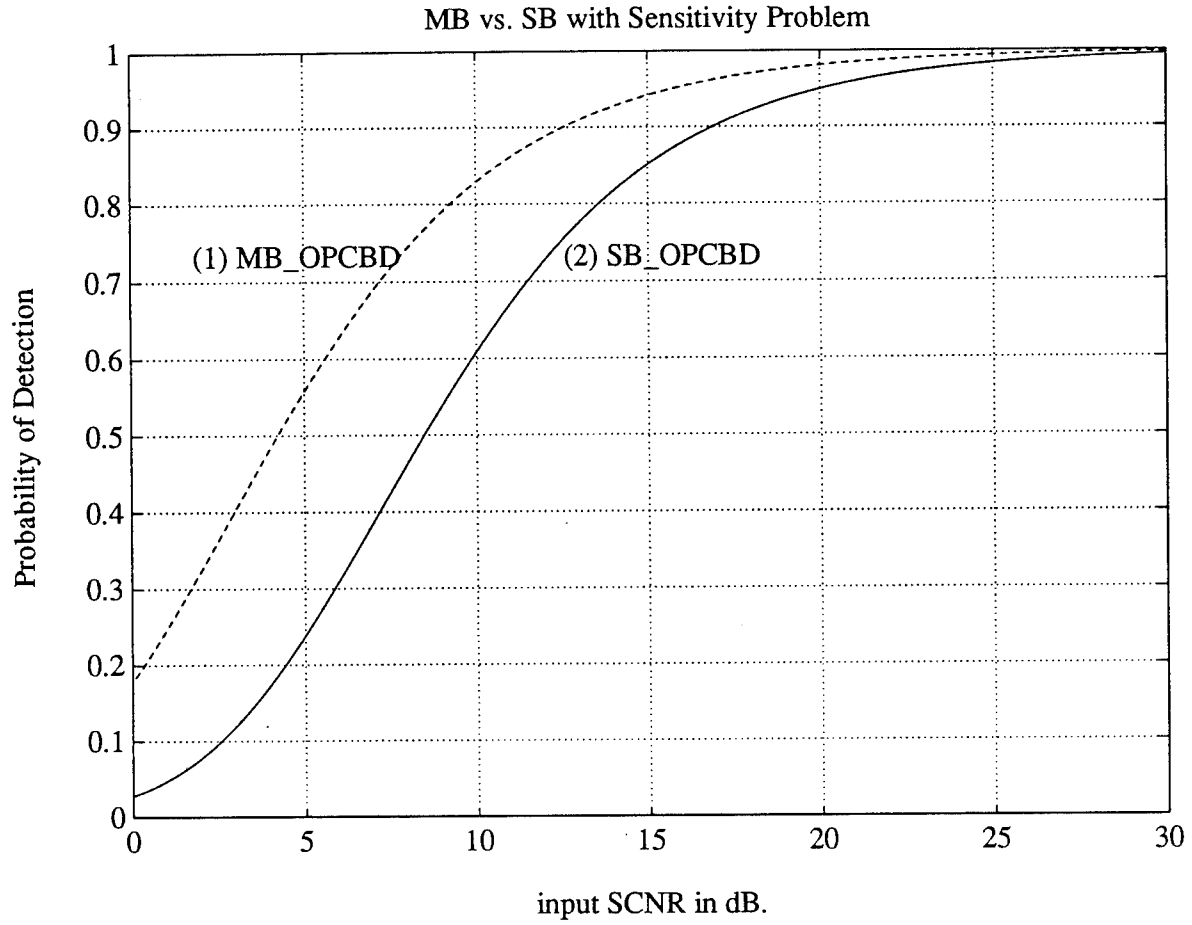
Figure 8: OMBPD vs. OSBPD with *Sensitivity Problem* under the Equal-$SCNR$ System Constraint when $\xi = 0$ degree : (1) for MB $\gamma_1 = .01$, $\gamma_2 = .1$, $\gamma_3 = .15$ and $\gamma_4 = .95$, and (2) for SB $\gamma = .2$

In the second part of this analysis, the performance evaluation of adaptive system over optimum system as well as MB signaling over SB signaling is presented based on the polaization canceler based detector. The adaptive implementation is compared with its optimum realization to provide a performance bound.

The polarimetric model parameters are as follows:

$$\mathbf{R}_c = \sigma_c^2 \cdot \begin{bmatrix} \varepsilon & \varrho\sqrt{\varepsilon} \\ \varrho^*\sqrt{\varepsilon} & 1 \end{bmatrix} \qquad (2-53)$$

which is similar to the single transmit and dual receiver version of a meadow clutter example given in [22]. The complex correlation coefficient ϱ between the voltages x_h and x_v is defined in Eq.(2-6) with $0 \le |\varrho| \le 1$. Together with degree of polarization parameter, it provides a useful description of the time-varying polarized waves. The power ratio between co-polarized and cross-polarized channels is specified by ε, with $0 \le \varepsilon \le$. It is shown in the MB modeling section that the magnitude of correlation coefficient is always less than and equal to the degree of polarization, $|\varrho| \le \gamma$. A deterministic target polarization vector ($\mathbf{p}_s$) requires an arbitrary choice of polarimetric phase, which has been shown in [22] that the phase value selected does not significantly alter performance of the adaptive detector whthe respect to the corresponding optimum performance. In the following we set $\mathbf{p}_s=[1,1]^T/\sqrt{2}$, $\sigma_c^2=4.75$, $\varepsilon = 0.58$, and $\varrho=.4$.

Under the system constraint characterized in Eq.(2-52), Fig.9 shows optimum/adaptive MBPC based detector performance when $CNR = 6.8$ dB., $K=2$, and $P_{fa} = 10^{-5}$ for SB ($J=1$) and MB ($J=4$) : (1)ASBPCBD, (2)OSBPCBD, (3)AMBPCBD, and (4)OMBPCBD. It indicates that the improvement due to MB signaling in the adaptive detector is much greater than that in optimum detector. MB signaling improves performance by increasing the quantity of independent and identically distributed (*i.i.d.*) date vectors available for clutter estimation. As a practical matter, this additional *i.i.d.* data vector for clutter statistic estimation is often required since an observation interval is severely limited due to the inhomogeneous nature of the enviornment. The total gain of the AMBPC over ASBPC is attribute to the combination of signal cancellation reduction, better adaptation, and a fluctuation reduction of the degree of target polarization, in addition to the well-known target amplitude fluctuation reduction.

Two principal results have been illustrated by each with different detectors :

(1) The MB signaling overcoms the problems occurred by SB signaling, which has been revealed with OMBPD algorthm.

(2) The MB signaling delivers adaptive processor much greater performance improvement than that observed for its optimum processor, which has been revealed based on optimum/adaptive MBPC based detector.
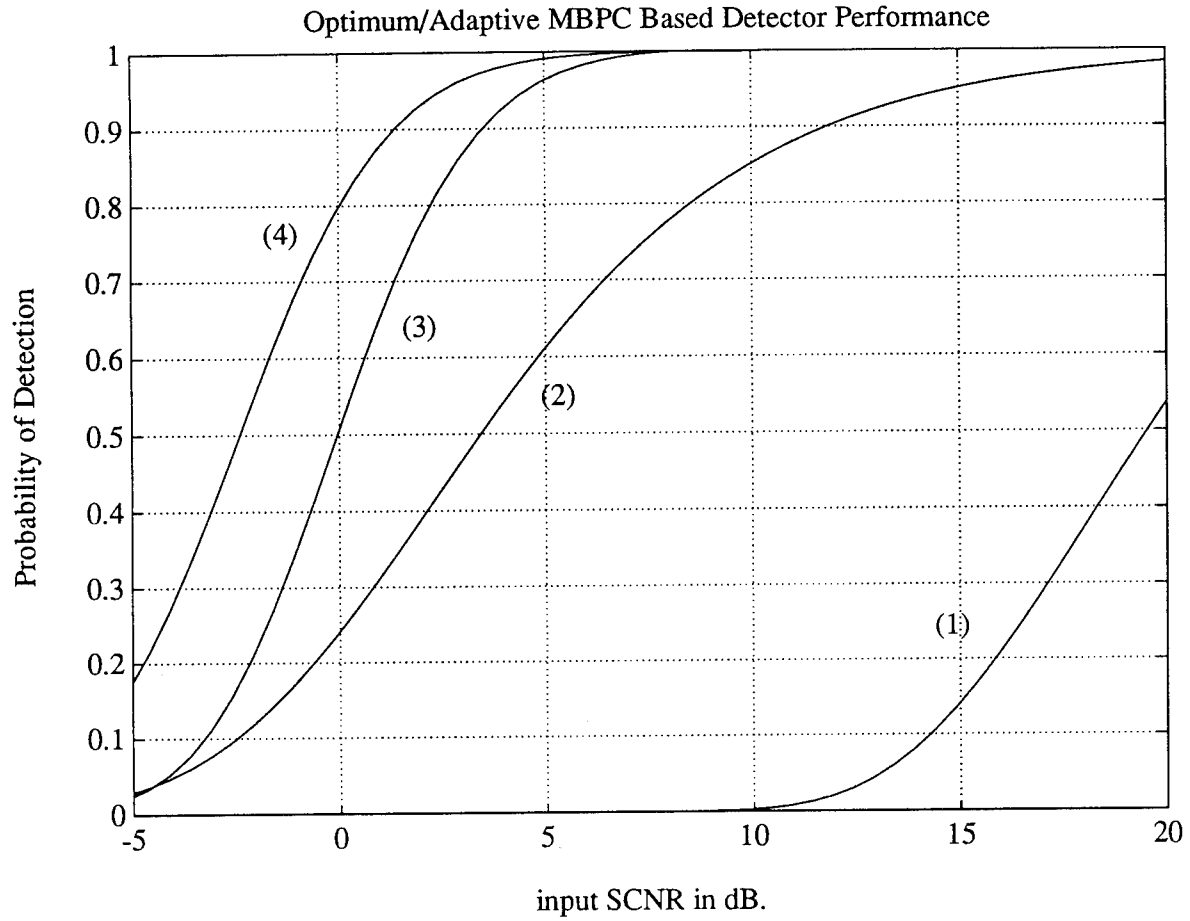
Figure 9: Optimum/Adaptive MBPC Based Detector Performance under the Equal-$SCNR$ System Constraint when CNR=6.8 dB., K=2, and $P_{fa} = 10^{-5}$ for SB (J=1) and MB (J=4) : (1)ASBPCBD, (2)OSBPCBD, (3)AMBPCBD, and (4)OMBPCBD.

2.2 Experimental Performance Demonstration

Our interest in this section is to compare the detection performance of the Adaptive Multiband Polarization Canceler (AMBPC) with the Adaptive Single Band Polarization Canceler (ASBPC) under the equal $SCNR$ system constraint using measured data. The following three sections are an approach and plan for demonstration, an experimental results, and conclusion and discussion.

2.2.1 Approach and Plan for Demonstration

The data collection activity consists of recording dual-polarized returns from clutter and targets of opportunity using the S-band radar system located at the Rome Laboratory (RL). The relevant S-band radar system parameters for this demonstration are listed in Tabel 1. We chose the number of frequency diverse subbands J to be 4, SB pulse width to be 8 microsecond, MB subpulse width to be 2 microsecond, and frequency separations to be 2 Mhz. with no additional subpulse modulation. Simple frequency diversity signaling was considered in this experiment as illustrated in Fig.11, where each subpulse of width $\tau' = \tau/J$ has a different carrier frequency with an arbituary narrow-band modulation of its own. These waveforms and their spectra are displayed in Fig.12. In order to minimize the injection of spur energy to other band, due to I and Q channel mismatch, non-symmetric frequencies selected relative to carrier frequency (3.35 GHz.) were chosen for the MB case. We transmitted a single vertically polarized and pulse-to-pulse interleaved SB and MB waveforms which should be capable of obtaining backscatter dynamics occurred almost at the same time. The performance comparison of ASBPC and AMBPC is presented by the simultaneous display of SB and MB test statistics with respect to range and pulse index. A configuration of the demonstration is shown in Fig.10. The pulse-to-pulse interleaved signaling for transmission is presented In Fig.11. Both orthogonal polarization channels (v and h) of SB and MB for clutter (H_0 hypothesis) and target plus clutter (H_1 hypothesis) data were received. The range window is set at inbetween 30 and 120 microseconds from time zero, which corresponds to 4.5 to 18 Kilometers in range. The digitized baseband outputs were buffered and transcribed to VAX-compatible 9-track digital magnetic tapes. Data analysis at Syracuse University was performed using software realizations of proposed processing algorithms.

Table 1. The relevant S-band radar system parameters.

Operating frequency	3.35 GHz.
Pulse Repetition Interval (PRI)	2 millisecond
Subband Separation	2 MHz.
Pulse Duration	8 microsecond
A/D Resolution	12 bit
A/D Sampling Frequency	10 MHz.
Number of Subbands (J)	4
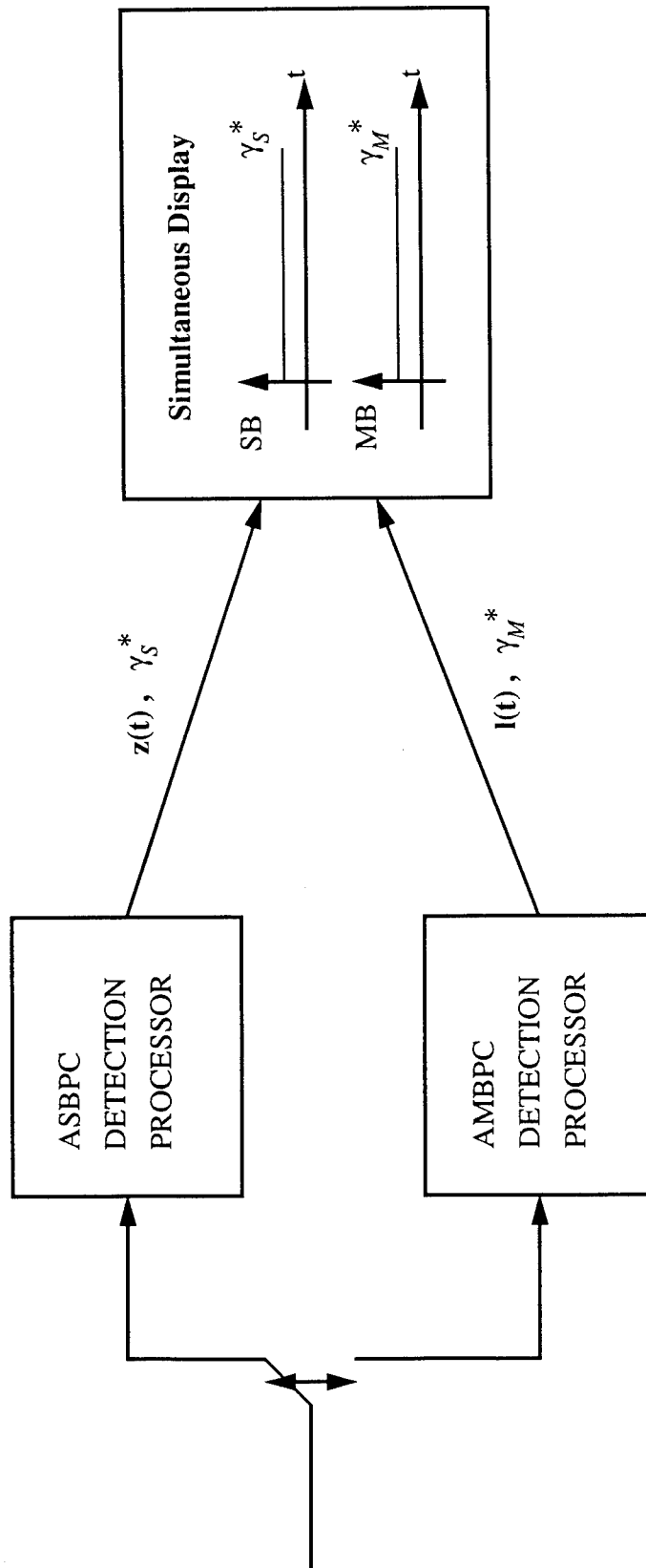
Figure 10: Configuration of the Demonstration.
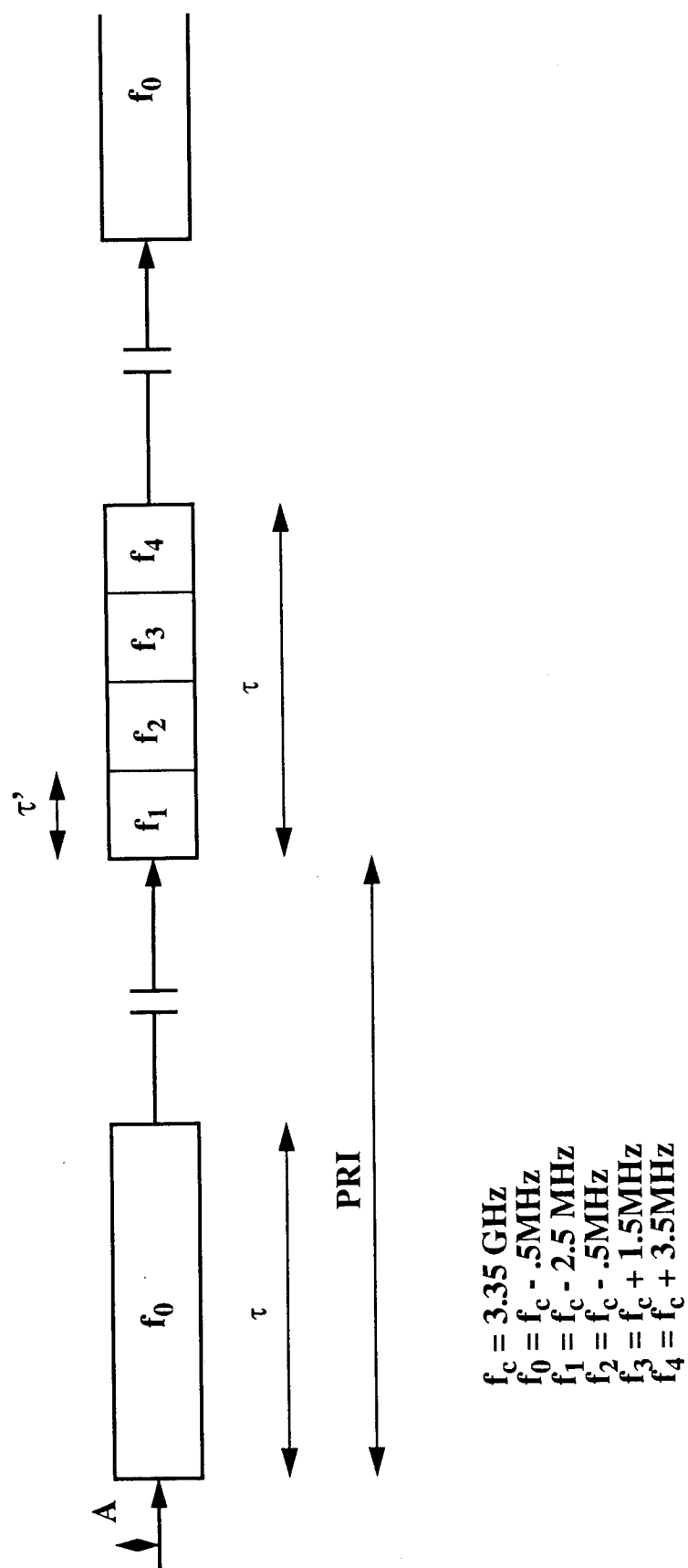
Figure 11: A Pulse-to-Pulse Interleaved Signal for Transmission.

$f_c = 3.35$ GHz
$f_0 = f_c - .5$MHz
$f_1 = f_c - 2.5$ MHz
$f_2 = f_c - .5$MHz
$f_3 = f_c + 1.5$MHz
$f_4 = f_c + 3.5$MHz
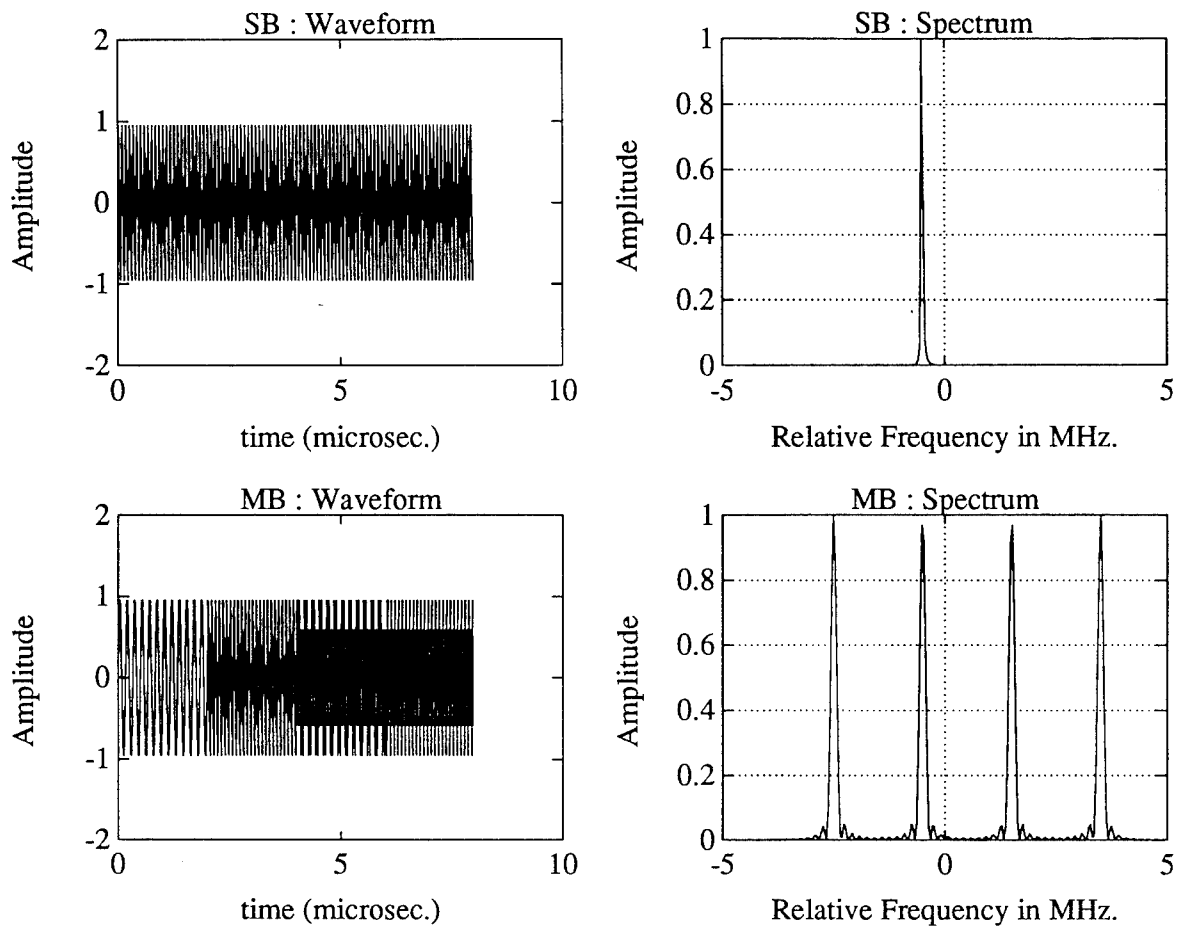
Figure 12: SB and MB : Waveforms and Their Spectra.

As far as canceler weight estimation is concerned, a minimization criterion is applied to the output power of the pulse smoothed data sets. For adaptation at the present range, the previous range index data were used to estimate weight. The impact of this weight window size in a nonstationary clutter enviornment is significant. The larger the size, the less tracking capability. As a comparison, we chose this weight window size to be 5, and the pulse smoothing size to be 5. The block-diagrams of the ASBPC and AMBPC based detectors are shown in Fig. 13 and Fig . 14, respectively.

For a given probability of false alarm ($P_{fa} = 10^{-5}$), and the estimated output power made it possible to set the thresholds for both detectors.
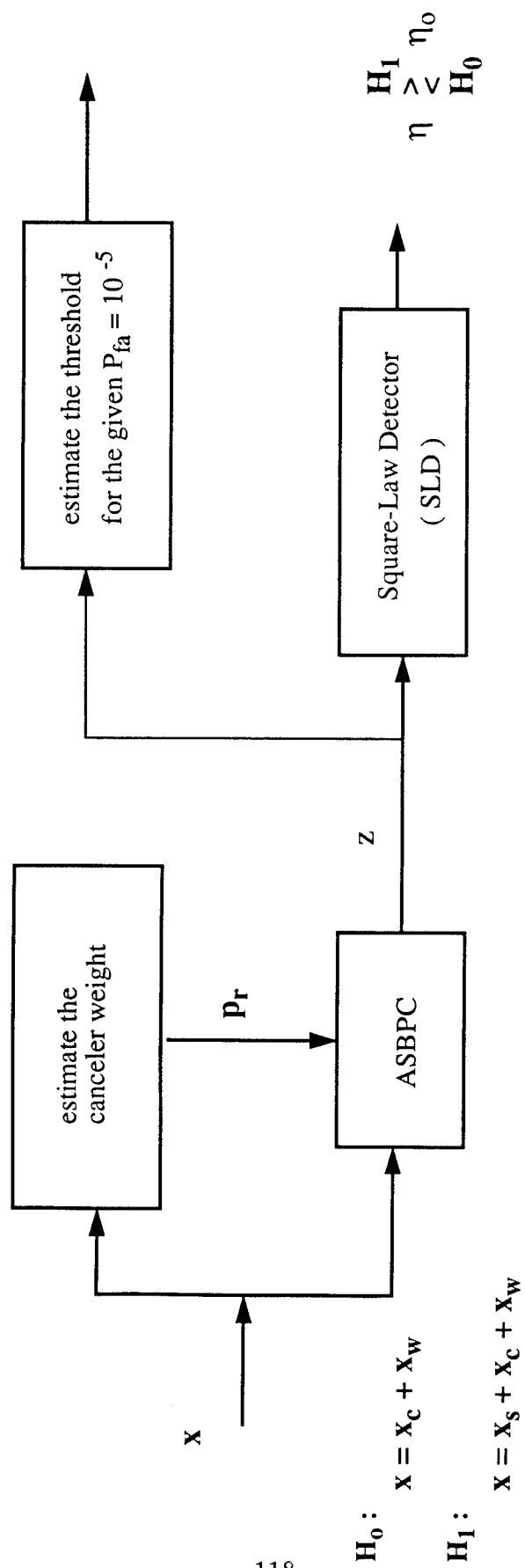
Figure 13: ASBPC based Detection Processor.
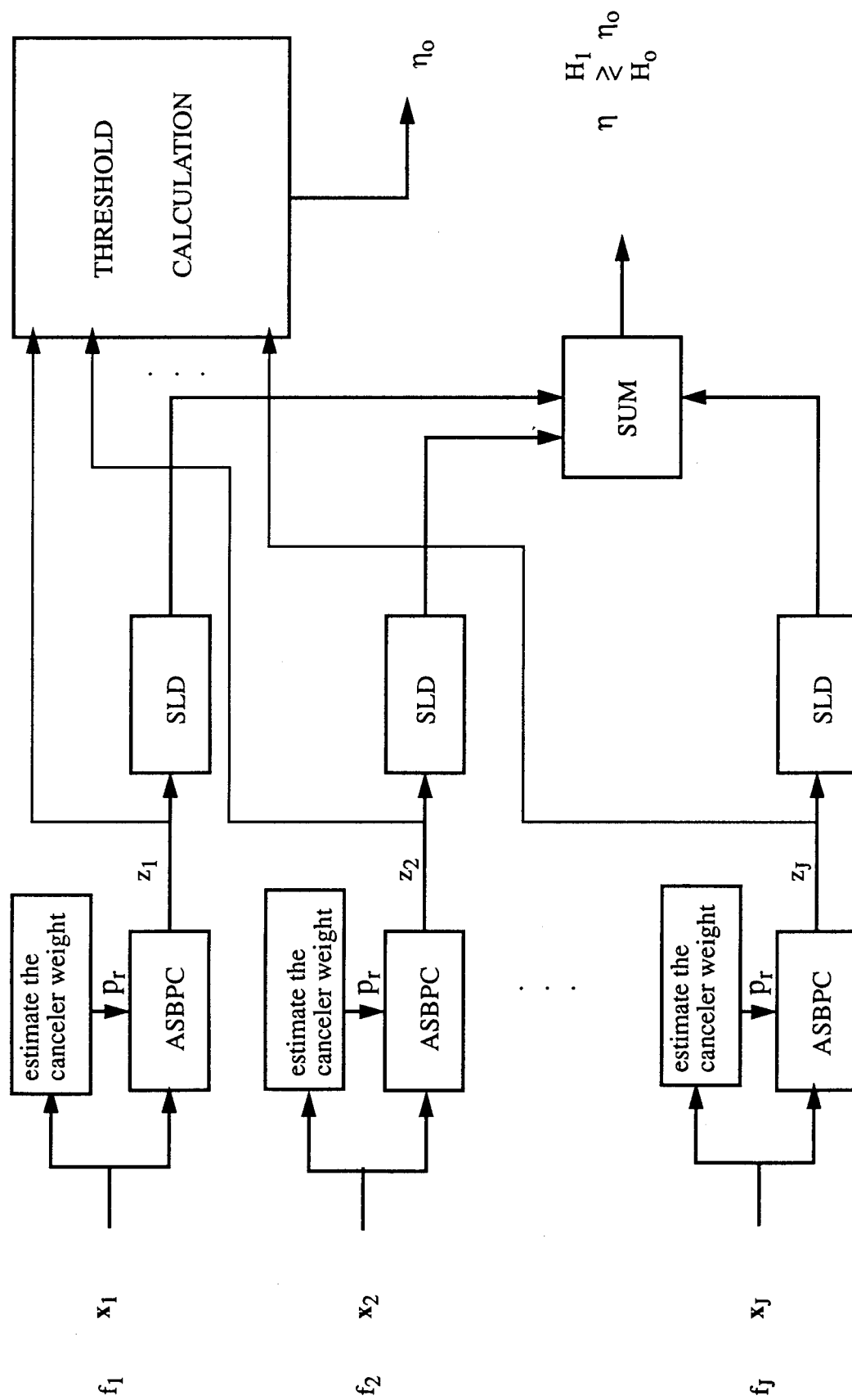
Figure 14: AMBPC based Detection Processor.

119

2.2.2 Experimental Results

Fig.15 shows a plot of detection statistic above the threshold for range and pulse index, includes SB and MB. As seen in this figure, the target is detected only in one return for SB, and detected almost all returns in MB case. The detection statistics of SB and MB vs. pulse index for the test cell containing the target is plotted in Fig .16 and 17, respectively. Also, Fig.18 is a plot of degree away from maximum response [3] vs. pulse index for both SB and MB case. For the MB case only that subband which most closely matches the maximum response is plotted. This improved detection performance of AMBPC based detector is due to reducing the polarization angle-similarity (between target and clutter) problem as seen in Fig.18.

---

[3]Maximum response occurs when the arget and clutter polarization angle difference is 90 degree

120

SB : Detection Statistic after thresholding

range index

pulse index

MB : Detection Statistic after thresholding

range index
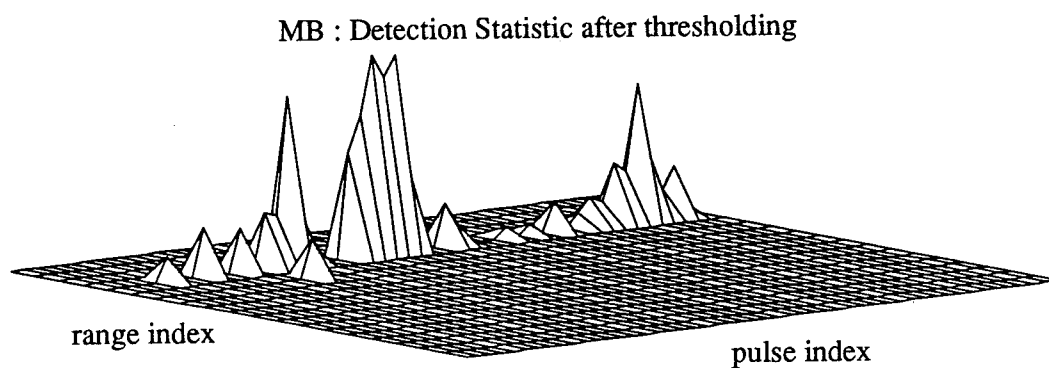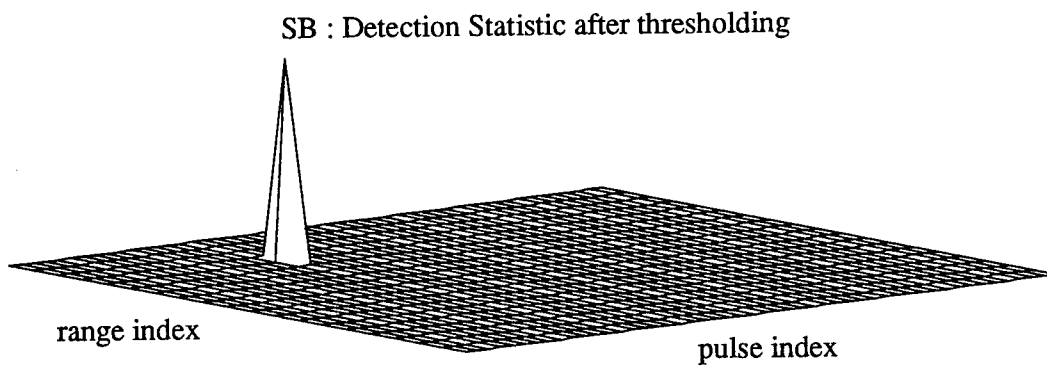
pulse index

Figure 15: Detection Statistic above thresholds $(P_{fa} = 10^{-5})$; target is detected only in one return for SB case, whereas target is detected in almost all returns for MB case.
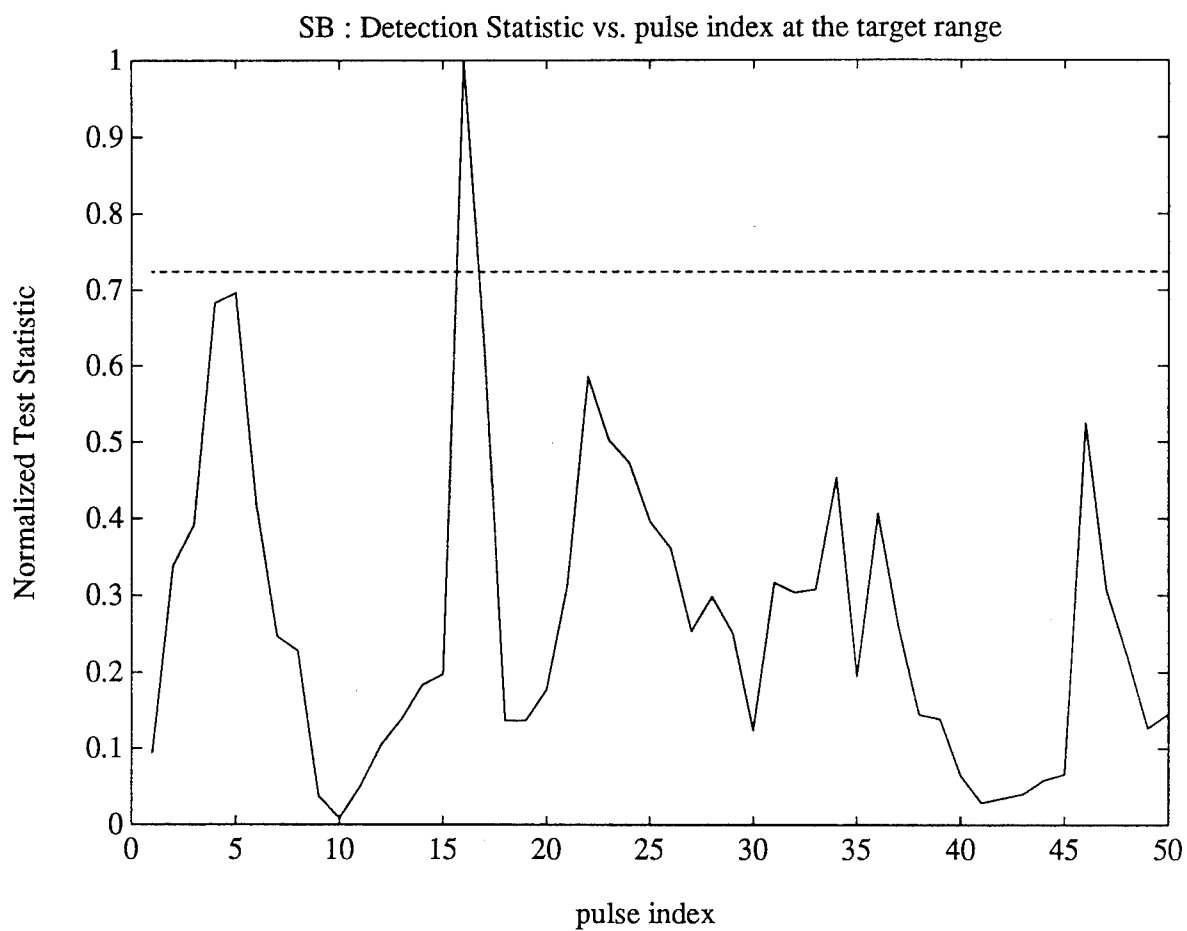
Figure 16: SB Test Statistic vs. pulse index with threshold ($P_{fa} = 10^{-5}$).

MB : Detection Statistic vs. pulse index at the target range
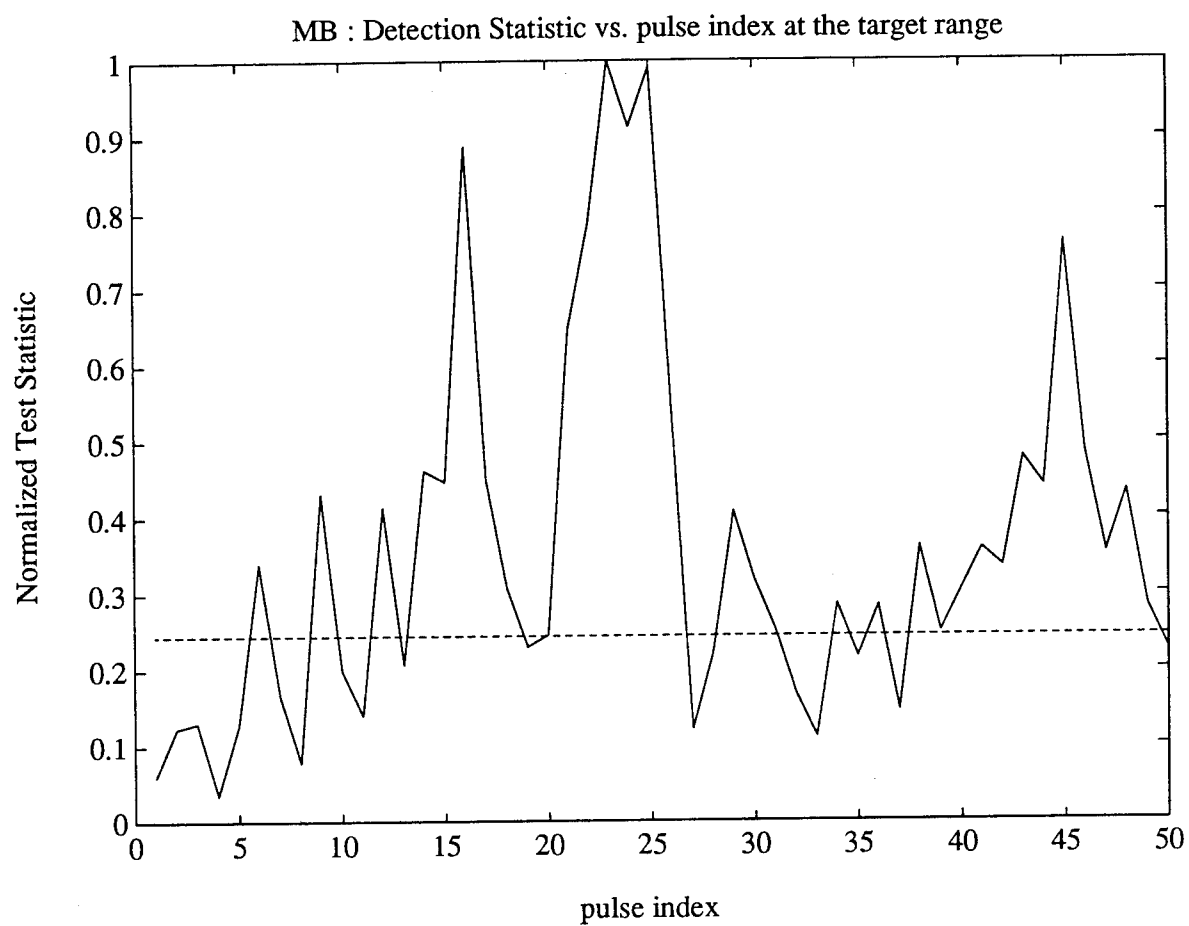
Figure 17: MB Test Statistic vs. pulse index with threshold ($P_{fa} = 10^{-5}$).
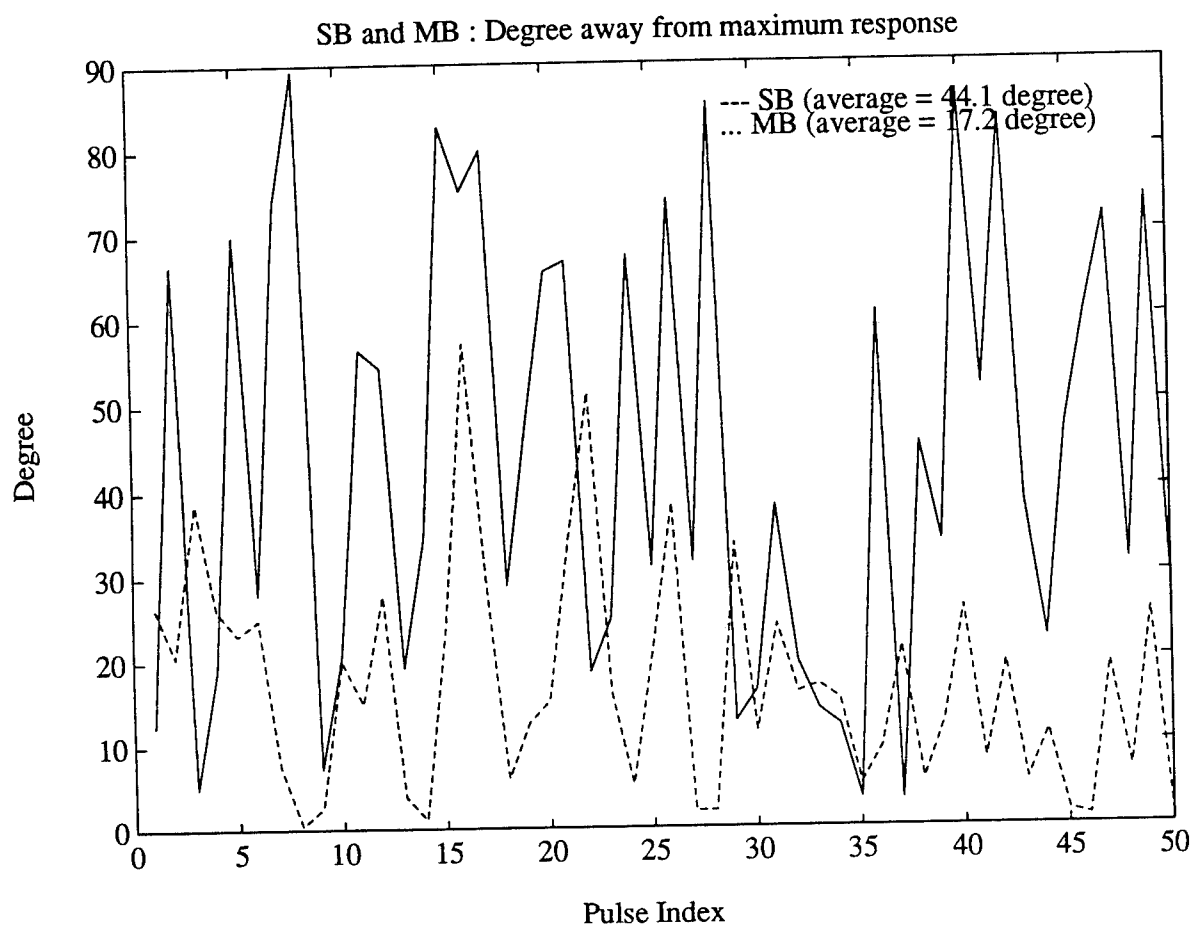
Figure 18: SB and MB : Target-clutter polarization angle difference away from the best one ; average = 44.1 degree for SB and 17.2 for MB.

2.2.3 Performance Demonstration Conclusion and Discussion

For the slowly/tangentially moving targets detection problem in active systems are solved using frequency diversity signaling as applied in the Adaptive Polarization Canceler demonstration presened in this section. It is shown to significantly outperform the conventional (no diversity) signaling under equal transmit energy constraints. The experiments showed that in cases where target and clutter polarization angle difference were similar, the SB processor severely attenuated the target along with the clutter. The AMBPC based detector, however, eliminates these signal cancellation and sensitivity problems since each frequency potentially yields different polarization states and different degree-of-polarizations for the same clutter. Neither the target is canceled in every subband of the MB processor, nor the very low degrr-of-polarization would have with a very high probability.

The results of this demonstration clearly reveal that the AMBPC based detector has the potential to almost completely eliminate the polarization angle-similarity problem (between target and clutter) associated with target detection via ASBPC based detector.

Advantages of frequency diversity in adaptive polarization processing are sufficient to justify an investigation of the adaptive Ultra Wide Band (UWB) polarization processing capabilities.

II.3 OPTIMUM UWB POLARIZATION PROCESSOR

3.1 Introduction

In order to improve the detection of targets in distributed clutter, one radar technique is to reduce the amount of signal energy backscattered by the clutter [38],[39],and [40]. This can be accomplished by reducing the range resolution cell of the radar using Ultra-Wideband (UWB) signaling [37] so that fewer scatterers are in the resolution cell of interest. UWB has been variously defined as one having a bandwidth 25 to 100% of the center frequency in the radiated spectrum. For any given frequency, this results in an unusually high resolution capability compared with most traditional radar approaches.

Due to the reduction of the range cell size, the familiar point-target modeling is no longer adequate to describe the received target return from the transmitted UWB waveform. In fact, the individual part of a target can be well resolved so that the multiple dominant scattering (MDS) centers of the target may appear in a number of well-separated range cells [41]. The effects of the clutter reduction and MDS target model on the system detection performance have been studied in [23],[44], where the detectability of the range-extended targets as a function of signal bandwidth has been considered based on single pulse processing. It has been shown that the performance improvement reaches maximum when the system utilizes the so-called critical bandwidth which just resolves the individual scatters. In the polarization processing, however, further increaing the signal bandwidth beyond the critical bandwidth will continuously offer the significant improvement of the detection performance even for single pulse processing. Polarization processing with UWB signaling for radar detection has unique advantage in addition to the existing UWB signaling advantages. That is, when UWB radar waveforms are used for increasing the down-range resolution, this can, in fact, provide the resolution between the scattering centers, and hence less ambiguous polarization state formed from its dominant scattering center. In fact, due to low radar resolution, many unresolved backscattering centers interact in generating the target return. Furthermore, the contributions of the backscattering centers, and particularly their relative phase, are quite sensitive to the target aspect. Consequently, during the observation time, polarization state descriptions of the target return are very unstable and ambiguous. For this reason, the UWB signaling excitation, and its polarization processing makes the exploitation

126

of the target information more profitable.

However, there are associated disadvantages as well, as evidenced by the preference to use the narrowest bandwidth consistent with need in order to minimize the processing burden. For example, increasing a bandwidth ten times has significant impact on the cost of system since, for a given surveillance volume, the number of resolution cells to be processed and the required processing for detection are both proportional to the bandwidth. In addition, the ten times increase in number of cells, for all else constant, implies about a ten times increase in the probability of false alarm or a small decrease in system sensitivity. For these reasons, UWB are used only when the increased percentage bandwidth presents a distinct advantage.

The limitations of UWB signaling in polarization processing have been studied in [43]. In the under-resolved and the over-resolved cases the polarization state of the target from the combined scatters, or of the individual scatterers is approximately well defined. However, in the almost resolved case applied by the critical bandwidth, the polarization state of the target within a range cell is not well defined. From this study, it can be concluded that for range extended targets complete polarization state descriptions can be precisely made only using monochromatic illumination (infinite radar range resolution length). The monochromatic restriction can be relaxed for the special case of a target with zero range extent. The quasi-monochromatic approximation will be valid only when the radar range resolution is significantly larger than the target range extent. Alternately, the approximation will be valid if the range resolution is significantly smaller than the range separation between individual scatterers and larger than the individual scatterer range extent. However, in the general case, precise and complete polarization scattering measurements cannot be made when the radar range resolution length approaches the range extent of the target or of the individual scatterers.

In addition to the limitation and disadvantages of UWB signalling in polarization processing, there needs to develop the mathematical representational technique for the UWB waveform data. People are familiar with the complex envelop representation for the return from NB signalling. The Relative Bandwidth (RBW) of the UWB system is large so that the complex envelop representation is not adequate. Also, a familiar-point target modeling for NB case is no longer adequate in UWB system. In this study, the waveform-based representational technique for the UWB data return is developed. This representation degenerates

to the conventional complex envelop representation under the assumption of small RBW and NB. For this reason we classify that as the most general representation for the large RBW signal.

A probabilistic target modeling for individual scattering centers is proposed, and shown to be consistent with the NB's point target modeling when all the MDS centers are added over the NB's resolution cell. The mathematical modeling of target, clutter and receiver noise plays a key role in the development of hypothesis testing algorithms. Following lists of assumptions are the frames for development of the UWB polarization waveform data modeling :

Assumption 1. The dominant scattering centers are well-separated in range, and the range resolution length must be large compared to its dominant scatterer's range extent.

Assumption 2. The target return from each dominant scattering center may be modeled over the observation interval as a deterministic vector with unknown parameters. The unknown amplitude may consist of the one-dominant scatterer and many small fluctuating scatterers, which correspond to one-dominant-plus Rayleigh amplitude fading.

Assumption 3. The UWB target modeling leads to the point-target modeling if we sum up all the scattering centers over the same range cell of NB system. *Assumption 4.* The UWB waveform returns from clutter part follow a zero mean Gaussian random process for h and v channel.

Assumption 5. Clutter enviornment over the observation range widow is homogeneous.

Assumption 6. The UWB receiver introduces zero-mean white Gaussian random process for receiver noise into each h and v channel. The receiver noise is independent from channel to channel.

The above assumptions are realistic and economical with regard to introduction of unknown parameters. These enable us to begin development of realizable processing algorithms. Furthermore, in order to make easy of deriving the optimum detection performance without loss of too much generality, following additional assumptions will be needed :

Assumption 7. The target amplitudes for individual dominant scattering centers are independent and identically distributed.

Assumption 8. The clutter and receiver noise in the particular observation range cell is assumed to be statistically independent of the clutter and receiver noise in every other

128

observation interval.

Assumption 9. The target scattering center locations are known a priori.

Assumption 10. The polarization states from the dominant scattering centers are assumed to be the same for all and known a priori.

The use of MB waveforms applied to various radar systems for improved target detection has been well-established [18],[19]. In Chapter 2, we demonstrated the advantages of frequency diversity signalling in a polarization canceler based radar system, which relies on the fact that by establishing a bank of adaptive polarizations for J subband frequency, the target return may be preserved in at least one of the diversity channels with high probability. Alternatively, the use of UWB signalling in polarization radar systems remains essentially unknown, it is _not_ well-established technique. In this chapter we will present the optimum UWB polarization processing to examine the state-of-the-art and the potential performance benefits and limitations of UWB technique, with particular emphasis on radar detection application. The extensive work was tasked with identifying and prioritizing optimum UWB polarization processing research to be persued and exploited. The aim of this chapter is to shed some light in the intriguing theories of optimum detection for UWB polarimetric features, and it will represent the fundamental basis for UWB signalling era in polarimetric radar signal processing.

In practice, the UWB signaling scheme can be implimented using many different approaches, asch as FM pulse modulation, phase coding, or impulsive excitation. Of these, impulse excitation requires special system performance because the wide bandwidth is instantaneous, and has in the past been the subject of some controversy due to postulated transient effects. The UWB signal we interested in this study is a linear FM type. Fig. 19 shows the UWB waveform and its spectrum with 50% RBW. In most situations, the entire target is covered by the radar beam. Consequently, only the range dimension of the resolution cell can be made smaller than the target size.

The ensuing material in this Chaper is organized as follows : Section 1 affords the waveform-based UWB polarimetric data modeling for large RBW, small RBW and NB cases, Section 2 considers their optimum processings and corresponding analytical detection performances when just one pulse is transmitted towards the target.
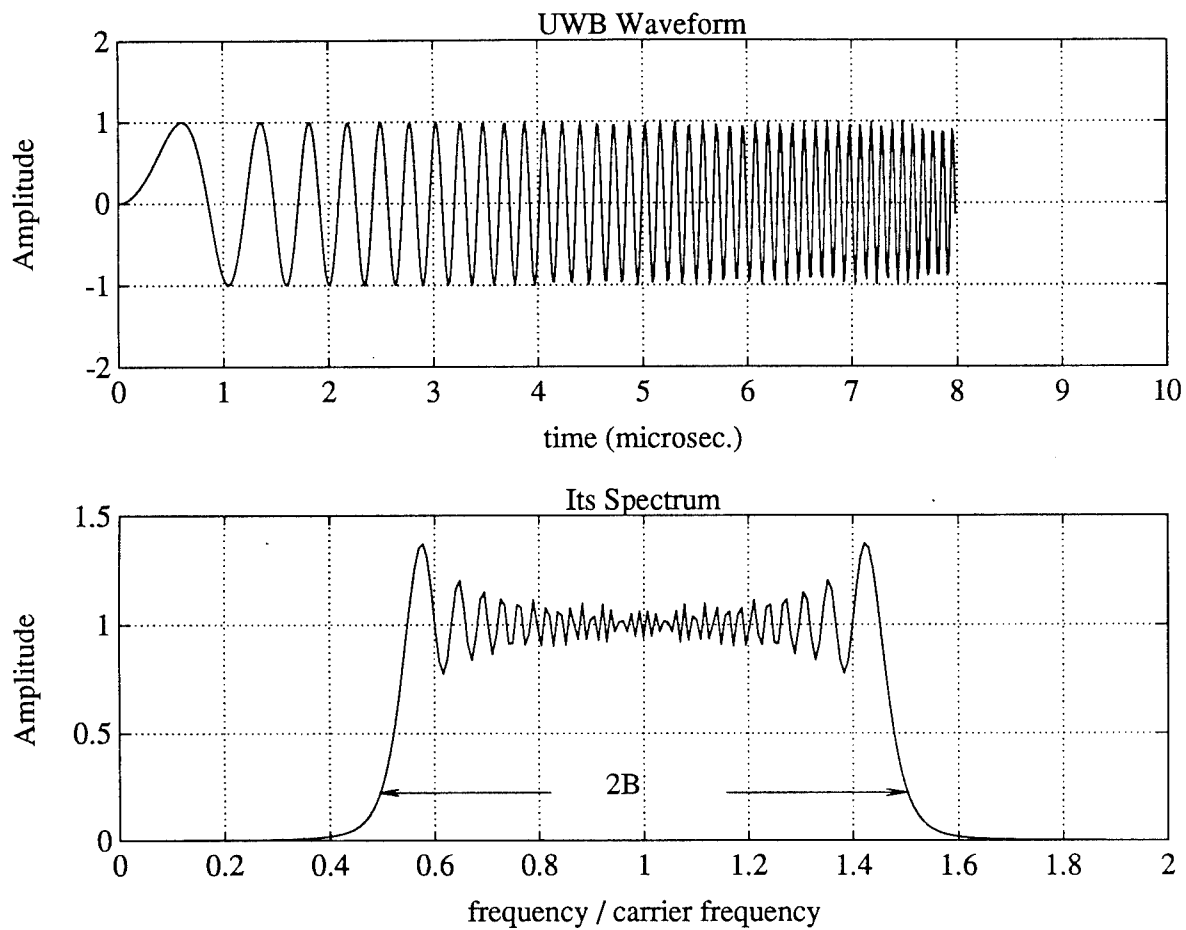
Figure 19: UWB Waveform and its Spectrum

3.2 UWB Data Modeling

3.2.1 Waveform-Based UWB Data Model

It is natural to assume that the relative bandwidth (RBW) of the UWB system is large (larger than 10%). In the case when the test cell size in range is significantly reduced, a target return from each resolution cell is contributed by the reduced number of closely spaced backscattering centers. Neither the conventional complex envelop representation, nor the familiar point-target modeling used in MB signalling case is adequate to describe the UWB waveform return. Therefore, the original real waveform representation of UWB signals will be used.

Let $\mathbf{u}(t)$, size 2×1, be the waveform vector received by an UWB radar system at the front end of its dual-polarized receiver. It consists of the returns from the target, clutter as well as the internal receiver noise,

$$H_1 : \mathbf{u}(t) = \mathbf{u}_s(t) + \mathbf{u}_c(t) + \mathbf{u}_w(t) \quad 0 < t < T_0 \tag{3-1}$$

$$H_0 : \mathbf{u}(t) = \mathbf{u}_c(t) + \mathbf{u}_w(t) \qquad 0 < t < T_0 \tag{3-2}$$

where T_0 is the total observation time. The dual-polarized receiver from a single polarized transmitter obtains the measurement from the Multiple Dominant Scatterers (MDS) which can be expressed in matrix form as

$$\begin{aligned}
\mathbf{U}(t) &= \begin{bmatrix} \mathbf{u}_1(t) & \mathbf{u}_2(t) & \cdots & \mathbf{u}_m(t) & \cdots & \mathbf{u}_M(t) \end{bmatrix} \\
&= \begin{bmatrix} u_{h1}(t) & u_{h2}(t) & \cdots & u_{hm}(t) & \cdots & u_{hM}(t) \\ u_{v1}(t) & u_{v2}(t) & \cdots & u_{vm}(t) & \cdots & u_{vM}(t) \end{bmatrix}
\end{aligned} \tag{3-3}$$

where two subscripts in last equation refer to the receiver polarization state and dominant scatterer index, $m = 1, 2, \cdots, M$, respectively. It indicates that the $2M$ waveform data are available to process.

The mth dominant scatterer waveform data $\mathbf{u}_m(t)$, 2×1, can be expressed in terms of received waveform $\mathbf{u}(t)$, i.e.,

$$\mathbf{u}_m(t) = \mathbf{u}(t + (m-1)T_M); \quad 0 < t < T_M \tag{3-4}$$

where T_M is the observation interval for a single dominant scatterer. Here it is assumed that the dominant scatterers are well separated in range, and the range resolution length must be large compared to its dominant scatterer range extent.

131

The target, clutter and receiver noise components contained in the received data will be modeled as follows.

Target Modeling

Let $f(t)$, $0 < t < T$, be the transmitted UWB waveform with an energy being unity. Since the signal transmitted at the moment t' will be received at moment t, the relation between target portion of received waveform $\mathbf{u}_{sm}(t)$ and transmitted signal $f(t')$ is given by

$$\mathbf{u}_{sm}(t) = \begin{bmatrix} b_{shm} \\ b_{svm} \end{bmatrix} \cdot f_m(t') = \mathbf{b}_{sm} \cdot f_{rm}(t') \qquad (3-5)$$

where $f_m(t')$ is a time delayed replica of transmitted waveform, with τ_m being the round-trip delay time for m^{th} scattering center and c being the propagation velocity,

$$t' = t - \tau_m = t - \frac{2 \cdot \lambda_{0m}}{c} \; ; \quad m = 1, 2, \cdots, M \qquad (3-6)$$

The attenuation factors for both h and v channel, b_{shm} and b_{svm}, represent the target backscatter, progagation loses, antenna responses, and the radar cross section of the mth dominant scattering center. The attenuation vector may be expressed with an unit normalized polarization state vector $\mathbf{p}_{sm}$ which is deterministic

$$\begin{bmatrix} b_{shm} \\ b_{svm} \end{bmatrix} = \alpha_m \begin{bmatrix} p_{shm} \\ p_{svm} \end{bmatrix} = \alpha_m \mathbf{P}_{sm} \qquad (3-7)$$

A probabilistic target model is employed such that the magnitude, $a = \alpha_m$ for all m, is assumed to be a random variable which is the resultant sum of all the scatterers within a range cell assumed to consist of the one-dominant scatterer and many small fluctuating scatterers, and its probability density function is given by

$$f_a(a) = \frac{9a^3}{2a_o^4} \cdot e^{(-3a^2/2a_o^2)}, \quad a \geq 0 \qquad (3-8)$$

where a_o is the most probable value of a. Since e_t represent the energy in transmitted signal $f(t)$; then the actual input energy is given by $a^2 e_t$. The definition of a becomes unique if reference scatterer energy e_t is normalized such that $2 \cdot e_t/N_0 = 1$, where $\mathbf{N}_0$ is the noise power spectral density level. The input signal-to-noise ratio (SNR_{in}) is related to signal amplitude a by

$$SNR_{in} = \frac{a^2 \cdot e_t}{N_0/2} = a^2 \qquad (3-9)$$

132

With the probability density of a given by Eq.(3-8), constant a_o can be related to the average SNR_{in} by averaging Eq.(3-9) with respect to a,

$$
\begin{aligned}
\overline{a^2} &= \int_0^\infty a^2 f_a(a) da \\
&= \int_0^\infty (\frac{9a^5}{2a_o^4}) \cdot e^{(-3a^2/2a_o^2)} da \\
&= \frac{4}{3}a_o^2 \qquad\qquad (3\text{-}10)
\end{aligned}
$$

Fig.(20) shows the target probability density function with different SNR_{in} values. We further assume that the random variables a are independent and identically distributed each other for all m. This target modeling for the high resolution radar has been used by many researchers and proven to be valid.

The mth scattering target waveform, therefore, can be written as

$$
\mathbf{u}_{sm}(t) = \alpha_m f_m(t - \tau_m)\mathbf{p}_{sm} = \alpha_m \mathbf{p}_{sm}(t - \tau_m) \qquad\qquad (3-11)
$$

The target portion of received waveform, finally, given by

$$
\mathbf{u}_s(t) = \mathbf{P}_s(t)\mathbf{a} \qquad\qquad (3-12)
$$

where

$$
\mathbf{P}_s(t) = [\mathbf{p}_{s1}(t - \tau_1), \cdots, \mathbf{p}_{sm}(t - \tau_m), \cdots, \mathbf{p}_{sM}(t - \tau_M)]; \quad (2 \times M) \qquad\qquad (3-13)
$$

and

$$
\mathbf{a} = \begin{bmatrix} \alpha_1 \\ \vdots \\ \alpha_m \\ \vdots \\ \alpha_M \end{bmatrix}; \quad (M \times 1) \qquad\qquad (3-14)
$$
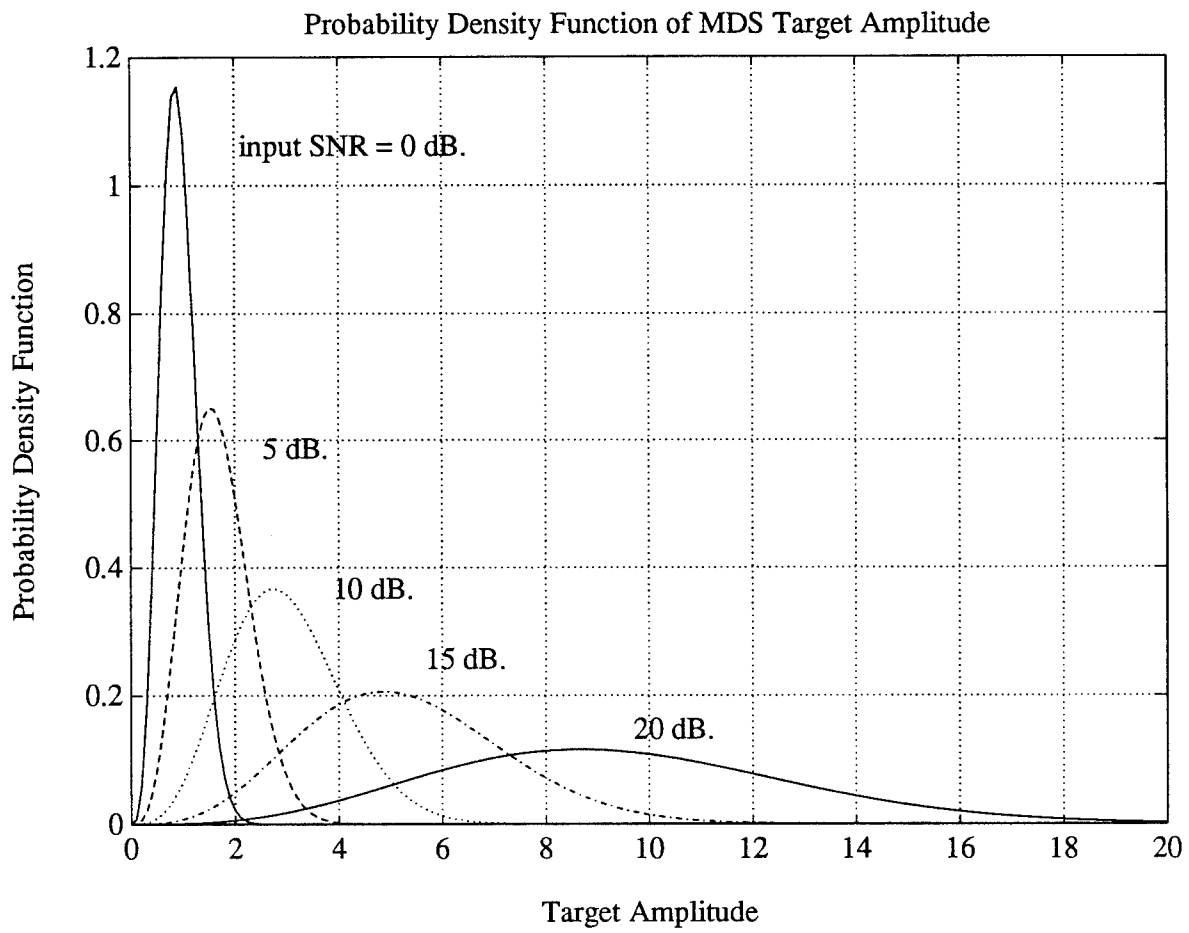
Figure 20: Probability Density Function of Target Amplitude

Clutter and Receiver Noise Modeling

The colored noise vector due to clutter is obtained by convolving (with respect to range) the transmit UWB signal $f(t)$ with the range-doppler variant scattering vector of the clutter process $\mathbf{b}_c(t - \lambda/2, \lambda)$, where

$$\mathbf{b}_c(t - \lambda/2, \lambda) = \left[\begin{array}{c} b_{ch}(t - \lambda/2, \lambda) \\ b_{cv}(t - \lambda/2, \lambda) \end{array} \right] \qquad (3-15)$$

The each elements of scattering matrix of the clutter is modeled as zero-mean Gaussian random process. The colored noise vector becomes

$$\mathbf{u}_c(t) = \sqrt{e_t} \int_{-\infty}^{\infty} \mathbf{b}_c(t - \lambda/2, \lambda) f(t - \lambda) \, d\lambda \qquad (3-16)$$

where t is time, λ is radar range expressed in units of time, and $\sqrt{e_t}$ is the energy of the transmitted signal. This expression represents the colored noise vector due to the clutter.

The clutter covariance functional matrix is defined as a 2×2 real symmetric matrix,

$$\mathbf{K}_c(t, z) = E\{\mathbf{u}_c(t)\mathbf{u}_c^T(z)\} \qquad (3-17)$$

Substituting $\mathbf{u}_c(t)$ into Eq.(3-17) and bringing the expectation operation into the integral, the clutter covariance matrix becomes

$$\mathbf{K}_c(t, z) = e_t \int_{-\infty}^{\infty} \int_{-\infty}^{\infty} E\{\mathbf{b}_c(t - \lambda/2, \lambda) f(t - \lambda)$$
$$[\mathbf{b}_c(z - \lambda_1/2, \lambda_1) f(z - \lambda_1)]^T\} d\lambda d\lambda_1 \qquad (3-18)$$

With some matrix rearrangement, Eq.(3-18) becomes

$$\mathbf{K}_c(t, z) = e_t \int_{-\infty}^{\infty} \int_{-\infty}^{\infty} f(t - \lambda) \cdot E\{\mathbf{b}_c(t - \lambda/2, \lambda) \mathbf{b}_c^T(z - \lambda_1/2, \lambda_1)\} \cdot$$
$$f(z - \lambda_1) d\lambda d\lambda_1 \qquad (3-19)$$

Assuming the returns from different range intervals are statistically independent and that the return from each interval is a sample vector function of a stationary zero-mean Gaussian random process, then the expectation term in Eq.(3-19) turns out

$$E\{\mathbf{b}_c(t - \lambda/2, \lambda) \mathbf{b}_c^T(z - \lambda_1/2, \lambda_1)\} = \mathbf{K}_{DR}(t - z, \lambda) \cdot \delta(\lambda - \lambda_1) \qquad (3-20)$$

135

where

$$\mathbf{K}_{DR}(t-z,\lambda) = E\left\{ \begin{bmatrix} [b_{ch}(t-\lambda/2,\lambda)b_{ch}(z-\lambda_1/2,\lambda_1)] & [b_{cv}(t-\lambda/2,\lambda)b_{ch}(z-\lambda_1/2,\lambda_1)] \\ [b_{ch}(t-\lambda/2,\lambda)b_{cv}(z-\lambda_1/2,\lambda_1)] & [b_{cv}(t-\lambda/2,\lambda)b_{cv}(z-\lambda_1/2,\lambda_1)] \end{bmatrix} \right\}$$

$$(3-21)$$

The subscript 'DR' denotes that the clutter is doubly spread in both doppler and range, and $\mathbf{K}_{DR}(t-z,\lambda)$ is known as *tensor correlation matrix* [ ]. Taking the expectation inside the matrices Eq.(3-21) becomes

$$\mathbf{K}_{DR}(t-z,\lambda) = \begin{bmatrix} [k_{h,h}(t-z,\lambda)] & [k_{v,h}(t-z,\lambda)] \\ [k_{h,v}(t-z,\lambda)] & [k_{v,v}(t-z,\lambda)] \end{bmatrix} \qquad (3-22)$$

Eq.(3-22) provides 4 different elements (discriminants) when one considers the statistical behavior of the polarization random process scattering matrix. Since the scattering matrix is a non-negative real process, then the number of independent elements reduces to 3, still providing a selection of discriminants.

After substituting Eq.(3-16) into Eq.(3-15) and carrying an integration with respect to λ_1, the clutter potion of the waveform covariance matrix finally becomes

$$\mathbf{K}_c(t,z) = e_t \int_{-\infty}^{\infty} f(t-\lambda)\mathbf{K}_{DR}(t-z,\lambda)f(z-\lambda)d\lambda \qquad (3-23)$$

It is also assumed that each element in $\mathbf{K}_c(t,z)$ is square-integrable and that the receiver noise and clutter components are independent. Then the total waveform covariance matrix of the receiver noise and clutter is given by

$$\mathbf{K}_n(t,z) = \frac{\mathbf{N_0}}{2}\mathbf{I}\,\delta(t-z) + \mathbf{K}_c(t,z) \qquad (3-24)$$

where $\mathbf{I}$ is an 2×2 identity matrix.

For the clutter part, the waveform covariance matrix $\mathbf{K}_c(t,\tau)$ can be approximated by [ ]

$$\mathbf{K}_c(t,\tau) = \frac{1}{2B}\mathbf{R}_c \cdot \delta(t-\tau) \qquad (3-25)$$

where $\mathbf{R}_c$, size 2×2, is the clutter covariance matrix. Therefore, the total covariance matrix of the clutter and receiver noise is given by

$$\mathbf{K}_c(t,\tau) = (\frac{1}{2B}\mathbf{R}_c + \frac{N_0}{2}\mathbf{I}) \cdot \delta(t-\tau) = \mathbf{R} \cdot \delta(t-\tau) \qquad (3-26)$$

where $\mathbf{R}$ is the total noise covariance matrix.

136

The waveform representation technique of UWB data given in this section provides most general in the sense that it is suitable for all types of waveforms. The target modeling is extended to two special cases : (1) The waveform that has very large bandwidth, but its RBW is less than 10%. (2) The narrowband waveform.

3.2.2 Special Case : Small Relative Bandwidth

The carrier frequency f_0 is verry high compared to the bandwidth of UWB system. As the relative bandwidth $RBW=B/f_0$ is less than 10%, the conventional orthogonal receiver using inphase and quadrature channels can be formed to reduce the effect of phase fluctuation. The complex envelop representation method for expressing the received target return will be utilized here. Let the transmitted UWB signal be

$$f(t) = c(t)e^{i2\pi f_0 t + i\theta(t)} \tag{3-27}$$

where $c(t)$ and $\theta(t)$ are the amplitude and phase modulation of the waveform. Applying it into Eq.(3-5) yields

$$
\begin{aligned}
\mathbf{u}_{sm}(t) &= \mathbf{b}_{sm}c(t - \tau_m) \, e^{i2\pi f_0 t - i2\pi f_0 \tau_m + i\theta(t-\tau_m)} \\
&= \mathbf{b}_{sm}\tilde{c}(t - \tau_m) \, e^{i2\pi f_0 t - i2\pi f_0 \tau_m}
\end{aligned}
\tag{3-28}
$$

where $\tilde{c}(t - \tau_m) = c(t - \tau_m)e^{\theta(t-\tau_m)}$. Obviously, the high frequency term can be removed by passband-to-baseband conversion. Thus after the passband-to-baseband and orthogonal preprocessing, the target complex envelop vector becomes

$$\tilde{\mathbf{u}}_{sm}(t) = \tilde{\mathbf{b}}_{sm}\tilde{c}(t - \tau_m). \tag{3-29}$$

Using Eq.(3-7) and Eq.(3-11) we get

$$\tilde{\mathbf{u}}_{sm}(t) = \tilde{\alpha}_m \tilde{c}(t - \tau_m)\tilde{\mathbf{p}}_{sm} = \tilde{\alpha}\tilde{\mathbf{p}}_{sm}(t - \tau_m) \tag{3-30}$$

where $\tilde{\alpha}_m$ is the complex random variable and its probability density function of an amplitude $a = |\tilde{\alpha}_m|$ is defined in Eq.(3-8).

Therefore, the target portion of received waveform for small RBW is given by

$$\tilde{\mathbf{u}}_s(t) = \tilde{\mathbf{P}}_s(t)\tilde{\mathbf{a}} \tag{3-31}$$

137

where

$$\tilde{\mathbf{P}}_s(t) = [\tilde{\mathbf{p}}_{s1}(t - \tau_1), \cdots, \tilde{\mathbf{p}}_{sm}(t - \tau_m), \cdots, \tilde{\mathbf{p}}_{sM}(t - \tau_M)]; \quad (2 \times M) \tag{3-32}$$

and

$$\tilde{\mathbf{a}} = \begin{bmatrix} \tilde{\alpha}_1 \\ \vdots \\ \tilde{\alpha}_m \\ \vdots \\ \tilde{\alpha}_M \end{bmatrix}; \quad (M \times 1) \tag{3-33}$$

3.2.3 Consistence of UWB and Narrow Band Models

The individual scattering radar return by UWB signalling has been modeled as one dominant plus Rayleigh fluctuating for each dominant scatterer amplitude distribution, and it is assumed that the dominant scatterers are independent each other. The low range radar return by NB signalling, however, has been modeled as Rayleigh fluctuating target. Following shows the consistency of two target models between the UWB and the NB system. A sufficient consistency can be checked by sum of all reflections within a NB range cell.

For the NB case, the target returns are actually composed of many scattering centers, so the total received target waveform is

$$\begin{aligned}
\tilde{\mathbf{u}}_s(t) &= \sum_m \tilde{\mathbf{u}}_{sm}(t) \\
&= \sum_m \tilde{\alpha}_m \tilde{c}(t - \tau_m) \tilde{\mathbf{p}}_{sm} \\
&\approx \tilde{\alpha}_0 \tilde{c}(t - \tau_0) \tilde{\mathbf{p}}_s
\end{aligned} \tag{3-34}$$

where $\tilde{\alpha}_0 = \sum_m \tilde{\alpha}_m$, $\tau_0 = \sum_m \tau_m / M$, and $\tilde{\mathbf{p}}_s = \sum_m \tilde{\mathbf{p}}_{sm} / M$. The central limit therom argument is applied to obtain the last equality in above equation. Then, $\tilde{\alpha}_0$ is a complex Gaussian random variable, which we originally used for target modeling of NB system. It turns out the UWB target modeling leads to the point target modeling if we sum up all the scattering centers over the same range cell determined in NB system.

138

3.3 Optimum Processors and their Detection Performance

3.3.1 Optimum UWB Polarization Based detector

Assume that the received data $\mathbf{u}(t)$, 2×1, has a waveform covariance matrix given as follows

$$\mathbf{K}(t, \tau) = \mathbf{R}\kappa(t, \tau) \qquad (3-35)$$

The input UWB waveform return process $\mathbf{u}(t)$ can be expended in scalar eign functions and vector coefficients system :

$$\mathbf{u}(t) = \sum_{k=1}^{\infty} \mathbf{u}_k \phi_k(t) \qquad (3-36)$$

where

$$\mathbf{u}_k = \int_0^{T_0} \mathbf{u}(t)\phi_k(t)dt \qquad (3-37)$$

Observe that the $\phi_k(t)$, k=1,2,$\cdots$, are the scalar eign functions and $\mathbf{u}_k$, k=1,2,$\cdots$, are the vector coefficients.

Under H_0, we would like to find a set of λ_k and ϕ_k such that

$$E(\mathbf{u}_k) = 0; \quad k = 1, 2, \cdots \qquad (3-38)$$

$$E(\mathbf{u}_k \mathbf{u}_i^H) = \mathbf{R}\lambda_k \delta_{ki} \qquad (3-39)$$

and

$$\int_0^{T_0} \phi_k(t)\phi_i(t)dt = \delta_{ki} \qquad (3-40)$$

These requirments need to satisfy the equation of

$$\mathbf{R}\lambda_k \phi_k(t) = \int_0^{T_0} \mathbf{K}(t, \tau)\phi_k d\tau \qquad (3-41)$$

where λ_k are the eignvalues of $\kappa(t, \tau)$ corresponding to the eigenfunction $\phi_k(t)$, and δ_{ki} has a non-zero value equal to 1 only if k=i.

Under the assumption that $\mathbf{u}(t)$ is a bivariate Gaussian process, $\mathbf{u}_k, k = 1, 2, \cdot$, are also bivariate Gaussian vectors independent each other based on Eq.(3-39). With constant d_0 independent of $\mathbf{u}_k$ the joint distribution of the first K vectors can be expressed as

$$f(\mathbf{u}_k, k = 1, 2, \cdots, K \mid H_0) = d_0 exp(-\frac{1}{2}\sum_{k=1}^{K} \frac{\mathbf{u}_k^H \mathbf{R}^{-1} \mathbf{u}_k}{\lambda_k}) \qquad (3-42)$$

Substitute Eq.(3-37) into the above equation yields

$$f(\mathbf{u}_k, k = 1, 2, \cdots, K \mid H_0) = d_0 exp(-\frac{1}{2} \int \int \frac{\mathbf{u}^H(t)\phi_k^*(t)\phi_k(\tau)\mathbf{R}^{-1}\mathbf{u}(\tau)}{\lambda_k} dt d\tau) \qquad (3-43)$$

As $k \to \infty$, define

$$q(t, \tau) = \sum_{k=1}^{\infty} \frac{\phi_k^*(t)\phi_k(\tau)}{\lambda_k} \qquad (3-44)$$

which is referred to as the inverse kernel of $\kappa(t, \tau)$. It is well known that $\kappa(t, \tau)$ and $q(t, \tau)$ has the following relation

$$\int \kappa(t, u)q(u, \tau)du = \delta(t - \tau) \qquad (3-45)$$

Therefore, the likelihood function with K approaches infinity under H_0 hypothesis becomes

$$f(\mathbf{u}(t) \mid H_0) = d_0 exp(-\frac{1}{2} \int \int \mathbf{u}^H(t)\mathbf{R}^{-1}q(t, \tau)\mathbf{u}(\tau)dt d\tau) \qquad (3-46)$$

In the case when $q(t, \tau) = \delta(t - \tau)$ which we specified in Eq.(3-22), we have

$$f(\mathbf{u}(t) \mid H_0) = d_0 exp(-\frac{1}{2} \int \mathbf{u}^H(t)\mathbf{R}^{-1}\mathbf{u}(t)dt) \qquad (3-47)$$

Under H_1, the likelihood function can be written similar way

$$f(\mathbf{u}(t) \mid H_1) = d_0 \cdot exp\{-\frac{1}{2} \int [\mathbf{u}(t) - \mathbf{u}_s(t)]^H \mathbf{R}^{-1}[\mathbf{u}(t) - \mathbf{u}_s(t)]dt\} \qquad (3-48)$$

The MDS target modeling which we developed in in waveform-based UWB modeling section presents the returns from all the scattering centers

$$\mathbf{u}_s(t) = \sum_{m=1}^{M} \alpha_m \mathbf{p}_{sm}(t - \tau_m) = \mathbf{P}_s(t) \cdot \mathbf{a} \qquad (3-49)$$

where τ_m is arrival time of mth scatterer, and $\mathbf{P}_s(t)$ and $\mathbf{a}$ are specified by Eq.(3-13) and Eq.(3-14), respectively. The exponent part of Eq.(3-48) after substituting Eq.(3-49) becomes

$$-\frac{1}{2} \int [\mathbf{u}(t) - \mathbf{u}_s(t)]^H \mathbf{R}^{-1}[\mathbf{u}(t) - \mathbf{u}_s(t)]dt \qquad (3-50)$$

$$= -\frac{1}{2}\{\int \mathbf{u}^H(t)\mathbf{R}^{-1}\mathbf{u}(t)dt - \int \mathbf{u}^H(t)\mathbf{R}^{-1}\mathbf{a}dt \qquad (3-51)$$

$$-\int \mathbf{a}^H \mathbf{P}_s^H(t)\mathbf{R}^{-1}\mathbf{u}(t)dt + \int \mathbf{a}^H \mathbf{P}_s^H(t)\mathbf{R}^{-1}\mathbf{P}_s(t)\mathbf{a}dt\} \qquad (3-52)$$

Let us define

$$\mathbf{G} = \int \mathbf{P}_s^H(t)\mathbf{R}^{-1}\mathbf{P}_s(t); \quad (M \times M) \qquad (3-53)$$

$$\mathbf{u} = \int \mathbf{P}_s^H(t)\mathbf{R}^{-1}\mathbf{u}(t)dt; \quad (M \times 1) \qquad (3-54)$$

Then Eq.(3-52) becomes

$$-\tfrac{1}{2}\{\int \mathbf{u}^H(t)\mathbf{R}^{-1}\mathbf{u}(t)dt - \mathbf{u}^H\mathbf{a} - \mathbf{a}^H\mathbf{u} + \mathbf{a}^H\mathbf{G}\mathbf{a}\}$$

$$= -\tfrac{1}{2}\{\int \mathbf{u}^H(t)\mathbf{R}^{-1}\mathbf{u}(t)dt + [\mathbf{a} - \mathbf{G}^{-1}\mathbf{u}]^H\mathbf{G}[\mathbf{a} - \mathbf{G}^{-1}\mathbf{u}] + \mathbf{u}^H\mathbf{G}^{-1}\mathbf{u}\} \qquad (3\text{-}55)$$

The uniformly most powerful test approach with respect to amplitude $\mathbf{a}$ to find the likelihood test is formulated, which implies that the random variable $\mathbf{a}$ to think of it as the constant ampplitude. It can be shown that the amplitude distribution statistics does not alter the likelihood ratio test.

As we are assuming the amplitude of the scatterers are unknown, the likelihood ratio test is formulated as following

$$\eta = \max_{\mathbf{a}}\{\frac{f(\mathbf{u}(t) \mid H_1)}{f(\mathbf{u}(t) \mid H_0)}\} \underset{H_0}{\overset{H_1}{\gtrless}} \eta_o \qquad (3-56)$$

Note that when $\mathbf{a} = \mathbf{G}^{-1}\mathbf{u}$, the maximum to $f(\mathbf{u}(t) \mid H_1)$ can be achieved, then

$$\eta = \exp\{\mathbf{u}^H\mathbf{G}^{-1}\mathbf{u}\} \underset{H_0}{\overset{H_1}{\gtrless}} \eta_o \qquad (3-57)$$

Since $\exp(\cdot)$ is a monitonically increasing function, the equivalent test becomes

$$\ell = \{\mathbf{u}^H\mathbf{G}^{-1}\mathbf{u}\} \underset{H_0}{\overset{H_1}{\gtrless}} \ell_o \qquad (3-58)$$

The optimum UWB dual-polarized channel receiver is designed for detecting a target in clutter as well as white noise. The optimum receiver follows the threshold comparison test accordingly with Eq.(3-58) where $\mathbf{G}$ and $\mathbf{u}$ satisfy the Eq.(3-53) and Eq.(3-54),respectively. A block diagram of the optimum UWB polarization processor is presented in Fig. 21
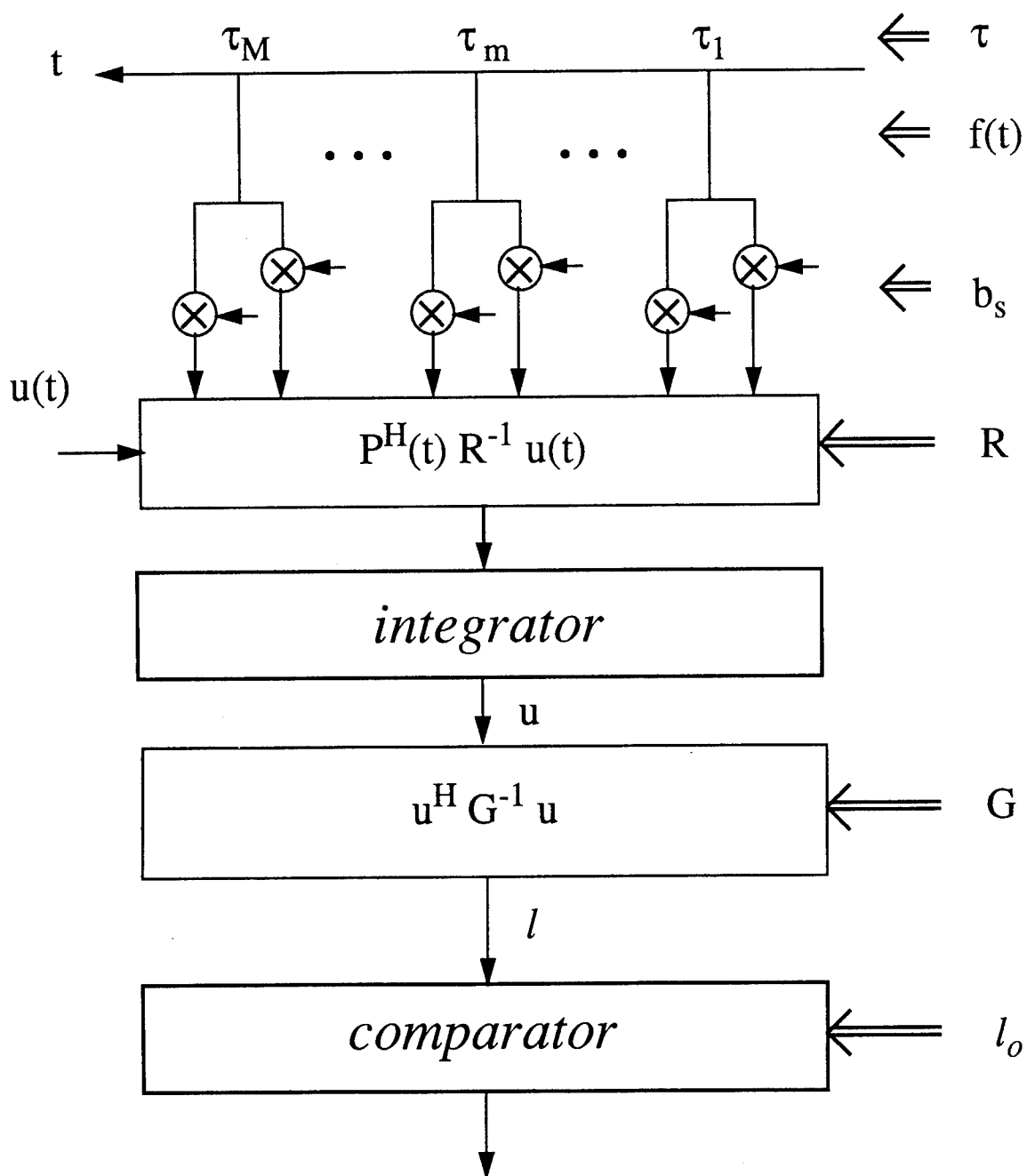
Figure 21: A block diagram of the optimum UWB polarization processing.

Under additional assumptions listed in introduction of UWB processing (Assumption 7 to 10), the derivations of detection and false alarm probabilities for the optimum UWB polarization processing are following : The test statistic ℓ under H_0 hypothesis will have a *Chi-Square* distribution since the random variable of decision statistics still preserve the Gaussionality as they are the linear combination of the input data vectors. with its probability of density function being

$$f_\ell(\ell \mid H_0) = \frac{1}{(M/2-1)!} \cdot \ell^{(M/2-1)} \cdot e^{-\ell}. \qquad (3-59)$$

The probalility of false alarm is thus

$$
\begin{aligned}
P_{fa} &= \int_{\ell_o}^{\infty} f_\ell(\ell \mid H_0) \, d\ell \\
&= e^{-\ell_o} \cdot \sum_{m=1}^{M/2-1} \frac{\ell_o^{M/2-m}}{(M/2-m)!}
\end{aligned}
\qquad (3\text{-}60)
$$

Probability density $f_\ell(\ell \mid H_1)$ is obtained by the method of characteristic functions. For this purpose $f_\ell(\ell \mid H_1)$ can be writtern as

$$f_\ell(\ell \mid H_1) = f_\ell(\ell \mid \bar{\mathbf{a}}, H_1) \qquad (3-61)$$

where $\mathbf{a}$ represents the random amplitudes $\{a_1, a_2, \cdots, a_M\}$ of each scattering centers. Characteristic function $C_\ell(s)_\mathbf{a}$ of sum random variable $\ell = \sum_{m=1}^{M/2} u_m^2$ is related to the characteristic functions of random variables u_m^2, $m = 1, 2, \cdots, M/2$, by

$$C_\ell(s)_\mathbf{a} = \prod_{m=1}^{M/2} C_{u_m^2}(s)_m \qquad (3-62)$$

Since $C_{u_m^2}(s)_m$ is the same for all m, Eq.(3-62) becomes

$$C_\ell(s)_\mathbf{a} = [C_{u_m^2}(s)_m]^{M/2} \qquad (3-63)$$

An expression for $C_{u_m^2}(s)_m$ is obtained from [5], with $M=2$ and $a = a_m$:

$$C_{u_m^2}(s)_m = \frac{(1+s)}{(1+\Delta/4)^2(\frac{1}{(1+\Delta/4)} + s)^2} \qquad (3-64)$$

Substituting Eq.(3-64) into Eq.(3-63) results in

$$C_\ell(s)_\mathbf{a} = \frac{(1+s)^{M/2}}{(1+\Delta/4)^M(\frac{1}{(1+\Delta/4)} + s)^M} \qquad (3-65)$$

143

The inverse Fourier transform of Eq.(3-65) is obtained from transform pair. This yields the following expression for $f_{ell}(\ell \mid H_1)$:

$$f_\ell(\ell \mid H_1) = \frac{\ell^{(M/2)-1} \cdot e^{-\ell/(1+\Delta/4)}}{(1+\Delta/4)^M((M/2)-1)!} \; {}_1F_1(-M/2, M/2; \frac{-\Delta/4\ell}{1+\Delta/4} \qquad (3-66)$$

where the confluent hypergeometric function ${}_1F_1(-M/2, M/2; c)$ is given by [5]

$$_1F_1(-M/2, M/2; c) = \sum_{m=0}^{M/2} \frac{(-1)^m[(M/2)!/(M/2-m)!]}{[(M/2+m-1)!/((M/2)-1)!]} \cdot \frac{c^m}{m!} \qquad (3-67)$$

Substituting Eq.(3-67) into Eq.(3-66), the probability density function of ℓ under H_1 turns into a density function specified by

$$f_\ell(\ell \mid H_1) = \frac{\ell^{(M/2)-1} \cdot e^{-\ell/(1+\Delta/4)} \cdot (M/2)!}{(1+\Delta/4)^M} \cdot \sum_{m=1}^{(M/2)} (\frac{\Delta/4}{1+\Delta/4})^m \cdot \frac{\ell^m}{m!((M/2)-m-1)!((M/2)-m)!} \qquad (3-68)$$

with Δ being the average signal-to-clutter-plus-noise ratio of the optimum receiver output, that is

$$\Delta = SNR_{in} \cdot \mathbf{p}_s^H \mathbf{R}^{-1} \mathbf{p}_s \qquad (3-69)$$

where SNR_{in} is the average input SNR defined in Eq.(3-9), and $\mathbf{p}_{s1} = \mathbf{p}_{s2} = \cdots = \mathbf{p}_{sM} = \mathbf{p}_s$ according to *Assumption 10*.

Then the probability of detection is found to be

$$P_d = \int_{\ell_o}^{\infty} \frac{\ell^{(M/2)-1} \cdot e^{-\ell/(1+\Delta/4)} \cdot (M/2)!}{(1+\Delta/4)^M} \cdot \sum_{m=1}^{(M/2)} (\frac{\Delta/4}{1+\Delta/4})^m \cdot \frac{\ell^m}{m!((M/2)-m-1)!((M/2)-m)!} dt \qquad (3-70)$$

The optimum UWB polarization processing developed so far is directly based on the received waveform without any preprocessing.

3.3.2 Optimum UWB Polarization Based detector with Small RBW

The orthgonal receiver structure and passband-to-baseband conversion are applicable to the dual-polarized UWB waveforms with small RBW. Let $\tilde{\mathbf{u}}(t)$ be the waveform vector after the processing and its carrier component being removed, it consists of

$$\tilde{\mathbf{u}}(t) = \tilde{\mathbf{u}}_s(t) + \tilde{\mathbf{u}}_c(t) + \tilde{\mathbf{u}}_w(t) \qquad (3-71)$$

where $\tilde{\mathbf{u}}_c(t)$ and $\tilde{\mathbf{u}}_w(t)$ are the complex random vectors representing the clutter and noise, respectively, and

$$\tilde{\mathbf{u}}_s(t) = \sum_{m=1}^{M} \tilde{\alpha}_m \tilde{\mathbf{p}}_{sm}(t - \tau_m) = \tilde{\mathbf{P}}_s(t)\,\tilde{\mathbf{a}} \qquad (3-72)$$

with $\tilde{\mathbf{P}}_s(t)$ being specified by Eq.(3-11) and $\tilde{\alpha}$ the complex amplitude of mth scatterer and the probability density of its magnitude being specified in Eq.(3-12).

Applying the optimum processing developed in the previous section to the complex waveform, the log-likelihood ratio test becomes

$$\ell = \tilde{\mathbf{u}}^H \tilde{\mathbf{G}}^{-1} \tilde{\mathbf{u}} \overset{H_1}{\underset{H_0}{\gtrless}} \ell_o \qquad (3-73)$$

where

$$\tilde{\mathbf{G}} = \int \tilde{\mathbf{P}}_s^H(t) \mathbf{R}^{-1} \tilde{\mathbf{P}}_s(t); \quad (M \times M) \qquad (3-74)$$

and

$$\tilde{\mathbf{u}} = \int \tilde{\mathbf{P}}_s^H(t) \mathbf{R}^{-1} \tilde{\mathbf{u}}(t) dt; \quad (M \times 1) \qquad (3-75)$$

Note that $\tilde{\mathbf{u}}_c(t)$ and $\tilde{\mathbf{u}}_w(t)$ are the complex Gaussian processes if $\mathbf{u}_c(t)$ and $\mathbf{u}_w(t)$ are real Gaussians. After the exact assumptions ,listed in Introduction section, being applied, the false alarm and detection probabilities are found to be, respectively,

$$
\begin{aligned}
P_{fa} &= \int_{\ell_o}^{\infty} f_\ell(\ell \mid H_0)\, d\ell \\
&= e^{-\ell_o} \cdot \sum_{m=1}^{M-1} \frac{\ell_o^{M-m}}{(M-m)!}
\end{aligned}
\qquad (3\text{-}76)
$$

and

$$P_d = \int_{\ell_o}^{\infty} \frac{\ell^{M-1} \cdot e^{-\ell/(1+\Delta/4)} \cdot M!}{(1+\Delta/4)^{2M}} \cdot \sum_{m=1}^{M} \left(\frac{\Delta/4}{1+\Delta/4}\right)^m \cdot \frac{\ell^m}{m!(M-m-1)!(M-m)!} dt \qquad (3-77)$$

with

$$\Delta = SNR_{in} \cdot \tilde{\mathbf{p}}_s^H \mathbf{R}^{-1} \tilde{\mathbf{p}}_s \qquad (3-78)$$

145

3.3.3 Optimum Narrowband Polarization Based detector

From Eq.(3-34)

$$\tilde{u}_s(t) = \tilde{\alpha}_0 \tilde{c}(t - \tau_0)\tilde{p}_s \qquad (3-79)$$

Substituting it into Eq.(3-74) and Eq.(3-75) yields

$$\tilde{G} = \int \tilde{P}_s^H(t)R^{-1}\tilde{P}_s(t)dt = \tilde{p}_s^H R^{-1}\tilde{p}_s \qquad (3-80)$$

and

$$\tilde{u} = \int \tilde{P}_s^H(t)R^{-1}\tilde{u}(t)dt = \tilde{p}_s^H R^{-1}y \qquad (3-81)$$

where y is obtained by the matched filtering

$$y = \int c^*(t - \tau_0)\tilde{u}(t)dt \qquad (3-82)$$

Note that R is defined by $R_c/2B + N_0 I/2$, which involves dual polarized scattering covariance matrix of the clutter.

Therefore, we have the test statistic

$$\ell = \frac{p_s^H R^{-1} y y^H R^{-1} p_s}{p_s^H R^{-1} p_s} = \mid w^H y \mid^2 \qquad (3-83)$$

with the weight vector being defined

$$w = \frac{R^{-1} p_s}{p_s^H R^{-1} p_s} \qquad (3-84)$$

We see that it turns into the familiar optimum processor of the conventional form.

As we have mentioned in Data Modeling section, the signal amplitude $\tilde{\alpha}_0$ is naturally turns into a complex Gaussian variable with zero-mean and variance σ_s^2. Thus the mean of y is both zero under hypotheses H_0 and H_1, and its covariance matrix is found to be $E(uu^H) = R$ under H_0, and $E(uu^H) = R + \sigma_s^2 p_s p_s^H$ under H_1. Then ℓ has a *Chi-Square* distribution under both H_0 and H_1,

$$f(\ell \mid H_0) = \exp(-\ell) \qquad (3-85)$$

and

$$f(\ell \mid H_1) = \exp(-\ell/(1 + \Delta)) \qquad (3-86)$$

146

with Δ being defined as

$$\Delta = \sigma_s^2 \mathbf{p}_s^H \mathbf{R}^{-1} \mathbf{p}_s \qquad (3-87)$$

Therefore, its false alarm and detection probabilities are given by, respectively,

$$P_f = \exp(-\ell_o) \qquad (3-88)$$

and

$$P_d = \exp(-\ell_o/(1+\Delta)) \qquad (3-89)$$

The optimum UWB polarization detection processing has been developed so far is assumed to have received M dual-polarized echoes scattered by a target illuminated by single polarized transmittion. The problem is to process in an optimum way the M dual-polarized echoes to detect a target against clutter background and receiver noise. This optimum processor requires a priori information about not only approximate locations of MDS centers but also the radar cross section distribution, which are not usually available to the processor in practice. The consequence of non-coherent integration approach without knowing these information will yield some performance degradation. Furthermore, the above waveform-based optimization procedurs involve integral and tensor equation which are very difficult to solve analytically. In general even the scalar case is not trivial. No further attempt was made to work out an specific example, since the main goal of this study is to compare the detection performance improvement of UWB system over the NB system in a polarization canceler based detector. However, the nature of these derived equations renders their solution a subject in itself. No further attempt was made to work out a specific example, since the main goal of this study is to compare the detection performance improvement of UWB system over the NB system. However, the nature of there derived equations render their solution a subject in itself.

II.4 THE DETECTION PERFORMANCE COMPARISON OF NB AND UWB SYSTEM

The detection Performances achievable by the NB, and UWB polarization processors are compared in this chapter. The small RBW-based optimum UWB and NB processors given in Chapter 3 are the candidates of the comparison.

In NB system, the bandwidth of the system, denoted by B_{NB}, is narrow, so that the signal return can be considered as point target, which corresponds to the data modeling discussed in section 4.1.3. In UWB system, on the other hand, the range resolution is significantly smaller than the range separation between individual scatterers and larger than the individual scatterer range extent, so that the returns of the M-MDS are assumed to be the independent random variables. This coresponds to a scatterer-to-scatterer one dominant plus Rayleigh fluctuation model as described in section 4.1.2. It is shown that the UWB target modeling degenerates to a point-target modeling once we sum up all scattering centers over the NB's range cell. The bandwidth of UWB system denoted by B_{UWB} is a lot larger than B_{NB}, $i.e., B_{UWB} >> B_{NB}$.

For UWB signalling scheme in target detection processor, it is widely known that high resolution can largely reduce the clutter power contained in a single range resolution cell, which it leads to a significant performance improvement in the presence of distributed clutter with high CNR. Also, the individual parts of a target can be well resolved so that the fluctuation of dominant scatterer is less than that of point target returns of the NB signalling. It produces the detection performance gain, and we called that as the target fluctuation reduction gain. Lastly, under an equal-transmitted energy constraint, the larger detection performance gain is expected for the target with more scattering centers, and we name the MDS gain.

In addition to modeling and processing complexity issues discussed earier, the promising features associated with the UWB signalling scheme in optimum system produces the *false alarm adjustment loss.* One should note that the global false alarm rate will raise in company with the increase of the range resolution, since the number of the test cells increases dramatically accordingly. To maintain the global false alarm at a desired level, the false alarm rate each test cell must be chosen lower than normal, which will certainly degrade the

system detection performance.

The following definitions are used for the comparison of two systems. The average clutter power for NB and UWB systems are defined as

$$\sigma_{c,NB}^2 = \frac{1}{2B_{SB}} \cdot tr(\mathbf{R}_{c,NB})/2 \qquad (4-1)$$

and

$$\sigma_{c,UWB}^2 = \frac{1}{2B_{UWB}} \cdot tr(\mathbf{R}_{c,UWB})/2 \qquad (4-2)$$

where $tr(\cdot)$ denotes the trace of the matrix, and $\mathbf{R}_c$ is the clutter scattering matrix (size 2×2). For the purpose of comparison, we set

$$\mathbf{R}_c = \mathbf{R}_{c,NB} = \mathbf{R}_{c,UWB} \qquad (4-3)$$

and the same $\mathbf{R}_c$ specified in Eq.(2-5) will be used, which is for the single transmit and dual-polarized receiver version of a meadow clutter example given in [22]. From Eq.(4-2) and Eq.(4-3), the clutter power constraint for the comparison is then,

$$\sigma_{c,NB}^2 = \beta_{BW}\, \sigma_{c,UWB}^2 \quad , \qquad (4-4)$$

where β_{BW} represents the bandwidth ratio, $i.e., \beta_{BW} = B_{UWB}/B_{NB}$. The bandwidth ratio of two UWB systems say UWB system 1 to UWB system 2 is defined and denoted by β_1. Also, the equal-$SCNR$ system constraint applied for the comparisons of NB vs. UWB system, which is

$$SCNR_{UWB,m} = \frac{SCNR_{NB}}{M} = \frac{SCNR_{UWB}}{M} \qquad (4-5)$$

where M denotes the number of MDS, and $SCNR_{UWB}$ and $SCNR_{NB}$ are the total $SCNR$ for UWB and NB system, respectively, and they are equal. Under these constraints specified by Eq.(4-5), therefore, the UWB system with the larger M has the lower $SCNR_{UWB,m}$ for each dominant scatterer. The equation also implies that the NB and UWB system will be compared under the same $SCNR$. As the processing scheme of UWB system differs significantly to that of NB system, due to their range resolution, target modeling, and type of clutter scattering, a fair comparison in a straighforward way faces the difficulties in explaining the results. Therefore, the isolation of each gain and lose achievable by the UWB system is presented indivisually. Performance evaluation will be carried out in the following on a basis of above constraints.

149

4.1 UWB System Gains with Respect to NB System

Since the range-cell size resolved by the bandwidth B_{UWB} becomes much smaller than that of B_{NB}, the clutter power induced in the system with the bandwidth B_{UWB} will be less returned by the factor of β_{BW}. This clutter power reduction will improve the detection performance. The detection performance curves for UWB polarization canceler based detector as a function of input SNR as shown in Fig.(22) are for the investigation of clutter power reduction effect of different bandwidth ratio (β_1). In order to single out the effect of clutter power reduction gain, the false alarm adjustment effect is omitted purposely. Instead, the false alarm probability is set to equal for different bandwith ratios. The detection performance curves for $\beta_1 = 1$, 10, 40, and 100 are displayed with $M=5$, $CNR=30$ dB., and the predetermined false alarm probability $P_{fa}=10^{-5}$. Fig.(23) is the clutter power reduction gain as a function of β_1 for $M=5$, $CNR=30$ dB. at the detection probabilities of .9, and the same false alarm probability condition is applied as in Fig. 22. As indicated in the figure, the clutter power reduction gain is about 10 dB. for $\beta_1=10$, and about 18 dB. for $\beta=100$. The detection performance gain is large.

The UWB system can resolve individual scatterers of a target. To the extent that scatterers of a target are resolved, their fluctuation is reduced as compared to that of returns from the a point target. Less target fluctuation will improve the detection performance. Fig. 3-10 presents the two curves, in which (a): optimum UWB polarization processor with $M=1$ and (b): optimum NB polarization processor, when $CNR=30$ dB. and $P_{fa} = 10^{-5}$. In order to extract the gain only due to less target fluctuation, the clutter power reduction gain is not included. It shows about 6.2 dB. gain over NB system for the 90 % detection probability, and the gain is gradually smaller while probability detection lower.

Under an equal-$SCNR$ system constraint, the larger detection performance gain is expected for the target with more dominant scatterers, and the gain from this effect named the MDS gain.

Effect of Clutter Power Reduction

(a):Bandwidth Ratio=1
(b):Bandwidth Ratio=10
(c):Bandwidth Ratio=40
(d):Bandwidth Ratio=100

- Optimum UWB Polarization Processor with Small RBW
- Single Pulse Based
- Pfa = .00001
- MDS : M=5
- CNR = 30 dB.
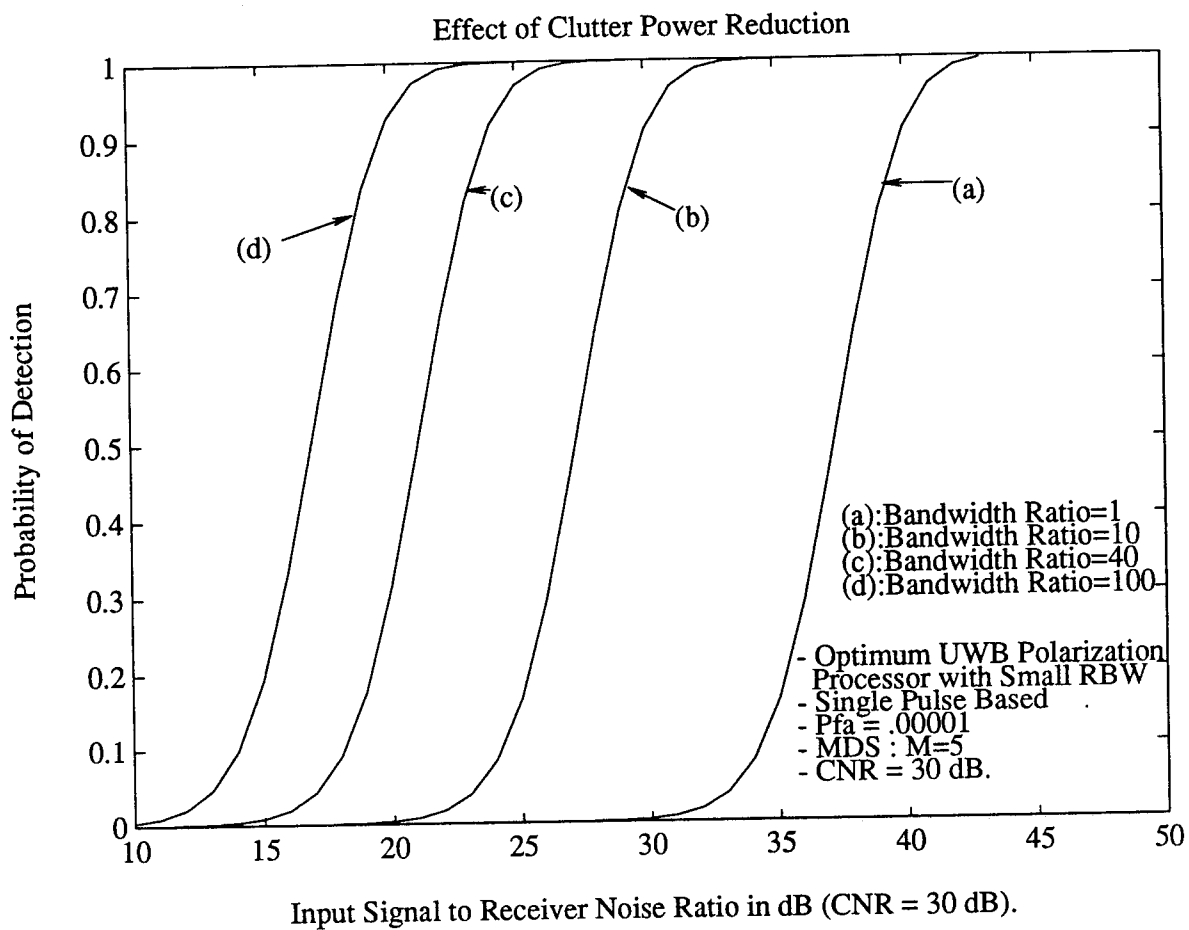
Figure 22: Probability of Detection vs. Input SNR for β_1=1, 10, 40, and 100 when $P_{fa} = 10^{-5}$, M=5, and CNR=30 dB.
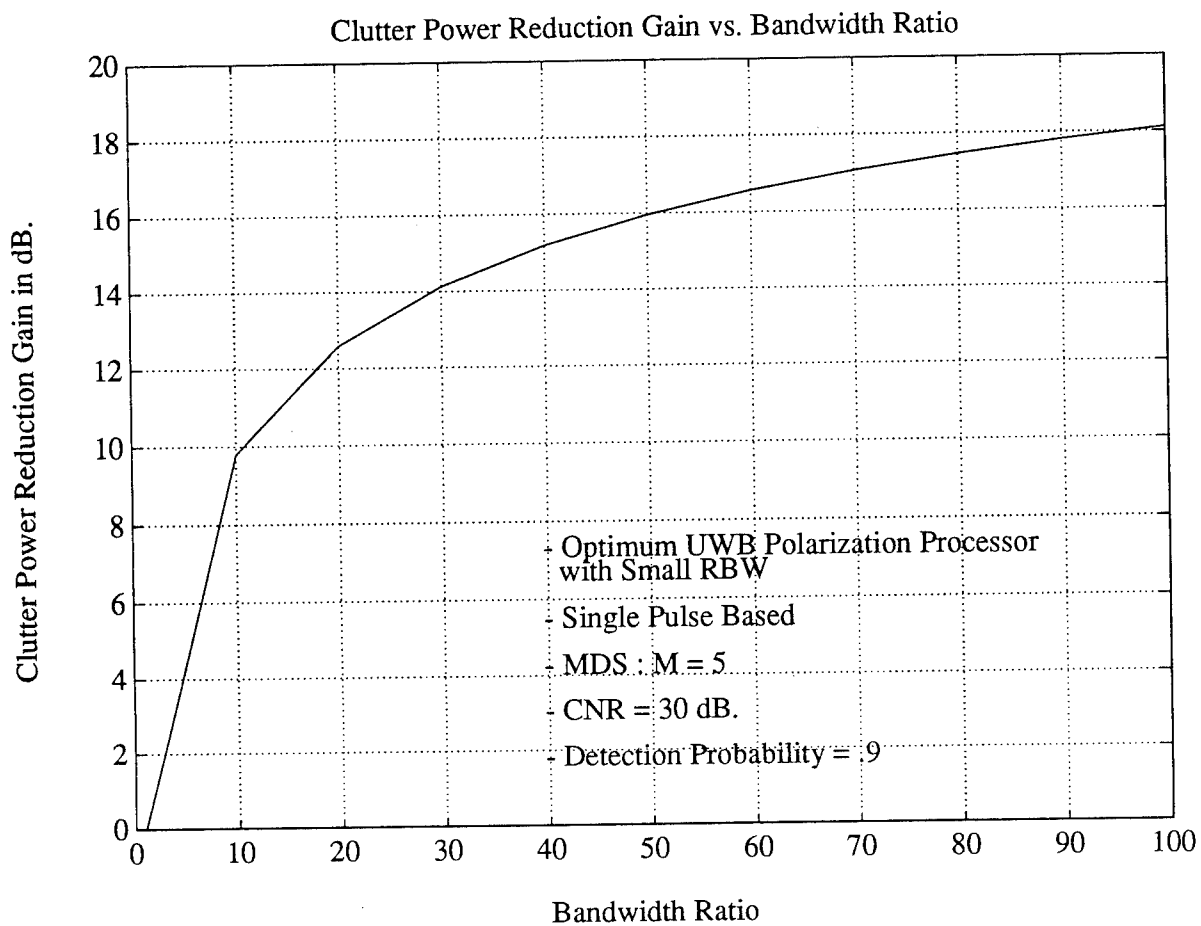
Figure 23: Clutter Power Reduction Gain vs. Bandwidth Ratio (β_1) for $P_d = .9$ when M=5, $P_{fa} = 10^{-5}$, and CNR=30 dB.

Target Fluctuation Reduction Gain

(a): Optimum UWB Polarization Processor
    MDS : M = 1

(b): Optimum NB Polarization Processor

- Single Pulse Based
- CNR = 30 dB.
- Pfa = .00001
- Without Clutter power
  Reduction Gain
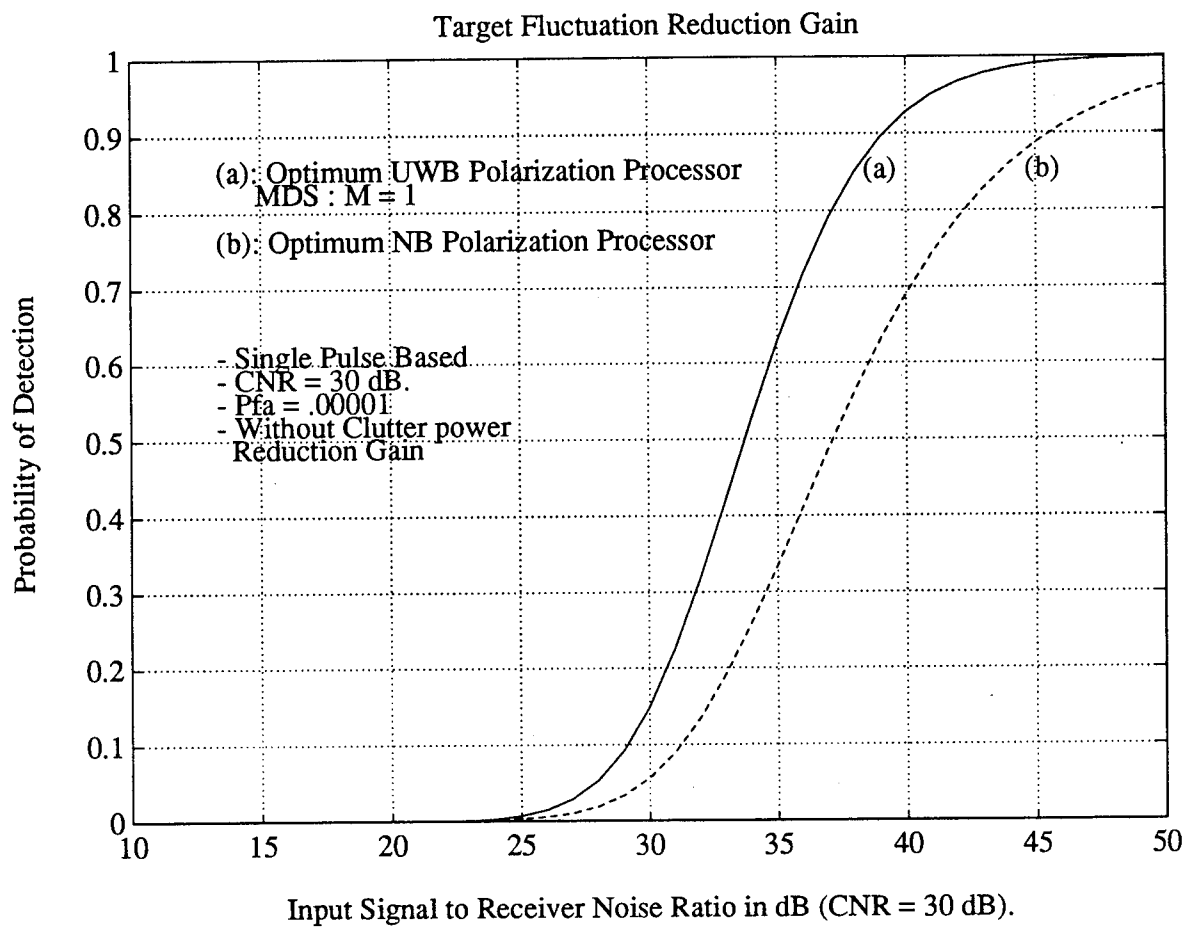
Figure 24: Probability of Detection vs. Input SNR when CNR=30 dB., and $P_{fa} = 10^{-5}$ without clutter power reduction gain. : (a) Optimum UWB (M=1) and (b) Optimum NB.

4.2 UWB System Lose with Respect to NB System

Since the range-cell size (range resolution length) resolved by the bandwith B_{UWB} becomes much small than that of B_{NB}, in the mean time the UWB system will have to process more range cells for a given range extent. It would introduce more global false alarm for the UWB system. Under the assumption that the decision are independently made in each range cells, to maintain the same level of global false alarm rate the probability of false alarm in each range cell has a relation that

$$P_{fa,g} = 1 - (1 - P_{fa})^{1/\beta_{BW}} \qquad (4-6)$$

where $P_{fa,g}$ and P_{fa} denote the probability of global false alarm and that of each cell false alarm, respectively, and β_{BW} is the bandwidth ratio of two system as defined in Eq.(4-4).

The detection performance curves for UWB polarization processor as a function of SNR as shown in Fig. 25 are for investigating the performance loss due to the false alarm constraint related by Eq.(4-6). The prespecified global false alarm probability is set at 10^{-5}, and compares the detection performances for β_1=1,10, and 100 when CNR=30 dB. and M=5. In order to single out the effect of the false alarm probability constraint, the clutter power is set to equal, not changing with the bandwidth. In fact, the performance loss factor, defind as the ration of SNR's requires by the two systems to achieve the same probability of detecton, is found to be [42]

$$\frac{SNR_1}{SNR_2} \approx \frac{ln(P_{fa,1})}{ln(P_{fa,2})} \approx \frac{ln(P_{fa})}{ln(P_{fa,g}/\beta_1)} \qquad (4-7)$$

where β_1 here represents the bandwidth ratio of UWB system 1 to UWB system 2, and $ln(\cdot)$ denotes an natural logarithm operator. According to Eq.(4-7), the performance loss factor is independent of the signal and clutter characteristics, and is related to the logarithm of the probability of false alarm only, which indicates a slight change even if false alarm probability varies several orders of magnitude. The actual performance loss factor as a fuction of β_1 is quantified and displayed in Fig. 26, and compared to analytical approximation quantities governed by Eq.(4-7). In order to maintain the same level of global false alarm in the given range extent requires lower false alarm rate in a single range cell and thus will degrade the system detection performance in polairzation processor. It is seen that, however, even for a very large bandwidth ratio, the detection performance loss is less than 2 dB.

Effect of False Alarm Adjustment

(a): Bandwidth Ratio = 100
(b): Bandwidth Ratio = 10
(c): Bandwidth Ratio = 1

- Optimum UWB Polarization
  Processor with Small RBW
- Single Pulse Based
- MDS : M=5
- CNR = 30 dB.

Probability of Detection

Input Signal to Receiver Noise Ratio in dB (CNR=30 dB).
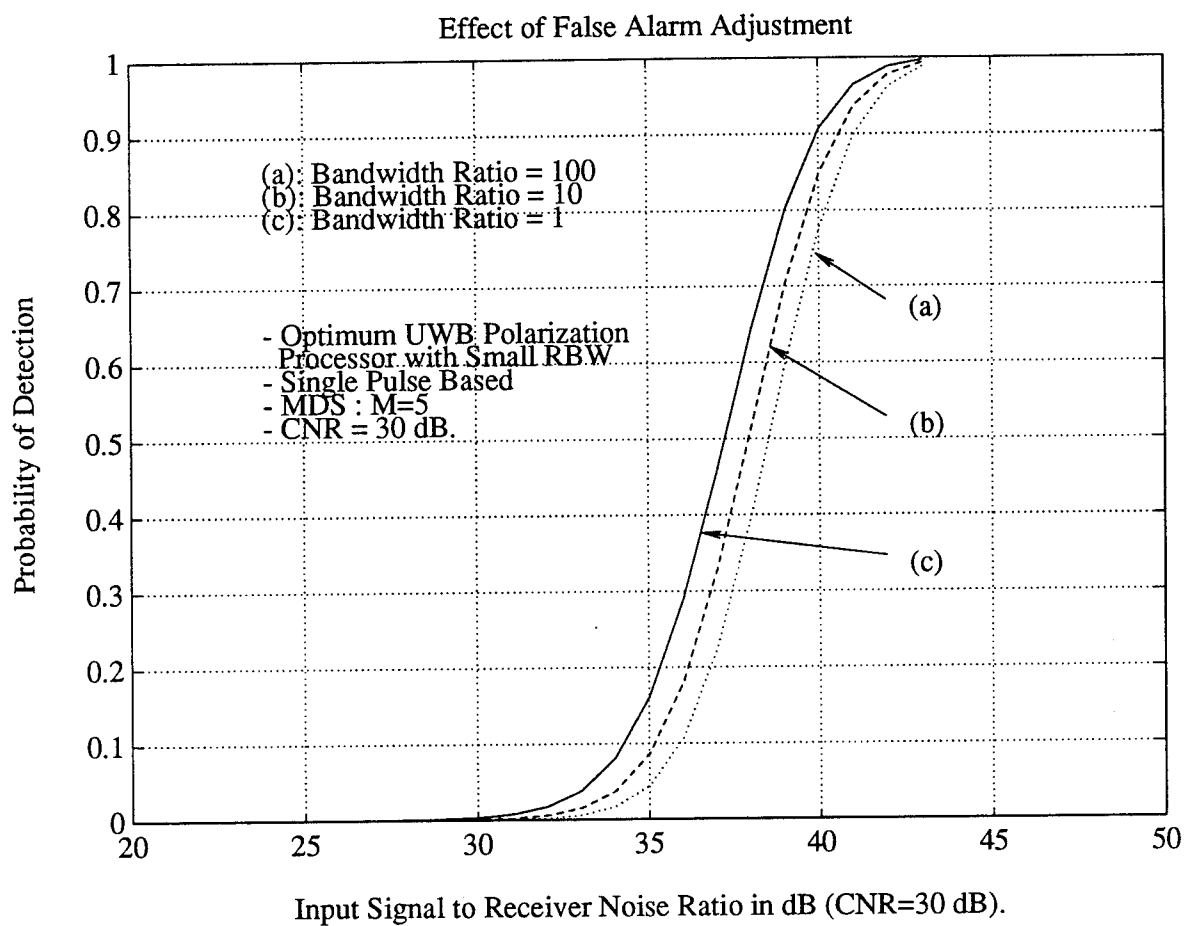
Figure 25: Effect of False Alarm Adjustment for β_1=1, 10, and 100 when M=5, CNR=30 dB. and the global false alarm probability $P_{fa,g} = 10^{-5}$.
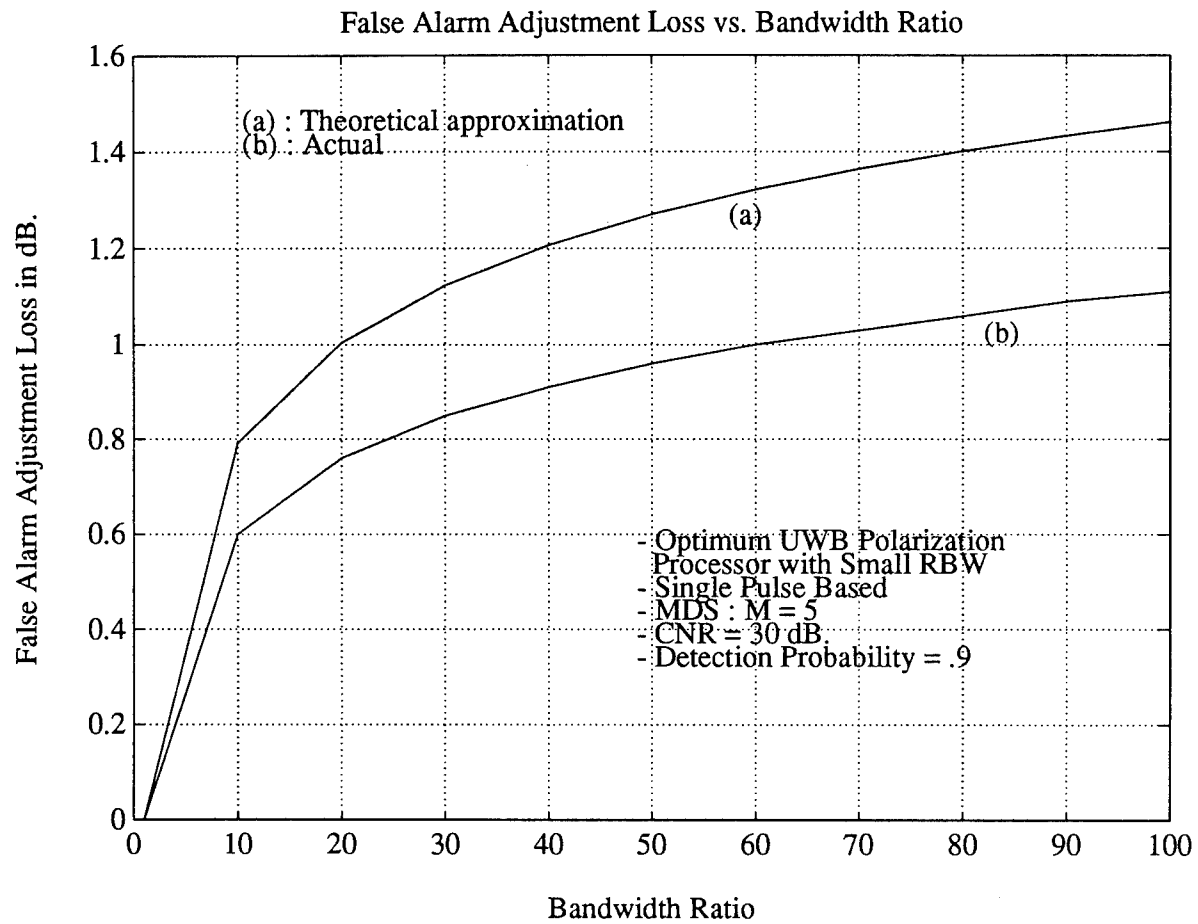
Figure 26: False Alarm Adjustment Loss Factor vs. Bandwidth Ratio when M=5, and CNR=30 dB. for 90% detecion probability : (a) theoretical Approximation and (b) Actual.

4.3 Overall Comparion

Based on the gains and loss earned by UWB signalling in optimum polarization processor, the detection performance curves for all the cases are plotted together in Fig.27. The detection performance is based on a basis of single pulse, $CNR=30$ dB., the global false alarm probability $P_{fa,g} = 10^{-5}$, and the bandwidth ratio $\beta_{BW}=30$. The false alarm adjustment loss has included in the UWB systems. The four curves represent : (a) Optimum UWB Polarization Processor with $M=5$, (b) Optimum UWB with $M=5$ and without the clutter power reduction gain, (c) Optimum UWB with $M=1$ and without the clutter power reduction gain, and (d) Optimum NB Polarization Processor. From this analysis, the UWB system gains are identified against NB system : (I) Target Fluctuation Reduction Gain, (II) MDS Gain (UWB $M=1$ to $M=5$), (III) Clutter Power Reduction Gain, and (IV) Optimum UWB Overall Gain.

As one can see from Fig.27, the big chunk of gain from UWB signaling is come due to the clutter power reduction. The next analysis provides the question if the MB signaling be able to achieve the UWB gains not including the clutter power reduction gain. Fig.28 presents the UWB equivalent gain (without clutter power reduction gain) achievable by the MB signaling on the basis of equal processing complexities (i.e., $M=J=5$). About 3.5 dB. larger gain is obtained by the UWB signaling for .9 detection probability, even without the clutter power reduction gain. It leads the conclusion that in the polarization processing for radar target detection the UWB signaling clearly yields the more gains than the MB signaling. The additional gain mainly attributes to the fluctuation reduction of target polarization; by increasing the down-range resolution, this can in fact provide the fine resolution between the scattering centers, and hence less ambiguous polarization state formed from its dominant scattering center. Together with the clutter power reduction gain, the UWB signaling scheme for the polariztion processing is the promising technique for the doppler ambiguous targets, with the expenses of processing complexities.

The UWB gains other than the clutter power reduction gain are something that one can not control of, since the number of MDS is determined by a particular target (3 to 5 can be the reasonable assumption of it [12]), and the target fluctuation gain does not change with the processing scheme. In the MB system, however, the number of frequency diversity

157

is something that one can control so as MB gain, and the previous experiment from Rome Laboratory shows that up to 12 frequency diversity can be utilized in order to obtain the *i.i.d.* data return. And, also, the UWB system requires to know the exact locations of dominant scatterers. The MB signaling scheme is attractive in those senses.
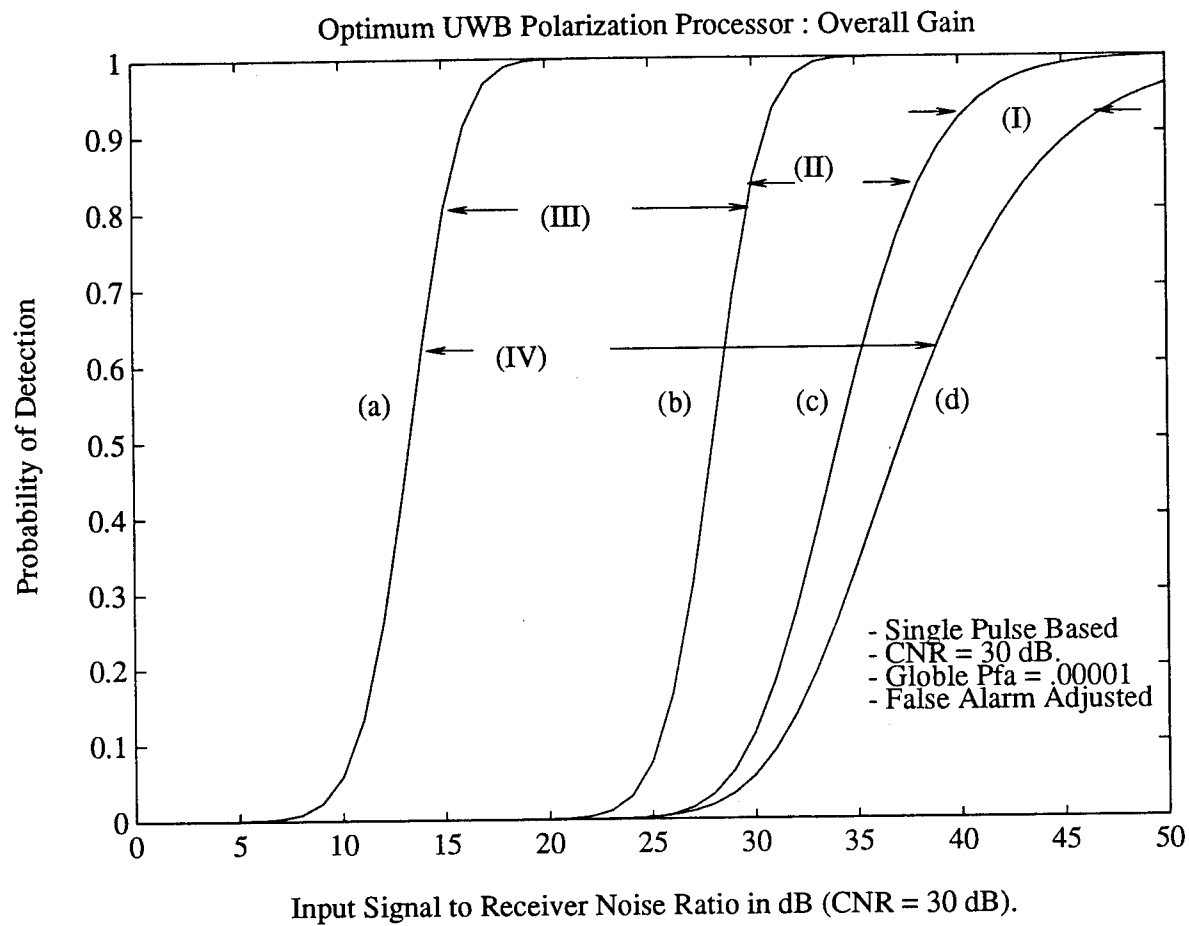
Figure 27: Optimum UWB Polarization Processor Overall Gain under the Equal-$SCNR$ System Constraint.
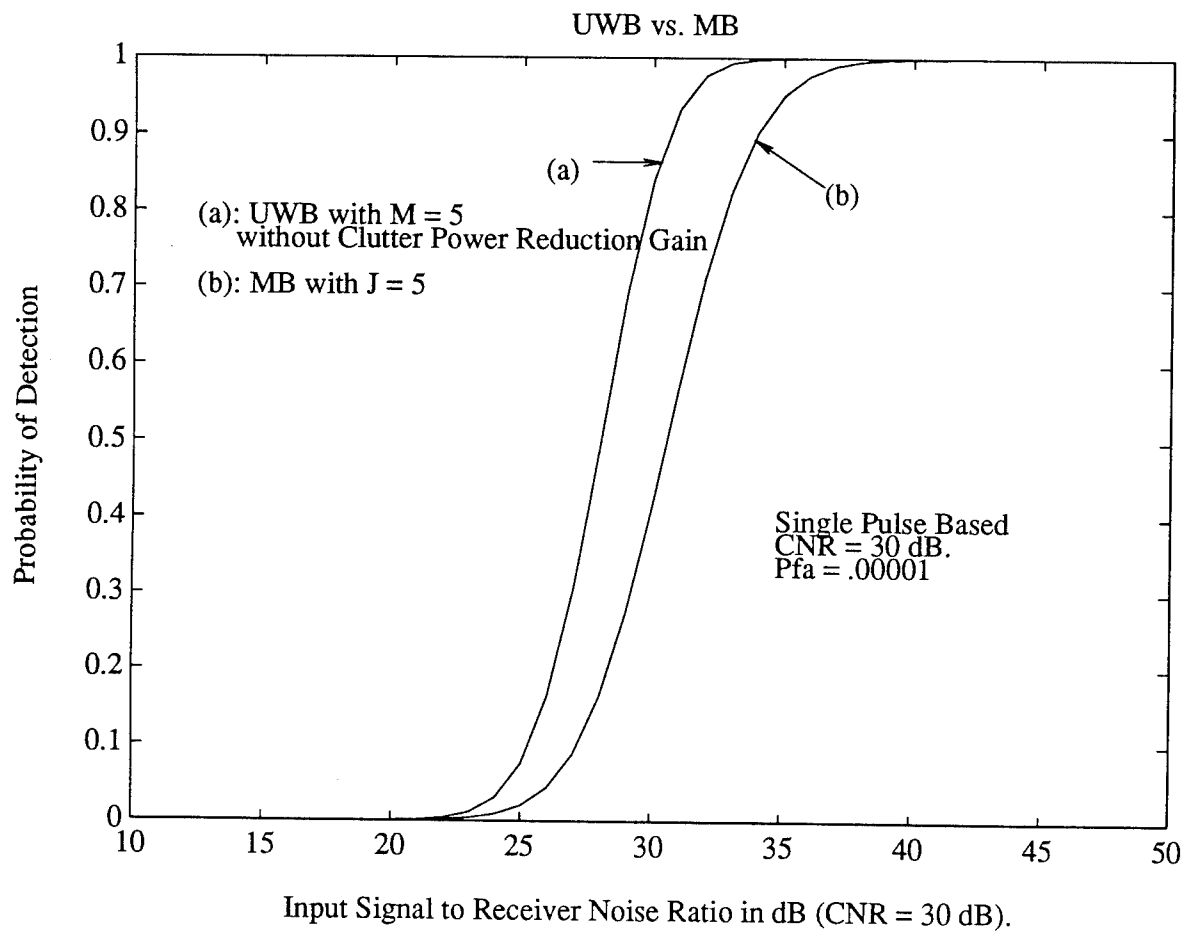
Figure 28: Optimum UWB polarization processor (M=5) vs. optimum MB polarization processor (J=5) both under the Equal-$SCNR$ System Constraint.

II.5 CONCLUSION AND DISCUSSION OF PART II

This part of report addresses the problem of detecting slowly/tangentially moving weak targets, which typically go undetected when only doppler processing is used. The proposed method of improving detection performance is to utilize the frequency variational signaling schemes in polarization processing. Two frequency variational signaling schemes are addressed : Multiband and Ultra-wideband. Signaling methods for obtaining the MB and UWB polarimetric data returns are discussed. Implementation and performance analysis of these technique are studied in detail. The well-known problems of single (narrow) band signaling with polairzation canceler based detector has been confirmed and the detection performance improvement by using MB signaling is revealed.

Under the toughest system constraint governed by Eq.(2-52), the MBPC based detector was compared with SBPC based detector, in terms of both the optimal solutions and their adaptive implementations. The AMBPC based detector elliminates the signal cancellation and sensitivity problem since each frequency potentially yields different polarization states and different degree-of-polarization; neither the target is canceled in every subband of the MB processor, nor the very low degree-of-polarization would appear in every band with a very high probability. Analytical and experimental results show that the total gian of the MB signaling over the SB signaling attributes to the combination of ellimination of signal cancellation, better adaptation, and a fluctuation reduction of the degree of target polarization, in addition to the well-known target amplitude fluctuation reduction. These results are obtained under the comparable target strength relative to clutter power.

Also it is observed that the performance improvement obtained by MB signaling, typically about 5 dB gain, may be inadequate for _weak_ target detection. Therefore, the UWB signaling scheme in polarimetric radar is examined for further performance improvement. An additional benefit arises from using UWB signaling, due to a reduction of resolution cell size which results in lower clutter backscatter competing with desired target returns. The main work is with identifying the potential of the optimum UWB polarization processor.

The log-likelihood ratio test for the optimum UWB polarization processing has been derived, together with the closed-form expressions of detection and false alarm probabilities. The optimum UWB polarization processing detection performance is compared with the

optimum NB polarization processing, and it is concluded that a significant performance gain can be achieved by using UWB signaling. The UWB gain is still larger than that of the MB signaling, even after excluding the clutter power reduction gain in UWB systems. The additional gain of 5 to 10 dB mainly attributes to the fluctuation reduction of target polarization when it is resolved into its multiple dominant scatters.

REFERENCES OF PART II

[1] H.L. Van Trees, *Detection Estimation and Modulation Theory*, Part I, New York : Wiley, 1968.

[2] H.L. Van Trees, *Detection Estimation and Modulation Theory*, Part III, New York : wiley, 1968.

[3] B. Widrow, and S.D. Stearns, *Adaptive Signal Processing*, Prentice-Hall, 1985.

[4] G. Strang, *Linear Algebra and Its Applications*, Academic Press, 1976.

[5] DiFranco, and Rubin, *Radar Detection*, Series in Information Theory, Prentice-Hall, 1968.

[6] Merrill I. Skolnik, *Introduction to Radar Systems*, Second Edition, McGraw-Hill Book Company, 1980.

[7] Donald R. Wehner, *High Resolution Radar*, Artech House, 1985.

[8] Robert M. Young, *An Introduction to Nonharmonic Fourier Series*, Academic Press, 1980.

[9] Henning F. Harmuth, *Nonsinusoidal Waves for Radar and Radio Communication*, Academic Press, 1981.

[10] D. Giuli, "Polarization Diversity in Radars," *Proc. IEEE,* vol. 74, No. 2, pp. 245-269, February 1986.

[11] A.J. Poelman, "Virtual Polarization Adaptation : A Method of Increasing the Detection Capability of a Radar System Through Polarization-Vector Processing," *Proc. Inst. Elec. Eng.*, pt. F, vol. 128, pp. 261-270, Oct. 1981.

[12] E. Dalle Mese, and D. Giuli, "Detection Probability of a Partially Fluctuating Target," *Proc. Inst. Elec. Eng.*, pt. F. vol. 131, pp. 179-182, Apr. 1984.

[13] M. Gherardelli, D. Giuli, and M. Fossi, "Suboptimum Adaptive Polarization Cancelers for Dual-Polarization Radar," *Proc. IEE,* vol. 135, pt. F, No. 1, pp 60-72, February 1988.

[14] D. Giuli, M. Fossi, and M. Gherardelli, "A Technique for Adaptive Polarization Filtering in Radars," *Proc. IEEE,* International Radar Conference, pp 213-219, Sept. 1985.

[15] M.C. Wicks, V.C Vannicola, K.C. Stiefvater, and R.D. Brown, "Polarization Radar Processing Technology," *Proc. IEEE,* 1990 International Radar Conference, pp. 409-416, May 1990.

[16] G.A. Deschamps, and P.E. Mast, "Poincare Shpere Representation of Partially Polarized Fields," *IEEE Trans. on Antenna and Propagation,* vol. AP-21, pp. 474- 478, 1973.

[17] R.D. Brown, and H. Wang, "Adaptive Multiband Polarization Processing for Surveillance Radar," submitted to *IEEE Trans. AES,* May 1991.

[18] H. Wang, and Jian-Xiong Zhu, "On Performance Improvement of Tone Frequency Estimation in Active Radar/Sonar Systems with Nonfluctuating targets," *IEEE Transactions on Acoustic, Speech, and Signal Processing,* vol. ASSP-36, No. 10, pp. 1582-1592, October 1985.

[19] H. Wang, and L. Cai, "On Adaptive Multiband Signal Detection with the SMI Algorithm," *IEEE Transactions on Arospace and Electronic Systems,* vol. AES-26, No. 5, pp. 768-773, September 1990.

[20] I.S. Reed, J.D. Mallitt, and L.E. Brennan, "Rapid Convergence Rate in Adaptive Arrays," *IEEE Transactions on Arospace and Electronic Systems,* vol. AES-10, No. 6, pp. 853-863, November 1974.

[21] Ranam Nitzberg, "Losses for Frequency Diversity Waveform Systems," *IEEE Tran. on Arosppace and Electronic Systems,* vol. AES-14, No. 3, May 1978.

[22] L.M. Novak, M.B. Sechtin, and M.J. Cardullo, "Studies of Target Detection Algorithms That Use Polarimetric Radar Data," *IEEE Transactions on Aerospace and Electronic Systems,* vol. AES-25, No. 2, pp. 150-165, March 1989.

[23] Raman Nitzberg, "Effect of a Few Dominant Specular Reflectors Target Model Upon Target Detection," *IEEE Transactions on Aerospace and Electronic Systems*, vol. AES-14, No. 4, pp. 670-673, July 1978.

[24] Itt Gilfillan, "Final Report on Polarization Processing Techniques Study," *Prepared for Rome Air Development Center*, Griffiss Air Force Base, Rome, New York, Nov. 27, 1979.

[25] Richard A. Altes, Stephen F. Connelly, James R. Miller, Kishan G. Mehrotra, and H. Liu, "Signal-Filter Design and System Performance for Polarimetric Radar," *Prepared for Rome Air Development Center*, griffiss Air Force Base, Rome, New York, July 1987.

[26] Werner Wiesbeck, and Daniel Kahny, "Single Reference, Three Target Calibration and Error Correction for Monostatic, Polarimetric Free Space Measurements," *Proceedings of the IEEE*, vol. 79, No. 10, pp 1551-1557, Oct. 1991.

[27] Neil K. Jablon, "Steady State Analysis of the Generalized sidelobe Canceller by Adaptive Noise Cancelling Techniques," *IEEE Trans. on Antennas and Propagation*, vol. AP-34, No. 3, pp. 330-337, March 1986.

[28] Ramon Nitzberg, "Canceler Performance Degradation Due to Estimation Noise," *IEEE Trans. on Aerospace and Electronic Systems*, vol. AES-17, No. 5, pp. 685-692, September 1981.

[29] Maurice Beale, "Detection Loss of the Sample Matrix Inversion Technique," *IEEE Trans. on Aerospace and Electronic Systems*, vol. AES-20, No. 6, pp. 824-829, November 1984.

[30] Xiu-Ying Hou, and Norihiko Morinaga, "Detection Performance in K-Distributed and Correlated Rayleigh Clutters," *IEEE Trans. on Aerospace and Electronic Systems*, vol. AES-25, No. 5, pp. 634-641, September 1989.

[31] L. Cai, *On Adaptive Multiband Detection of Targets in Nonstation ary/Nonhomogeneous Interference*, Ph.D. dissertation, Syracuse University, 1990.

[32] W.M. Boerner, and Y. Yamaguchi, "A State-of-the-Art Review in Radar Polarimetry and its Application in Remote Sensing," *IEEE Trans. on Aerospace and Electronic Systems*, vol. AES-5, No. 6, June 1990.

[33] D.T. Gjessing, and J. Hjelmstad, "Adaptive Radar in Remote Sensing Using Space, Frequency, and Polarization Processing," *IEE Radar-82 International Conference*, pp. 1, 1982.

[34] H.J. Eom, and A.K. Fung, "A Scatter Model for Vegetation up to Ku-Band," *Remote Sensing of Environment 15*, pp. 185-198, Elsevier Publish ing Co., 1984.

[35] E.J. Kelly, "Adaptive Detection in Non-stationary Interference, Part I, II, and III," Massachusetts Institute of Technology, Lincoln Laboratory, Technical Report 761, Group 96, August 1987.

[36] J.S. Bird, "Subclutter Visibility for Low-Doppler Targets," *Proceedings of the 1984 International Symposium on Noise and Clutter Rejection in Radars and Imaging Sensors*, pp. 47-59, 1984.

[37] Charles Fowler, John Entzminger, and James Corum, "Assessment of Ultra-Wideband (UWB) Technology," *IEEE IEEE Transactions on Aerospace and Electronic Systems Magazine*, pp. 45-49, November 1990.

[38] Sebastian Riegger, and Werner Wiesbeck, "Wide-Band Polarimetry and Complex Radar Cross Section Signatures," *Proceedings of the IEEE*, vol. 77 NO. 5, pp. 649-658, May 1989.

[39] Lev Y. Astanin, Alexander A. Kostylev, "Ultra Wideband Signals - A New Step in Radar Development," *Proceedings of CIE 1991, International Conference on Radar*, Beijing China, Oct. 22-24, 1991.

[40] A. Farina, F. Scannapieco, and F. Vinelli, "Target Detection and Classification with Polarimetric High Range Resolution Radar," *Direct and Inverse Methods in Radar Polarimetry*, Sep. 18-24, 1988.

[41] Lujing Cai and Hong Wang, "Target Detection with Coherent Multiple Pulse Processing in Ultra-Wideband Systems," *Proceedings of CIE 1991, International Conference on Radar*, Beijing China, Oct. 22-24, 1991.

[42] M. Rackson, P Wei, and T. Meyer, "High Resolution Polarimetric Radar Precision Limits," *Proc. of the IEEE National Radar Conference*, Atlanta, Georgia, pp. 8-10, 1984

[43] P.K. Hughes, "A High-Resolution Radar Detection Strategy," *IEEE Trans. on Aerospace and Electronic Systems*, vol. AES-19, No. 5, pp. 663-667, September 1983.

[44] W. f. Herdeg, U. Fuchs, H. Wendel, "Polarization Parameters from Wide-Band High Resolution Radar Imagery," *Proceeding of the IEEE 1990 International Radar Conference*, pp. 543-557, May 1990.

Contract No. F30602-91-C-0035

ULTRA WIDE BAND (UWB) RADAR DETECTION ANALYSIS AND DEMONSTRATION PROGRAM

Phase II: 16 June 92 - 31 Dec 94

Final Technical Report

Vol. I

Submitted by

D. D. Weiner
Principal Investigator
Syracuse University
Electrical & Computer Engineering Department
121 Link Hall
Syracuse, NY 13244
Tel/Fax: (315) 443-4428

TABLE OF CONTENTS

FIGURES

Figure 1: Pitch-frequencies corresponding to the keys 'c' and 'g' in a piano. These correspond to the major diatonic scale of western music. The spacing is very nonuniform, and will appear to be almost uniform on a logarithmic scale.

Figure 2: A baseband T-pulse with zero mean and no intersymbol interference.

Figure 3: Spectrum of the zero mean baseband T-pulse.

Figure 4: Derivative of a narrow Gaussian pulse. The sampling interval T is 0.15 light-meters.

Figure 5: Synthesized current response at the center of a thin wire activated by a narrow pulse from the broadside. Sampling interval is 0.15 light-meters.

Figure 6: DFT amplitude spectrum (DB) of the derivative of the Gaussian pulse. The frequency resolution is 1/(128T).

Figure 7: DFT amplitude spectrum (DB) of the current response (40T thru 167T) excited by a narrow Gaussian pulse. The frequency resolution is 1/128T) the sampling interval T is 0.15 light-meters.

Figure 8: An optimum baseband signal of duration 127T. The in-band energy is 99.995% with the bandwidth 2/(128T). The computing frequency resolution was 30 times higher.

Figure 9: DFT amplitude spectrum (DB) of the baseband signal. The frequency resolution is 1/(128T).

Figure 10: Modulated signal of duration 127T and center frequency 25/(128T). The corresponding baseband signal has maximum energy (99.995%) within the bandwidth 2/(128T). The computing frequency resolution was 30 times higher.

Figure 11: DFT amplitude spectrum (DB) of the modulated signal. The center frequency is 25/(128T). The frequency resolution is 1/(128T).

Figure 12:   Fourier transforms (log magnitude) of windows of
                (a) Rectangular
                (b) Bartlett
                (c) Hanning
                (d) Hamming
                (e)Blackman

Figure 13:   Synthesized current response at the center of a thin wire
                activated by a narrow band electric field pulse from the
                broadside. The center frequency of that pulse is 25 sampling
                interval is 0.15 light-meters.

Figure 14:   DFT amplitude spectrum (DB) of the current response (129T
                thru 256T) the exciting pulse has center frequency 25/(129T).
                The frequency resolution is 1/(128T). The sampling interval T
                is 0.15 light-meters.

1. <u>OVERVIEW</u>

This paper describes the T-pulse methodology. T-pulse stands for a time limited pulse whose energy may be concentrated in an extremely narrow band. Since they are narrowband signals, conventional hardware can be used to transmit and receive T-pulses. A T-pulse may or may not have any direct current or DC value. From a practical point of view, the T-pulse should have no DC since an antenna cannot transmit DC signals.

This report is divided into two parts. The first part presents the T-pulse as a mathematical tool which can be used for accurate and precise time-frequency localization of signals. This is useful when the T-pulse technique is used in the receiver as a signal processing technique. The second part describes the T-pulse as a waveform design technique, which can be used for target identification. This section is relevant when a T-pulse needs to be transmitted. Added constraints like zero intersymbol interference may be added to the design of a T-pulse, making it a versatile tool. A user oriented computer program is presented for efficient generation of the T-pulse.

The objectives of this report have been:

(1)   The development of analytic tools required for the analysis of broadband waveforms.

(2)   The synthesis of waveforms which provide optimum performance. Various waveform design procedures such as T-pulse, K-pulse and E-pulse are presented.

171

(3)   The development of a user-friendly computer program so that the generalized T-pulse can easily be synthesized once the design objectives have been selected. An example is presented on how to utilize the T-pulse for target identification.

For the first objective, a survey is made of various analytic tools including the short time Fourier techniques, the Gabor transform and the wavelet transform. The strengths and weaknesses of each of the methods have been outlined.

This brings us to the second objective, namely of synthesis. For practical reasons, it is necessary to have an interrogating waveform that is finite in the time domain. However, a time limited waveform cannot simultaneously be bandlimited. It is necessary to design the shape of the waveform such that most of the energy is concentrated in a narrow band and that outside the band, the energy drops pretty fast.

For the synthesis procedure, it is necessary to generate waveforms that are limited in time, with its energy concentrated in a narrow band. In addition, since one is interested in transmitting this waveform through an antenna, the waveform must have zero direct current value. This is an important criteria. These two constraints then would give rise to waveforms that will generally oscillate and this oscillation would die out after a few zero crossings (one or two at most) in order for the waveform to have finite time duration. If we have an oscillatory waveform, it is imperative that the waveform be orthogonal to its shifted versions. This would guarantee that if one has a receiver sampling the radar returns from various

range-bins, then the observation would be in independent bins for different waveforms transmitted at different times. Mathematically, this is equivalent to saying that the waveform must have no "inter-symbol" interference. Equivalently it is said that the waveforms are "orthogonal nyquist signals".

All the above attributes are desirable in a waveform to provide good detection performance. The T-pulse is such a procedure, where any performance criteria can be incorporated into the computer oriented design. The computer program optimizes various contradictory requirements of small bandwidth, limited time, no direct current value and zero intersymbol interference and provides the generalized T-pulse. Hence from a theoretical performance criteria of a synthesized waveform, the generalized T-pulse meets all the design criteria.

The next phase of the work involves generation of the T-pulses. It is desired to take the synthesized waveform and pass it through an arbitrary waveform generator to obtain a generalized T-pulse. This would be the baseband T-pulse. This can be amplified and transmitted directly or can be translated in frequency through (amplitude) modulation, amplified and then transmitted. The shape of the T-pulse depends on what criteria are being utilized for efficient target detection and what type of targets one is looking for. The generalized T-pulse excites the target in a narrow band of frequencies. If the target has a resonance in that frequency band then the radar return is strong, if the target has no resonance in the band of the transmitted T-pulse then the radar return is very weak. This is equivalent to "zooming" into a narrow band and evaluating detection performance

in that band. This type of detection is useful in providing for identification performance. For example, if the resonant frequencies of special artifacts of two targets are different, then the T-pulse return would also be different. Since the transfer function of a linear system provides the finger print of the system, the generalized T-pulse provides the transfer function of the target in the narrowband in which the energy of the T-pulse resides. Hence high resolution discrimination is provided. The T-pulse is particularly useful when one is looking for special artifacts like engine blade rotation, which are extremely narrow band signatures. An example is presented to illustrate its salient features.

In other techniques of resonance extraction, one has to look at the late time response of the target and from the late time response extract target poles. The T-pulse can provide the same information about poles in the frequency domain without radiating an impulse. One can interrogate the target at a few "spot frequency bands" using the T-pulse and then utilizing various extrapolation techniques like Cauchy's method [26-28] or the Matrix Pencil Method [29-31] extrapolate/interpolate the resonances of the target. With such techniques, it is not necessary to measure the entire frequency band response. A few measurements may be all that is required to generate information over a decade bandwidth. One of the objectives of the next phase would be to demonstrate this experimentally using various laboratory devices.

The first half of the report describes the analytical techniques for waveform design and the last half describes the synthesis procedure. Finally, a user oriented

computer program is presented to design generalized T-pulses for radar target detection.

2. INTRODUCTION

In nature, one does not encounter pure single tone signals, but signals whose "frequency content" varies with time. Generally, frequency is defined as a phenomenon where the period of zero crossings of a signal has a fixed duration for all times and frequency is related to the period. However, one may define the term "instantaneous frequency" by defining signals whose frequency content changes as a function of time or duration of the signal. A good example of that is speech, where the instantaneous frequency may change from 0-20 kHz depending on the system. Hence it is interesting to develop methodologies which can be introduced to analyze such signals.

In modern times such concepts have been proven to be useful in modern radar system analysis. Conventionally, radar has dealt with pure cw signals which are either frequency modulated or turned off and on to generate pulses. However, there are other radar systems which deal with wideband pulses. Hence in understanding how such radar systems work it is necessary to understand time-frequency representation of waveforms and how they are characterized and analyzed. One of the objectives of this study is to look at various methodologies for analyzing broadband signals, particularly those in which the instantaneous frequency changes with time. Secondly, it is necessary to design wave shapes

175

and/or waveforms for such systems which upon transmission will enhance the detection performance over conventional narrowband systems.

In this study, we look at the classical Fourier transforms, Gabor transforms and the wavelet transforms which have been utilized for characterizing waveforms whose frequency content changes with time. One of the main features that distinguishes the three transforms is the choice of the window function. The purpose of the window function is to localize the information about the signal in both space and time. To this end, the T-pulse technique provides a very flexible window function which can be generated a - priori utilizing computerized optimization techniques. Once such methodologies are known, one can then utilize special pulse shapes to enhance detection performance. Hence waveform shaping and analysis of waveshapes is the main theme of this paper.

The second part of this paper describes various pulse shaping techniques like the E-pulse and the K-pulse and their philosophies. The newly developed T-pulse technique is also described and shown how flexible it is. Since the T-pulse is designed through a process of numerical optimization, various constraints like no DC value or zero intersymbol interference can be added to the computer aided waveform design technique without any difficulty. A user-oriented computer program is presented in the appendix to generate T-pulses with desired properties.

3. MATHEMATICAL BACKGROUND

This section summarizes the various analytical tools that perform time-frequency analysis. The three techniques that are most popular are the Fourier Transform, the Gabor Transform and the Wavelet Transform. These techniques are presented both from a continuous and a discrete time signal point of view.

The basic difference that distinguishes the three transform techniques as a time-frequency localization tool is the choice of a "window function". The "window function" is essentially an artifact through which we observe the data. For each of the three transforms the window function has certain fixed properties. Thereby, each of these analysis techniques has preferred domains over which their application provides good results. One of the objectives of this report is to generalize these analysis techniques and describe a window function that is very flexible and can deal with a very broad class of practical target identification problems. The continuous time signal transform techniques are presented first, followed by the discrete version.

4. CONTINUOUS TRANSFORMS

4.A FOURIER TRANSFORM

The classical Fourier Transform technique is utilized to find the frequency content of a particular waveshape p(t) which has occurred just once and has existed for a time interval [0,T] and is non-existent for any other times. It is well known that the frequency content of such a signal p(t) is given by the Fourier

transform $P(\omega)$ so that

$$P(\omega) = \int_{-\infty}^{\infty} p(t) \; e^{-j\omega t} \; dt = \int_{0}^{T} p(t) \; e^{-j\omega t} \; dt \qquad (4.1)$$

(4.1) can be interpreted as modulating the function $p(t)$ by $e^{-j\omega t}$ and then integrating it. The Fourier Transform is defined for all values of the variable t [i.e. from $-\infty \leq t < \infty$], whereas the Fourier series of the function $p(t)$ is defined to be periodic. That is, $p(t)$ repeats itself after every period (e.g.; 2π). Hence $p_F(t)$, the Fourier series of $p(t)$, is defined as

$$p_F(t) = \sum_{n=-\infty}^{\infty} c_n \; e^{+jnt} \qquad (4.2)$$

where

$$c_n = \frac{1}{2\pi} \int_{0}^{2\pi} p(t) \; e^{-jnt} \; dt \qquad (4.3)$$

So for a Fourier series, the function $p(t)$ is decomposed into a sum of orthogonal functions $c_n \; e^{jnt}$. Observe that the orthogonal functions into which $p(t)$ is decomposed in (4.2) is generated by integer dilations of a single function e^{jt}. Also note that the function $p_F(t)$ is periodic with period 2π. In contrast, in the Fourier Transform, the spectrum is decomposed into noninteger dilations of the function e^{jt}, as we know

178

$$p(t) = \frac{1}{2\pi} \int_{-\infty}^{\infty} P(\omega) \, e^{j\omega t} \, d\omega \qquad (4.4)$$

The problem in analyzing signals which are limited in time, i.e. they exist over a finite time window and are zero elsewhere, by Fourier Transform techniques, is that such functions can not simultaneously be bandlimited. Hence, to represent signals p(t) which exist for $0 \leq t \leq T$, the Fourier Transform is generally not the best way to characterize such signals. However, a short time Fourier Transform has been utilized to analyze such signals in the time-frequency plane.

By its very definition, the Fourier transformation uses the entire signal and permits analysis of only the frequency distribution of energy of the signal as a whole [1]. To solve this problem, many who do spectral analysis have taken a piecewise approach. The signal is broken up into contiguous pieces and each piece is separately Fourier transformed. The resulting family of Fourier transformations is then treated as if it were the basis for a joint time-frequency energy distribution [1-4].

In the short time Fourier transform, the function p(t) is multiplied by a window function w(t) and the Fourier transform is calculated. The window function is then shifted in time and the Fourier transform of the product is computed again. So for a fixed shift β of the window w(t), the window captures the features of the signal p(t) around β. The window helps to localize the time domain data, before obtaining the frequency domain information. Hence, the short time

Fourier transform is given by

$$P_{STFT}(\omega) = \int_{-\infty}^{\infty} p(t) \; w(t-\beta) \; e^{-j\omega t} \; dt \qquad (4.8)$$

and when w(t)=1 for all t, one obtains the classical Fourier Transform.

The problem here is that as the window function gets narrower, the localization information in the frequency domain is compromised. In other words, as the frequency domain localization gets narrower, the window gets wider, so that localization information in the time domain gets compromised due to the uncertainty principle [The uncertainty in time Δt and the uncertainty in angular frequency $\Delta\omega$ are related by $\Delta\omega \cdot \Delta t \geq 0.5$].

Since the requirements in the time localization and frequency resolution are conflicting, one has to make some judicious choices. The best window w(t) depends on what is the meaning of the term "best"?

The above problem has solutions only under certain conditions. For example, if we require the function w(t) to be symmetric and that its energy be confined to certain band $|\omega| \leq B$, then we know the optimum function w(t) is given by the prolate spheroidal functions. Other criteria such as signal-to-noise ratio can also be utilized in designing the function w(t) or utilizing other "criteria for best" [4-7].

To obtain the original signal back from the short time Fourier Transform, we observe [4]

180

$$p(t) \ w(t-\beta) = \frac{1}{2\pi} \int\limits_{-\infty}^{\infty} P_{STFT} \ (\omega, \beta) \ e^{j\omega t} \ d\omega \qquad (4.9)$$

If we set $\beta = t$, then

$$p(t) \ w(0) = \frac{1}{2\pi} \int\limits_{-\infty}^{\infty} P_{STFT} \ (\omega, t) \ e^{j\omega t} \ d\omega \qquad (4.10)$$

So that we can recover the original signal $p(t)$ for all t as long as $w(0) \neq 0$. If $w(0) = 0$, then choose some value of β. Observe that it is not necessary to know $w(t)$ for all t, in order to recover $p(t)$ from its short time Fourier transform.

Alternately, one can also recover $p(t)$ from (4.9) by multiplying both sides by $\overline{w}(t-\beta)$ and integrating with respect to β. The overbar denotes complex conjugate.

Then,

$$p(t) = \frac{1}{2\pi} \cdot \frac{\displaystyle\int\limits_{-\infty}^{\infty} \int\limits_{-\infty}^{\infty} P_{STFT} \ (\omega, \beta) \ \overline{w}(t-\beta) \ e^{j\omega t} \ d\omega \ d\beta}{\displaystyle\int\limits_{-\infty}^{\infty} |w(t-\beta)|^2 \ d\beta} \qquad (4.11)$$

This of course assumes $\int\limits_{-\infty}^{\infty} |w(t-\beta)|^2 \ d\beta$ is finite. However, if the window function is infinite, then one can multiply both sides of (4.9) by another sequence $r(t)$, such

that

$$\int_{-\infty}^{\infty} \bar{r}(t-\beta) \ w(t-\beta) \ d\beta \ = \ 1 \qquad (4.12)$$

An attempt was made by Gabor [8] in 1946 to develop a methodology where a function can be simultaneously localized in time and frequency. If that is possible, then the "frequency content" of any signal can easily be obtained by observing the response in certain narrow frequency bands. Hence it is possible to track the instantaneous frequency of a signal.

In order to simplify the presentation, we introduce the generalized form of Parseval's theorem for two functions p(t) and q(t) and their Fourier transforms $P(\omega)$ and $Q(\omega)$. So that

$$<p;q> \ = \ \int_{-\infty}^{\infty} p(t) \ \bar{q}(t) \ dt \ = \ \frac{1}{2\pi} \ \int_{-\infty}^{\infty} P(\omega) \ \bar{Q}(\omega) \ d\omega \ = \ \frac{1}{2\pi} \ <P;Q> \qquad (4.13)$$

where $\langle \bullet;\bullet \rangle$ denotes the inner product between two functions and the overbar denotes the complex conjugate. Note that if

$$q(t) \ = \ \delta(t) \quad \text{and} \quad Q(\omega) \ = \ e^{-j\omega t} \qquad (4.14)$$

then (4.13) divided by (4.14) defines the inverse transform and if

$$Q(\omega) \ = \ 2\pi\delta(\omega) \quad \text{and} \quad q(t) \ = \ e^{j\omega t} \qquad (4.15)$$

then (4.15) when substituted in (4.13) defines the forward Fourier transform.

In the next section we see how Gabor through the choice of certain window functions made possible not only to localize a signal in the time domain, but was also able to localize its frequency content in a narrow frequency band.

4.B   GABOR TRANSFORM [1, 8, 9]

The objective of the Gabor transform is to expand p(t) into a set of functions that are simultaneously limited in both time and frequency. This is in contrast to Fourier transform where, the expansion is done by functions $e^{-j\omega t}$ which are not time limited, but highly localized in frequency.

Even though from a strict mathematical point of view, it is not possible to localize a function simultaneously both in the time and frequency domain, however this can be achieved from a practical stand point. Let us illustrate this considering a family of functions q(t) such that a member $q_\alpha(t)$ is defined as

$$q_\alpha(t) = \frac{1}{2\sqrt{\pi\alpha}} e^{-\frac{t^2}{4\alpha}} \qquad (4.16)$$

Then the product p(t) $q_\alpha(t)$ can be localized in time from a practical standpoint if $\alpha > 0$. This is because, beyond a certain value $t=T_1$, the function $q_\alpha(t)$ practically decays down to zero and so will the product p(t) $q_\alpha(t)$. Next, we introduce another parameter β, so that the function $w_{\alpha,\beta}(t)$ (which is real) is defined by

$$w_{\alpha,\beta}(t) = w_\alpha(t-\beta) = \frac{1}{2\sqrt{\pi\alpha}} \, e^{-\frac{(t-\beta)^2}{4\alpha}} = q_{\alpha,\beta}(t) \qquad (4.17)$$

Hence β is a shift parameter and now the functions $w_{\alpha,\beta}(t)$ can span any function $p(t)$ for all possible choices of the parameter α and β. Now if we look at the Fourier transform of the product of the two functions $p(t) \, w_{\alpha,\beta}(t)$, which is called the Gabor transform $[G_{\alpha,\beta}(\omega)]$, then

$$G_{\alpha,\beta}(\omega) = \int_{-\infty}^{\infty} p(t) w_{\alpha,\beta}(t) \, e^{-j\omega t} \, dt \qquad (4.18)$$

Note that

$$\int_{-\infty}^{\infty} w_{\alpha,\beta}(t) \, d\beta = \int_{-\infty}^{\infty} w_\alpha(t-\beta) d\beta = 1 \qquad (4.19)$$

Hence integrating (4.18) with respect to β and substituting (4.19) one obtains

$$\int_{-\infty}^{\infty} G_{\alpha,\beta}(\omega) \, d\beta = \int_{-\infty}^{\infty} p(t) \, e^{-j\omega t} \, dt = P(\omega) \qquad (4.20)$$

So the Fourier transform of the function $p(t)$, given by $P(\omega)$ results by integrating the Gabor transform with respect to all possible delay parameters β.

184

Since $<p;q> = \dfrac{1}{2\pi} <P;Q>$ and if $q(t) = w_{\alpha,\beta}(t)\, e^{j\omega t}$, then

$$\int_{-\infty}^{\infty} p(t)\, \bar{q}(t)\, dt = \int_{-\infty}^{\infty} p(t) w_{\alpha,\beta}(t)\, e^{-j\omega t}\, dt = G_{\alpha;\beta}(\omega) = \dfrac{1}{2\pi} \int_{-\infty}^{\infty} P(\Omega)\, \bar{Q}(\Omega)\, d\Omega \quad (4.21)$$

and since $w_{\alpha,\beta}(t)$ is real

$$Q(\Omega) = \int_{-\infty}^{\infty} e^{j\omega t} w_{\alpha,\beta}(t)\, e^{-j\Omega t}\, dt = \int_{-\infty}^{\infty} \dfrac{1}{2\sqrt{\pi\alpha}}\, e^{-\frac{(t-\beta)^2}{4\alpha}}\, e^{j(\omega-\Omega)t}\, dt \quad (4.22)$$

$$= e^{-j(-\omega+\Omega)^2\alpha}\, e^{-(-\omega+\Omega)\beta}$$

Since $\int_{-\infty}^{\infty} e^{-P^2 x^2 \pm qx}\, dx = e^{q^2/4P^2} \cdot \dfrac{\sqrt{\pi}}{P}$

$$G_{\alpha,\beta}(\omega) = \dfrac{1}{2\pi} \int_{-\infty}^{\infty} P(\Omega)\, e^{+j(\Omega-\omega)\beta}\, e^{-(\Omega-\omega)^2\alpha}\, d\Omega = \dfrac{e^{-j\omega\beta}}{2\pi} \int_{-\infty}^{\infty} P(\Omega)\, e^{-(\Omega-\omega)^2\alpha}\, e^{j\Omega\beta}\, d\Omega$$

$$= \dfrac{e^{-j\omega\beta}}{2\sqrt{\pi\alpha}} \int_{-\infty}^{\infty} P(\Omega)\, w_{1/(4\alpha)}(\Omega-\omega)\, e^{j\Omega\beta}\, d\Omega$$

$$(4.23)$$

It is clear from (4.23) that the Gabor transform also localizes the Fourier transform $P(\Omega)$ of $p(t)$ exactly, to give its local spectral information. Hence, not only is the function $p(t)$ localized in time by the function $w_{\alpha,\beta}(t)$, but also its transform $P(\omega)$ is localized in frequency by the function $w_{1/(4\alpha),\beta}(\Omega)$. The width of the window function

in time domain, Δ_t, is then obtained as

$$\Delta_t = \frac{1}{\|w_\alpha\|} \left\{ \int_{-\infty}^{\infty} t^2 \, w_\alpha^2(t) \, dt \right\}^{1/2} \tag{4.24}$$

We have

$$\|w_\alpha\|^2 = \int_{-\infty}^{\infty} \frac{1}{4\pi\alpha} \, e^{-\frac{t^2}{2\alpha}} \, dt = \frac{1}{\sqrt{8\pi\alpha}} \tag{4.25}$$

and

$$\int_{-\infty}^{\infty} \frac{t^2 \, e^{-\frac{t^2}{2\alpha}}}{4\pi\alpha} \, dt = \sqrt{\frac{\alpha}{8\pi}} \tag{4.26}$$

Hence

$$\Delta_t = \left\{ \frac{1}{\sqrt{8\pi\alpha}} \right\}^{-1/2} \left\{ \sqrt{\frac{\alpha}{8\pi}} \right\}^{1/2} = \sqrt{\alpha} \tag{4.27}$$

and the width in the frequency domain $\Delta\omega$ is given by

$$\Delta_\omega = \left\{ \Delta_\omega \right\}_{w_{1/(4\alpha)}} = \frac{1}{2\sqrt{\alpha}} \tag{4.28}$$

So the function p(t) is localized in time at $\beta \pm \frac{\sqrt{\alpha}}{2}$ and in frequency at $\Omega \pm \frac{1}{4\sqrt{\alpha}}$. Note that

$$\Delta_t \cdot \Delta_\omega = \frac{1}{2} \qquad (4.29)$$

So the width of the time-frequency window is unchanged for observing the spectrum at all frequencies. In fact it is seen that the Gabor transform is essentially a short time Fourier transform with the smallest time-frequency window.

4.C WAVELET TRANSFORM

A property not possessed by the window function of the Gabor transform is the additional condition

$$\int_{-\infty}^{\infty} w_{\alpha,\beta}(t) \, dt = 0 \qquad (4.30)$$

namely, the average value of the window is zero. This property gives an extra degree of freedom for introducing a dilation (or scale) parameter in order to make the time-frequency window flexible. With this dilation parameter, the integral wavelet transform provides a flexible time-frequency window which automatically narrows when observing high frequency components and widens when studying low frequency components. Hence it is in tune with our auditory and visual sense

perceptions which at least in the first step processes signals in this fashion. This explains the evolution of the musical scale in the west. For example Figure 1 shows the location of the notes c and g in the major diatonic scale for several octaves [4]. On a lograthimic scale they would appear to be nearly equi-spaced. Thus the notes c and g become sparser and sparser as the frequency increases.

The window function in the wavelet transform takes the form as

$$w_{\alpha,\beta}(t) = \frac{1}{\sqrt{|\alpha|}} \ w\left(\frac{t-\beta}{\alpha}\right) \qquad (4.31)$$

The above function is admissible provided (4.30) is satisfied. The integral wavelet transform of p(t) is defined by WT_p

$$WT_p = \int_{-\infty}^{\infty} p(\tau) \ \bar{w}_{\alpha,\beta}(\tau) \ d\tau = \frac{1}{\sqrt{|\alpha|}} \int_{-\infty}^{\infty} p(\tau) \ \bar{w}\left(\frac{\tau-\beta}{\alpha}\right) \ d\tau \qquad (4.32)$$

with $\alpha \neq 0$.

Then if the center of the window function w(t) is given by t^* and the width of the window is given by Δ_t^w then the function $w_{\alpha,\beta}(t)$ is a window function with the center at $\beta + \alpha t^*$ and width $\alpha \Delta_t^w$.

Note

$$W_{\alpha,\beta}(\omega) = \frac{1}{\sqrt{|\alpha|}} \int_{-\infty}^{\infty} e^{-j\omega t} \, w\left(\frac{t-\beta}{\alpha}\right) dt \tag{4.33}$$

$$= \frac{\alpha}{\sqrt{|\alpha|}} \, e^{-j\beta\omega} \, W(\alpha\omega)$$

where $W(\omega)$ is the Fourier transform of $w(t)$.

From Parseval's relation (4.21), the wavelet transform WT_p of p is given by

$$WT_p = \frac{1}{2\pi} \int_{-\infty}^{\infty} \frac{\alpha}{|\sqrt{\alpha}|} \, P(\omega) \, \overline{e^{-j\beta\omega} \, W(\alpha\omega)} \, d\omega \tag{4.34}$$

The window function in the frequency domain is centered at ω^* and has a

width $\dfrac{2\Delta_\omega^w}{\alpha}$, with the exception of the multiplicative factor $\dfrac{\alpha}{2\pi|\sqrt{\alpha}|}$ and the phase

factor $e^{j\beta\omega}$.

The wavelet transform provides local information in the frequency window

$$\left[\frac{\omega*}{\alpha} - \frac{\Delta_\omega^w}{2\alpha}; \frac{\omega*}{\alpha} + \frac{\Delta_\omega^w}{2\alpha}\right] \tag{4.35}$$

Note that in the wavelet type of analysis, if ω^* of $W(\alpha\omega)$ is assumed to be positive,

then the ratio

$$\left[\frac{\text{center frequency}}{\text{bandwidth}} = \frac{\omega*/\alpha}{2\Delta^w_{\omega/\alpha}} = \frac{\omega*}{2\Delta^w_\omega} \right] \qquad (4.36)$$

is independent of the scaling factor α. The class of bandpass filters represented by (4.35) as a function of α has the property (4.36) and are called constant Q-filters. This type of processing is done by the human ear at least in the first stage of signal detection [4].

From the Wavelet transform given by (4.32) or (4.34), the original function can be recovered utilizing

$$p(t) = \frac{1}{C_w} \int_{-\infty}^{\infty} \int_{-\infty}^{\infty} WT_p \ w_{\alpha,\beta}(\alpha) \ \frac{d\alpha}{\alpha^2} \ d\beta \qquad (4.37)$$

where, $\alpha > 0$

$$C_w = \int_{-\infty}^{\infty} \frac{|W(\omega)|^2}{|\omega|} \ d\omega \qquad (4.38)$$

Hence (4.38) implies only certain classes of window functions can be utilized in the wavelet transform, namely those whose responses decay at least as fast as $\frac{1}{\sqrt{|\omega|}}$ as $\omega \to \infty$.

The convergence of the integral in (4.37) is defined in a weak sense [2], i.e. taking the inner product of both sides of (4.37) with any function $g(x) \ \varepsilon \ \mathcal{L}^2$ and commuting the inner product with the integral over α,β in the right hand side

190

leads to the true formula. Since for any absolutely integrable function $W(\omega)$ - the Fourier transform of $w(t)$ - is continuous, (4.8) can only be satisfied provided

$$W(0) = 0$$

or equivalently $\int_{-\infty}^{\infty} w(x) \, dx = 0$ i.e. the wavelet $w(x)$ has no DC value.

In the continuous domain, all three techniques (Fourier, Gabor, Wavelet) have good theoretical properties. The question is what happens in the discrete domain. Do all these properties carry over to the discrete domain or do certain additional constraints need to be imposed.

5. <u>DISCRETE TRANSFORMS</u>

5.A DISCRETE SHORT TIME FOURIER TRANSFORM (DSTFT)

The discrete representation of (4.8) is given by [4]

$$P_{DSTFT}(z,\beta) = \sum_{n=-\infty}^{\infty} p(n) \, w(n-\beta) \, z^{-n} \qquad (5.1)$$

where

$$z = e^{+j\omega} \qquad (5.2)$$

where $p(n)$ are the sampled versions of $p(t)$ and β is an integer and so the window values are sampled at $w(n-\beta)$. The inverse DSTFT of P_{DSTFT} is given by

$$p(n) \, w(n-\beta) = \frac{1}{2\pi} \int_0^{2\pi} P_{DSTFT}(z,\beta) \, z^n d\omega \qquad (5.3)$$

If we set $\beta = n$, then

$$p(n) = \frac{1}{2\pi w(0)} \int_0^{2\pi} P_{DSTFT}(z,n) \, z^n \, d\omega \qquad (5.4)$$

Hence one can recover $p(n)$ as long as $w(o) \neq 0$. If $w(0)=0$ then one chooses a value of β, for which $w(m)=w(n-\beta) \neq 0$ and the procedure continues.

An alternative representation can be made, provided it is such that

$$\sum_m |w(m)|^2 = 1 \qquad (5.5)$$

For (5.4), $p(n)$ is recovered by

$$p(n) = \frac{1}{2\pi} \int_0^{2\pi} \left(\sum_{m=-\infty}^{\infty} P_{DSTFT}(z,m) \, \bar{w}(n-m) \right) z^n d\omega \qquad (5.6)$$

It is interesting to note that the inversion formula is not unique. For example if z_0 is a zero of the z-transform of the conjugate of the window function, i.e. z_0 is a zero of the polynomial

$$W_1(z) = \sum_{k=-\infty}^{\infty} \bar{w}(k) \, z^{-k} \qquad (5.7)$$

then if we replace $P_{DSTFT}(z, m)$ in (5.6) by $P_{DSTFT}(z, m) + z_0^m$

192

then (5.6) is still satisfied. This is in contrast to the conventional Fourier transform, which provides a unique inverse.

5.B   DISCRETE GABOR TRANSFORM

In the discrete Gabor transform, the objective is to represent the signal $p(t)$, by a series as

$$p(t) \sim \hat{p}(t) = \sum_{k=-\infty}^{\infty} \sum_{\ell=-\infty}^{\infty} a_{k\ell} \ \psi_{k\ell}(t) \tag{5.8}$$

where

$$\psi_{k\ell}(t) = e^{-\alpha^2(t-t_k)^2} \ e^{j(2\pi f_\ell t k)} \tag{5.9}$$

Gabor presented a heuristic argument for iteratively estimating the coefficients $a_{k\ell}$ so as to obtain an approximation $\hat{p}(t)$. However, no justification of this process was given [5].

Martin Bastiaans [7] used a different set of expansions to

$$g_{k\ell}(t) = (\frac{2}{\sigma})^{1/4} \ e^{-\frac{\pi}{\sigma}(t-kT)^2} \ \frac{e^{j2\pi \ell t}}{T} \ e^{-j\pi k\ell} \tag{5.10}$$

show that the representation (5.9) actually forms a complete set and that the representation error $p(t) - \hat{p}(t)$ goes to zero for a sufficiently large number of basis

functions. The important difference between the representation (5.9) and (5.10) is the choice

$$t_k = kT \tag{5.11}$$

and

$$f_\ell = \frac{\ell}{T} \tag{5.12}$$

where T is the sampling interval.

One of the objectives of this representation is to look at the cell centered at the point $(t_k; f_\ell)$ in the time frequency plane and how its surrounding regions are distributed. The main objectives of the representation (5.8) is that if the signal within the window $NT - \frac{T}{2} \le t \le NT + \frac{T}{2}$ contains a pure sinusoid of frequency f_o, then we would hope that the expression

$$P(NT,f,T) = \int_{NT-T/2}^{NT+T/2} p(t)\, e^{-j2\pi ft}\, dt \tag{5.13}$$

and that $|P(NT,f,T)|^2$ would have a significant magnitude primarily near f_o. However, if one looks at the representation of $p(t)$ given by (5.8) and (5.9), then it is not at all clear that there would not be any leakage from nearby cells where k = N+1, N+2 or N-1, N-2 and so on, to $|P(NT,f,T)|^2$. Indeed the leakage from neighboring cells can produce erroneous interpretations as described in [6]. This

194

is because neither (5.9) nor (5.10) has a finite support in the time domain. They extend for all times. One would expect the signals centered around the cell NT to contribute to P(NT, t, f) if and only if the time domain support in the representation in (5.8) is finite. Otherwise the results are not relevant. This is why Lerner [8] extended the representation in (5.10) to have the basis signals of the general form:

$$v_{k\ell}(t) = v(t-kT) \ e^{\frac{j2\pi\ell t}{T}} \qquad (5.14)$$

v(t) being a "convenient" finite energy function whose energy is concentrated near t=0 and whose energy spectrum $|v(\omega)|^2$ is concentrated near $\omega=0$. This was later modified by Roach [6] who demonstrated that unless the function v(t) is of finite support in the time domain, representation of the form (5.8) produces an energy spectrum $|P(NT,f,T)|^2$ which has no clear relationship to the signal in the corresponding interval in time. Note that this precludes the Gaussian function or the prolate spheroidal functions as possible window functions since they are of infinite duration!

It has been shown that for a proper time-frequency representation, the expansion must be of the form [9]

$$\hat{p}(t) = \sum_{k=k_s}^{k_f} \sum_{\ell=-m}^{m} c_{k\ell} \ \psi_{k\ell}(t) \qquad (5.15)$$

where

$$\psi_{k\ell}(t) = \begin{cases} \sqrt{w(t-t_k)} \ e^{j\omega t} & ; \ |t-t_k| \le T/2 \\ 0 & ; \ |t-t_k| > T/2 \end{cases} \qquad (5.16)$$

The requirement of the window function w(t) is that $W(\omega)$ must have an infinite number of equally spaced zeros. Under that condition

$$c_{k\ell} = \int_{t_k-T/2}^{t_k+T/2} p(t) \ \sqrt{w(t-t_k)} \ e^{-j2\pi Q \ell t} \ dt \qquad (5.17)$$

where Q is the frequency spacing. The interesting point in (5.17) is that the coefficient for a given segment in time is completely independent of the signal outside the kth cell since the coefficients in different time segments are orthonormal, the total energy in the signal is then the sum of all the individual coefficients squared.

It is interesting to observe that (5.16) and (5.17) have close resemblance to the windowed Fourier transform presented in the earlier section, when the window function becomes a rectangular window. However, any window function which results from the convolution of any rectangular pulse with a symmetric window function will provide the mathematical requirements for w(t) in (5.16) and (5.17).

196

5.C DISCRETE WAVELET TRANSFORM

If in the continuous wavelet transform, one uses integer values for some integers k,n in (4.32) and assumes $\beta = 2^k nT$ (one can assume T=1, without loss of generality for the discrete case) and $\alpha = 2^k$ then the discrete wavelet transform of p(t) is given by [4]

$$WT_p(k,n) = \int_{-\infty}^{\infty} p(t) \, 2^{-k/2} \, \bar{w}(2^{-k} \, t-nT) dt \qquad (5.18)$$

The inverse transform is given by

$$p(t) = \sum_{k=-\infty}^{\infty} \sum_{n=-\infty}^{\infty} WT_p(k,n) \, 2^{-k/2} \, w(2^{-k}t-nT) \qquad (5.19)$$

under the condition that the window functions

$$w_{\alpha,\beta}(t) = w_{k,n}(t) = 2^{-k/2} \, w(2^{-k} \, t-nT) \qquad (5.20)$$

are orthonormal, i.e.,

$$\int_{-\infty}^{\infty} w_{k,n}^*(t) \, w_{p,q}(t) \, dt = \delta(k-p) \, \delta(n-q) \qquad (5.21)$$

The shift integers n are chosen in such a way that $w(2^{-k} \, t-nT)$ covers the whole line for all values of t. The wavelet transform thus separates the "object" into different components in its transform domain and studies each component with a resolution matched to its scale.

The wavelet series amounts to expanding the function p(t) in terms of

wavelets $w_{k,n}(t)$, so that

$$p(t) = \sum_{k,n=-\infty}^{\infty} C_{k,n} w_{k,n}(t) \qquad (5.22)$$

If we further assume that the wavelets $w_{k,n}(x)$ are orthogonal [i.e. (5.21) holds], then

$$C_{k,n} = <p; \psi_{k,n}> \qquad (5.23)$$

By comparing (5.18) and (5.23) it is apparent that the $(k,n)^{th}$ wavelet coefficient of f is given by the integral wavelet transform of p if the same orthogonal wavelets are used in both the integral wavelet transform and in the wavelet series. So the wavelet series provides an approximation for p which is not necessarily the least squares ($\mathcal{L}^2$) orthogonal projection that a Fourier Series provides.

Also, the wavelets provide an unconditional basis for $\mathcal{L}^i$ for $1 < i < \infty$. Since $\mathcal{L}^1$ has no unconditional bases, wavelets cannot do the impossible but still they can do a better job than Fourier Expansion by displaying no Gibb's phenomenon for approximating functions that are discontinuous. However if the wavelets used in the approximation are not discontinuous like the Haar wavelets (or Walsh functions) but utilizes continuous functions instead then the Gibb's phenomenon is visible in the wavelet approximation. The problem now at hand is are there any numerically stable algorithms to compute the wavelet coefficients $C_{k,n}$ in (5.23)?

Specifically in real life p is not a given function but is a sampled function. Computing the integrals of $<p; w_{k,n}>$ then requires a quadrature formula. For the smallest value of k, often referred to by the scale parameter, i.e. most negative k, this will not involve many samples of p and one can do the computation quickly. For large scales, however, one faces large integrals, which might considerably slow down the computation of the wavelet transform of any given function. Especially for on-line implementations, one should avoid having to compute these long integrals. One way out is the technique used in multirate/multiresolution analysis, by introducing an auxiliary function $\phi(x)$, so that [2]

$$w(x) = \sum_{m=-\infty}^{\infty} d_m \, \phi(x-m) \tag{5.24}$$

and

$$\phi(x) = \sum_{m=-\infty}^{\infty} c_m \, \phi(2x-m) \tag{5.25}$$

where in each case only a finite number of coefficients c_m and d_m are different from zero.

Here ϕ does not have integral zero but ψ does, and ϕ is normalized such that

$$\int_{-\infty}^{\infty} \phi(x)\,dx = 1 \tag{5.26}$$

and we define $\phi_{k,n}$ even though ϕ is not a wavelet, i.e.

$$\phi_{k,n} = 2^{-k/2} \phi(2^{-k}x-n) \qquad (5.27)$$

Since $\phi(x)$ satisfies an dilation equation in (12), $\phi(x)$ is called the scaling function.

So

$$<p; w_{k,n}> = \sum_{m=-\infty}^{\infty} d_m <p; \phi_{k,n+m}> \qquad (5.28)$$

So the problem of finding the wavelet coefficient is to that of computing $<p; \phi_{j,k}>$. Note

$$<p; \phi_{k,n}> = \sum_{m=-\infty}^{\infty} c_m <p; \phi_{k-1;2n+m}> \qquad (5.29)$$

so that $<p; \phi_{k,n}>$ can be computed recursively starting from the smallest scale (most negative k) to the largest. The advantage of this procedure is that it is numerically robust - namely - even though the wavelet coefficients $C_{k,n}$ in (5.23) are computed with low precision - say with a couple of bits - one can still reproduce p with comparatively much higher precision [2].

In summary, what we have done is as follows: Consider p(t) as a function of time. We have taken the spectrum of p(t) and have separated the spectrum into octaves of widths $\Delta\omega_k$ that is, frequency band ω has been divided into $[2^k\pi$ to $2^{k+1}\pi]$ for all values of k, and now we define wavelets in each frequency bin $\Delta\omega_k$ and approximate p(t) by it. If we choose

$$\phi(t) = \frac{\sin \pi t}{\pi t} \qquad (5.30)$$

$$\psi(t) = 2\phi(2t) - \phi(t) \qquad (5.31)$$

then the wavelet expansion of p(t) with respect to ψ is

$$w_{k,n}(t) = 2^{k/2}\, \psi(2^k t - n) \quad \text{(with } T=1\text{)} \qquad (5.32)$$

$$p(t) = \sum p_k(t) = \sum_{k,n} C_{k,n}\, \psi_{k,n}(t) \qquad (5.33)$$

The functions $w_{k,n}(t)$ are orthonormal because their bandwidths are non overlapping, namely for a fixed k, $p_k(\omega)$, has the bandwidth $\Delta\omega_k$ which is $[2^k\pi, 2^{k+1}\pi]$. So the wavelet expansion of a function is complete in the sense that it makes an approximation by orthogonal functions which have non overlapping bandwidth.

As concluded by Vaidyanathan [4], even though the continuous wavelet transform has a wider scope with deeper mathematical issues, the discrete wavelet transform is quite simple and can be explained in terms of basic filter theory. Even before the development of wavelets, nonuniform filter banks have been used in speech processing by [12, 13]. The motivation was that the nonuniform bandwidths could be used to exploit the nonuniform frequency resolution of the human ear [14]. So if the wavelet application is already in the digital domain, it is really not necessary to understand the deeper results of the scaling function $\phi(t)$ and wavelets w(t). In this case, all we need to focus on is the dilation and the shift

principle to generate a complete basis.

Moreover, the question of how adequately the DC value of the function p is approximated by the wavelet series is a problem since the wavelets do not have any DC value. However, in numerical analysis, one may be required to expand a function p in a basis which should have a DC value!

6. DIFFERENT PULSE SHAPING TECHNIQUES

There are various pulse shaping techniques for radar target identification such as example, the K-pulse and E-pulse. The differences between the T-pulse and the K-pulse and E-pulse are delineated next.

6.A K-pulse [15-17]

The objective behind the K-pulse is as follows. Consider a linear system with the transfer function H(s), defined by

$$H(s) = \frac{N(s)}{D(s)} \qquad (6.1)$$

where N(s) is a numerator polynomial and D(s) is the denominator polynomial. Both are assumed to have finite degrees, namely

$$N(s) = a_o + a_1 s + a_2 s^2 \ \ldots \ + a_n s^n \qquad (6.2)$$

$$D(s) = b_o + b_1s + b_2s^2 \ldots + b_m s^m \qquad (6.3)$$

In general, the impulse response h(t) derived from H(s) would be causal (i.e. h(t) $\equiv$ 0 for t<0) and would exist up to t $\rightarrow$ ∞. If the transfer function H(s) has poles (i.e. $b_i \neq 0$), then the impulse response cannot be of finite duration.

However, suppose that the system H(s) is excited by a pulse d(t), where d(t) is the inverse transform of D(s). So, since D(s) is an all-zero system, the waveform is time limited. If the waveform d(t) excites H(s), this waveform will cancel the response due to the poles of the target and the target return will be due to N(s).

In summary, the basic philosophy of the K-pulse is to excite a target by a waveshape d(t) which is the inverse transform of the denominator polynomial D(s) only. This in turn will produce a target return n(t) due to N(s) which will be of finite duration. Hence, if the K-pulse of a target is properly designed, then the response of that target due to the K-pulse will be of finite duration whereas if the K-pulse is not matched to the target then the response of the target due to the K-pulse will continue for a long time. The crux of the problem in engineering the K-pulse lies in determining D(s) and then synthesizing the pulse d(t) which will be the characteristic response of that target only.

6.B   E-Pulse [18,19]

There is another waveform design technique that has been developed for radar target discrimination. This is called the E-pulse technique. In the E-pulse,

the objective is to excite the target with the mirror image of the impulse response. So if the impulse response of the target is h(t), then the excitation waveform has to be h(-t). Under this circumstance, this response corresponds to that of a matched filter. It is well known that the output of a matched filter produces a sharp peak in the response maximizing the instantaneous energy from the target when the waveform is matched to it. The E-pulse is also related to Prony's method [20].

7. DEVELOPMENT OF THE T-PULSE

In both the K-pulse and the E-pulse approaches one has to know what the target response is before the waveshapes can be designed. Without an apriori knowledge of the target, it is difficult to proceed in the design of K-pulses and E-pulses. In the T-pulse approach, the waveshape design is independent of the target. In this case, the objective is to produce a time limited waveform, whose spectral energy would be concentrated in a narrow band.

Theoretically, if a waveform is of finite duration in time, it cannot simultaneously be bandlimited [21-23]. Hence, the objective is to design a time domain waveform whose 99.9% of the energy would be concentrated in the narrow spectral band Δf. We will limit our discussion to low pass signals since any bandpass signals can be represented by a modulated low pass signal. The problem of finding a waveshape for construction of a discrete finite duration signal whose

spectral energy is maximized in a given band has been outlined in [24]. The constructed signal is also orthogonal to the block shifted version of itself. In this presentation, an additional constraint is put on the waveshape in which the waveform has no DC value. This is because if a particular waveshape needs to be transmitted through an antenna then this constraint is useful, as antennas cannot radiate DC.

The construction of the T-pulse is carried out in the discrete domain. Let us assume a discrete signal sequence f(m), which is defined for m=0,1,2,..., N_m-1 and is identically zero outside these N_m values. Let us assume there are N_s samples in one baud time (in an approximate way, the baud time is the time duration between zero crossings of a signal), then the total number of baud times N_c is,

$$N_c = N_m/N_s \qquad (7.1)$$

The DFT of the signal f(m) is given by

$$F(k) = \frac{1}{\sqrt{N_k}} \sum_{m=0}^{N_m-1} f(m) \exp\left(\frac{-j2\pi km}{N_k}\right) \qquad (7.2)$$

for k = 0, 1, ..., N_k-1.

So in the frequency domain, N_k is the total number of samples of the DFT sequence F(k). In the frequency domain, if we assume there are N_r samples per baud rate (inverse of baud time) then

$$N_k = N_r \cdot N_s \qquad (7.3)$$

and increasing N_r increases the resolution in the frequency domain.

In the T-pulse construction, the objective is to maximize the inband energy within the set $\phi = \{-N_b \leq k \leq N_b\}$. Or equivalently, it minimizes the energy outside the N_b samples. In addition, the waveshape has to be orthogonal with its shifted version and this will minimize the intersymbol interference. This implies that

$$\sum_{m=0}^{N_m-1} f(m)\ f(m+kN_s) - \delta(k) = 0 \qquad (7.4)$$

$$\text{for} \quad k=0,\ 1,\ ...,\ N_c-1$$

where $\delta(k)$ is the impulse function. This guarantees that if the waveform is shifted by a baud time or its multiples, then the waveshape is orthogonal to itself. Note that when k=0, it is the square of the function itself and no constraint need to be put on that. In addition, we need to put in a DC constraint, i.e. the waveshape should have no DC component. Hence

$$\frac{1}{N_m} \sum_{m=0}^{N_m-1} f(m) = 0 \qquad (7.5)$$

So the cost function J_c, that will be minimized is

$$J \ \Delta \ w_e\ E_{out} + w_m\ e_m^2 + \sum_{p=0}^{N_c-1} w_k\ e_p^2 \qquad (7.6)$$

where w_e, w_m and w_k are various weights to the errors E_{out}, e_m, e_k. The weights

should be adjusted in a search procedure that has been designed to minimize J.

In addition,

$$E_{out} = \text{out of band energy} = E - E_{in}$$

$$= \sum_{m=0}^{N_m-1} |f(m)|^2 - \sum_{k=-N_b}^{N_b} |F(k)|^2 \tag{7.7}$$

and

$$e_m \ \Delta \ \sum_{m=0}^{N_m-1} f(m) \tag{7.8}$$

$$e_p \ \Delta \ \sum_{m=0}^{N_m-1} f(m) \ f(m+pN_s) \quad \text{for} \quad p=1, 2, ..., N_c-1 \tag{7.9}$$

Equivalently,

$$J = w_e \left[\sum_{m=0}^{N_m-1} |f(m)|^2 - \frac{1}{N_k} \sum_{m=0}^{N_m-1} \sum_{n=0}^{N_m-1} f(m)f(n) \frac{\sin\left\{ \frac{2\pi(n-m)}{N_k}\left(N_b+\frac{1}{2}\right)\right\}}{\sin\left\{\pi \frac{(n-m)}{N_k}\right\}} \right] \tag{7.10}$$

$$+ \sum_{p=0}^{N_c-1} w_k \left[\sum_{m=0}^{N_m-1} f(m) \ f(m+pN_s) - \delta(p) \right]^2 + \frac{w_m}{N_m^2}\left[\sum_{m=0}^{N_m-1} f(m) \right]^2$$

In summary, the following observations are of importance.

1) Note that the objective is to minimize the cost function J, such that E_{out} is minimum with $e_m=0$, and $e_p=0$ for $p=0, 1, ..., N_c-1$.

2) The weights w_e, w_m and w_p ($p=0, 1, ..., N_c-1$) should be adjusted in a search procedure to achieve the above goal.

The minimization process can be outlined as follows:

Step 1: Choose an initial guess for f(m) and initial guess for the weights w_e, w_m and w_k, $k=0, ..., N_c-1$.

Step 2: Compute the gradient of the functional J, with respect to f(m). This is given by

$$\frac{\partial J}{\partial f(m)} = 2w_e \left[\sum_{m=0}^{N_m-1} f(m) \left\{ 1 - \frac{1}{N_k} \sum_{n=0}^{N_m-1} f(n) \frac{\sin\left[\frac{2\pi(n-m)}{N_k}(N_b+\frac{1}{2})\right]}{\sin\left[\frac{\pi(n-m)}{N_k}\right]} \right\} \right]$$

$$+2 \sum_{p=0}^{N_c-1} w_p \left(\left[\sum_{m=0}^{N_m-1} f(m)f(m+pN_s) - \delta(p) \right] \cdot \left[\sum_{m=0}^{N_m-1} \{f(m)+f(m+pN_s)\} \right] \right) \quad (7.11)$$

$$+ \frac{2w_m}{N_m^2} \sum_{m=0}^{N_m-1} f(m)$$

assuming f(m) is real.

Next an optimum step length to update the signal sequence f(m) is chosen through one dimensional searches.

Step 3: If the norm of the previous gradient vector is not small enough, go to step 2. Otherwise see whether the orthogonality errors $|e_p|$ for p=1, 2, ..., N_c-1 are small enough. If the errors are small enough stop the process. If the errors are still considered to be large, increase each w_p (k=1, 2, ..., N_c-1) by a factor and then go to step 2.

Note that throughout the process, w_e is the fixed nonzero value, since the absolute value of the total energy is not important. However, w_e can be increased during the process if the inband energy to generate the T-pulse is unexpectedly low. This may happen as the cost function may have more than one local minima and increasing w_e can make one jump out of an undesired local minimum.

8.   PROGRAM DESCRIPTION FOR T-PULSE GENERATION

This section describes a user oriented computer program to generate a T-pulse. The inputs required are the number of sample points that will constitute the waveform, the number of baud times and the percentage bandwidth over which the energy is concentrated. The description of the program along with sample output is given in the Appendix. This designs the baseband signal. To shift the energy spectrum into another band, a narrowband cw signal is amplitude

modulated by the baseband T-pulse. Hence the final waveform has a very narrowband and can easily be transmitted by conventional antennas. Since the effective bandwidth of the T-pulse is small, the problem of the phase center of the antenna changing and producing a distorted wideband pulse, thus does not exist.

At the end of the computer program description, an example is presented showing the synthesized T-pulse in the time domain in Figure 2 and its spectra in Figure 3.

The T-pulse was designed for $N_{baud}=4$ and $N_{band}=130$ and for 100 samples. Note that the T-pulse has zero mean and is orthogonal to its shifted versions. The second figure shows the spectra of the T-pulse. It is seen that the bandwidth of the T-pulse is 13 units as seen from the FFT.

9. AN APPLICATION OF THE T-PULSE

In this section, an example is presented to illustrate the utility of the T-pulse for target identification.

Consider the following experiment. Take a 2m long thin wire dipole of radius 0.01m. Consider that a narrowband Gaussian pulse excites this dipole from the broadside direction. The Gaussian pulse is of the form $A \exp[(t-t_o)^2]$, where t_o = 2.5 light meters (lm). [A light meter is defined as the time taken by light to travel 1 meter. Hence 1 light meter = 3.33 nanosec]. Since the data will be discrete, assume the sampling time T to be 0.5 nsec = 0.15 light meter. Now

assume that the derivative of the Gaussian pulse excites the dipole from the broadside direction [25]. The derivative of the Gaussian pulse is shown in Figure 4. Observe that the exciting pulse approaches zero after t = 6.0 lm. Next compute the current at the center of the dipole utilizing the conjugate gradient method [24]. Here the hyperbolic wave equation is transformed to a boundary value problem which is solved to a prespecified degree of accuracy, so that the current induced at the center of wire is known very accurately. This is achieved by minimizing the residual over a space and time grid. The synthesized current response at the center of the thin wire is shown in Figure 5. Figure 6 shows the DFT (Discrete Fourier Transform) amplitude spectrum of the first 128 points (samples) of the exciting pulse of Figure 4. It is seen that the input has a wide spectrum, extending to a frequency index of 40. In Figure 7, the amplitude spectrum of the tail of the induced current, i.e. for $t \geq 6$ lm, is presented. From Figure 7, we can observe four resonances for the wire, which are located at the frequency indices k=4, 13, 24 and 26 or f = 0.0625, 0.203, 0.375 and 0.406 (in GHz). Note that the frequency f is related to the frequency index k by $f = k/(128T)$ for a 128 - point DFT. It is important to note that for an ideal 2-m dipole the resonant frequencies should be f = 0.075, 0.225, 0.375, ... these are computed from $f_i = ic/(2L)$, where c is the velocity of light, L is the length of the dipole (= 2m) and i is an odd integer. The first three resonant frequencies detected in Figure 7 appear to approximately match the first three ideal frequencies. The fourth resonant frequency is perhaps due to the vector addition of the infinite number of poles located in the complex

210

plane. This fourth resonant frequency is not due to computational error involved in the computer codes. This variable has been eliminated by solving the wave equation in an iterative fashion by minimizing the error over a time-space grid and thereby obtaining the solution to a high degree of accuracy ($\sim 10^{-5}$) [24].

The objective of this example is the following: It is possible to excite the resonances at k=24 and k=26 without exciting the resonances at k=13 and 5. Since the resonance at k=13 is approximately 20 dB below the fundamental and the resonances at k=24 and k=26 are 33 dB below the first resonance [as per Figure 7], it is important that the first two resonances not be excited if we want to "zoom in" at k=24 and k=26. To this end the T-pulse is designed. A baseband T-pulse is designed as shown in Figure 8 utilizing the algorithm presented in the previous section. Figure 8 is a baseband T-pulse of duration D = 127, T = 63.5 nsec = 19.05 lm, and with in-band energy of 99.995% contoured within the bandwidth of 2/64 GHz. The DFT amplitude of the baseband signal is shown in Figure 9. It is seen that the spectrum drops to 40 dB in a frequency index of 2 units. Now if we want to translate the spectrum to k=24, we simply amplitude modulate a sine function of k=25 by the baseband T-pulse. This produces the T-pulse of Figure 10. The amplitude spectrum of the modulated T-pulse is shown in Figure 11. Observe that the amplitude spectrum is 70 dB down at k=13 and about 80 dB down at k=5. As one sees, the sidelobes in the spectrum are almost 50 dB from the main peak and half width of the main lobe is about two times the reciprocal of 128T. Hence, through this T-pulse one can excite the higher order resonances without exciting

the dominant resonances.

At this point, one might ask, why not use a cw signal, since basically we are exciting the target with an essentially monochromatic signal. The problem is that from a practical standpoint, the pulse that one has to generate cannot be of infinite duration. If the signal were of infinite duration then it would truly be cw. We have to gate the cw signal - which implies that the carrier frequency is windowed. If we use a conventional windowing technique like rectangular, Bartlett (triangular), Hanning, Hamming or Blackman it will be impossible to obtain a spectrum like that of Figure 9. Figure 12 shows the spectrum of conventional window functions. Comparing Figures 11 and 12 it is clear that with conventional windows it is not possible to obtain such a low sidelobe.

We now let the optimal modulated T-pulse shown in Figures 8 and 9 (which are considered to be the derivatives of the impinging electric field pulses) excite the dipole. Figure 13 shows the current response produced by the pulse with center frequency k=25. As one observes, after the exciting pulse dies out, i.e. for $t \geq 19.2$ light-meters, the current has a strong tail, which indicates that the preselected resonant frequency (k=25) is close to some actual resonant frequency of the target. The other interesting feature to note is that the target has two resonances. This interesting modulation phenomenon in the tail of the current of Figure 13 is clearly explained by Figure 14 which shows the DFT amplitude spectrum of that tail. The two dominant frequencies k=24 and k=26 in the tail of the current produce the beat phenomenon since they are within the passband of the incident

pulse as shown in Figure 11. The plots of Figure 14 also confirm the presence of a double resonance as shown in Figure 7.

The strength of the T-pulse technique is now clear. Through the T-pulse it is possible to zoom into a narrow spectral band of the response to observe special artifacts which can be certain specific "fingerprints" of the target. For example in this case, the modulated response can be treated as a characteristic feature from wire-like targets. Given that, it is now possible to zoom into the response of the target to see if such features exist!

The second salient feature of the T-pulse is that it is an extremely narrowband signal. Hence conventional transmitting and receiver systems may be used to carry out experiments utilizing the T-pulse. Dispersion, which is a great evil for broadband systems has practically no effect on the T-pulse. Hence, conventional narrowband antennas may be used to transmit and receive T-pulses.

10. HARDWARE REQUIREMENTS

The T-pulse is an extremely narrowband pulse which can be used to modulate any carrier frequency. Hence the effective bandwidth of the transmit and receive pulses are very small. Hence any conventional off - the shelf equipment can be used to generate, transmit and receive T-pulses. Since the effective bandwidth of the pulse is extremely small, broadband antennas like log periodic, equiangular spirals which are highly dispersive antennas can be used

without any problem to process T-pulses.

The T-pulse in the time domain can easily be constructed from single frequency measurements. This can be accomplished either through Cauchy's method [26, 28] or through Hilbert Transform techniques [32].

11. CONCLUSION

The versatility of the T-pulse technique has been presented both from a mathematical transform point of view and also as a waveshaping technique. The strengths of the T-pulse technique has been delineated and an example has been presented to illustrate how the T-pulse technique can be actually implemented in practice.

12. REFERENCES

1. C. K. Chui, "An introduction to wavelets", Academic Press, New York 1992.

2. I. Daubechies, "Ten lectures on wavelets", SIAM, CBMS, Vol. 6, Philadelphia, 1992.

3. R. Gopinath and C. S. Burrus, "Wavelet transforms and filter banks", in Wavelets - A Tutorial in Theory and Applications, C. K. Chui (ed.), pp. 603-654, Academic Press, 1992.

4. P. P. Vaidyanathan, "Multirate systems and filter banks", Prentice Hall, New Jersey, 1993.

5. F. I. Tseng, T. K. Sarkar and D. D. Weiner, "A novel window for harmonic analysis", IEEE Trans. on Acoustics, Speech and Signal Processing", pp. 177-188, April 1981.

6. W. F. Walker, T. K. Sarkar, F. I. Tseng and D. D. Weiner, "Carrier frequency estimation based on the location of the spectral peak of a windowed sample of carrier plus noise", IEEE trans. on Inst. and Meas., Vol. IM-31, pp. 239-249, Dec. 1982.

7. W. F. Walker, T. K. Sarkar, F. I. Tseng and J. Cross, "Optimum windows for carrier frequency estimation", IEEE Trans. on Geoscience Electronics, Vol. 21, pp. 446-454, Oct. 1983.

8. D. Gabor, "Theory of communications", Journal of the Institute for Electrical Engineers", pp. 429-457, Nov. 1946.

9. J. E. Roach, "A vector space approach to time-variant energy spectral analysis", Ph.D. Thesis, Syracuse University, Syracuse, New York, 1982.

10. M. Bastiaans, "Gabor's expansion of a signal into gaussian elementary signals", Proc. of the IEEE, Vol. 68, April 1980, pp. 538-539.

11. R. Lerner, "Representation of signals", Chapter 10 in Lectures on Communication System Theory, E. Baghdady, ed., McGraw-Hill, New York, 19961.

12. G. A. Nelson, L. L. Pfeiffer and R. C. Wood, "High speed octave band digital filtering", IEEE Trans. on Audio and Electroacoust., Vol. AU-20, pp. 8-65, March 1972.

13. R. W. Schafer, L. R. Rabiner and O. Herrmann, "FIR digital filter banks for speech analysis", Bell System Technical J., Vol. 54, pp. 531-544, March 1975.

14. J. L. Flanagan, "Speech analysis, synthesis and perception", Springer-Verlag, New York, 1972.

15. E. M. Kennaugh, "The K-pulse concept", IEEE Trans. Antennas and Propagation", Vol. AP-29, pp. 327-331, Mar. 1981.

16. L. C. Chan, D. L. Moffatt and L. Peters, "A characterization of subsurface radar target", Proc. IEEE, Vol. 67, pp. 991-1000, July 1979.

17. C. W. Chuang and D. L. Moffatt, "Natural resonance of radar target via prony's method and target discrimination", IEEE Trans. on Aerospace and Electronics", Vol. AES-12, pp. 583-589, Sept. 1976.

18. K. M. Chen and D. Westmorland, "Radar waveform and application for exciting single mode backscatters from a sphere and application for target discrimination: Radio Science, Vol. 17, No. 3, pp. 574-588, May 1982.

19. E. J. Rothwell, K-M Chen and D. P. Nyquist, "Extraction of the natural frequencies of a radar target from a measured response using E-pulse techniques", IEEE Trans. Ant. Propagat., Vol. AP-35, June 1987, pp. 715-720.

20. Y. Hua and T. K. Sarkar, "A discussion of E-Pulse method and Prony's method for Radar Target Resonance Retrieval from Scattered field", IEEE Trans. on Antennas and Propagation, Vol. 37, No. 7, pp. 944-946, July 1989.

21. I. Gerst and J. Diamond, "The elimination of intersymbol interference by input signal shaping", Proc. IRE, Vol. 19, pp. 1195-1203, 1963.

22. P. H. Halpern, "Optimum finite duration nyquist signals", IEEE Trans. Commun., Vol. Com-27, pp. 886-888, June 1979.

23. E. Panayirci and N. Tugbay, "Optimum design of finite duration nyquist signals", Signal Processing, Vol. 7, pp. 57-64, 1984.

24. Y. Hua and T. K. Sarkar, "Design of optimum discrete finite duration orthogonal nyquist signals", IEEE Trans, on Acoustics, Speech and Signal Processing, Vol. 36, No. 4, April 1988, pp. 606-608.

25. T. K. Sarkar, S. M. Rao and S. A. Dianat, "The Application of the Conjugate Gradient Method to the Solution of Transient Electromagnetic Scattering from Thin Wire", Radio Science, Sept. 1984, pp. 1319-1326.

26. K. Krishnamoorthy, T. K. Sarkar, X. Yang, E. K. Miller and G. J. Burke, "Use of Frequency Derivative Information to Reconstruct the Scattered Electric Field of a Conducting Cylinder over a wide Frequency Band", Journal of Electromagnetic Waves and Applications, Vol. 5, No. 6, pp. 653-663. Also in Computer Physics Communications, Vol. 68, 1991, pp. 126-144.

27. K. Kottapolli, T. K. Sarkar, Y. Hua, E. K. Miller and G. J. Burke, "Accurate Computation of Wideband Response of Electromagnetic Systems Utilizing Narrow-Band Information", IEEE Trans. on MTT, April 1991, pp. 682-687.

28. T. K. Sarkar, H. Wang, R. Adve, M. Moturi and M. Wicks, "Evaluation of a Casual Time Domain Response from Bandlimited Frequency Domain Data", in Directions in Electromagnetic Wave Modelling, Ed. by H. Bertoni et.al., Plenum Press, 1993.

29. Y. Hua and T. K. Sarkar, "Generalized Pencil-of-Functions method for Extracting the Poles of an Electromagnetic System from its Transient Response", IEEE Trans. on Antennas and Propagation, Vol. 37, No. 2, pp. 229-234, February 1989.

30. Z. Maricevic, T. K. Sarkar, Y. Hua and A. R. Djordjevic, "Time Domain Measurements with the Hewlett Packard Network Analyzer HP8510 Using the Matrix Pencil Method", IEEE Trans. on MTT, March 1991, pp. 538-547.

31. Y. Hua and T. K. Sarkar, "On SVD for Estimating Generalized Eigenvalues of Singular Matrix Pencil in Noise", IEEE Trans. on Acoustics, Speech and Signal Processing, April 1991, Vol. 39, pp. 892-900.

32. T. K. Sarkar, H. Wang, R. Adve, M. Moturi and M. Wicks, "Evaluation of a Casual Time Domain Response from Bandlimited Frequency Domain Data", in Directions in Electromagentic Wave Modelling, Ed. by H. Bertoni et.al., Plenum Press, 1993.

Appendix A1: <u>Computer Program Description</u>

```
C---------------------------------------------------------------------
C COMPUTER PROGRAM DESCRIPTION
C MAIN PROGRAM.
C T-pulse with zero mean and shift orthogonality. Programmed by Y.Hua.
C     !!
C THE DIMENSION STATEMENTS SHOULD BE CHANGED FOR SIGNALS OF MORE THAN
C 300 POINTS OR MORE THAN 10 BAUD TIME DURATIONS.
C     !!
C IPM(4)--NSAM,NCON,NRES,NBAND;
C B(300,300)--MATRIX;
C F(300)--SIGNAL VECTOR;
C GJC(300)--GRADIENT VECTOR;
C D(10)--WEIGHT VECTOR ON ORTHOGONALITY ERRORS EXCEPT THAT D(1) IS THE
C     WEIGHT ON THE TOTAL ENERGY DEVIATION FROM UNITY;
C RATE(10)--FACTORS TO INCREASE D(10);
C WEI--WEIGHT ON ENERGY;
C WR--FACTOR TO INCREASE WEI;
C WMEAN -- weight on mean;
C WMEANR -- factor to increase WMEAN;
C ERROR--USED TO CHECK THE NORM OF GRADIENT;
C LIMITA--LIMIT ON ITERATION A;
C LIMITB--LIMIT ON ITERATION B;
C AR--STEP LENGTH;
C XJ--ENERGY PERCENTAGE WITHIN GIVEN BANDWIDTH;
C XCON(10)--NORMALIZED ERRORS ASSOCIATED WITH ORTHOGNALITY CONSTRAINS
C          EXCEPT THAT XCON(1) IS TOTAL ENERGY IN THE SAMPLE SEQUENCE;
C XGJC--GRADIENT NORM;
C NST--TOTAL NUMBER OF SAMPLES BEING CONSIDERED;
C
C
C
      INTEGER YES
      REAL*8 B(300,300),GJC(300),F(300),XGJC,AR,XJ,XCON(10),D(10),WEI,WR
      REAL*8 ACC,XMAX,XIND
      real*8 WMEAN, WMEANR
      DIMENSION RATE(10),LIMIT(2)
      COMMON B,WEI,IPM(4),WMEAN
C
C INPUT IPM(4)(NSAM,NCON,NRES,NBAND) FROM TERMINAL.
      WRITE(6,1000)
1000  FORMAT(1X,'INPUT THE PARAMETERS(NSAM,NCON,NRES,NBAND):',
     1 /,1X,'(INTEGERS ONLY! AND NCON<=10, NSAM*NCON<=300,NCON<=NRES)')
      READ(5,1010) (IPM(I),I=1,4)
1010  FORMAT(I)
C
C CHECK DATA.
      write(6,1212) (ipm(i),i=1,4)
1212  format(1x,'NSAM,NCON,NRES,NBAND: ',4i4,1x,1a)
      CALL BMATX
      NST=IPM(1)*IPM(2)
C
C PROGRAM INITIALIZES F(*) AS A RECTANGULAR WINDOW IN THE MIDDLE .
      DO 20 I=1,NST
20    F(I)=0.
      NST2=NST/2
      DO 21 I=1,IPM(1)/2
      F(NST2+I)=1.
21    F(NST2-I+1)=-1.
      IF(FLOAT(NST2).NE.FLOAT(NST)/2.) F(NST2+IPM(1)/2+1)=1.
C
C DESIGNER INITIALIZES F(*) THROUGH FILE DATA.DAT
3110  WRITE(6,1110)
1110  FORMAT(1X,'DO YOU WANT TO ININIALIZE THE SIGNAL F?
```

219

```
C-----------------------------------------------------------------------
C COMPUTER PROGRAM DESCRIPTION
C MAIN PROGRAM.
C T-pulse with zero mean and shift orthogonality. Programmed by Y.Hua.
C    !!
C THE DIMENSION STATEMENTS SHOULD BE CHANGED FOR SIGNALS OF MORE THAN
C 300 POINTS OR MORE THAN 10 BAUD TIME DURATIONS.
C    !!
C IPM(4)--NSAM,NCON,NRES,NBAND;
C B(300,300)--MATRIX;
C F(300)--SIGNAL VECTOR;
C GJC(300)--GRADIENT VECTOR;
C D(10)--WEIGHT VECTOR ON ORTHOGONALITY ERRORS EXCEPT THAT D(1) IS THE
C     WEIGHT ON THE TOTAL ENERGY DEVIATION FROM UNITY;
C RATE(10)--FACTORS TO INCREASE D(10);
C WEI--WEIGHT ON ENERGY;
C WR--FACTOR TO INCREASE WEI;
C WMEAN -- weight on mean;
C WMEANR -- factor to increase WMEAN;
C ERROR--USED TO CHECK THE NORM OF GRADIENT;
C LIMITA--LIMIT ON ITERATION A;
C LIMITB--LIMIT ON ITERATION B;
C AR--STEP LENGTH;
C XJ--ENERGY PERCENTAGE WITHIN GIVEN BANDWIDTH;
C XCON(10)--NORMALIZED ERRORS ASSOCIATED WITH ORTHOGNALITY CONSTRAINS
C         EXCEPT THAT XCON(1) IS TOTAL ENERGY IN THE SAMPLE SEQUENCE;
C XGJC--GRADIENT NORM;
C NST--TOTAL NUMBER OF SAMPLES BEING CONSIDERED;
C
C
C
      INTEGER YES
      REAL*8 B(300,300),GJC(300),F(300),XGJC,AR,XJ,XCON(10),D(10),WEI,WR
      REAL*8 ACC,XMAX,XIND
      real*8 WMEAN, WMEANR
      DIMENSION RATE(10),LIMIT(2)
      COMMON B,WEI,IPM(4),WMEAN
C
C INPUT IPM(4)(NSAM,NCON,NRES,NBAND) FROM TERMINAL.
      WRITE(6,1000)
1000  FORMAT(1X,'INPUT THE PARAMETERS(NSAM,NCON,NRES,NBAND):',
     1 /,1X,'(INTEGERS ONLY! AND NCON<=10, NSAM*NCON<=300,NCON<=NRES)')
      READ(5,1010) (IPM(I),I=1,4)
1010  FORMAT(I)
C
C CHECK DATA.
      write(6,1212) (ipm(i),i=1,4)
1212  format(1x,'NSAM,NCON,NRES,NBAND: ',414,1x,1a)
      CALL BMATX
      NST=IPM(1)*IPM(2)
C
C PROGRAM INITIALIZES F(*) AS A RECTANGULAR WINDOW IN THE MIDDLE .
      DO 20 I=1,NST
20    F(I)=0.
      NST2=NST/2
      DO 21 I=1,IPM(1)/2
      F(NST2+I)=1.
21    F(NST2-I+1)=-1.
      IF(FLOAT(NST2).NE.FLOAT(NST)/2.) F(NST2+IPM(1)/2+1)=1.
C
C DESIGNER INITIALIZES F(*) THROUGH FILE DATA.DAT
3110  WRITE(6,1110)
1110  FORMAT(1X,'DO YOU WANT TO ININIALIZE THE SIGNAL F?
```

```
      1(YES=1 OR NO=0)')
       READ(5,1016) YES
1016   format(I)
       IF(YES.NE.1) GOTO 2000
       write(6,1919)
1919   format(1x,'initial signal is read from data.dat.')
       OPEN(UNIT=1,FILE='DATA.DAT',STATUS='OLD')
       READ(1,1130)(F(I),I=1,NST)
1130   FORMAT(1X,5F13.8)
C
C INPUT D(*),RATE(*),WEI,WR,WMEAN,WMEANR,ERROR,LIMITA AND LIMITB FROM TERMINAL.
2000   WRITE(6,1020) IPM(2)
1020   FORMAT(1X,'INPUT INITIAL (D(I),I=1,',I2,'):',
      1/,1X,'(REAL NUMBERS ONLY!)')
       READ(5,1140) (D(I),I=1,IPM(2))
1140   FORMAT(F)
       WRITE(6,1150) IPM(2)
1150   FORMAT(1X,'INPUT (RATE(I),I=1,',I2,'):',
      1/,1X,'(REAL NUMBERS ONLY!)')
       READ(5,1140)(RATE(I),I=1,IPM(2))
       WRITE(6,1152)
1152   FORMAT(1X,'INPUT WEI AND WR')
       READ(5,1153)WEI,WR
1153   FORMAT(F)
C-----
       WRITE(6,1154)
1154   FORMAT(1X,'INPUT WMEAN AND WMEANR:')
       READ(5,1153) WMEAN,WMEANR
C
       WRITE(6,1160)
1160   FORMAT(1X,'INPUT ERROR:')
       READ(5,1131) ERROR
1131   FORMAT(F)
       WRITE(6,1180)
1180   FORMAT(1X,'INPUT LIMITA AND LIMITB:',/,1X,
      1'(INTEGERS ONLY!)')
       READ(5,1011)(LIMIT(I),I=1,2)
1011   FORMAT(I)
C
C ITERATION A STARTS.
3000   DO 25 ITERA=1,LIMIT(1)
       WRITE(6,1040) ITERA
1040   FORMAT(/,1X,'ITERATION A=',I3)
       DO 100 I=1,IPM(2)
100    D(I)=D(I)*RATE(I)
       WEI=WEI*WR
C-----
       WMEAN=WMEAN*WMEANR
C
       CALL SGJC(D,F,GJC)
C
C ITERATION B STARTS.
       DO 30 ITERB=1,LIMIT(2)
       CALL ARPHA(D,F,GJC,AR)
       DO 60 J=1,NST
60     F(J)=F(J)-AR*GJC(J)
       CALL SGJC(D,F,GJC)
       XGJC=0.
       DO 40 J=1,NST
40     XGJC=XGJC+GJC(J)*GJC(J)
       XGJC=(XGJC**0.5)/FLOAT(NST)
       IF(XGJC.LT.ERROR) GOTO 50
30     CONTINUE
C
C ITERATION B ENDS.
       WRITE(6,1050) XGJC
```

```
1050  FORMAT(1X,'LIMIT OF ITERATION B REACHED.',
     1/,29X,'GRADIENT NORM=',F13.8)
50      XJ=0.
        DO 70 J=1,NST
        ACC=0.
        DO 73 I=1,NST
73      ACC=ACC+B(J,I)*F(I)
70      XJ=XJ+F(J)*ACC
        DO 80 J=1,IPM(2)
        XCON(J)=0.
        NJ=(J-1)*IPM(1)
        DO 80 I=1,NST-NJ
80      XCON(J)=XCON(J)+F(I)*F(I+NJ)
        DO 75 J=2,IPM(2)
75      XCON(J)=XCON(J)/XCON(1)
        XJ=XJ/XCON(1)
C
C-----compute the mean:
        ACC=0.
        DO 81 J=1,NST
81      ACC=ACC+F(J)
        ACC=ACC/NST
C
        WRITE(6,1060) XJ
1060  FORMAT(11X,'IN-BAND ENERGY=',F13.8)
        WRITE(6,1070) (I,XCON(I),I=1,IPM(2))
1070  FORMAT(1X,'CONSTRAINT',I2,'=',F13.8)
C-----
        WRITE(6,1071) ACC
1071  FORMAT(1X,'MEAN = ',F13.8)
C
25      CONTINUE
C
C ITERATION A ENDS.
        WRITE(6,1090)
1090  FORMAT(/,1X,'THE PREVIOUS PROCESS COMPLETED.')
        WRITE(6,1092) (D(I),I=1,IPM(2))
1092  FORMAT(1X,'D=',4F15.3)
        WRITE(6,1102)WEI,WR
1102  FORMAT(1X,'WEI=',F13.3,2X,'WR=',F13.3)
C-----
        WRITE(6,1103) WMEAN,WMEANR
1103  FORMAT(1X,'WMEAN=',F13.3,2X,'WMEANR=',F13.3)
C
        WRITE(6,1091)
1091  FORMAT(1X,'DO YOU WANT TO CONTINUE?(YES=1 OR NO=0)')
        READ(5,1016) YES
        IF(YES.NE.1) GOTO 3010
        WRITE(6,2050)
2050  FORMAT(1X,'USING THE SAME PARAMETERS AS SET BEFORE ?
     1(YES=1 OR NO=0)')
        READ(5,1016) YES
        IF(YES.EQ.1) GOTO 3000
        GOTO 2000
C
C DISPLAY FINAL SIGNAL AT TERMINAL.
3010  WRITE(6,1080) (F(I),I=1,NST)
1080  FORMAT(1X,'F=',5F13.8)
C
C STORE RESULTS IN TPULSE.DAT AFTER SCALING.
        XMAX=0.
        DO 12 I=1,NST
        IF(XMAX.GE.DABS(F(I))) GOTO 12
        XMAX=DABS(F(I))
        XIND=F(I)
12      CONTINUE
```

```
      DO 22 I=1,NST
22    F(I)=F(I)/XIND

      WRITE(2,4000) (I-1,F(I),I=1,NST)
4000  FORMAT(1X,I3,F15.10)
      WRITE(2,4010)(IPM(I),I=1,4)
4010  FORMAT('NSAM=',I3,'  NCON=',I3,'  NRES=',I3,'  NBAND=',I3)
      WRITE(2,1060) XJ
      WRITE(2,1070)(I,XCON(I),I=1,IPM(2))
C-----
      WRITE(2,1071) ACC
C
      STOP
      END
C---------------------------------------------------------------
C GENERATION OF MATRIX B.
C INPUT:IPM(4)(NSAM,NCON,NRES,NBAND)--THROUGH COMMON STATEMENT
C OUTPUT:MATRIX B--THROUGH COMMON STATEMENT.
      SUBROUTINE BMATX
      REAL*8 B(300,300),PI,XI,XJ,XNF,XBAND,WEI
      COMMON B,WEI,IPM(4)
      XBAND=FLOAT(IPM(4))
      XNF=FLOAT(IPM(3)*IPM(1))
      PI=3.14159265359D0
      NST=IPM(1)*IPM(2)
      NFT=IPM(1)*IPM(3)
      DO 20 I=1,NST
      XI=FLOAT(I)
      DO 10 J=1,I-1
      XJ=FLOAT(J)
      B(I,J)=DSIN(2.*PI*(XI-XJ)*(XBAND+0.5)/XNF)/DSIN(PI*(XI-XJ)/XNF)
10    B(J,I)=B(I,J)
      B(I,I)=2.*(XBAND+0.5)
20    CONTINUE
      DO 5 I=1,NST
      DO 5 J=1,NST
5     B(I,J)=B(I,J)/DFLOAT(NFT)
      RETURN
      END
C---------------------------------------------------------------
C GENERATION OF GRADIENT GJC.
C INPUT:WEIGHT VECTOR D(*);SIGNAL VECTOR F(*);
C INPUT THRU COMMON: IPM(4)(NSAM,NCON,NRES,NBAND);MATRIX B;WMEAN
C OUTPUT:GRADIENT VECTOR GJC(*).
      SUBROUTINE SGJC(D,F,GJC)
      REAL*8 B(300,300),GJC(300),F(300),X,Y,X1,Y1,XX(10),D(10),WEI
      REAL*8 WMEAN
      COMMON B,WEI,IPM(4),WMEAN
      NST=IPM(1)*IPM(2)
      NFT=IPM(1)*IPM(3)
      DO 5 K=1,IPM(2)
      XX(K)=0.
      NK=(K-1)*IPM(1)
      DO 15 M=1,NST-NK
15    XX(K)=XX(K)+F(M)*F(M+NK)
5     CONTINUE
      XX(1)=XX(1)-1.
      DO 10 I=1,NST
      X=0.
      DO 20 K=1,IPM(2)
      NK=(K-1)*IPM(1)
      X1=0.
      Y1=0.
      IF((I+NK).LE.NST) X1=F(I+NK)
      IF((I-NK).GE.1) Y1=F(I-NK)
      Y=XX(K)*(X1+Y1)
```

223

```
20      X=X+Y*D(K)
        Y=0.
        DO 40 J=1,NST
        DEL=0.
        IF(I.EQ.J) DEL=1.
40      Y=Y+(B(I,J)-DEL)*F(J)
10      GJC(I)=2.*(X-Y*WEI)
c
c-----add the component due to the constraint on mean:
        X=0
        DO 50 I=1,NST
50      X=X+F(I)
        X=X/NST**2
        DO 60 I=1,NST
60      GJC(I)=GJC(I)+2.*WMEAN*X
c
        RETURN
        END
C-------------------------------------------------------------------------
C FIND A OPTIMUM STEP LENGTH(AR) IN A GIVEN DIRECTION.
C INPUT:WEIGHT VECTOR D(*);SIGNAL VECTOR F(*);
C INPUT:GRADIENT VECTOR GJC(*).
C INPUT THRU COMMON:IPM(4)(NSAM,NCON,NRES,NBAND);MATRIX B;WMEAN
C OUTPUT:OPTIMUM STEP LENGTH AR.
        SUBROUTINE ARPHA(D,F,GJC,AR)
        REAL*8 B(300,300),GJC(300),F(300),AR,GJC1,X,Y,D(10),WEI
        REAL*8 AA(10),BB(10),CC(10),DD,EE,T(4),ACC
        real*8 wmean
        COMMON B,WEI,IPM(4),wmean
        NST=IPM(1)*IPM(2)
        NFT=IPM(1)*IPM(3)
        DO 20 K=1,IPM(2)
        NK=(K-1)*IPM(1)
        AA(K)=0.
        BB(K)=0.
        CC(K)=0.
        DO 20 M=1,NST-NK
        AA(K)=AA(K)+F(M)*F(M+NK)
        BB(K)=BB(K)+GJC(M)*F(M+NK)+F(M)*GJC(M+NK)
20      CC(K)=CC(K)+GJC(M)*GJC(M+NK)
        AA(1)=AA(1)-1.
        DD=0.
        EE=0.
        DO 30 I=1,NST
        ACC=0.
        DO 35 J=1,NST
        DEL=0.
        IF(I.EQ.J) DEL=1.
35      ACC=ACC+(B(I,J)-DEL)*GJC(J)
        DD=DD+GJC(I)*ACC
30      EE=EE+F(I)*ACC
        DD=DD*WEI
        EE=EE*WEI
        DO 40 I=1,4
40      T(I)=0.
        DO 50 K=1,IPM(2)
        T(4)=T(4)+D(K)*CC(K)*CC(K)
        T(3)=T(3)+D(K)*BB(K)*CC(K)
        T(2)=T(2)+D(K)*(2.*AA(K)*CC(K)+BB(K)*BB(K))
50      T(1)=T(1)+D(K)*AA(K)*BB(K)
        T(4)=2.*T(4)
        T(3)=-3.*T(3)
        T(2)=-DD+T(2)
        T(1)=EE-T(1)
c       Note: The gradient along the 1-D path should be expressed as
c             2*(T(1)+T(2)*ar+T(3)*ar**2+T(4)*ar**3).
```

```
c
c-----add the component due to the constraint on mean:
      dd=0.
      ee=0.
      do 55 i=1,nst
      dd=dd+f(i)
55    ee=ee+gjc(i)
      dd=dd/nst
      ee=ee/nst
      t(1)=t(1)-wmean*dd*ee
      t(2)=t(2)+wmean*ee*ee
c
      IF(T(1).LE.0.) GOTO 60
      STOP 'ERROR 2: wrong direction in 1-D search.'
60    X=0.
      Y=0.0000001
      DO 70 I=1,100
      GJC1=0.
      DO 80 J=1,4
80    GJC1=GJC1+T(J)*Y**(J-1)
      IF(GJC1.GE.0.) GOTO 90
      X=Y
70    Y=2.*Y
      STOP 'ERROR 3: the other side of the valley could not be reached.'
90    DO 100 I=1,100
      AR=(X+Y)/2.
      GJC1=0.
      DO 110 J=1,4
110   GJC1=GJC1+T(J)*AR**(J-1)
      IF(GJC1.GT.0.) Y=AR
      IF(GJC1.LE.0.) X=AR
      IF(ABS(X-Y).LT.1.E-10) GOTO 45
100   CONTINUE
      STOP 'ERROR 1: convergence in 1-D search did not occur.'
45    RETURN
      END
```

Appendix A2: <u>Sample Output: TPULSE.DAT</u>

```
 0   -0.0063850000
 1   -0.0132712891
 2   -0.0204579788
 3   -0.0270813198
 4   -0.0321861728
 5   -0.0348180783
 6   -0.0341271503
 7   -0.0294743808
 8   -0.0205297471
 9   -0.0073512550
10    0.0095651566
11    0.0292730909
12    0.0504059947
13    0.0712521744
14    0.0898723721
15    0.1042535544
16    0.1124886082
17    0.1129682948
18    0.1045694324
19    0.0868221517
20    0.0600393773
21    0.0253935161
22   -0.0150713911
23   -0.0584992558
24   -0.1013549779
25   -0.1396278262
26   -0.1690900018
27   -0.1855978616
28   -0.1854252520
29   -0.1655839682
30   -0.1241206550
31   -0.0603617531
32    0.0249158261
33    0.1294061761
34    0.2492998162
35    0.3794175417
36    0.5134491901
37    0.6442857369
38    0.7644256221
39    0.8664298739
40    0.9433959791
41    0.9894179579
42    1.0000000000
43    0.9723933671
44    0.9058309560
45    0.8016406199
46    0.6632266012
47    0.4959176201
48    0.3066896079
49    0.1037800503
50   -0.1037800503
51   -0.3066896079
52   -0.4959176201
53   -0.6632266012
54   -0.8016406199
55   -0.9058309560
56   -0.9723933671
57   -1.0000000000
58   -0.9894179579
59   -0.9433959791
60   -0.8664298739
61   -0.7644256221
62   -0.6442857369
```

```
63   -0.5134491901
64   -0.3794175417
65   -0.2492998162
66   -0.1294061761
67   -0.0249158261
68    0.0603617531
69    0.1241206550
70    0.1655839682
71    0.1854252520
72    0.1855978616
73    0.1690900018
74    0.1396278262
75    0.1013549779
76    0.0584992558
77    0.0150713911
78   -0.0253935161
79   -0.0600393773
80   -0.0868221517
81   -0.1045694324
82   -0.1129682948
83   -0.1124886082
84   -0.1042535544
85   -0.0898723721
86   -0.0712521744
87   -0.0504059947
88   -0.0292730909
89   -0.0095651566
90    0.0073512550
91    0.0205297471
92    0.0294743808
93    0.0341271503
94    0.0348180783
95    0.0321861728
96    0.0270813198
97    0.0204579788
98    0.0132712891
99    0.0063850000
NSAM= 25   NCON=  4   NRES=100   NBAND=130
           IN-BAND ENERGY=      0.99978340
 CONSTRAINT 1=     1.00120665
 CONSTRAINT 2=     0.00025773
 CONSTRAINT 3=     0.00091064
 CONSTRAINT 4=     0.00112901
 MEAN  =     0.00000000
```

Figure 1: Pitch-frequencies corresponding to the keys 'c' and 'g' in a piano. These correspond to the major diatonic scale of western music. The spacing is very nonuniform, and will appear to be almost uniform on a logarithmic scale.

Figure 2: A baseband T-pulse with zero mean and no intersymbol interference.
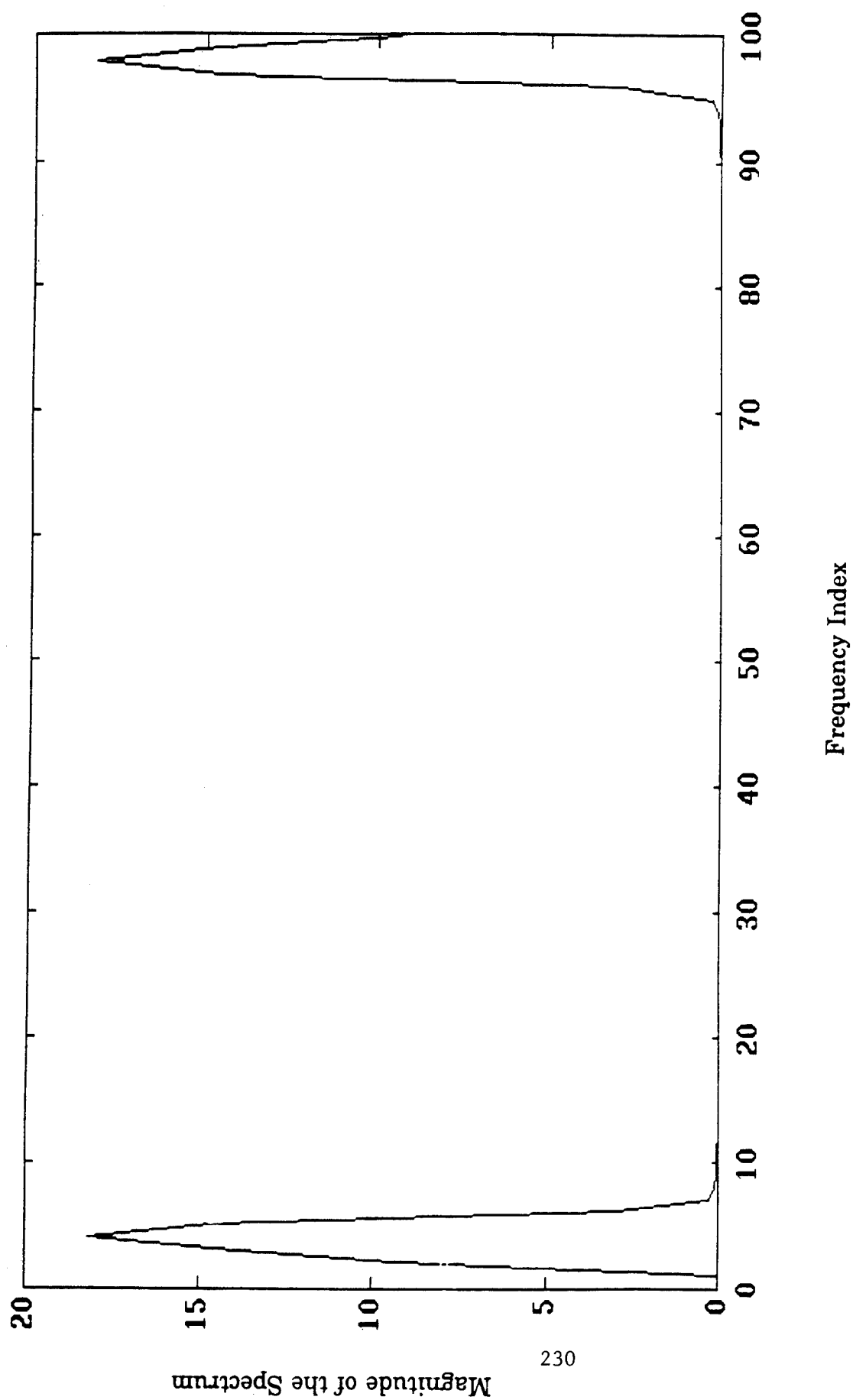
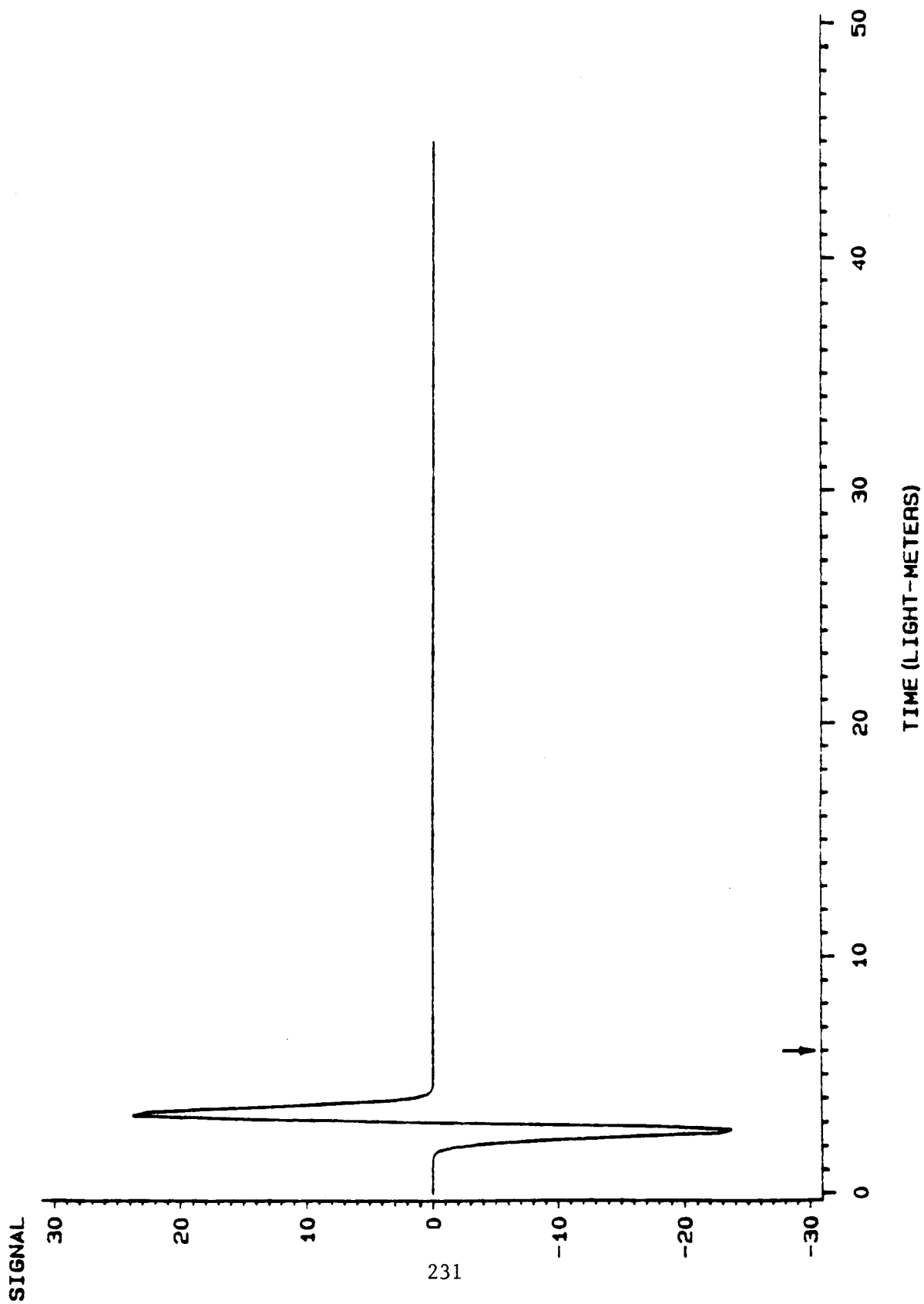Figure 3:   Spectrum of the zero mean baseband T-pulse.

Figure 4: Derivative of a narrow Gaussian pulse.
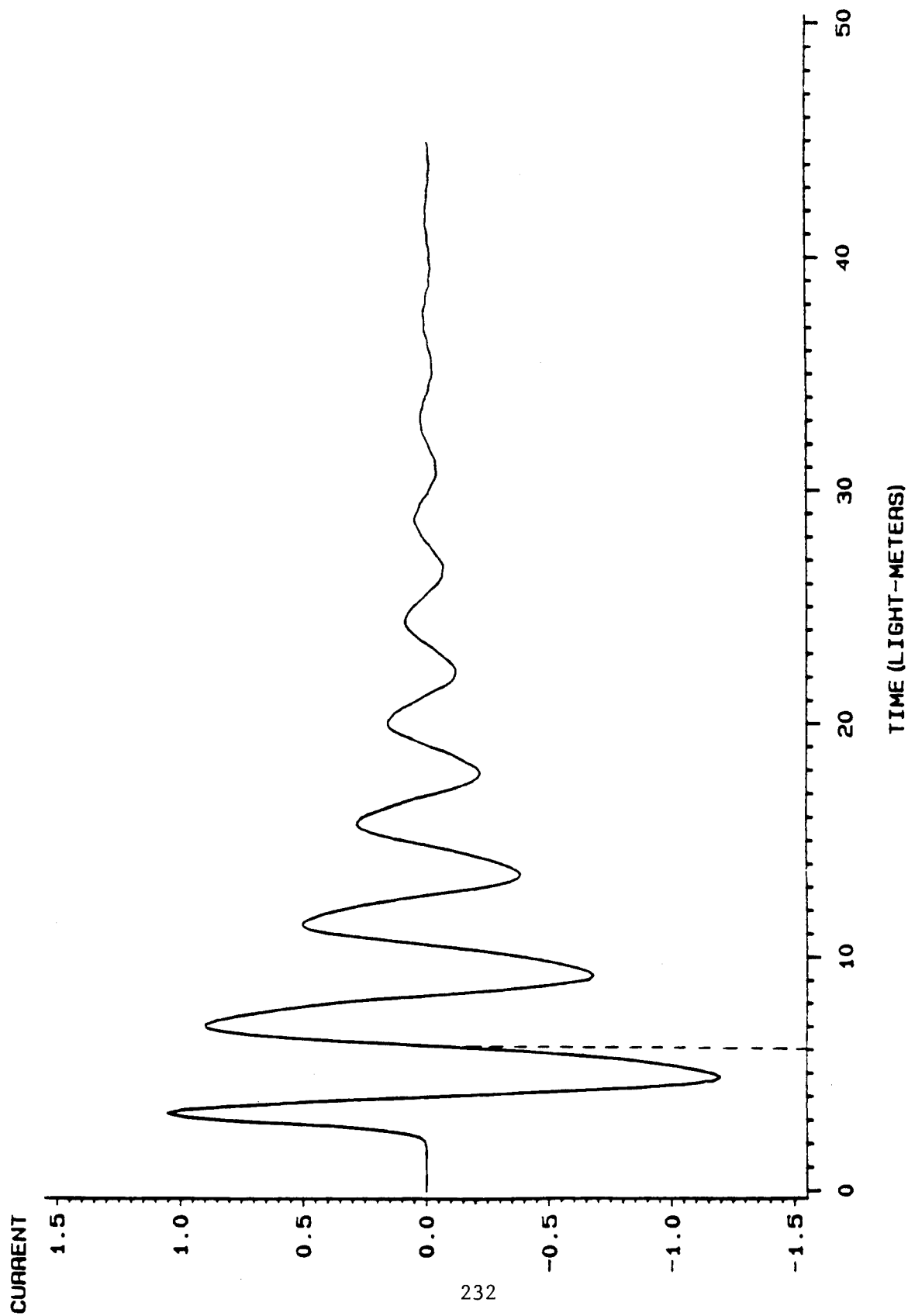The sampling interval T is 0.15 light-meters.

Figure 5: Synthesized current response at the center of a thin wire activated by a narrow pulse from the broadside. Sampling interval is 0.15 light-meters.

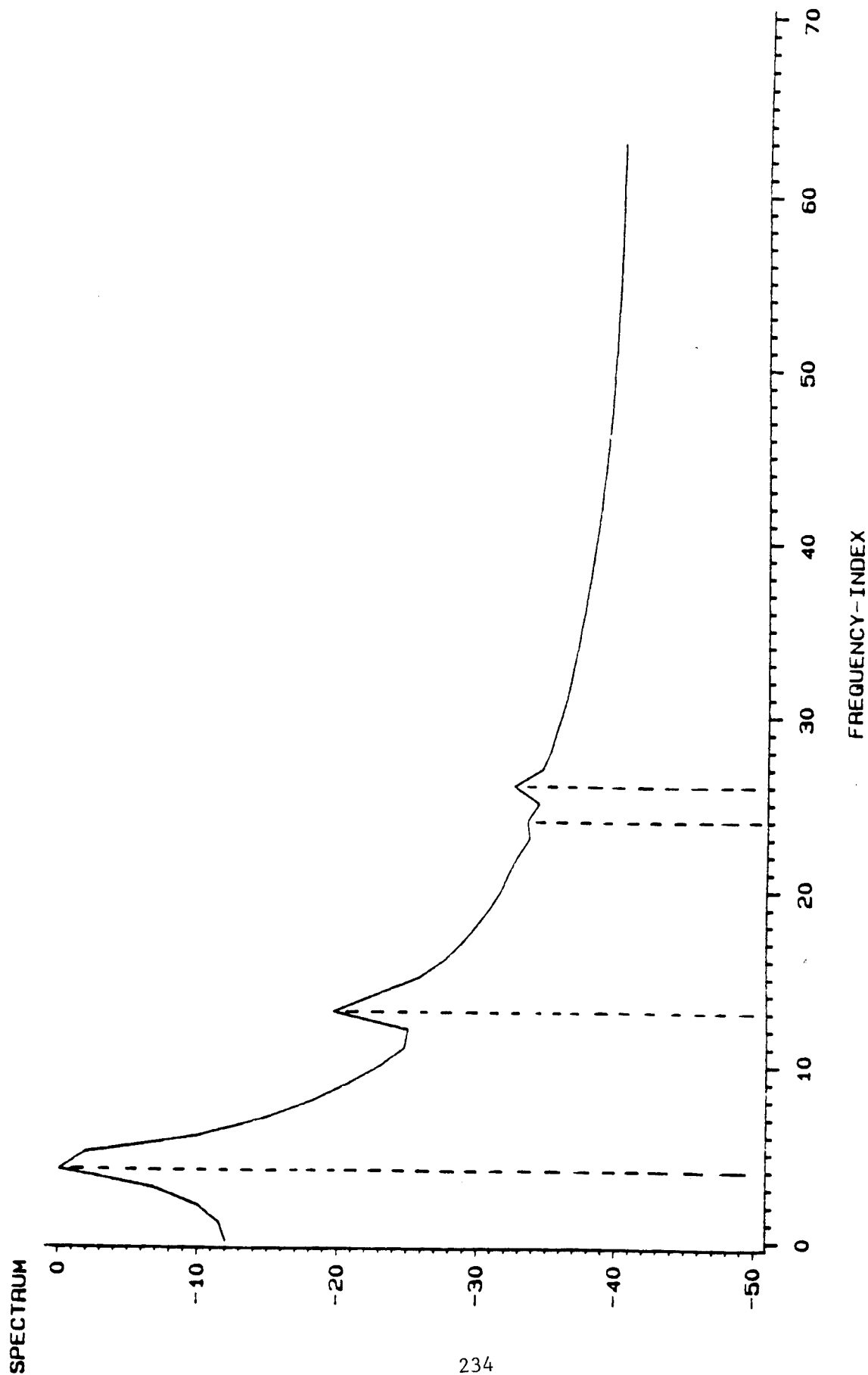Figure 6: DFT amplitude spectrum (DB) of the derivative of the Gaussian pulse. The frequency resolution is $1/(128T)$.

Figure 7:   DFT amplitude spectrum (DB) of the current response (40T thru 167T) excited by a narrow Gaussian pulse. The frequency resolution is 1/128T) the sampling interval T is 0.15 light-meters.
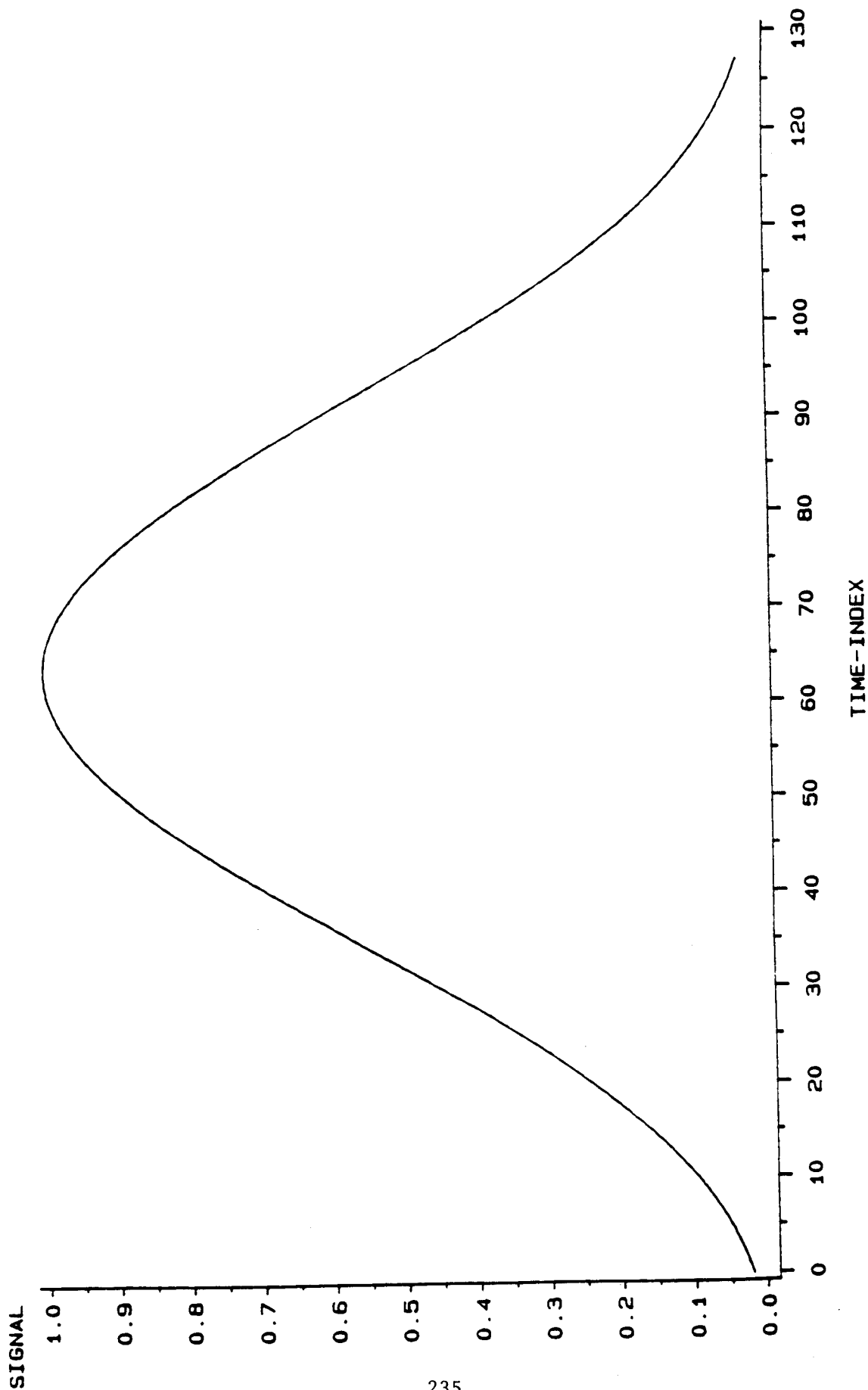
Figure 8: An optimum baseband signal of duration 127T. The in-band energy is 99.995% with the bandwidth 2/(128T). The computing frequency resolution was 30 times higher.

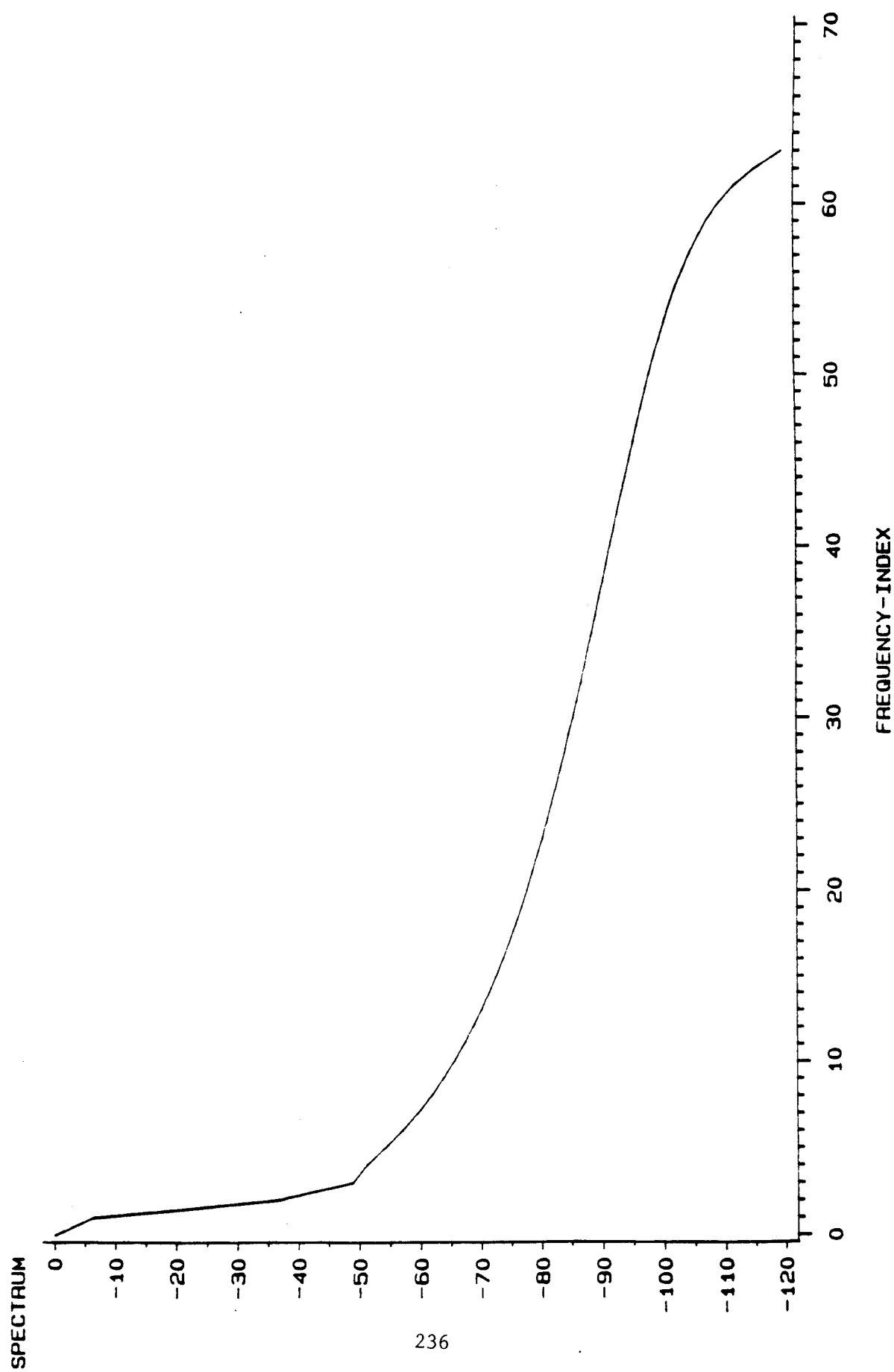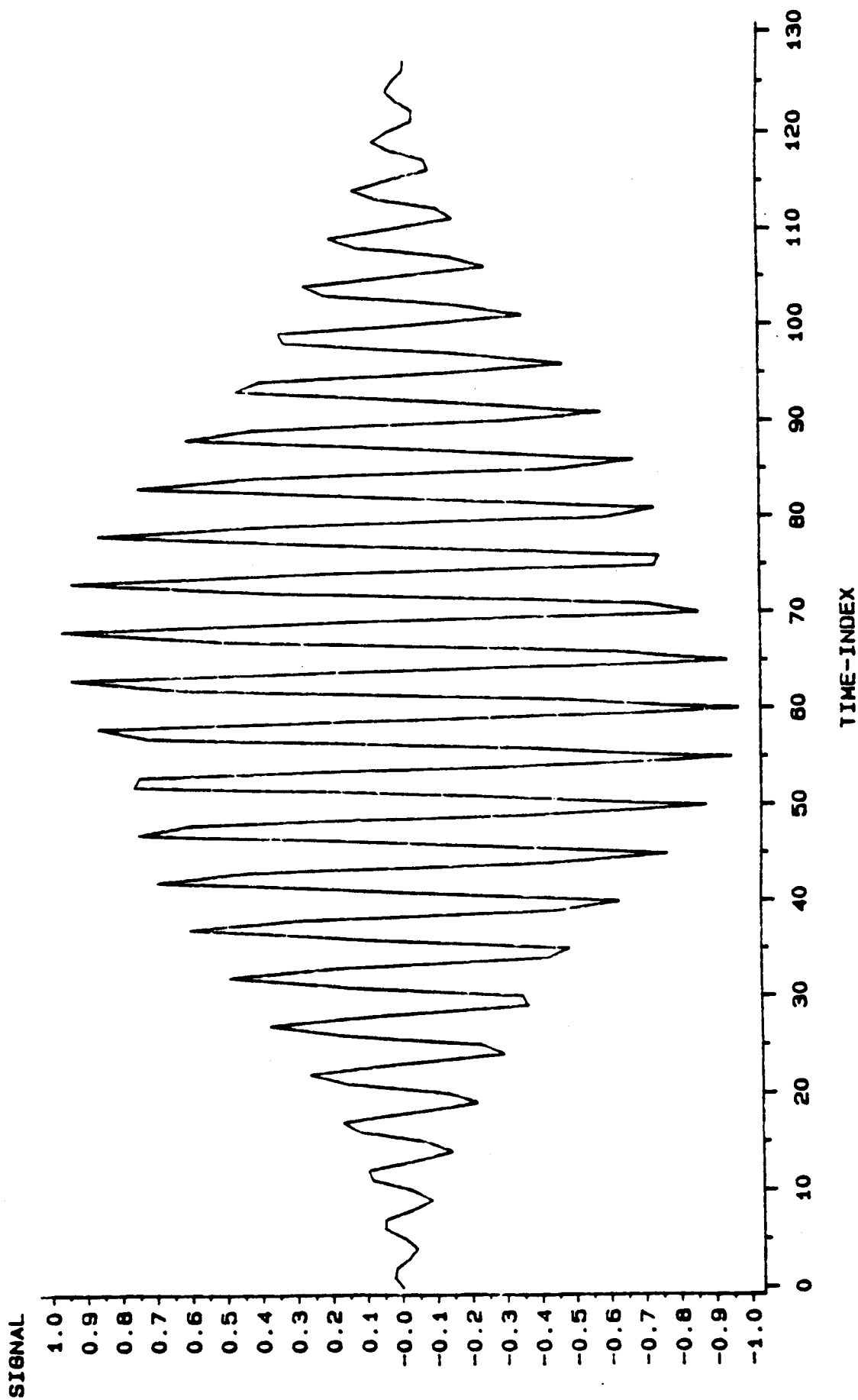Figure 9: DFT amplitude spectrum (DB) of the baseband signal. The frequency resolution is 1/(128T).

Figure 10:   Modulated signal of duration 127T and center frequency
25/(128T). The corresponding baseband signal has maximum
energy (99.995%) within the bandwidth 2/(128T). The
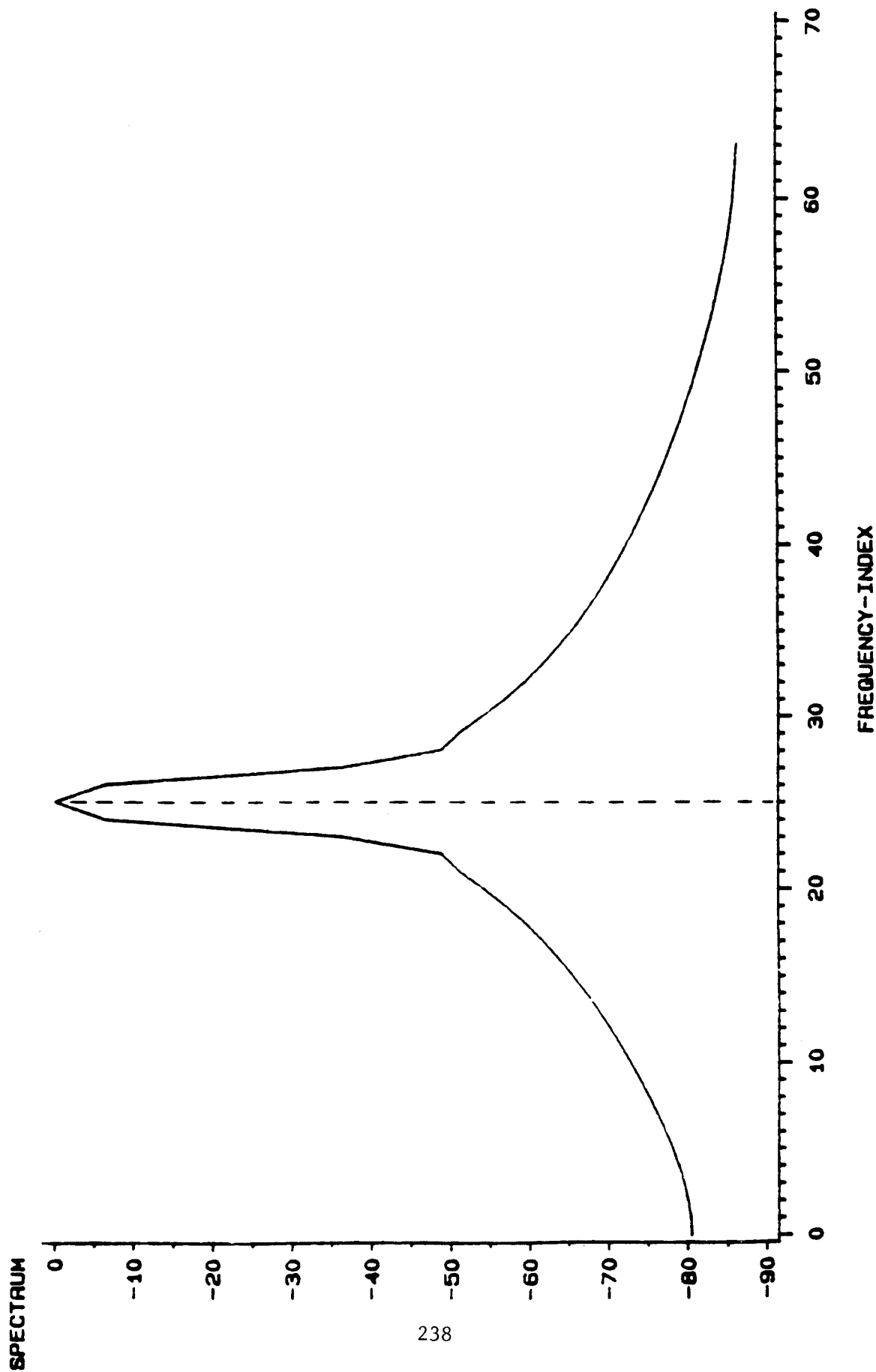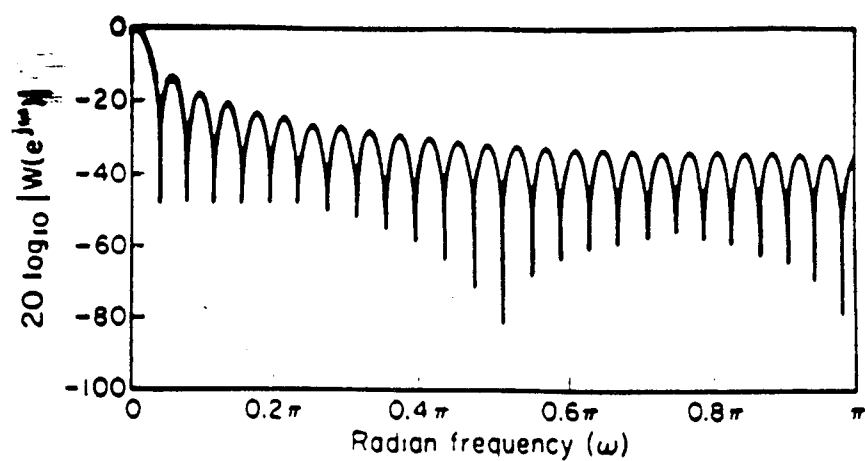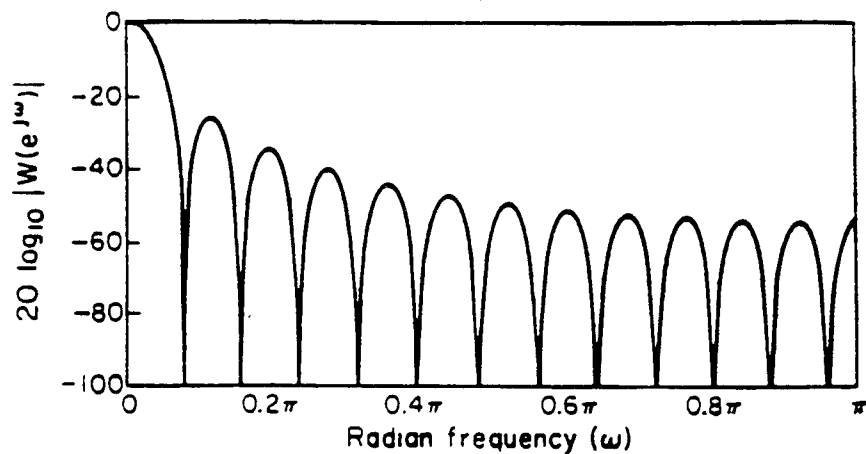computing frequency resolution was 30 times higher.

SPECTRUM

Figure 11:   DFT amplitude spectrum (DB) of the modulated signal. The center frequency is 25/(128T). The frequency resolution is 1/(128T).
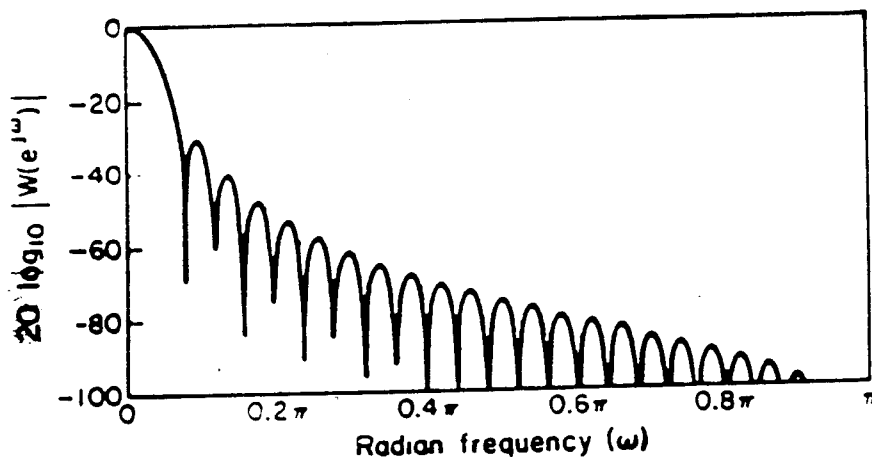
Figure 12:   Fourier transforms (log magnitude) of windows of
              (a) Rectangular
              (b) Bartlett
              (c) Hanning   239

Figure 12:   Fourier transforms (log magnitude) of windows of
                    (d) Hamming
                    (e)Blackman
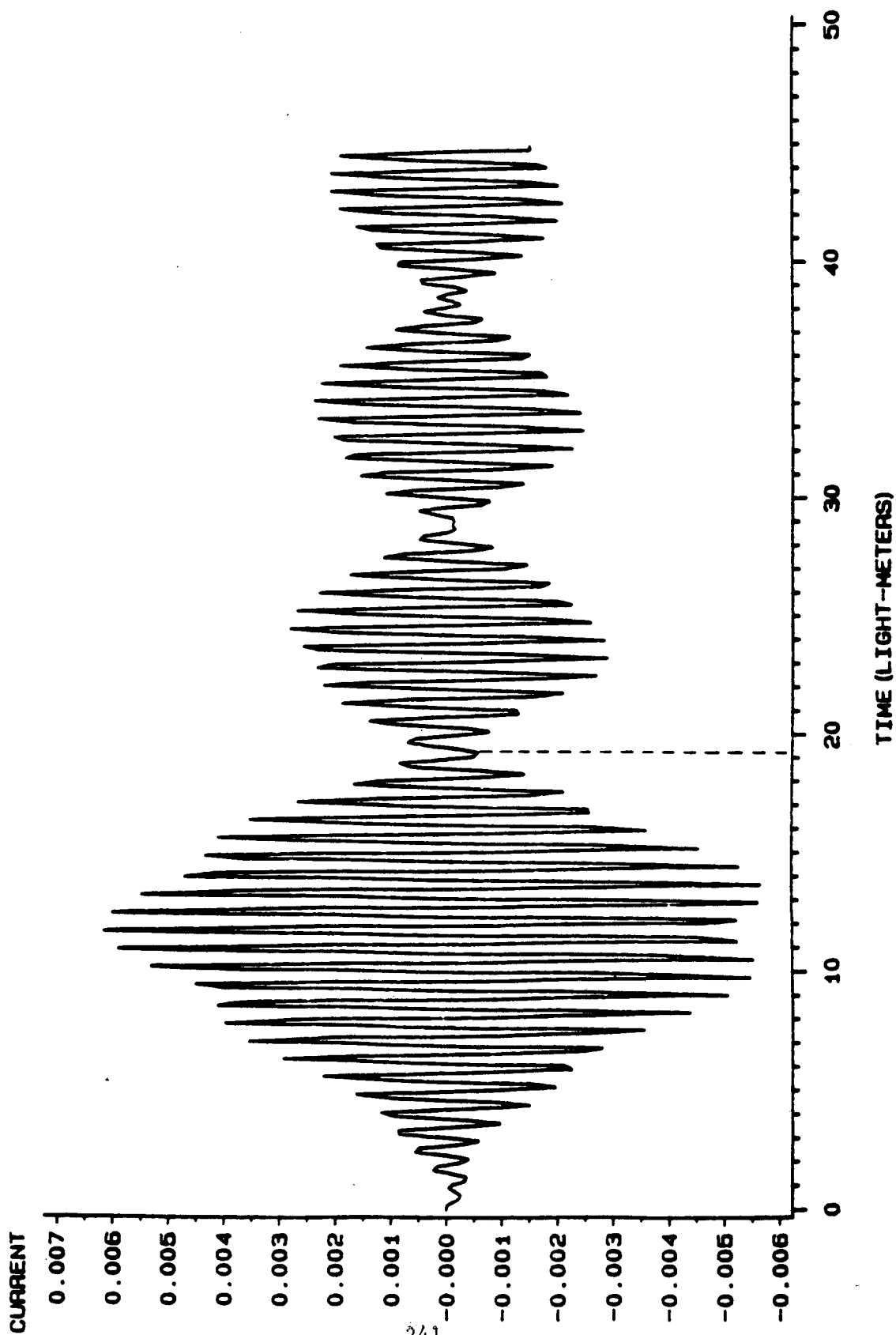
Figure 13: Synthesized current response at the center of a thin wire activated by a narrow band electric field pulse from the broadside. The center frequency of that pulse is 25 sampling interval is 0.15 light-meters.

Figure 14: DFT amplitude spectrum (DB) of the current response (129T thru 256T) the exciting pulse has center frequency 25/(129T). The frequency resolution is 1/(128T). The sampling interval T is 0.15 light-meters.
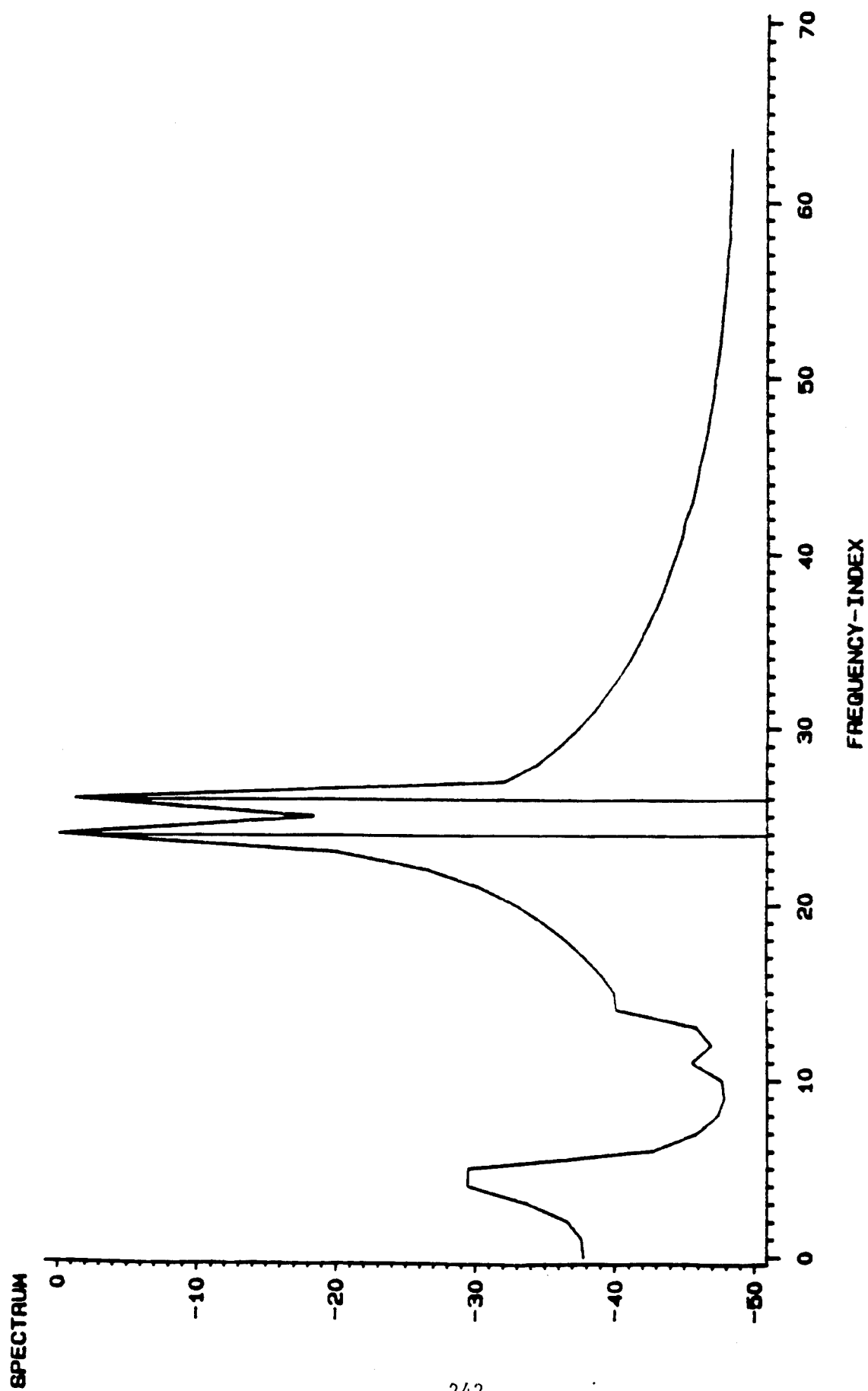
DISTRIBUTION LIST

addresses	number of copies
RL/OCSS ATTN: MR. CLIFFORD TSAO 26 ELECTRONIC PKY GRIFFISS AFB NY 13441-4514	3
SYRACUSE UNIVERSITY ELECTRICAL & COMPUTER ENGR DEPT 121 LINK HALL SYRACUSE NY 13244	2
RL/SUL TECHNICAL LIBRARY 26 ELECTRONIC PKY GRIFFISS AFB NY 13441-4514	1
ADMINISTRATOR DEFENSE TECHNICAL INFO CENTER DTIC-FDAC CAMERON STATION BUILDING 5 ALEXANDRIA VA 22304-6145	2
ADVANCED RESEARCH PROJECTS AGENCY 3701 NORTH FAIRFAX DRIVE ARLINGTON VA 22203-1714	1
NAVAL WARFARE ASSESSMENT CENTER GIDEP OPERATIONS CENTER/CODE QA-50 ATTN: E RICHARDS CORONA CA 91718-5000	1
WRIGHT LABORATORY/AAAI-2 ATTN: MR FRANKLIN HUTSON WRIGHT-PATTERSON AFB OH 45433-6543	1
AFIT/LDEE 2950 P STREET WRIGHT-PATTERSON AFB OH 45433-6577	1

```
WRIGHT LABORATORY/MLPO                              1
ATTN:  D.L. DENISON
WRIGHT-PATTERSON AFB OH 45433-6533


WRIGHT LABORATORY/MTEL                              1
WRIGHT-PATTERSON AFB OH 45433


WRIGHT LABORATORY/FIVS/SURVIAC                      1
WRIGHT-PATTERSON AFB OH 45433


AAMRL/HE                                            1
WRIGHT-PATTERSON AFB OH 45433-6573


AUL/LSE                                             1
BLDG 1405
MAXWELL AFB AL 36112-5564


US ARMY STRATEGIC DEF                              1
CSSD-IM-PA
PO BOX 1500
HUNTSVILLE AL 35807-3801


COMMANDING OFFICER                                 1
NAVAL AVIONICS CENTER
LIBRARY D/765
INDIANAPOLIS IN 46219-2189


COMMANDING OFFICER                                 1
NCCOSC RDTE DIVISION
CODE 02748, TECH LIBRARY
53560 HULL STREET
SAN DIEGO CA 92152-5001


CMDR                                               1
NAVAL WEAPONS CENTER
TECHNICAL LIBRARY/C3431
CHINA LAKE CA 93555-6001
```

```
CDR, U.S. ARMY MISSILE COMMAND                    2
REDSTONE SCIENTIFIC INFO CENTER
AMSMI-RD-CS-R/ILL DOCUMENTS
REDSTONE ARSENAL AL 35898-5241


ADVISORY GROUP ON ELECTRON DEVICES              2
ATTN:  DOCUMENTS
2011 CRYSTAL DRIVE,SUITE 307
ARLINGTON VA 22202


REPORT COLLECTION, RESEARCH LIBRARY             1
MS P364
LOS ALAMOS NATIONAL LABORATORY
LOS ALAMOS NM 87545


AEDC LIBRARY                                    1
TECH FILES/MS-100
ARNOLD AFB TN 37389


COMMANDER/USAISC                                1
ATTN:  ASOP-DO-TL
BLDG 61801
FT HUACHUCA AZ 85613-5000


AIR WEATHER SERVICE TECHNICAL LIB               1
FL 4414
SCOTT AFB IL 62225-5458


AFIWC/MSO                                        1
102 HALL BLVD STE 315
SAN ANTONIO TX 78243-7016


NSA                                             1
ATTN: D. ALLEY
DIV X911
9800 SAVAGE ROAD
FT MEADE MD 20755-6000

DOD                                             1
R31
9800 SAVAGE ROAD
FT. MEADE MD 20755-6000
```

```
DIRNSA                                              1
R509
9800 SAVAGE ROAD
FT MEADE MD 20775


NSA/CSS                                             1
R9
FORT GEORGE G. MEADE MD 20755-6000


DEFENSE TECHNOLOGY SEC ADMIN (DTSA)                 1
ATTN:  STTD/PATRICK SULLIVAN
400 ARMY NAVY DRIVE
SUITE 300
ARLINGTON VA 22202

TECHNOLOGY SERVICE CORP                             1
6515 MAIN STREET
TRUMBULL CT 06611
```

Rome Laboratory

Customer Satisfaction Survey

RL-TR-_____

Please complete this survey, and mail to RL/IMPS,
26 Electronic Pky, Griffiss AFB NY 13441-4514. Your assessment and
feedback regarding this technical report will allow Rome Laboratory
to have a vehicle to continuously improve our methods of research,
publication, and customer satisfaction. Your assistance is greatly
appreciated.
Thank You

_____

_____

Organization Name:_____(Optional)

Organization POC: _____(Optional)

Address:_____

1.   On a scale of 1 to 5 how would you rate the technology
developed under this research?

    5-Extremely Useful   1-Not Useful/Wasteful

                    Rating_____

Please use the space below to comment on your rating. Please
suggest improvements. Use the back of this sheet if necessary.

2.   Do any specific areas of the report stand out as exceptional?

                    Yes___ No_____

    If yes, please identify the area(s), and comment on what
aspects make them "stand out."

3. Do any specific areas of the report stand out as inferior?

Yes___ No___

If yes, please identify the area(s), and comment on what aspects make them "stand out."

4. Please utilize the space below to comment on any other aspects of the report. Comments on both technical content and reporting format are desired.

MISSION

OF

ROME LABORATORY

Mission. The mission of Rome Laboratory is to advance the science and technologies of command, control, communications and intelligence and to transition them into systems to meet customer needs. To achieve this, Rome Lab:

    a. Conducts vigorous research, development and test programs in all applicable technologies;

    b. Transitions technology to current and future systems to improve operational capability, readiness, and supportability;

    c. Provides a full range of technical support to Air Force Materiel Command product centers and other Air Force organizations;

    d. Promotes transfer of technology to the private sector;

    e. Maintains leading edge technological expertise in the areas of surveillance, communications, command and control, intelligence, reliability science, electro-magnetic technology, photonics, signal processing, and computational science.

The thrust areas of technical competence include: Surveillance, Communications, Command and Control, Intelligence, Signal Processing, Computer Science and Technology, Electromagnetic Technology, Photonics and Reliability Sciences.